TAILORING THERMAL RADIATIVE PROPERTIES AND ENHANCING NEAR-FIELD RADIATIVE HEAT FLUX WITH ELECTROMAGNETIC METAMATERIALS

A Dissertation
Presented to
The Academic Faculty

by

Xianglei Liu

In Partial Fulfillment
of the Requirements for the Degree
Doctor of Philosophy in the
George W. Woodruff School of Mechanical Engineering

Georgia Institute of Technology
May 2016

TAILORING THERMAL RADIATIVE PROPERTIES AND ENHANCING NEAR-FIELD RADIATIVE HEAT FLUX WITH ELECTROMAGNETIC METAMATERIALS

Approved by:

Dr. Zhuomin Zhang, Advisor
George W. Woodruff School of
Mechanical Engineering
Georgia Institute of Technology

Dr. Martin Maldovan
School of Physics
Georgia Institute of Technology

Dr. Baratunde A. Cola
George W. Woodruff School of
Mechanical Engineering
Georgia Institute of Technology

Dr. Michael Filler
School of Chemical &
Biomolecular Engineering
Georgia Institute of Technology

Dr. Satish Kumar
George W. Woodruff School of
Mechanical Engineering
Georgia Institute of Technology

Date Approved: Feb. 19th, 2016

ACKNOWLEDGEMENTS

First and foremost, I would like to express my sincere thanks to my advisor and mentor Dr. Zhuomin Zhang for his guidance and encouragement throughout my Ph.D. studies. Looking back, I am very grateful for his offering me the opportunity of joining in the Nanoscale Thermal Radiation Lab five years ago. At that time, I was totally unfamiliar with thermal radiation and it was Dr. Zhang who brought me to this very interesting field without whom this dissertation would have never become reality. I benefited tremendously from the inspiring discussions with him, and the confidence and courage he gave me to face the challenges. I would also like to thank my Committee members: Dr. Baratunde A. Cola, Dr. Satish Kumar, Dr. Martin Maldovan, and Dr. Michael Filler for their valuable suggestions.

My sincere appreciation also goes to my former and current group members. It is a really wonderful thing to discuss and collaborate with them during my Ph.D. study. I want to thank Dr. Xiaojia Wang for her help to use integrating spheres and TAAS, and Dr. Liping Wang for his assistance with learning theories at the first year of my Ph.D. studies. I would also like to thank Bo Zhao, Zihao Zhang, Trevor Bright, Jesse Watjen, and Peiyan Yang for fruitful collaborations and interactions.

In addition, I would also like to thank the Department of Energy and National Science Foundation for partially supporting the work in this dissertation.

Finally, I am greatly indebted to my parents and sisters for their love and encouragement through all these years. I also want to thank numerous friends for their company and support.

TABLE OF CONTENTS

LIST OF FIGURES

LIST OF SYMBOLS

Variables

c	speed of light in vacuum
d	gap separation distance
$\mathbf{D}$	matrix
e	charge of electron, 1.6022×10^{-19} C
$\mathbf{E}$	electric field
f	volume filling fraction
g	gravitational acceleration rate
$\overline{\overline{\mathbf{G}}}$	Green's function
h	thickness
$\hbar$	Planck's constant divided by 2π
H	thickness
$\mathbf{H}$	magnetic field
$\mathbf{I}$	unit matrix
J	current
$\mathbf{J}$	current vector
$\mathbf{k}$	wavevector
k	index or wavevector magnitude
k_B	Boltzmann's constant, 1.3065×10^{-12} m^2 kg s^2 K^{-1}
l	index
m	mass
$\mathbf{M}$	transfer matrix
n	refractive index

N	carrier concentration, number of layers, or diffraction order
P	period
$\mathbf{P}$	polarization vector or propagation matrix
q	heat flux or elementary charge
Q	heat flux
r	Fresnel reflection coefficient
$\mathbf{r}$	position vector
R	reflectance
$\mathbf{R}$	reflection coefficient matrix
$\mathbf{S}$	Poynting vector
t	Fresnel transmission coefficient or layer thickness
T	transmittance or temperature
W	width
x,y,z	Cartesian coordinates

Greek Symbols

β	transverse wavevector
γ	z-component of wavevector
δ	Dirac delta function or lateral shift
δ_{nj}	Kronecker delta
Δ	relative rotation angle
ε	dielectric function
ε'	real part of dielectric function
ε''	imaginary part of dielectric function

$\bar{\bar{\varepsilon}}$	dielectric tensor
Θ	mean energy of Planck oscillator
κ	extinction coefficient
λ	wavelength
μ	magnetic permeability or chemical potential
ν	wavenumber
ξ	energy transmission coefficient
ϕ	azimuthal angle
τ	relaxation time
ω	angular frequency
σ	Stefan-Boltzmann constant or electrical conductivity

Subscripts/Superscripts

0	0^{th} index or free space
d	dielectric
E	extraordinary wave
f	film
i,j,k	index
m	metal
O	ordinary wave (TE wave)
p	p polarization
s	s polarization
x,y,z	component direction

LIST OF ABBREVIATIONS

1D	one-dimensional
2D	two-dimensional
D-Si	doped silicon
D-SiNW	doped silicon nanowires
D-SiNH	doped silicon nanoholes
EMT	effective medium theory
EOT	extraordinary transmission
FDTD	finite difference time domain
FEM	finite element method
HMM	hyperbolic metamaterials
LDOS	local density of states
MPs	magnetic polaritons
RCWA	rigorous coupled wave analysis
PA	proximity approximation
PFA	proximity force approximation
SPPs	surface plasmon polaritons
SPhPs	surface phonon polaritons
TE	transverse electric
TM	transverse magnetic
TPV	thermophotovoltaic

SUMMARY

All substances above zero kelvin temperature emit fluctuating electromagnetic waves due to the random motions of charge carriers. Controlling the spectral and directional radiative properties of surfaces has wide applications in energy harvesting and thermal management. Artificial metamaterials have attracted much attention in the last decade due to their unprecedented optical and thermal properties beyond those existing in nature. This dissertation aims at tailoring radiative properties at infrared regime and enhancing the near-field radiative heat transfer by employing metamaterials.

A comprehensive study is performed to investigate the extraordinary transmission, negative refraction, and tunable perfect absorption of infrared light. A polarizer is designed with an extremely high extinction ratio based on the extraordinary transmission through perforated metallic films. The extraordinary transmission of metallic gratings can be enhanced and tuned if a single layer of graphene is covered on top. Metallic metamaterials are not the unique candidate supporting exotic optical properties. Thin films of doped silicon nanowires can support negative refraction of infrared light due to the presence of hyperbolic dispersion. Long doped-silicon nanowires are found to exhibit broadband tunable perfect absorption.

Besides the unique far-field properties, near-field radiative heat transfer can be mediated by metamaterials. Bringing objects with different temperatures close can enhance the radiative heat flux by orders of magnitude beyond the limit set by the Stefan-Boltzmann law. Metamaterials provide ways to make the energy transport more efficient. Very high radiative heat fluxes are shown based on carbon nanotubes, nanowires, and nanoholes using effective medium theory (EMT). The quantitative application condition of EMT is presented for metallodielectric metamaterials. Exact formulations including the scattering theory and Green's function method are employed to investigate one- and

two-dimensional gratings as well as metasurfaces when the period is not sufficiently small. New routes for enhancing near-field radiative energy transport are opened based on proposed hybridization of graphene plasmons with hyperbolic modes, hybridization of graphene plasmons with surface phonon modes, or hyperbolic graphene plasmons with open surface plasmon dispersion relation. Noncontact solid-state refrigeration is theoretically demonstrated to be feasible based on near-field thermal radiation.

In addition, the investigation of near-field momentum exchange (Casimir force) between metamaterials is also conducted. Simultaneous enhancement of the near-field energy transport and suppress of the momentum exchange is theoretically achieved. A design based on repulsive Casimir force is proposed to achieve tunable stable levitation. The dissertation helps to understand the fundamental radiative energy transport and momentum exchange of metamaterials, and has significant impacts on practical applications such as design of nanoscale thermal and optical devices, local thermal management, thermal imaging beyond the diffraction limit, and thermophotovoltaic energy harvesting.

CHAPTER 1

INTRODUCTION

Thermal radiation is one of the most general phenomena in the universe. Any materials at temperatures higher than absolute zero emit electromagnetic waves due to the thermal fluctuations of free charges or ions. As one of the two fundamental modes of heat transfer, thermal radiation plays an important role in many engineering applications or instruments, such as combustion, heat management of space crafts, nonintrusive temperature measurement, high temperature heat exchangers, and waste heat harvesting [1-3]. Thermal radiation is also pertinent to our daily life, e.g., the sunshine we can observe is due to the thermal radiation of the sun. The thermal equilibrium achieved through the radiative energy exchange between the sun and the earth enables a suitable surface temperature of the earth for us to live.

With the advances of nanofabrication and characterization techniques in the past 30 years, people start to go beyond conventional bulk materials for the pursuit of tunable radiative properties to meet different needs. A particular kind, metamaterials, artificial nanostructures with subwavelength scale of units, have attracted much attention in the past two decades due to the exotic optical, electric, and thermal properties [4-7]. Both spectral and directional radiative properties can be mediated by patterning bulk materials into metamaterials, and this technique has wide applications in solar energy harvesting, radiation cooling, sensing, thermophotovoltaic (TPV) devices, subwavelength thermal imaging, and so forth. Thermal emission of periodic metamaterials is governed by the Stefan-Boltzmann law for the total emissive power and by Planck's law for spectral

emission, modified by the corresponding surface emissivity [1, 2]. However, at the micro- and nanoscales, when the geometric dimension is comparable to the characteristic wavelength of thermal radiation ($\lambda_{\mathrm{Th}}=\hbar c/k_{\mathrm{B}}T$), wave interference and photon tunneling must be considered and the resulting radiative energy exchange can greatly exceed the limit set by blackbodies [3]. Besides energy, photons also possess momentum. Indeed, the momentum exchange always accompanies the near-field radiative energy transport. The momentum exchange between macroscopic bodies is also called Casimir force, originally discovered in 1948 [8], which asserts that there exists an attractive force between two neutral conductors separated by vacuum at zero absolute temperature. The near-field energy transfer and Casimir interaction of metamaterials may exhibit extraordinary properties beyond the capabilities of bulk materials.

1.1 Tailoring Radiative Properties at Infrared Regime by Metamaterials

The radiative properties of a medium especially at the infrared wavelengths explicitly or implicitly indicate its thermal and electric properties. Interactions of metamaterials with electromagnetic waves enable unprecedented control of radiative properties, such as extraordinary transmission, negative refraction, and perfect absorption. Resonance excitations enable extreme light confinements, making nanoscale light manipulations beyond the diffraction limit possible. In addition, the strong light-matter interaction helps to design compact nanodevices and relieves the difficulty of the integration of bulky optical devices.

It was found that perforated films can support extraordinary optical transmission (EOT) with efficiencies that are orders of magnitude beyond geometry-based classic

theory [9]. This interesting phenomenon has received extensive attention due to the wide applications of designing lab-on-chip optic devices, such as polarizers, filters, and sensors. Around the same time, double negative materials with simultaneously negative values of permeability and permittivity are experimentally demonstrated [10], although envisioned by Veselago in 1968 [11]. Double negative materials possess novel optical properties, such as negative refraction, reversal of Doppler shift, and realization of perfect lens. Nevertheless, the loss of double negative materials is very high since resonances need to be excited. Novel metamaterials with low loss are desired and are attracting much attention.

Increasing materials' absorptance has attracted considerable interest due to the wide applications, such as solar cells, spectroscopic and thermophotovoltaic (TPV) systems, free space dissipaters, and bolometers [1-3]. Spectrally and spatially coherent absorbers or emitters can be achieved by exciting surface plasmon or phonon polaritons [4-6], photonic crystals [7,8], resonance microcavities [9,10], and Fabry-Perot type resonances [11,12]. The resonance emission or absorption peaks are usually sensitive to the incidence angle and polarization. Due to increasing energy needs and environmental concerns, many efforts are still needed to design wavelength-selective and broadband diffuse absorbers/emitters, which are important for enhancing TPV cell efficiency for harvesting waste heat as well as for improving thermal management in space.

1.2 Near-Field Radiative Energy Transport by Metamaterials

The fluctuation-dissipation theorem (FDT) attributes the origin of thermal emission as due to the random motion of charges, which in turn, produces a fluctuating

current [12, 13]. Fluctuational electrodynamics, which combines FDT with Maxwell's electromagnetic wave theory, is able to describe both the far-field and near-field thermal radiation phenomena. While the time average of the electromagnetic field due to the randomly fluctuating current is zero, the energy density can be very high near the surface and the Poynting vector depends on the correlation of the fluctuating currents. When two objects are placed in close proximity, evanescent waves with large wavevectors can tunnel through the space that separates the objects. This provides additional modes or heat transfer channels beyond what are available between objects placed far apart [14, 15].

FDT was developed in the late 1950's and applied to calculate near-field radiation between parallel plates in late 1960's. Furthermore, the theoretical prediction was evidenced by experiments performed early 1970's, in spite of limited geometric arrangements and separation distances. It is not until the turn of the 21st century when near-field thermal radiation begins to receive a great deal of attention. Research on nanoscale thermal radiation lags behind for more than a decade than that on micro/nanoscale heat conduction and convection that have become active since early 1990's [16, 17]. Understanding near-field thermal radiation between nanostructures not only has a great interest from the fundamental physics aspect, but also has promising applications such as energy harvesting, local thermal control and management, thermal modulation, nanoscale infrared imaging and mapping, and nanomanufacturing [5, 18-21]. Metamaterials open new possibilities to enhance the radiative heat flux, improve the efficiency of near-field energy harvesting, and realize novel contactless thermal devices.

1.3 Near-Field Momentum Exchange (Casimir Force) by Metamaterials

Since being discovered in 1948 [8], the Casimir effect has attracted intensive attention especially in the last two decades when it has gone through significant progresses benefiting from current nanofabrication techniques and development of new calculation methods [13, 22-27]. Recent experimental setups and computational capabilities are able to consider complex geometries beyond simple planar configurations [28-39], two-dimensional (2D) materials [40-45], and effects of thermal fluctuations [46-51]. Nevertheless, the basic mechanism of these different Casimir interactions is the same, a dispersion force induced by quantum and thermal fluctuations. The changing of quantized electromagnetic field in the vacuum gap due to presence of boundary conditions is attributed to the usual attraction force between neutral objects; otherwise no force will exist given that there are no real photons (0 K) or fields according to classical electrodynamics. Despite its quantum nature, the Casimir interaction is a macroscopic phenomenon and has played an important role in condensed matter physics, particle physics, as well as cosmology [22]. The attractive Casimir force per unit area between two perfect metals at 0 K is given as $F_{\mathrm{C}} = \pi^2 \hbar c \Big/ \left(240 d^4\right)$, where d is the gap spacing, $\hbar$ is reduced Planck constant, c is the speed of light in vacuum [8]. Its magnitude increases quickly with decreasing gap spacing, and the corresponding pressure exerted is even larger than atmospheric pressure at d = 10 nm. This nontrivial long-range interaction will cause the malfunctioning of microelectromechanical systems (MEMS) and nanoelectromechanical systems (NEMS) due to the induced stiction and friction problems. As a result, it may impede on Moore's law, which says that the packing density of transistors doubles approximately every two years. The near-field momentum

exchange between metamaterials is nontrivial, and they may provide approaches to relieve the stiction problem.

1.4 Outline

This thesis is divided into 7 chapters. Chapter 2 gives an introduction of some theoretical backgrounds including the effective medium theory (EMT), hyperbolic metamaterials, and fundamentals of near-field thermal radiation and Casimir force. Chapter 3 covers the unusual radiative properties at infrared regime theoretically achieved by appropriately designed metamaterials, such as highly efficient polarizer, blocking-assisted transmission, negative refraction, and tunable perfect absorption. Chapter 4 discusses the near-field radiative heat transfer between metamaterials based on EMT and gives its quantitative validity condition for multilayered metamaterials. Chapter 5 presents the enhanced near-field thermal radiation by metamaterials based on exact formulations, and new physical mechanisms to improve near-field heat transfer are proposed. The manipulation of Casimir force between metamaterials including suppressing the Casimir force and applying repulsive Casimir force to realize stable levitation is covered in Chapter 6. Finally, chapter 7 presents the overall conclusion of this work and potential for future continuation of this work.

CHAPTER 2

THEORETICAL BACKGROUND

This Chapter provides the approaches and concepts needed for the calculation and understanding both the far-field and near-field radiative properties of metamaterials. In Sec. 2.1, the effective medium theory is introduced and applied to obtain the anisotropic dielectric function of different metamaterials including nanowires, nanoholes, multilayers, and gratings. Section 2.2 introduces the concept of hyperbolic metamaterials briefly, and the difference between two types of hyperbolic dispersions is discussed. The fundamentals and formulations to calculate the near-field energy transport and momentum exchange are covered in Sec. 2.3 and 2.4, respectively.

2.1 Effective Medium Theory

Metamaterials are constructed of at least two different materials in order to realize exotic optical, electric or thermal properties. However, when the characteristic dimension of considered metamaterials (period P) is considerably smaller than the wavelength (λ) of the incident radiation, the essentially inhomogeneous medium can be treated as an effective medium with a homogeneous dielectric function. The Maxwell-Garnett (MG) theory and the Bruggeman (BR) approximation are two homogenization methods that have been widely used for obtaining approximate dielectric functions of an inhomogeneous medium with different material constituents based on field averaging. The MG theory is used in this dissertation, since it is valid for dilute nanoscale structures such as carbon nanotubes, nanowires, and silver nanorods [52-57].

In the MG theory, the effective properties of a composite medium are obtained by treating one constituent of the composite as the host and all other constituents as embedded grains (fillers), which are not in contact with one another. Four different nanostructures, i.e., doped silicon nanowires, nanoholes, multilayers, and one-dimensional (1D) gratings as shown in Figure 2.1, are taken as examples to show how to use EMT to obtain their effective dielectric functions.

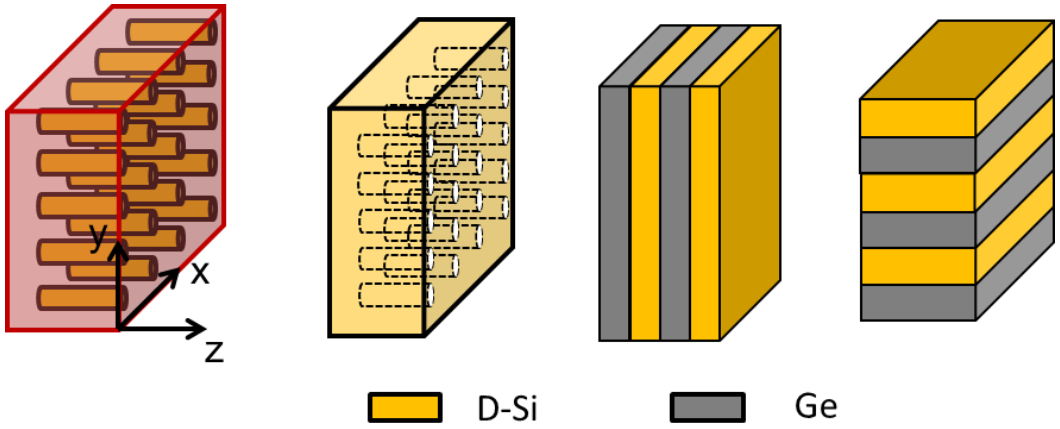

Figure 2.1 Four different nanostructures: nanowires, nanoholes, multilayers, gratings.

For D-SiNWs, vacuum is treated as the host with D-Si as the filler. For D-SiNHs on the other hand, D-Si is the host. When the electric field is along the optical axis (*z* direction), the dielectric function for both nanowires and nanoholes is given as

$$\varepsilon_z = 1 - f + \varepsilon_{\text{D-Si}} f \tag{2.1}$$

Here, ε_z is essentially governed by a diluted Drude model, since it is just the weighted average of the dielectric functions of doped silicon and vacuum. Note that Eq. (2.1) can be obtained from different effective medium approximations and should be valid for any *f*. The Drude model of D-Si may be written as $\varepsilon(\omega) = \varepsilon_\infty - \omega_p^2 / (\omega^2 + i\gamma\omega)$, where ε_∞ is a

high-frequency constant, ω_p is the plasma frequency, and γ is the scattering rate [58]. The plasma frequency for D-SiNWs is $\sqrt{f}$ times that of D-Si; and the high-frequency term for D-SiNWs is $(1-f+f\varepsilon_\infty)$, which varies from 1 for f = 0 to ε_∞ for f = 1. When the electric field is perpendicular to the optical axis, the ordinary dielectric function ε_x, which is equal to ε_y, of nanowires is governed by [55]

$$\varepsilon_{x,\mathrm{NW}} = \frac{\varepsilon_{\text{D-Si}} + 1 + (\varepsilon_{\text{D-Si}} - 1) f}{\varepsilon_{\text{D-Si}} + 1 - (\varepsilon_{\text{D-Si}} - 1) f} \tag{2.2}$$

Note that $\varepsilon_{x,\mathrm{NW}}$ given above can be expressed as a Lorentz model, and detailed derivations can be found from [55]. From a physical point of view, it is because the free electrons in nanowires are bounded by surrounding vacuum [54]. It is assumed that Eq. (2.2) is applicable to any f until it reaches the maximum limit of $\pi/4$, when the diameter of the Si wire is the same as the period of the unit cell. This is a reasonable assumption as long as the Si wires are separated from each other. For nanoholes, Si should be treated as the host and the vacuum holes should be treated as the filler. In this case, $\varepsilon_{x,\mathrm{NH}}$ can be calculated from the Maxwell-Garnett theory as follows

$$\varepsilon_{x,\mathrm{NH}} = \varepsilon_{\text{D-Si}} \frac{\varepsilon_{\text{D-Si}} f + (2 - f)}{\varepsilon_{\text{D-Si}} (2 - f) + f} \tag{2.3}$$

Unlike in the case of nanowires, $\varepsilon_{x,\mathrm{NH}}$ is dominated by a modified Drude model prescribed by Eq. (2.3), because free electrons in the nanohole structure are not bounded due to the interconnection of the doped silicon material.

The dielectric functions of the D-Si/Ge multilayer in orthogonal directions are given by

$$\varepsilon_{\mathrm{O}} = \varepsilon_{\mathrm{Ge}}(1-f) + \varepsilon_{\mathrm{D\text{-}Si}} f \tag{2.4a}$$

$$\varepsilon_{\mathrm{E}} = \frac{\varepsilon_{\mathrm{Ge}}\varepsilon_{\mathrm{D\text{-}Si}}}{(1-f)\varepsilon_{\mathrm{D\text{-}Si}} + \varepsilon_{\mathrm{Ge}} f} \tag{2.4b}$$

Here, ε_{O} (ordinary) and ε_{E} (extraordinary) are the dielectric functions for electric field perpendicular and along the optical axis, respectively. Note that for the multilayer configuration, $\varepsilon_x = \varepsilon_y = \varepsilon_{\mathrm{O}}$ and $\varepsilon_z = \varepsilon_{\mathrm{E}}$. The above dielectric functions also apply to 1D gratings but with $\varepsilon_z = \varepsilon_{\mathrm{O}}$ instead. It should be noted that for the multilayered structure, both the Maxwell-Garnett and Bruggeman effective medium approaches give the same expressions, i.e., Eqs. (2.4a) and (2.4b). Detailed discussions of the effective medium approximations can be found from Refs. [59, 60].

2.2 Hyperbolic Metamaterials

According to EMT, multilayers, nanowires, and nanoholes can be homogenized into a uniaxial medium. And, such a uniaxial anisotropic medium can be characterized by a dielectric tensor diag($\varepsilon_{\mathrm{O}}, \varepsilon_{\mathrm{O}}, \varepsilon_{\mathrm{E}}$). When the dielectric functions for both directions are positive (negative), the material is called dielectric (metal). When the anisotropic optical responses to orthogonal directions are so extreme that the corresponding dielectric functions have different signs. This kind of metamaterials is called hyperbolic metamaterials (HMMs) due to the supporting of hyperbolic dispersions, in contrast to elliptic dispersions of conventional isotropic or anisotropic materials. To be more specific, when $\varepsilon'_{\mathrm{O}} > 0$ and $\varepsilon'_{\mathrm{E}} < 0$ (where prime denotes the real part), the material is named as type I HMMs, the reverse scenario is called type II HMMs [61].

One distinguishing feature of hyperbolic metamaterials is that the anisotropic hyperbolic dispersion is open rather than closed. The supported photonic density of states is diverging rather than being finite, and the electromagnetic waves with high wavevectors can be supported to be propagating. Subsequently, hyperbolic metamaterials enable many exciting applications such as negative refraction, subwavelength imaging, nanolithography, ultrafast spontaneous emission, and super-Plancian thermal radiation [61, 62]. Type I HMMs, such as nanowires [63, 64] and metal-dielectric multilayers [65], have been demonstrated to support low-loss negative refraction in the visible range. Substituting metallic nanostructures with doped semiconductors may extend the negative refraction to the infrared regime. Super-Planckian thermal radiation were theoretically demonstrated based on type I HMMs [66-68]. The investigation of type II HMMs in terms of the potential of enhancing near-field radiative heat transfer is recently conducted by us [69].

Graphite and CNT are examples of type II and type I HMMs, respectively, and their dielectric functions are given by Figure 2.2. The dielectric functions of graphite at room temperature for electromagnetic waves from near infrared to millimeter region are obtained from Refs. [70, 71], and their real parts are shown in Figure 2.2 (a). Two type II hyperbolic regions are delineated: one at angular frequencies below 2.1×10^{13} rad/s (due to free electrons) and the other ranging from 3.0×10^{13} rad/s to 1.8×10^{14} rad/s (associated with the interband transition). The effective dielectric functions of CNTs are shown in Figure 2.2 (b). Two type I hyperbolic bands are identified: a low frequency region at angular frequencies from 1.4×10^{13} rad/s to 2.1×10^{13} rad/s and the other from 3.0×10^{13} rad/s to 1.3×10^{14} rad/s.

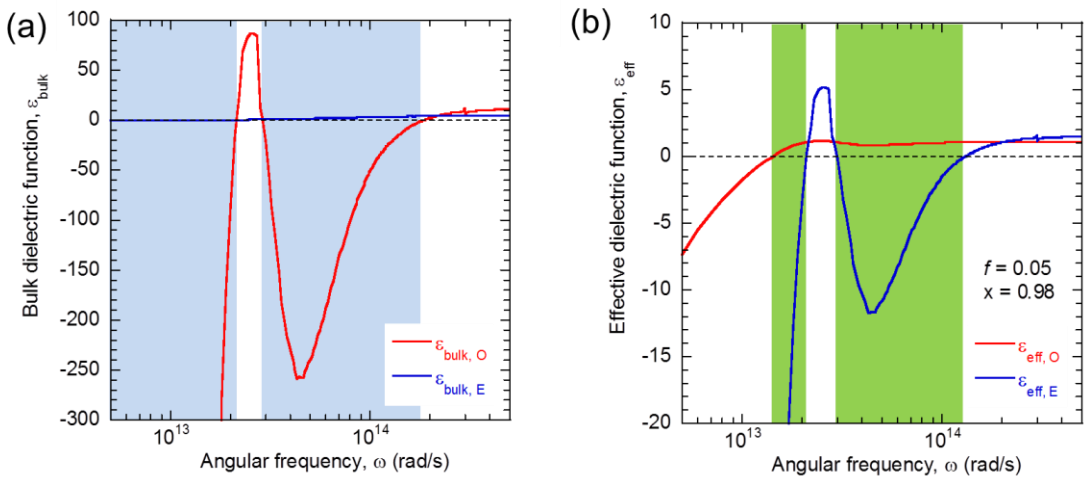

Figure 2.2 Dielectric functions (real part only) for ordinary and extraordinary waves. (a) Graphite. (b) CNT with the filling ratio of 0.05 and alignment factor of 0.98.

2.3 Fundamentals of Near-Field Thermal Radiation

As is well known, thermal radiation is originated from fluctuating currents due to thermal motion of charge carriers as shown in Figure 2.3. Fortunately, these chaos like fluctuating currents can be quantified in terms of the optical response (dielectric function) of emitters [72]. For an anisotropic, local, and nonmagnetic medium with time-reversal symmetry at local thermal equilibrium, the correlation function of fluctuating currents can be expressed as [12, 13, 73]

$$\left\langle J_i(\mathbf{r},\omega) J_k^*(\mathbf{r}',\omega') \right\rangle = \frac{4\omega\varepsilon_0 \Theta(\omega,T)\varepsilon_{ik}''(\mathbf{r},\omega)}{\pi} \delta(\mathbf{r}-\mathbf{r}')\delta(\omega-\omega') \qquad (2.5)$$

where subscripts i or k refer to the vector component, < > represents ensemble average, Θ is the mean energy of a Planck oscillator that is a function of frequency ω and temperature T [3], ε_0 is the vacuum permittivity, ε_{ik}'' is the imaginary part of the dimensionless dielectric tensor component, and $\delta(\mathbf{r}-\mathbf{r}')$ or $\delta(\omega-\omega')$ is the Dirac delta function indicating spatial or temporal incoherence, respectively. For isotropic media,

$\varepsilon''_{ik} = \varepsilon''\delta_{ik}$ where ε'' is the imaginary part of the dielectric function and δ_{ik} is the Kronecker delta. The near-field radiative heat flux between two anisotropic media, at temperatures of T_1 and T_2, respectively, separated by a vacuum spacing as illustrated in Figure 2.3 is given as

$$q = \int_0^\infty \frac{1}{2}\left\langle \mathrm{Re}[\mathbf{E}(\mathbf{r},\omega)\times\mathbf{H}^*(\mathbf{r},\omega)]\right\rangle d\omega \tag{2.6}$$

where the integrand is the Poynting vector component perpendicular to the interface. For the parallel-plate configuration, the Poynting vector in the vacuum gap is independent of the location since there is no dissipation or dispersion. The electric and magnetic fields can be expressed by corresponding dyadic Green function and fluctuating currents [3], and combining with Eqs. (2.5) and (2.6), the radiative heat flux can be written as

$$\begin{aligned} q = {} & \frac{2k_0^2}{\pi}\int_0^\infty \left[\Theta(\omega,T_1)-\Theta(\omega,T_2)\right]d\omega \\ & \times \int_{V'} \mathrm{Re}\left[j \sum_{i,k=x,y,z} \varepsilon''_{ik}(\omega)(G^E_{xi}G^{H*}_{yk} - G^E_{yi}G^{H*}_{xk})\right] dV' \end{aligned} \tag{2.7}$$

Here, $k_0 = \omega/c$ is the wavevector in vacuum with c being the speed of light in vacuum, $j = \sqrt{-1}$, V' is the source region (emitter), and the electric dyadic Green function G^E and magnetic dyadic Green function G^H relate the electric field in the vacuum gap to the unit source current in the emitter [3]. The calculation of dyadic Green function for general anisotropic medium has been a mature technique and can be obtained using various methods such as eigenfunction expansion, matrix formulation, and Fourier transform method [74]. For more general anisotropic materials with a non-unity permeability tensor μ_{ik}, an extra term similar to Eq. (2.5) but with permittivity tensor

changed to be corresponding permeability without correlations between electric and magnetic currents should be added into the right side of Eq. (2.5) [13, 75, 76]. As a result, magnetic metamaterials will provide an extra channel taking into account magnetic surface plasmon resonance (featured with oscillating currents at the interface of vacuum and magnetic materials rather than oscillating charges as the case of common surface resonances for TM waves) associated with TE waves for radiative energy exchange [13, 75-78].

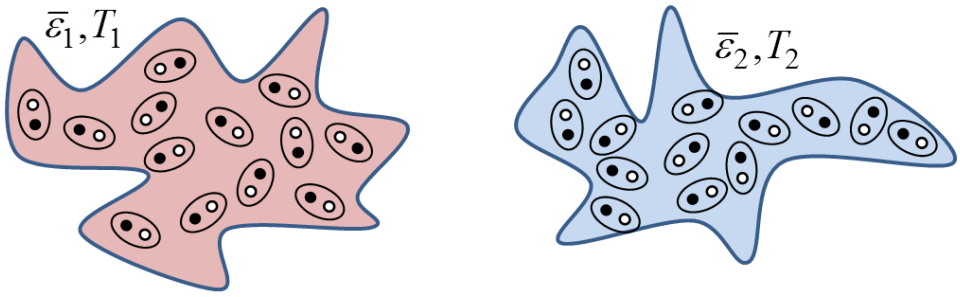

Figure 2.3 Near-field thermal radiation between anisotropic materials with arbitrary shapes

2.3.1 Near-Field Thermal Radiation between Anisotropic Medium

For planar anisotropic materials, q can be expressed in another way based on k-space integration instead of the volume integration by employing the scattering theory [68, 79]

$$q = \frac{1}{8\pi^3}\int_0^\infty \left[\Theta(\omega, T_1) - \Theta(\omega, T_2)\right] d\omega \int_0^\infty \int_0^\infty \xi\left(\omega, k_x, k_y\right) dk_x dk_y \qquad (2.8)$$

where k_x and k_y are the transverse wavevector in x and y direction, respectively, and $\xi(\omega, k_x, k_y)$ is called the *energy transmission coefficient* or *photon tunneling probability*.

Equation (4) can be obtained by recasting the spatial dyadic Green functions into *k*-space Green functions using the Fourier transform. The energy transmission coefficient can be expressed in a matrix formulation as [68, 79]

$$\xi\left(\omega, k_x, k_y\right) = \begin{cases} \mathrm{Tr}\left[(\mathbf{I}-\mathbf{R}_2^*\mathbf{R}_2)\mathbf{D}(\mathbf{I}-\mathbf{R}_1\mathbf{R}_1^*)\mathbf{D}^*\right], & \beta < k_0 \\ \mathrm{Tr}\left[(\mathbf{R}_2^*-\mathbf{R}_2)\mathbf{D}(\mathbf{R}_1-\mathbf{R}_1^*)\mathbf{D}^*\right]e^{-2|k_{z0}|d}, & \beta > k_0 \end{cases} \tag{2.9}$$

where $\beta = \sqrt{k_x^2 + k_y^2}$ is the magnitude of the lateral wavevector, d is the vacuum gap between the two semi-infinite media, $k_{z0} = \sqrt{k_0^2 - \beta^2}$ is the z-component wavevector in vacuum, and the star means Hermitian adjoint. When $\beta > k_0$, k_{z0} is purely imaginary and photon tunneling can occur at close proximity, resulting in significant enhancement of radiative transfer especially when surface modes or hyperbolic modes exist, as will be discussed later. The 2 × 2 Fresnel's reflection matrix for incidence from vacuum to medium i = 1 or 2 is expressed as

$$\mathbf{R}_i = \begin{bmatrix} r_{\mathrm{ss}}^i & r_{\mathrm{sp}}^i \\ r_{\mathrm{ps}}^i & r_{\mathrm{pp}}^i \end{bmatrix} \tag{2.10}$$

The element r_{sp}^i represents the case of cross-polarization when an incident wave with s polarization becomes p polarized after being reflected by medium i, and this rule applies to other three terms. These reflection coefficients can be obtained by applying boundary conditions that tangential electric and magnetic fields are continuous across each interface. For uniaxial media with optical axis lying vertically or horizontally, explicit expressions of reflection coefficients can be found in Ref. [68]. The matrix **D** is a

Fabry-Pérot-like term considering scattering interactions in the vacuum cavity between the two anisotropic media and is given by Refs. [66, 68, 79]

$$\mathbf{D} = \left(\mathbf{I} - \mathbf{R}_1 \mathbf{R}_2 e^{2jk_{z0}d} \right)^{-1} \tag{2.11}$$

Note that Eq. (2.8) holds for general materials with arbitrary permittivity and permeability, although the expressions for the transmission coefficients are more complicated for magnetic materials. For isotropic media with both electric and magnetic responses, the formulations can be found in Refs. [75-77].

2.3.2 Near-Field Thermal Radiation between Periodic Metamaterials

The calculation of near-field thermal radiation between periodic metamaterials is complex compared with homogeneous isotropic or anisotropic medium. In this dissertation, semi-analytical and numerical methods are used to consider 1D and 2D metamaterials, respectively, and will be discussed in this section.

(a) Rigorous coupled-wave analysis (RCWA)

Bimonte and Santamato [80] related the fluctuating electromagnetic fields outside a hot surface at thermal equilibrium to only its scattering properties such as reflection coefficient. As a result, the heat transfer between two nonequilibrium objects can be predicted based only on their scattering coefficient since objects radiate independently [81]. The formula for near-field heat transfer between two 1D gratings as shown in Figure 2.4 is given as [82, 83]

$$q = \frac{1}{2\pi^3} \int_0^\infty \left[\Theta(\omega, T_1) - \Theta(\omega, T_2) \right] d\omega \int_0^{\pi/p} \int_0^\infty \xi(\omega, k_x, k_y) dk_x dk_y \tag{2.12}$$

where p is the period in the x direction, and the k_x is folded into the first Brillouin zone.

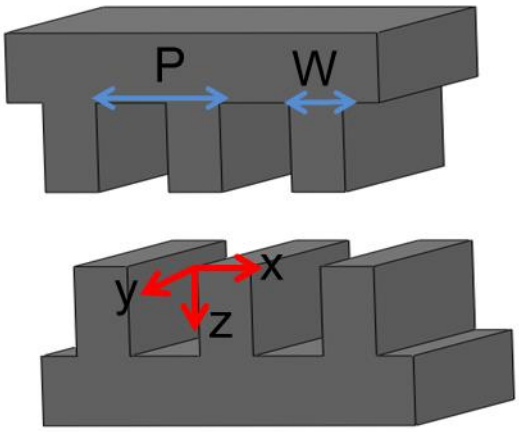

Figure 2.4 Near-field energy transport and momentum exchange between 1D gratings.

The expression of energy transmission coefficient $\xi\left(\omega, k_x, k_y\right)$ is shown as [82-84]

$$\xi\left(\omega, k_x, k_y\right) = \mathrm{Tr}\left(\mathbf{D}\mathbf{W}_1\mathbf{D}^*\mathbf{W}_2\right) \tag{2.13a}$$

$$\mathbf{D} = \left(\mathbf{I} - \mathbf{S}_1\mathbf{S}_2\right)^{-1} \tag{2.13b}$$

$$\mathbf{W}_1 = \sum\nolimits_{-1}^{\mathrm{pw}} - \mathbf{S}_1 \sum\nolimits_{-1}^{\mathrm{pw}} \mathbf{S}_1^* + \mathbf{S}_1 \sum\nolimits_{-1}^{\mathrm{ew}} - \sum\nolimits_{-1}^{\mathrm{ew}} \mathbf{S}_1^* \tag{2.13c}$$

$$\mathbf{W}_2 = \sum\nolimits_{1}^{\mathrm{pw}} - \mathbf{S}_2^* \sum\nolimits_{1}^{\mathrm{pw}} \mathbf{S}_2 + \mathbf{S}_2^* \sum\nolimits_{1}^{\mathrm{ew}} - \sum\nolimits_{1}^{\mathrm{ew}} \mathbf{S}_2 \tag{2.13d}$$

where $\mathbf{S}_1 = \mathbf{R}_1$ and $\mathbf{S}_2 = e^{ik_{z0}d}\mathbf{R}_2 e^{ik_{z0}d}$. Here, $\mathbf{R}_1$ and $\mathbf{R}_2$ are the reflection matrices for medium 1 and medium 2 that are obtained by using the rigorous coupled-wave analysis (RCWA). The basic idea is that the fields for homogenous layer and grating region are written as Rayleigh expansions and Fourier series, respectively. Employing boundary conditions by making tangential fields equal will help to obtain every unknown Rayleigh terms which constitute $\mathbf{R}_1$ and $\mathbf{R}_2$. Operators $\sum\nolimits_{-1(1)}^{\mathrm{pw(ew)}}$ identifying propagating and evanescent modes are presented in Ref. [83]. This is a *k*-space method based on scattering theory, and is mainly for 1D periodic photonic crystals. It can be extended for arbitrary

2D periodic or aperiodic metamaterials though the memory requirement will arise tremendously.

(b) Finite-difference time-domain (FDTD) method

Equation 2.7 can be generally applied to arbitrary nanostructures as long as the dyadic Green functions are determined. One way to obtain the Green's functions is to use the finite-difference time-domain (FDTD) method based on a brute-force approach [85, 86]. Basically, one electric dipole considering three different orientations is placed inside the source, and then the corresponding electric or magnetic dyadic Green function is obtained by dividing the Fourier transform of the time-dependent electric field or magnetic field over that of the current induced by the dipole. The calculation should be repeated by scanning the dipole over the whole source region. As a result, the calculation is computationally intensive since the number of dipoles can be very large to guarantee sufficient accuracy in the solutions.

Alternatively, by using Langevin approach, a fluctuating term is added to Newton's equation of motion, which can be solved directly by FDTD to get the radiative heat flux [87-90]. Treating charge carriers as damped harmonic oscillators driven by an external field **E** and a random force representing uncorrelated thermal fluctuations, the polarization equation can be expressed as follows [88-90].

$$\frac{d^2\mathbf{P}}{dt^2} + \gamma \frac{d\mathbf{P}}{dt} + \omega_0^2 \mathbf{P} = \sigma \mathbf{E} + \mathbf{K}(t) \tag{2.14}$$

where **P** is the polarization, γ is the frictional coefficient, ω_0 is the resonance frequency, σ is the strength related to conductivity, and **K** is the random force term. The correlation function of **K** can be found by combining Eq. (2.5) with the Fourier transform into time domain as shown in Refs. [88-90]. Though volume integration is circumvented, this is a

statistical method (Monte Carlo) using randomly generated current distributions, and the obtained heat flux should be ensemble averaged over many (such 50) independent simulations until the solution converges.

2.4 Fundaments of Casimir Force

Near-field thermal radiation and Casimir interactions are two of the few macroscopic manifestations of quantum mechanical electromagnetic fluctuations. The Casimir force per unit area between isotropic substrates separated by a fluid can be described by the general Lifshitz's theory as [91-93]

$$F_{\text{plane}} = \frac{k_B T}{\pi} {\sum_{n=0}^{\infty}}' \int_0^{\infty} k_{zn} \left(\frac{r_1^{\text{s}} r_2^{\text{s}} e^{-2k_{zn}d}}{1 - r_1^{\text{s}} r_2^{\text{s}} e^{-2k_{zn}d}} + \frac{r_1^{\text{p}} r_2^{\text{p}} e^{-2k_{zn}d}}{1 - r_1^{\text{p}} r_2^{\text{p}} e^{-2k_{zn}d}} \right) \beta d\beta \quad (2.15)$$

where $\beta = \sqrt{k_x^2 + k_y^2}$ is the tangential wavevector, $k_{zn} = \sqrt{\varepsilon_f \, \omega_n^2 / c^2 + \beta^2}$ is the vertical wavevector of the intervening fluid, subscripts "s" and "p" represent *s*- and *p*-polarization waves. r_1 and r_2 are the Fresnel reflection coefficients evaluated at Matsubara frequencies for the fluid interface with substrate 1 and 2, respectively. Equation (2.15) holds if the substrate is a three-layer structure provided the reflection coefficient is obtained using Airy's formula [3].

For calculating the Casimir force or momentum exchange between 1D gratings as shown in Figure 2.4, the semi-analytical RCWA is used again. Assuming the top and the bottom grating are in thermally equilibrium having the same temperature of *T*. The Casimir force in the *z* direction per unit area can be calculated using exact scattering theory based on the following expression [29, 32, 47]:

$$F = 2\pi k_B T \sum_{n=0}^{\infty}{}' \int_{-\infty}^{\infty} \int_{-\pi/P}^{\pi/P} \mathrm{tr}\left[(\mathbf{1} - \mathbf{M}_n)^{-1} \partial_z \mathbf{M}_n \right] dk_x dk_y \qquad (2.16)$$

where the prime in the summation operator means the n = 0 term should be taken with a factor of 0.5. Both quantum and thermal fluctuations are taken into account, so the summation should be exerted over Matsubara frequencies $i\omega_n = i\,2\pi n k_B T/\hbar$, where n is an integer ranging from 0 to infinity and k_B is the Boltzmann constant. The default temperature T is set to be 300 K. Matrix $\mathbf{M}_n$ can be described by reflection coefficients $\mathbf{R}_1$ and $\mathbf{R}_2$ at Matsubara frequencies [47], which consider all possible polarization states and are obtained by using the RCWA for specified k_x and k_y values [47, 83, 84, 94, 95]. It takes about one hour to calculate the Casimir force between the two gratings with specific geometric parameters at a certain gap distance using a dual eight core XEON E5-2687W workstation.

CHAPTER 3

UNUSUAL RADIATIVE PROPERTIES OF METAMATERIALS AT INFRARED REGIME

Metamaterials enable unprecedented control of light propagation and absorption. The infrared regime is mainly forced since this is where the thermal radiation of practical devices mainly exists. Chapter 3 presents some unusual radiative properties achieved at infrared regime by appropriately designing metamaterials. Section 3.1 presents a design of wide-angle broadband polarizers in the near infrared region with both good transmission and extremely high extinction ratio. In Sec. 3.2, covering 1D and 2D Ag gratings with a single-layer graphene is found to counterintuitively increase the transmission several fold in certain wavelength region, and the underlying mechanism for this counterintuitive blocking-assisted transmission is attributed to the excitation of a localized resonance. Section 3.3 theoretically demonstrates metal-free all-angle negative refraction with low loss in the mid-infrared region using D-SiNW arrays. In Sec. 3.4, a tunable perfect absorption is theoretically demonstrated. Section 3.5 briefly summarizes the main contribution of this chapter.

3.1 A Highly Efficient Polarizer

Polarizers play an important role in optical devices and systems, such as the Faraday isolators, modulators, fiber-optic networks, as well as imaging and laser systems. High-efficiency near-infrared polarizers are especially important for laser systems and optical communications. Compared with conventional bulky polarizers, such as calcite

prisms and pile of plates, which are difficult to integrate with other components, wire-grid polarizers can be used to produce compact and integrated optical devices. Anodization and elctrodeposition [96], e-beam lithography [97, 98], interference lithography [99], and nanoimprint lithography [100, 101] have already been used to fabricate wire-grid polarizers applicable to the near-infrared region. The performance of a polarizer can be characterized by a high transmittance for one polarization and very low transmittance for another polarization. Appropriate lateral shift is suggested to enhance the transmission of double-layer periodic gratings at certain wavelength region [99, 102-105]. Chan et al. [105] experimentally demonstrated an extraordinary transmission for transverse magnetic (TM) waves in a double-layer grating nanostructure. Yang and Lu [106] designed an extra-broadband polarizer by incorporating dual-layer aluminum grating on both sides of the CaF_2 substrate. This structure was predicted to have an extinction ratio, the ratio of transmittance for TM waves to that of TE (electric field is perpendicular to the incidence plane) waves, exceeding 10^7 and transmission over 64 % in the wavelength (λ) region from 0.3 to 5 μm. The highest extinction ratio was predicted to be 10^9 at λ = 5 μm [106]. Peltzer et al. [107] designed and fabricated a near-infrared polarizer with a theoretically predicted extinction ratio as high as 10^{11} in a narrow spectral region.

Here, a design of a broadband polarizer with high transmittance (near 90 %) and extremely high extinction ratio (exceeding 10^{16}) for 1.6 μm < λ < 2.3 μm is proposed. The structure proposed is based on a 1D double-layer structure, which is periodic along the *x* direction and extends to infinity in the *y* direction, as shown in Figure 3.1(a). A thin SiO_2 (glass) spacer is sandwiched between two identical silver gratings, which are shifted

laterally by half the period. In other words, the centerlines of the ridges in the top grating coincide with those of the slits in the bottom grating. The structure is characterized with a base set of parameters given in the following: the period P = 500 nm, spacer thickness t_s = 30 nm, Ag grating thickness t_m = 400 nm, and slit width W_g = 150 nm. Radiation is incident from air at an incidence angle of θ_i. The analysis is based on FDTD method using a commercial package (Lumerical Solutions, Inc.) and RCWA algorithm [104, 108]. The dielectric function of Ag as a function of the angular frequency ω is obtained using the Drude model: $\varepsilon_{Ag}(\omega) = \varepsilon_\infty - \omega_p^2 / (\omega^2 - i\gamma\omega)$ with a scattering rate $\gamma = 2.7\times10^{13}$ rad/s, plasma frequency $\omega_p = 1.39\times10^{16}$ rad/s, and a high-frequency constant $\varepsilon_\infty = 3.4$ [109]. For SiO_2, the refraction index is taken as 1.43 with negligible loss in the considered wavelength region from 1 to 3 μm [110].

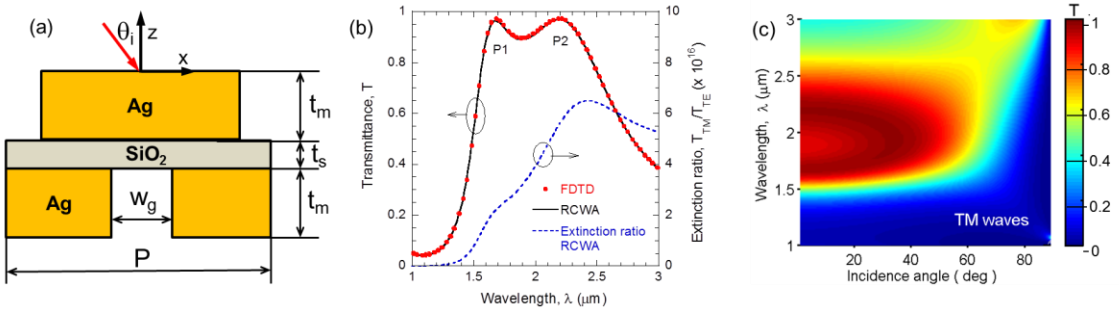

Figure 3.1 The proposed nanostructure and its performance as an IR polarizer: (a) Schematic of a period of the double-layer grating; (b) Spectral transmittance for TM waves and the extinction ratio at normal incidence; (c) Contour plot of the transmittance as a function of the wavelength and angle of incidence for TM waves. The parameters used for the calculation are P = 500 nm, t_m = 400 nm, t_s = 30 nm, and W_g = 150 nm.

Figure 3.1(b) shows the calculated transmittance for TM waves at normal incidence using both FDTD and RCWA methods, which give essentially the same results,

as well as the extinction ratio calculated with RCWA. Transmittance higher than 89 % is predicted in a broad wavelength region from 1.6 to 2.3 μm. The extinction ratio is surprisingly high, exceeding 3×10^{16} across the aforementioned spectral region with high transmittance. For a homogeneous Ag thin film, the normal transmittance is lower than 10^{-16} with a film thickness of 400 nm and lower than 10^{-20} with a thickness of 500 nm. Therefore, it is not surprising why the transmittance of the proposed structure is so low for TE waves. Due to the extremely low transmittance values for TE waves, results obtained from the FDTD simulation tend to fluctuate and are not reliable because of the numerical errors. However, the RCWA algorithm uses double-precision data type. The accuracy of the RCWA model is limited only by the number of diffraction orders used. By increasing the number of diffraction order, convergence can be reached even with ultralow transmittance values. The transmittance for a homogeneous film predicted using RCWA is essentially the same as that calculated from thin-film topics at extremely low transmittance (down to 10^{-30}). It should be noted that the extremely high extinction ratio will be important for devices or systems that require ultrahigh polarization purity such as high power laser systems and high contrast modulators. If used in Faraday isolators, the proposed polarizer will help to suppress the back light completely, given that transmittance down to 10^{-11} is still measurable [111]. The transmittance spectra are featured with two peaks labeled as P1 and P2. Note that P1 is at λ = 1.69 μm with T = 97.3 % and P2 is at λ = 2.10 μm with T = 97.4 %. Moreover, in the high transmission regime, the average reflectance for TM waves is only 3.6 % (the maximum value is about 8.1 %). On the other hand, the reflectance for TE waves is greater than 99.5 % in the

aforementioned region. Therefore, the proposed structure can also be used as a polarization-selective beamsplitter [112].

Figure 3.1(c) displays the transmittance contour as a function of the wavelength and incidence angle. Note that the plane of incidence is always perpendicular to the *y*-axis to avoid conical refraction when depolarization can occur [108]. It can be seen that the transmittance is still high until the incidence angle exceeds 60°. It should be noted that the transmittance for TE waves (not shown) remains to be extremely low at oblique incidence. That means the polarizer has a large angle tolerance, which makes it useful not only for well collimated beams, but also for diverging and converging beams. The two peaks approach each other with increasing incident angles and finally merge together when the incidence angle exceeds 25°.

For practical applications, the proposed structure may be fabricated onto a suitable substrate material such as SiO_2 or CaF_2. If the slit region is filled with a dielectric rather than air, the fabrication process will not be too difficult because similar structures have been fabricated by others [105, 107, 113, 114]. High performance is still expected when the slit region is filled with a dielectric material, although some tuning of the parameters is necessary for wavelength selection. Moreover, the dielectric in the silt region (different from the material used as the spacer) could be removed by wet etching in the final step if necessary. Attention is now turned to the underlying mechanisms that give rise to the high and broadband transmission for TM waves.

Extraordinary transmission through double-layer gratings with or without lateral shift has been investigated by many researchers [99, 103, 106, 115-117]. Different mechanisms were used to explain this phenomenon, such as coupled surface plasmons,

waveguide modes, or Fabry-Perot resonances. Recently, Huang and Peng [118] put forward a general charge-oscillation theory to explain the extraordinary transmission through various sub-wavelength decorated metallic structures. Nonetheless, few of them could predict the location of the transmission peak quantitatively. Here, the two transmission peaks are attributed to magnetic polaritons (MPs) which refer to the coupling between the external electromagnetic waves and the induced current loop in a micro/nanostructure [104, 119]. Two simple inductor-capacitor (LC) circuit models are developed after carefully analyzing the magnetic field distribution and current density vectors in the near-field regime to quantitatively predict the locations of the transmission peaks P1 and P2, respectively, as shown in Figure 3.2.

For the first peak (P1), the dimensionless field distribution is shown in Figure 3.2(a) with color denoting $\left|H_y / H_0\right|^2$ and arrows representing the current density vectors. Here, H_0 is the amplitude of the magnetic field for the incident wave. There exists strong field enhancement in the slit and the SiO_2 spacer region but not in the overlapping area between the top and bottom gratings. Following the current density vectors distribution, a LC model shown in Figure 3.2(c) is developed to predict the resonance wavelength for P1. Note that the field distributions in the top and bottom slits are almost the same due to the structure symmetry, so that only one LC circuit either in the top or bottom slit region is needed to predict the resonance wavelength (or frequency). The simple LC circuit model assumes that MPs are localized without coupling to each other. The inductances are given as follows:

$$L_1 = L_{e,1} = \frac{W_g}{\varepsilon_0 \omega_p^2 \delta l} \tag{3.1}$$

$$L_2' = L_2 = L_{e,2} + L_{m,2} = \frac{(P - 2W_g)}{4\varepsilon_0 \omega_p^2 \delta l} + \frac{\mu_0 (P - 2W_g) t_s}{8l} \tag{3.2}$$

$$L_3 = L_{e,3} + L_{m,3} = \frac{t_m}{\varepsilon_0 \omega_p^2 \delta l} + \frac{\mu_0 W_g t_m}{2l} \tag{3.3}$$

where μ_0 and ε_0 are the permeability and permittivity of vacuum, respectively, and l is the structure thickness in the y direction. Here, $L_{e,1}$, $L_{e,2}$, and $L_{e,3}$ are the kinetic inductances that account for the contribution of drifting electrons, while $L_{m,2}$ and $L_{m,3}$ are the mutual inductances between parallel plates [104, 119]. It is assumed that all induced electric current in the metal flows within a penetration depth defined as $\delta = \lambda / 4\pi\kappa$, where κ is the extinction coefficient of Ag [3]. In Figure 3.2(c), C_{g1} and C_s are the parallel-plate capacitances of the gap (slit) and spacer, respectively, and are given as

$$C_{g1} = \frac{c_1 \varepsilon_0 t_m l}{W_g} \quad \text{and} \quad C_s = \frac{c_2 \varepsilon_0 \varepsilon_d (P - 2W_g) l}{4t_s} \tag{3.4}$$

where ε_d is the permittivity of SiO_2. The coefficients c_1 and c_2 take into account the nonuniform charge distribution and are often treated as adjusting parameters [104, 119, 120]. In the present study, good agreement between the resonance wavelengths calculated by the rigorous numerical solutions and the LC model are obtained using $c_1 = c_2 = 0.6$. The reason that c_1 is less than 1 is due to the nonuniform distributions of the field and current density in the slit region. The reason that c_2 is close to 0.5 is because only part of the overlapping region between the upper and lower gratings is included in the LC circuit.

The MP resonance condition in this LC circuit can be determined by zeroing the total impedance, and then the (angular) resonant frequency is obtained as follows.

$$\omega_{p1} = \sqrt{\left(\frac{2}{C_s} + \frac{1}{C_{g1}}\right)\frac{1}{L_1 + 2L_2' + 2L_2 + 2L_3}} \tag{3.5}$$

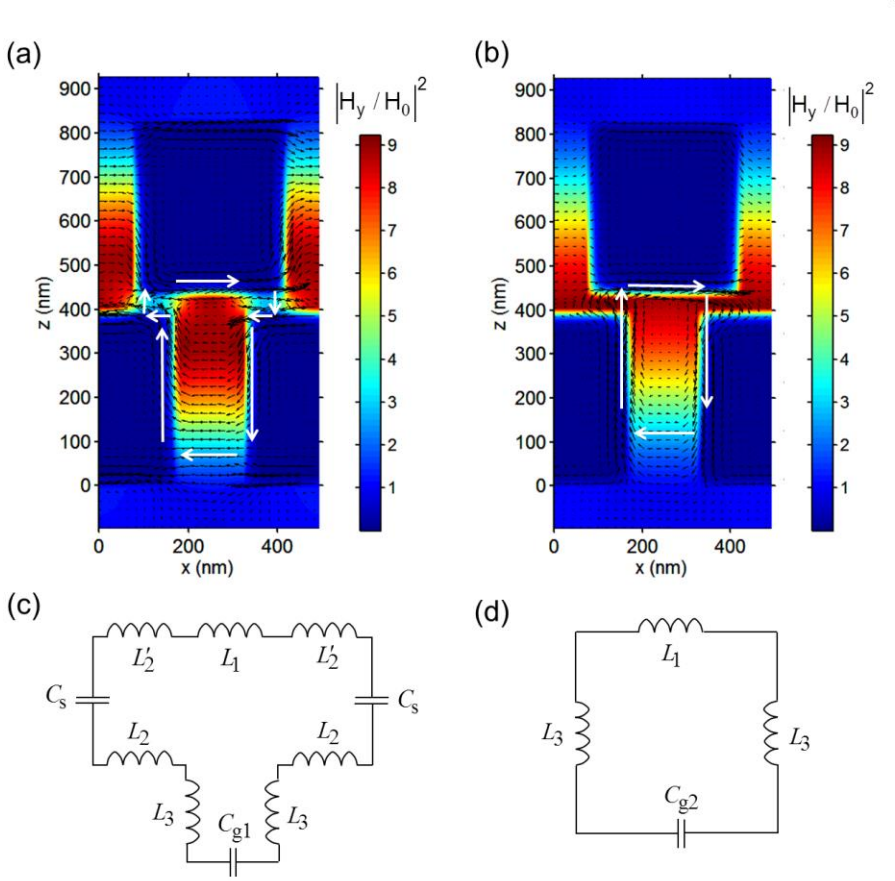

Figure 3.2 The enhancement of the magnetic field and current loop when the MPs are excited and the simple LC circuit models: (a,b) $\left|H_y / H_0\right|^2$ for P1 and P2, respectively. (c,d) LC models for P1 and P2, respectively.

For the second peak (P2), the dimensionless field distribution is shown in Figure 3.2(b), which is featured with the strong field confinement in the whole spacer and slit

region. The current density in the spacer between the region where the top and bottom gratings overlap is so large that the impedance could be neglected. Consequently, it appears as if the side wall of the bottom grating is extended all the way to the top grating, as illustrated in the LC model shown in Figure 3.2(d). Here, the slit or gap capacitance C_{g2} considering this extending effect is given as

$$C_{g2} = \frac{c_3 \varepsilon_0 t_m l}{W_g} + \frac{c_4 \varepsilon_0 \varepsilon_d t_s l}{W_g} \tag{3.6}$$

Similar to c_1 and c_2 in the previous model, c_3 and c_4 are introduced to account for the nonuniform charge distribution and are taken as adjustable parameters. Good agreement between the resonance wavelengths predicted by the LC model and the rigorous solutions is obtained with $c_3 = 0.3$ and $c_4 = 1$. The reason that c_3 is much smaller than c_1 can be explained as due to the fact that the electromagnetic fields are confined mainly in the region close to the spacer when P2 is excited. Inside the spacer region, however, the field is greatly enhanced and almost uniformly distributed so that c_4 should be close to 1. The resonance frequency for P2 of this circuit is given as

$$\omega_{p2} = \sqrt{\frac{1}{C_{g2}(L_1 + 2L_3)}} \tag{3.7}$$

The resonance wavelengths predicted by the LC models are 1.674 μm (P1) and 2.298 μm (P2), which agree well with the values of 1.685 μm (P1) and 2.195 μm (P2) obtained by numerical simulations. It should be noted that the maximum absorptance in the high transmittance band is only 3.2 %; therefore, the strong field confinement mainly helps light to penetrate through this structure. The LC models not only provide a physical

interpretation of the extraordinary transmission, but also allow quantitative predictions of the geometric effect on the resonance condition as discussed in the following.

It is important to understand the dependence of transmittance on the various geometric parameters in order to design polarizers suitable for specific applications. This is done by varying some parameters while fixing the rest as in the base set mentioned before. The results are shown in Figure 3.3, where the color contours are from the full-wave numerical simulations and the dashed lines are from the LC circuit models. The circle and triangle marks indicate the excitation of P1 and P2, respectively, with the base set of parameters. When the Ag grating thickness t_m increases, the high transmittance region will redshift (i.e., toward longer wavelengths), as shown in Figure 3.3(a). Similar trends have been observed earlier [103]. The peak wavelengths can be well predicted by the LC models. The redshift for P1 (or P2) can be understood based on the increasing capacitance C_{g1} (or C_{g2}) and inductance L_3 with t_m. Note that the extinction ratio also increases with t_m, since the transmittance for TE waves will decrease as t_m increases. Therefore, even greater extinction ratio could be obtained with the proposed structure at slightly longer wavelengths. When t_m is on the order of 100 nm (not shown in the figure), the trends for P1 and P2 are the same but the deviation of the LC circuit model from the full-wave calculation becomes large. This could be due to the different field distributions because the slit region becomes very wide and shallow. Furthermore, when the metal thickness is comparable to the penetration depth in Ag, which is on the order of 10 nm, the deviation of LC model from the full-wave calculation becomes prominent. For this case, the current will flow through the whole metallic layer and the LC circuit models must be modified to consider such effect.

Figure 3.3(b) shows that when the spacer thickness t_s is reduced, P1 will redshift but P2 will blueshift and they will degenerate into one peak when $t_s < 20$ nm. For P1, the spacer capacitance C_s increases with decreasing t_s, so that the resonance wavelength will increase. For P2, on the other hand, C_{g2} decreases with decreasing t_s due to the second term, so that the resonance wavelength will also decrease. When t_s exceeds 50 nm, the LC model predictions start to deviate from the full-wave simulation. In this case, near-field coupling between the top and bottom grating becomes weak. Furthermore, the field distributions may largely deviate from those for the base parameters, resulting in a breaking down of the LC circuit models.

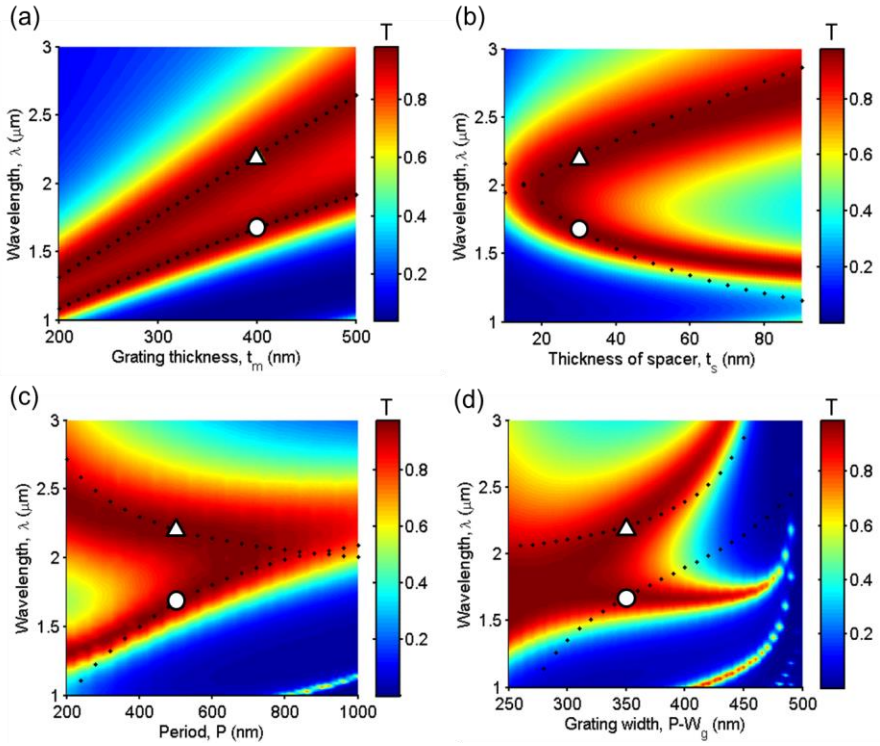

Figure 3.3 The effect of certain geometric parameters on the normal transmittance for TM waves using the parameters given in Figure 3.1 as the base set: (a) Ag grating thickness t_m; (b) Spacer thickness t_s; (c) Period P by keeping $W_g / P = 0.3$; (d) Grating strip width $P - W_g$. Note that the circle and triangle marks indicate the locations of P1 and P2, respectively, according to the base parameters.

To study the scaling effect, both the slit width W_g and the period P are changed, while their ratio is fixed to be 0.3. When the structure is scaled down, a broader high transmission region is obtained as shown in Figure 3.3(c). On the other hand, the two peaks merge when $P > 600$ nm. The LC models agree reasonably well with the full-wave results, except when the period is less than 300 nm. For very small P, the penetration depth in Ag may become comparable with the width of the ridge, so that the field for different periods may couple with each other.

The effect of slit width W_g is also examined by fixing the grating period and other parameters and the results are shown in Figure 3.3(d), where the abscissa is the ridge width ($P - W_g$). When $P - W_g > 350$ nm, the two peaks further split and the enhancement of transmittance with reducing slit width for some wavelengths is counter-intuitive. For broadband polarizer, the performance is still good when $P - W_g = 400$ nm (i.e., with a slit width of 100 nm only). For even smaller slit width, the structure can be used as a narrow band polarizer. Blocking-enhanced transmission has been predicted in 1D double-layer gratings [103, 121] and experimentally demonstrated for a 2D periodic structure [113]. Because the LC models were developed considering the field distributions using the base parameters, large deviations occur when $P - W_g$ is far away from 350 nm. The agreement in the predicted trends suggests that the excitation of MPs is still responsible for the transmission enhancement of the two branches. However, more suitable LC circuit may need to be developed according to the field distributions. It should be noted that a weak branch appears in the wavelength range from 1 to 1.5 μm when $P - W_g > 400$ nm. This branch can be quantitatively explained with a LC model considering the coupling

between the top and bottom gratings in the spacer region where the ridges overlap, although the details are not shown here.

3.2 Blocking-Assisted Transmission

In stark contrast to opaque metallic films, perforated films might support EOT with efficiencies that are orders of magnitude beyond geometry-based classic theory. This interesting EOT phenomenon has received extensive attention since the seminal work [9]. Simple metallic 1D gratings and 2D pillar arrays exhibit EOT, and the transmittance is usually broadband in the low-frequency region since no resonances are excited. However, this property impedes the above nanostructures to be used as sensors or color filters in long wavelengths although extraordinary transmission is supported. Graphene, a 2D layered material with carbon atoms arranged in a honeycomb lattice, exhibits metallic behavior when chemical doping or electric gating is applied [122-124]. This 2D Dirac material supports unprecedented optical properties beyond conventional metals such as extreme light confinement, low loss, high carrier mobility, and tunable graphene plasmon frequency ranging from near-infrared to terahertz [125]. The section theoretically demonstrates that it is possible to achieve resonance transmission of simple 1D gratings and 2D pillar arrays in the infrared wavelength region by depositing monoatomic layer of graphene. The blockage of this 2D conductive film can counterintuitively enhance the transmission performance.

Consider a graphene-covered 1D Ag grating as shown in Figure 3.4 (a). The grating or slit array is periodic along the x direction and extends to infinity in the y direction with a period P, height h, and slit width b. The incidence angle is θ, and thus the

incident wavevector can be written as $(-k_0 \sin\theta, 0, -k_0 \sin\theta)$ with k_0 as the wavevector in the free space. Only TM waves with magnetic field along the *y* direction are considered since the transmittance for TE waves is essentially zero for 1D grating. In the mid-infrared wavelength region, the optical response of 1D metal grating to TE waves can be approximated by a diluted Drude model weighted by the volume filling ratio [68], and this metallic response precludes the penetration through of TE waves.

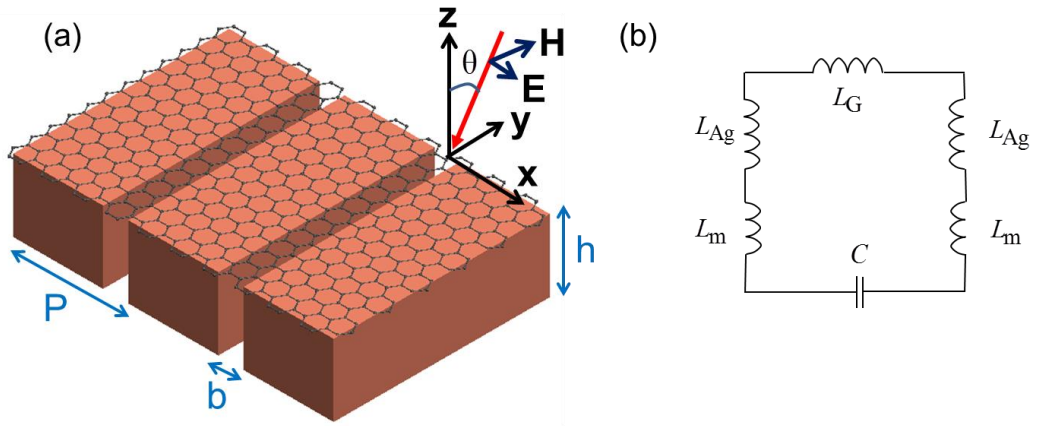

Figure 3.4 (a) Schematic of graphene-coated 1D Ag grating. Only TM wave is considered. Note that θ is the incidence angle, *P* the period, *b* the slit width, and *h* the grating height; (b) LC model for prediction of the resonance wavelength.

Optical conductivity of graphene σ, which includes both interband and intraband (Drude-like) contributions, depends on the chemical potential μ, electron scattering time τ, and temperature *T*, and is given as [126, 127]

$$\sigma = \sigma_{\text{Inter}}(\omega, \mu, T) + \sigma_{\text{Drude}}(\omega, \mu, T) \tag{3.8}$$

$$\sigma_{\text{Inter}} = \frac{e^2}{4\hbar}\left[G\left(\frac{\hbar\omega}{2}\right) + i\frac{4\hbar\omega}{\pi}\int_{\eta=0}^{\infty} \frac{G(\eta) - G(\hbar\omega/2)}{(\hbar\omega)^2 - 4\eta^2} d\eta \right] \tag{3.9}$$

$$\sigma_{\text{Drude}} = \frac{i}{\omega + i/\tau}\frac{e^2}{\pi\hbar^2}2k_B T \ln\left[2\cosh\left(\frac{\mu}{2k_B T}\right)\right] \tag{3.10}$$

where $G(\eta) = \sinh(\eta / k_B T) / [\cosh(\eta / k_B T) + \cosh(\mu / k_B T)]$. The graphene conductivity used in this work is calculated by setting $\tau = 10^{-13}$ s and temperature T = 300 K. The chemical potential μ can be tuned by chemical doping or electrostatic gating.

The computation for 1D grating and 2D nanopillars is based on RCWA and FDTD, respectively. Besides, equivalent circuit models are employed to help to elucidate the underlying mechanism for the blocking-enhanced transmission. The LC model corresponding to Figure 3.4 (a) can be described as in Figure 3.4 (b). The air inside the slit acts as a dielectric capacitor with a capacitance of $C = \varepsilon_0 hl/b$, where l is a prescribed length in the y direction. The Ag walls around the slit and graphene serve as conductors, and their kinetic inductances are determined by [128, 129]

$$L_{\text{Ag}} = -\frac{h}{\varepsilon_0 \omega^2 l \delta}\frac{\varepsilon'_{\text{Ag}}}{\left(\varepsilon'^2_{\text{Ag}} + \varepsilon''^2_{\text{Ag}}\right)} \tag{3.11}$$

$$L_{\text{G}} = \frac{c_1 b}{\omega l}\frac{\sigma''}{\left(\sigma'^2 + \sigma''^2\right)} \tag{3.12}$$

where δ is the penetration depth expressed as $\lambda/(4\pi\kappa)$ that takes into account the effective cross-section area for the induced current. Note that λ is the wavelength in vacuum and κ is the extinction coefficient of Ag. Coefficient c_1 is introduced because the length of graphene involved in the resonance is longer than the slit width due to the finite cross-section width of current in the slit wall. It could be affected by the slit width or period; however, $c_1 = 1.3$ is chosen in the present study as a reasonable representative value. The mutual inductance is given as $L_{\text{m}} = \mu_0 hb/2l$ [128, 130], where μ_0 is the

permeability of vacuum. This LC model can be confirmed by the distribution of current density shown in the next section. By zeroing the total impedance $i\omega\left(2L_{\mathrm{Ag}}+L_{\mathrm{G}}+2L_{\mathrm{m}}-\omega^{-2}C^{-1}\right)$, the resonance wavelength of MP can be obtained as

$$\lambda_{\mathrm{MP}}=2\pi c_0\sqrt{\left(2L_{\mathrm{Ag}}+L_{\mathrm{G}}+2L_{\mathrm{m}}\right)C} \tag{3.13}$$

Figure 3.5 (a) gives the transmittance for plain and graphene-coated grating at normal incidence with P = 1000 nm, b = 50 nm, h = 200 nm, and μ = 0.8 eV. The transmittance of plain grating is much greater than the filling ratio of the slit area 0.05 and monochromatically increases with wavelength. Nevertheless, the transmission selectivity is too poor to make 1D grating available as color filters or sensors in the long wavelength. When the wavelength is much longer than the period, according to effective medium theory [55, 68, 131], 1D and 2D nanopillars can be homogenized as uniaxial materials with optical axis lying tangentially and longitudinally, respectively. At normal incidence, the wavevector in the longitudinal direction (z axis) depends only on the effective dielectric function in the tangential direction. For both 1D nanopillars (only for TM waves) [68] and 2D nanopillars [55, 131], the imaginary part of this effective dielectric function approaches to zero especially with increasing wavelengths. That is because at low frequencies (long wavelengths), Ag acts like a perfect conductor with diminishing electric fields inside. Thus the electric field is nontrivial only in the slit region. Then nanopillars behave as a dielectric with low loss and a finite thickness, as a result, the transmittance of plain grating is high, and tends to further increase with wavelength. After depositing atomic thin graphene layer, a resonance transmission is clearly shown with a peak near λ = 10 μm. A transmission preference occurs in contrast

to the previous incoherent transmittance. For wavelengths ranging from 5 to 13.5 μm, covering the Ag grating with graphene improves its transparency. The maximum transmittance reaches 0.81 at λ = 9.72 μm, 3.5 times as high as that of the plain grating. This anomalous improvement is robust and alignment-free compared with using double-layer grating since graphene is a continuous sheet. The reflectance at 9.72 μm (not shown) is reduced substantially from 0.76 to 0.02, leading to an antireflection effect. The absorptance (*A*) of the plain grating is negligible (not shown) but increases to 0.17 at the resonance after being covered with graphene. Note that the absorptance of free-standing graphene is very low (less than 1%) in the mid-infrared region, suggesting that gratings can significantly enhance graphene absorption. This might be important for improving the performance of graphene-based optical devices relying on its absorption properties such as ultrafast optoelectronics enabled by the vanishing effective mass of free carriers in graphene. Similar phenomena of enhancing the absorption of graphene have recently been demonstrated in the visible and near-infrared region [132, 133]. Away from the resonance with wavelengths longer than 13.5 μm, coating metallic graphene will deteriorate the transmittance. This is not surprising since doped graphene is essentially a thin metallic film and has a low transmittance in the far-infrared region.

Figure 3.5 (b) displays the transmittance contour of 1D grating, showing the dependence on both the wavelength and incidence angle, while other parameters are the same as those used in Figure 3.5 (a). Clearly, the wavelength of the transmission peak is insensitive to the incidence angle; this is a distinct characteristic of magnetic polariton (MP) [129, 134-137], which will be further confirmed by the field and current density distribution. MP is the strong coupling between the magnetic resonance inside a

micro/nanostructure and the external electromagnetic waves. The time-varying magnetic field parallel to the *y*-direction creates an oscillating current loop in the *x*-*z* plane, which generates a localized enhanced electromagnetic field that indicates diamagnetic response [32]. Another interesting feature is the broadband high transmittance close to grazing incidence. This is associated with deep metallic gratings and has been explained previously based on either spoof surface plasmons [138] or impedance matching [139].

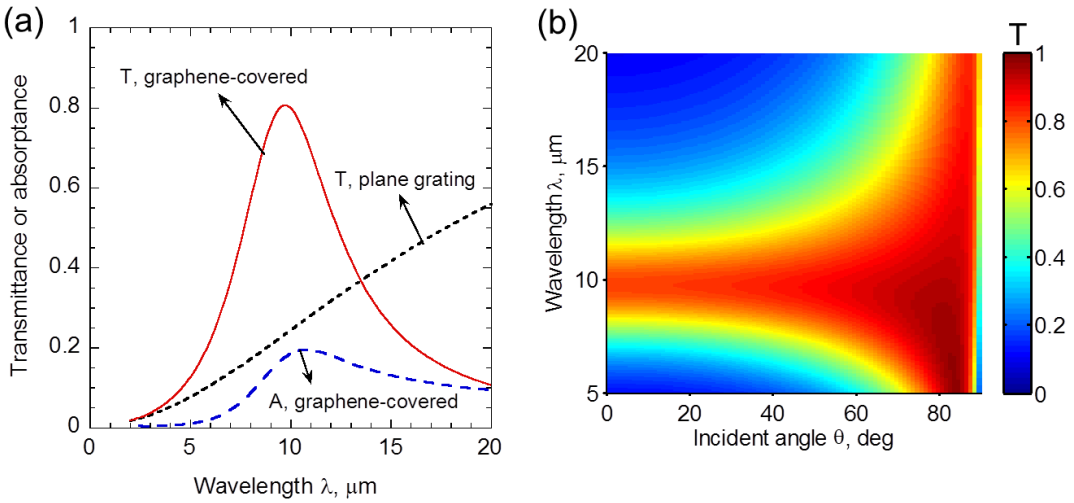

Figure 3.5 (a) Normal transmittance and absorptance spectra for plain and graphene-covered gratings; (b) Contour plot of the transmittance as a function of wavelength and incidence angle. The parameters are P = 1 μm, b = 50 nm, h = 200 nm, μ = 0.8 eV.

The magnetic field and current density vectors near the slit are shown in Figure 3.6 (a) to elucidate the underlying mechanism for the anomalous blocking-assisted transmission. The contour is for $\left|H_y / H_0\right|^2$ and black arrows represent the instantaneous current density vectors. Note that z = 0 and z = –0.2 μm denote the upper and lower boundaries of the Ag grating, respectively. Large field enhancement exists in the slit region (–0.025 < x < 0.025 μm) especially near the graphene, suggesting a localized

resonance. High field concentration can also be seen from the contour plots of electric fields as shown in Figure 3b. The relative field amplitude in the incident vacuum region is close to one, suggesting that the reflection is very small. The current density in the graphene is very high and is denoted as the white arrows pointing left. There is a displacement current in the air gap pointing right as indicated in Figure 3.6 (a). Combined with the counter-parallel current density vectors in Ag, it can be seen that a closed current loop is formed around the slit region as indicated by the oval, manifesting the existence of a magnetic resonance. The distribution of the current density vectors agrees with the LC model given in Figure 1b, which is thus reasonable to be used for predicting the MP resonance wavelength.

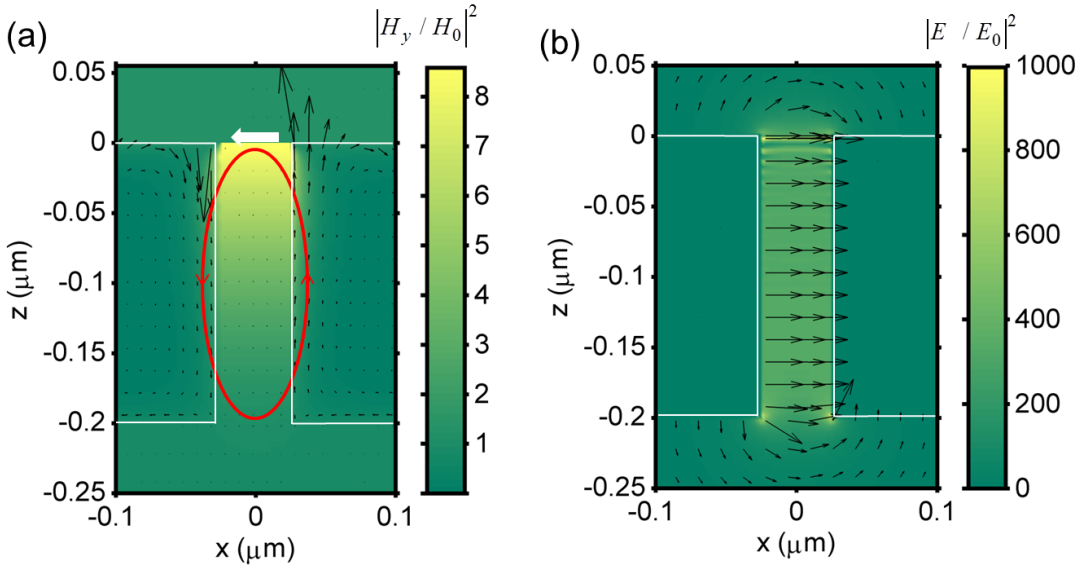

Figure 3.6 (a) Enhancement of the magnetic field $|H_y / H_0|^2$ at 9.72 μm where MP resonance is excited. (b) Enhancement of the electric field $|E / E_0|^2$ with black arrows as the electric field vectors.

The resonance wavelength predicted by the LC models given in Eq. (3.13) is 9.57 μm, which agrees well with 9.72 μm obtained by numerical simulations. The insensitivity of resonance transmission to the incident angle as shown in Figure 3.5 (b) can be explained by Eq. (3.13) since there are no terms related to θ. Therefore, the transmission peak is due to the excitation of MP resonance. This MP resonance is not achievable in the infrared region without the coated single layer graphene sheet, which provides the dominant inductance required for the LC resonance. Strong localized field in the slit region due to resonance excitation helps photons pass through and reduces the reflection [129]. Note that graphene has been demonstrated to tune the resonances of metallic antennas since evanescent waves with large-wavevectors can couple with the graphene plasmons [140, 141]. Graphene ribbons or gratings can launch graphene plasmons directly to achieve some resonance effects since the momentum mismatch can be provided by the surface diffraction [142, 143]. The angle-insensitive MP resonance assisted by graphene at low frequencies discussed here is different from the above-mentioned scenarios.

The effects of various geometric parameters and chemical potential of graphene on the transmittance at normal incidence are shown in Figure 3.7 by changing one parameter while maintaining other parameters at the default values as those in Figure 3.4 (a). The prediction from the LC model as indicated by the cross mark generally agrees well with that from the RCWA. As shown in Figure 3.7 (a), the resonance wavelength monotonically increases with grating height. This trend can be easily predicted by Eq. (3.13) since both L_{Ag} and C increase with h. With increasing chemical potential, the number of free electrons in graphene increases, leading to a higher conductivity. Then L_G

decreases; according to Eq. (3.13), this gives a blueshift of MP resonance as shown in Figure 3.7 (b). With increasing chemical potential, the coherence (Q factor) is improved with smaller full width at half maximum. By employing complex nanopillars with different parameters, such as chemical potentials and grating height, used in neighboring periods [144-146], the transmission can be tuned to be multiband to meet different demands.

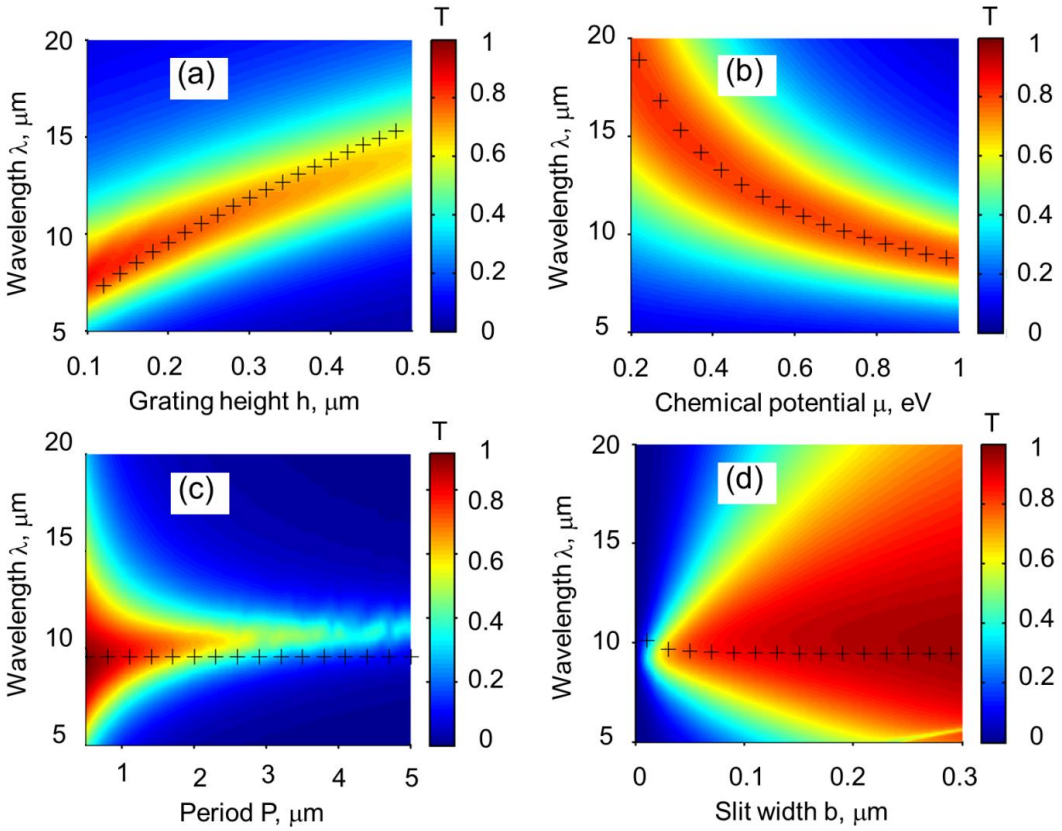

Figure 3.7 Normal transmittance contours with varying parameters: (a) Grating height; (b) Chemical potential; (c) Period; (d) Slit width.

Figure 3.7 (c) illustrates the effects of period on the transmittance. The transmission peak is not sensitive to the period, and this can be explained by the LC model since MP is a localized resonance and there are no terms related to the period in Eq. (3.13). Similar results were found in [130] for deep gratings without graphene

coverage. The bandwidth of the transmittance peak is tunable and becomes narrower at larger P. This phenomenon is desired for filters that allow radiation in certain desired wavelength region to pass. However, the transmission intensity will deteriorate to some extent at large period while keeping the same slit width. Another tunable parameter is the slit width, whose effect is shown in Figure 3.7 (d). The transmission peak appears to be insensitive to b and this can also be predicted by the LC model. Note that the capacitance C is inversely proportional to b while both L_G and L_m are linearly proportional to b. Given that L_{Ag} is small compared with L_G, the resonant wavelength should be almost independent of b according to Eq. (3.13). The deviation between the LC model and RCWA simulations may be due to the approximation of c_1, as well as the nonuniform charge distribution that could affect the gap capacitance [35]. Overall, the simple LC model not only provides a physical interpretation of the anomalous transmission, but also allows quantitative understanding of the dependence of the resonance condition on the geometric and materials properties.

The imaginary part of the conductivity of doped graphene is positive, leading to a negative real part of the dielectric permittivity according to the finite-thickness model [35]. Therefore, doped graphene has a metallic characteristic. One might wonder whether the previously discussed blocking-assisted resonance transmission will hold if graphene is replaced by a thin layer of conventional metal film. As shown in Figure 3.8 (a), similar anomalous transmittance phenomenon is supported in a narrower band when a Ag film with various thicknesses is deposited on the top side of the grating. Assuming the bulk dielectric function applies to thin Ag film without considering the increased scattering rates due to electron collisions with boundaries, the peak transmission calculated using

RCWA occurs at λ = 3.54 μm for a thickness of 0.5 nm as shown in Figure 3.8 (a). This is in good agreement with the value of 3.76 μm predicted by Eq. (3.13) where L_G becomes $-\frac{c_1 b}{\varepsilon_0 \omega^2 l d}\frac{\varepsilon'_{Ag}}{\left(\varepsilon'^2_{Ag}+\varepsilon''^2_{Ag}\right)}$, where d is the thickness of the Ag film. The agreement in the resonance wavelength between LC model and exact numerical method holds for different film thicknesses as shown in Figure 3.8 (b). Decreasing Ag film thickness will redshift and broaden the transmission as shown in Figure 3.8 (a), which is similar to the effect of decreasing graphene chemical potential as shown in Figure 3.7 (b). This is due to the increased kinetic inductance of Ag film. Increasing Ag thickness will have the opposite effect. The transmission peak can be easily tuned by controlling the thickness of Ag film, but it should be noted that fabrication of a uniform suspended Ag film of sub-nanometer thickness across the slit region is very challenging with present-day technologies. Therefore, doped graphene has advantageous over metallic films in terms of enhancing the transmission magnitude and coherence of gratings or slit arrays since its fabrication and transfer techniques have been successfully demonstrated.

Covering graphene on both sides of the Ag grating can lead to similar resonance transmission as show in Figure 3.9a for different chemical potentials at normal incidence. The chemical potential is assumed to be the same for both the top and bottom graphene. The resonance wavelength increases with decreasing chemical potential, which has the same trend as Figure 3.7 (b). The field plot for μ = 0.8 eV at resonance wavelength of 6.87 μm is given in Figure 3.9 (b), which clearly shows that there are two split localized resonances excited near the bottom and top graphene sheet respectively. As indicated by the arrows, two identical current loops but with opposite directions are supported. The

LC model in Figure 3.4 (b) and Eq. (3.13) can be used directly to predict the resonance position considering that half of the total grating height should be used. The resonance peak is then predicted to be 6.68 μm. This agrees with the peak location occurring at λ = 6.87 μm obtained by using RCWA as shown in Figure 3.9 (a). The peak transmittance is still around 80%, but the resonance wavelength decreases by approximately $\sqrt{2}$ from 9.72 μm to 6.87 μm after covering graphene on both sides. This is because the capacitance is reduced by 50% while the total kinetic inductance barely changes due to the dominant contribution of graphene, whose inductance is independent of the grating height. These examples not only help further demonstrate the validity of the LC model and confirm the MP resonance excitation, but also suggest alternative methods for tuning the transmission peaks.

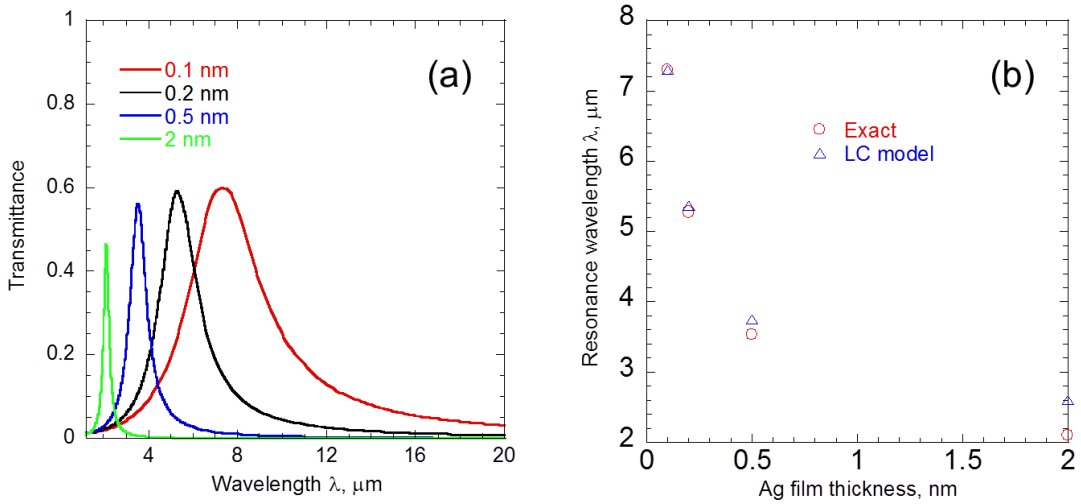

Figure 3.8 (a) Transmittance spectra when covering a thin Ag film of various thicknesses on top of the Ag grating; (b) The resonance wavelength versus film thickness obtained by using exact method and LC model.

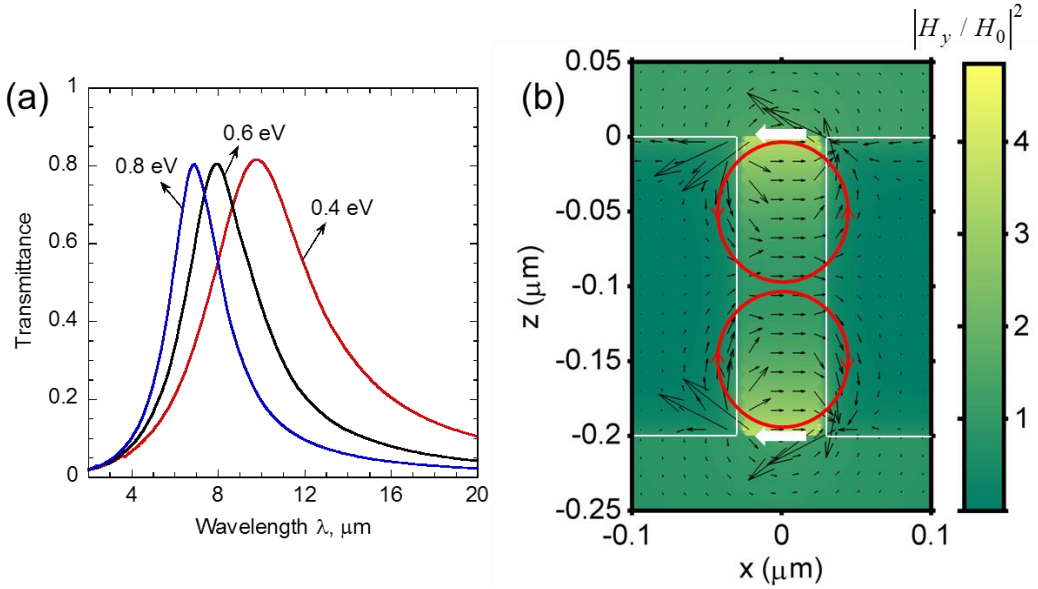

Figure 3.9 (a) Transmittance spectra for Ag grating with graphene coverage on both sides; (b) Magnetic field at resonance peak of 6.87 μm.

The aforementioned blocking-assisted transmission is supported only by TM waves for 1D grating while the transmittance of TE waves is so small that adding graphene will have negligible effects. As a result, the proposed structure can be used for polarizers with better performance than plain 1D Ag grating. Nevertheless, for some applications such as transparent electrodes, polarization-insensitivity might be desired, otherwise half of the total energy will be lost. This necessitates the analysis of 2D pillars whose schematic is shown in Figure 3.10 (a). P_x (b_x) and P_y (b_y) are the period (slit width) in the x and y directions, respectively, and h_2 is the grating thickness. Figure 3.10 (b) gives the transmission of plain and graphene-covered 2D pillar arrays at normal incidence with $P_x = P_y = 1$ μm, $b_x = b_y = 0.05$ μm, and $h_2 = 0.2$ μm for different values of chemical potentials. Similar anomalous enhanced transmission over plain 2D pillar arrays can be clearly observed by coating a single layer of graphene sheet. The transmission performance of 2D pillar arrays does not change much compared with 1D counterparts at

the same geometric parameters and graphene chemical potential. One distinction from 1D grating is that there is no difference between TE and TM waves at normal incidence for 2D pillars due to the structure symmetry. Therefore, graphene-covered 2D metallic grating can be used for transparent electrodes, filters, or sensors with no polarization preference.

Similar blocking-assisted transmission by graphene can be found in subwavelength gratings made of other metals (Au or Al) or doped semiconductors (such as doped silicon) or polar materials (such as SiC), although the results are not presented here. Depositing graphene or atomically thin metal film on one side or two sides of the grating helps to excite and tune the resonances, whose net effects are not limited to enhancing the transmission and coherence. Meanwhile, the light is concentrated in a small slit region beyond the diffraction limit [147]. This might assist the light management of long wavelengths in deep subwavelength scale and enhance matter-wave interactions, such as Raman scattering, spontaneous emission, and nonlinear processes, by using simple 1D or 2D gratings. In addition, devices such as polarizers or filters based on the proposed configuration is very thin, only about 2% of the wavelength, and thus can be easily incorporated with other compact optical devices. It can also work independently when mounted on different transparent substrates in the infrared region such as silicon.

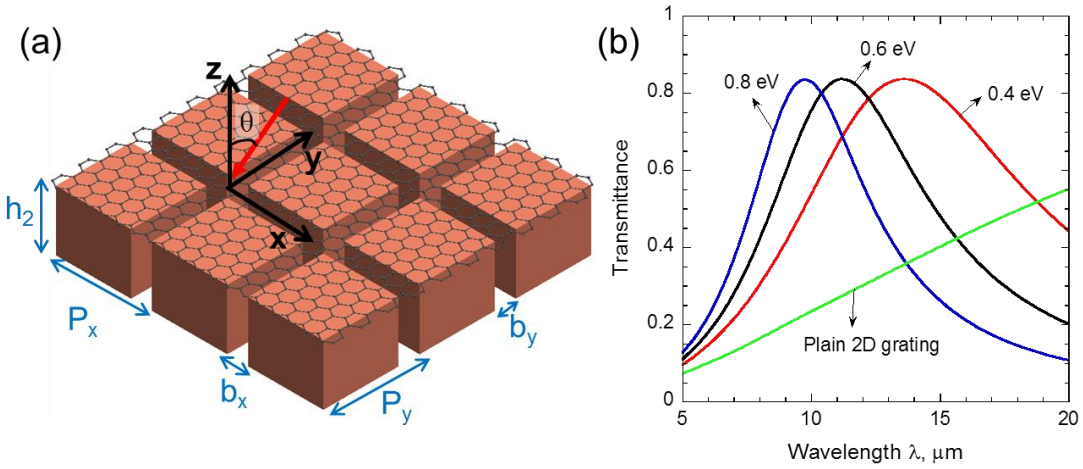

Figure 3.10 (a) Schematic of graphene-covered 2D pillar arrays with periods and slit widths in *x* and *y* directions as P_x, P_y, b_x, b_y. h_2 is the grating height. (b) Transmittance of plain and graphene-covered 2D pillar arrays at normal incidence for different chemical potentials.

3.3 Loss-Assisted Negative Refraction

Negative refraction has attracted much attention in recent years due to its potential applications for flat lens and sub-diffraction imaging [3, 148, 149]. Double negative materials (DNG) with both permeability and permittivity being negative have been realized to bend light negatively by using artificial nanostructured metamaterials, such as combinations of split-ring resonators and nanowires [10, 150], nanostrip pairs [151], and fishnet structures [152-154]. DNG was experimentally demonstrated by Shelby et al. [150] in the microwave region; and since then, the desire for sub-diffraction imaging with higher resolution triggered interest to extend negative refraction to the near-infrared [152] and visible region [153, 154]. For more information, one could refer to recent review papers [148, 155, 156]. Nevertheless, since resonance is usually needed to obtain negative permeability, losses are usually too high for it to be used in practical optical devices. Besides, the performance sustains only for narrow ranges of wavelengths and incidence angles due to the conditions required to excite magnetic resonances. Single

negative material (SNG) with only the permittivity being negative, such as thin silver films, could also support negative refraction [157-159], but the light penetration depth is very small because only evanescent waves can exist in these materials.

More recently, uniaxial materials with permittivities having different signs for ordinary (electric field is perpendicular to the optical axis) and primary extraordinary waves (electric field is parallel to the optical axis), also known as hyperbolic or indefinite metamaterials, were proposed as good candidates for all-angle negative refraction [160]. Focusing and negative refraction have been experimental demonstrated in the visible and microwave region using either one-dimensional metal-dielectric multilayers[161] or metallic nanowires [63, 162]. By employing multilayered hyperbolic metamaterials based on doped semiconductors, all-angle negative refraction has also been realized in the mid-infrared [163] and more recently near-infrared regions. Nevertheless, for multilayered metamaterials, the negative refraction performance is narrow-band, and a Lorentzian resonance generally needs to be excited to obtain the negative permittivity for primary extraordinary waves while no resonances are needed for nanowires [162].

Here, low-loss negative refraction is demonstrated for all angles and in a broad wavelength range based on doped silicon nanowire (D-SiNW) arrays with hyperbolic dispersion. The mid-infrared region is of interest due to potential applications for near-field radiation heat transfer analysis [66, 158], thermal imaging [164], and designing flat lenses and collimators for the infrared region. The mechanism for low-loss is explained by using loss-enhanced transmission, along with impedance matching and the absence of resonances. The proposed structure only uses doped silicon, which is abundant and

cheap; besides, Si is nontoxic and has relatively mature processing technology and better integration compatibility with nanoelectronics over metals.

The diameter and thickness of the nanowires are *d* and *H*, respectively. A plane electromagnetic wave is incident from air at an incidence angle of θ_0. The array period is *a* thus the volume filling ratio can be calculated by $f = 0.25\pi d^2 / a^2$. D-SiNW arrays are a mixture of air and nanowires. However, when the characteristic dimension of nanowires *d* is considerably smaller than the wavelength of the incident light, the inhomogeneous medium can be treated as an effective medium with a homogeneous dielectric function. This has been verified by FDTD method [165] and finite-element method (FEM) [162]. Only TM waves with magnetic field perpendicular to the plane of incidence are considered in this work. In this case, the anisotropic dielectric function of the D-SiNW array is a second-order tensor [165, 166] :

$$\overline{\overline{\varepsilon}} = \begin{pmatrix} \varepsilon_x & 0 & 0 \\ 0 & \varepsilon_y & 0 \\ 0 & 0 & \varepsilon_z \end{pmatrix} = \begin{pmatrix} \varepsilon_{\mathrm{O}} & 0 & 0 \\ 0 & \varepsilon_{\mathrm{O}} & 0 \\ 0 & 0 & \varepsilon_{\mathrm{E}} \end{pmatrix} \tag{3.14}$$

The dispersion relation of the effective homogeneous medium is given as

$$\frac{k_x^2}{\varepsilon_z} + \frac{k_z^2}{\varepsilon_x} = \frac{\omega^2}{c_0^2} = k_0^2 \tag{3.15}$$

Let $\varepsilon_x = \varepsilon_x' + i\varepsilon_x''$ and $\varepsilon_z = \varepsilon_z' + i\varepsilon_z''$. When $\varepsilon_x' > 0$ and $\varepsilon_z' < 0$, negative energy refraction will be supported.[65, 162]. The wavelength-dependent ε_x' and ε_z' are shown in Figs. 3.11 (a) and (b), respectively, for different doping levels when the volume filling ratio *f* is set as 0.1 (default in this paper).

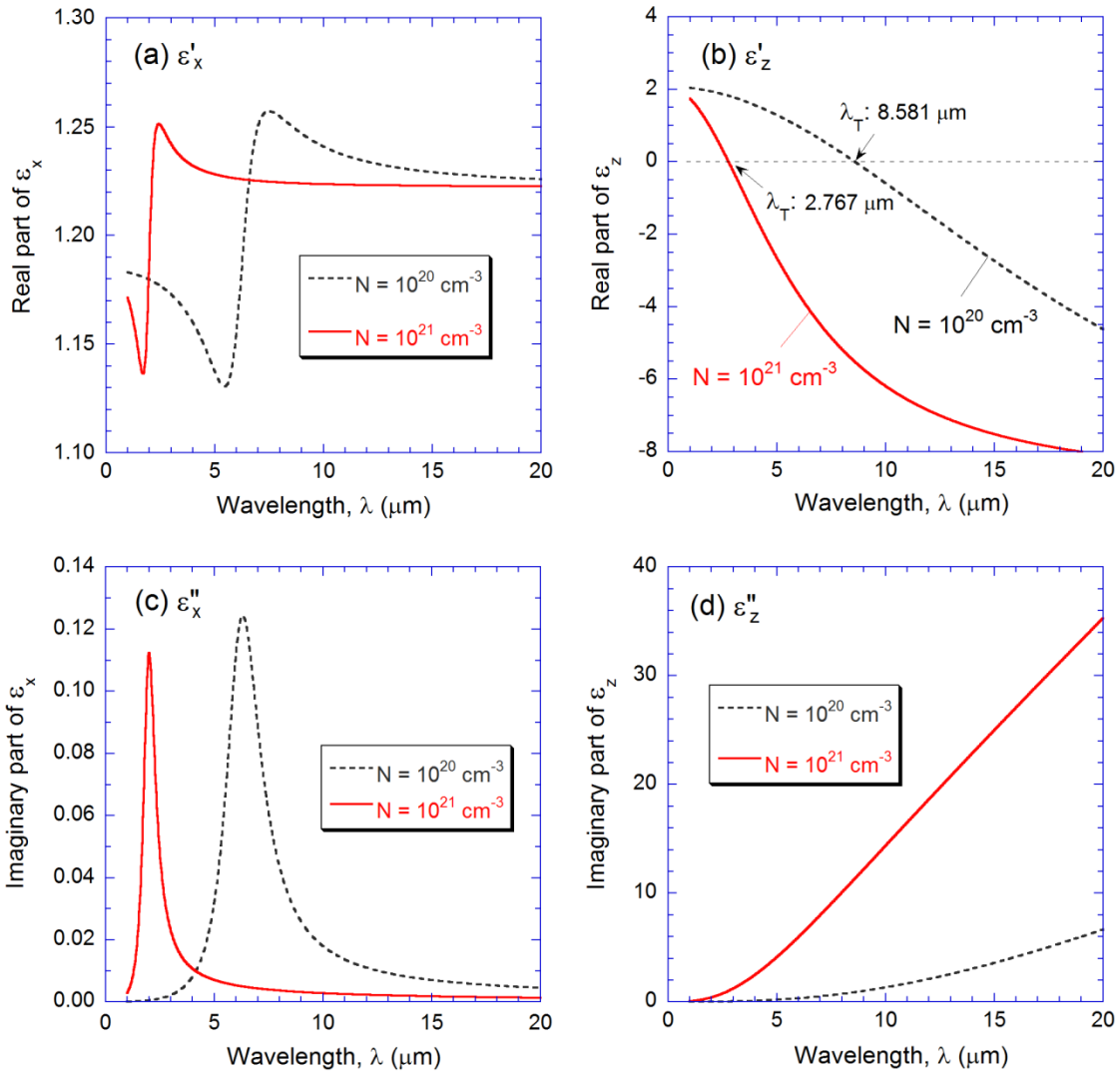

Figure 3.11 Effective permittivities of D-SiNW arrays with f = 0. 1. (a) Real part of permittivity for primary ordinary wave; (b) Real part of permittivity for primary extraordinary wave; (c) Imaginary part of permittivity for primary ordinary wave; (d) Imaginary part of permittivity for primary extraordinary wave.

Note that ε'_x is almost a constant near 1.2 across the whole wavelength range, though there is a Lorentz resonance featured with higher absorptance and a small bump of ε'_x. On the other hand, ε'_z decreases monotonously with increasing wavelength. The transition wavelength at which $\varepsilon'_z = 0$ is denoted as λ_T. It can be seen that λ_T = 8.581 μm and 2.767 μm and for doping level N equal to $N_1 = 10^{20}$ cm^{-3} and $N_2 = 10^{21}$ cm^{-3},

respectively. Therefore, high doping levels will blueshift the transition, so will increasing the volume filling ratio though not shown here. The values of ε_x'' and ε_z'' are shown in Figs. 3.11 (c) and (d), respectively. It can be seen that ε_x'' is almost negligible even when Lorentz resonances occur. Note that ε_z'' is much greater than ε_x'' , especially at higher doping levels due to the increased number of free carriers. At first glance, this seems to be an undesired feature as a large ε_z'' implies high loss for primary extraordinary waves. However, as to be shown later, higher loss actually can help enhance the transmission at oblique incidence, i.e., reducing the loss in this type of hyperbolic metamaterial.

The tangent of the refraction angle for the wavevector is $\tan\theta_k = k_x / \mathrm{Re}(k_z)$ and that for the Poynting vector can be expressed as

$$\tan\theta_s = \frac{S_x}{S_z} = \frac{\mathrm{Re}(k_x/\varepsilon_z)}{\mathrm{Re}(k_z/\varepsilon_x)} \tag{3.16}$$

where S_x and S_z are the components of the Poynting vector **S**, and k_z can be solved from Eq. (3.15) as $k_z = k_0\sqrt{\varepsilon_x - (\varepsilon_x/\varepsilon_z)\sin^2\theta_0}$ since $k_x = k_0\sin\theta_0$. It should be noted that both the Poynting vector and wavevector will be positively refracted when the wavelength λ is shorter than the transition wavelength for given doping level and filling ratio. The isofrequency contour in this case is elliptic since both ε_z' and ε_x' are positive. When λ = 10 μm, due to the hyperbolic dispersion, negative refraction of the Poynting vector occurs for both doping levels at any oblique incident angle, as shown in Figure 3.12 (a). For $N = N_2$, the magnitude of θ_s becomes much smaller with a maximum of 1.5°, meaning that the waves will propagate nearly parallel to the nanowires inside the D-SiNW array for any incidence angles. This phenomenon makes the array act as an optical

collimator, which could find potential applications in sensors and detectors to increase the acceptance angles. The collimation effect has recently been shown in epsilon-near-zero (ENZ) metamaterials [167] ; however, it will be difficult to fabricate broadband ENZ materials.

The dimensionless hyperbolic isofrequency contour is given in Figure 3.12 (b) for $N = N_1$ and $\lambda = 10$ μm to theoretically demonstrate the negative refraction of the Poynting vector, which is normal to the isofrequency surface. As the incident angle increases, $|\theta_s|$ increases monotonically and gradually reaches the maximum for $\theta_0 = 90°$. Note that the propagation loss, determined by Im(k_z) is very small, even though the values of ε_z'' as shown in Figure 3.11 (d) are quite large. The mechanism will be explained later.

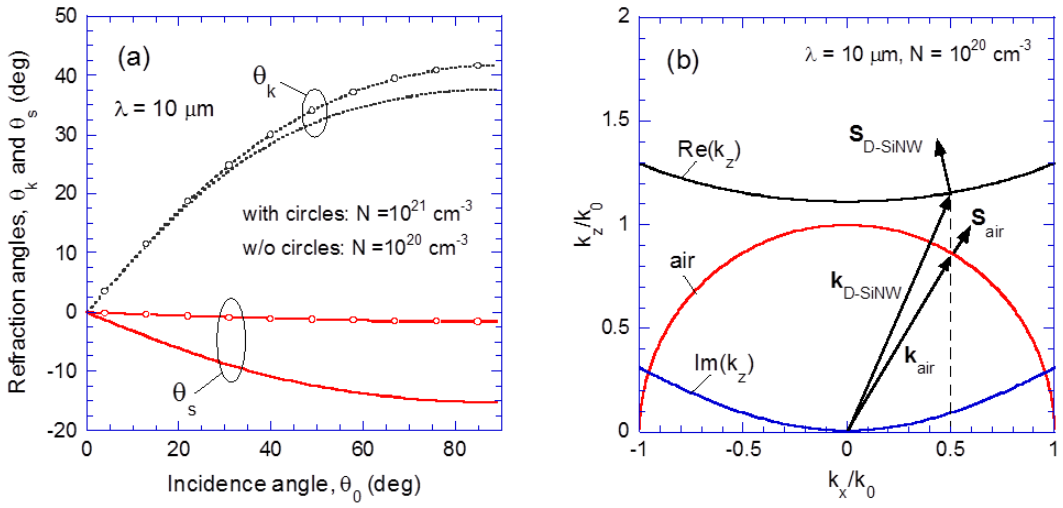

Figure 3.12 (a) Refraction angles for wavevector and Poynting vector versus incidence angle for $\lambda = 10$ μm; (b) Normalized hyperbolic isofrequency contour for $N = N_1$ and λ = 10 μm, where Re(k_z) and Im(k_z) are for D-SiNW array.

The field distribution can be obtained by FDTD for a Gaussian beam incident from air. Consider a D-SiNW array with thickness H = 20 μm and $N = N_1$, the magnetic

field distributions are shown in Figs. 3.13 (a) and (b) using the commercial FDTD software (Lumerical Solutions, Inc.) with a Gaussian beam with a width of 20 μm at λ = 10 μm and θ_0 = 20°. The interface between air and the D-SiNW array is delineated as thin horizontal lines at z = ±10 μm. Figure 3.13 (a) is for the actual 3D nanowires structures with a = 2 μm and f = 0.1 (i.e., d = 714 nm). Some vertical fringes represent the boundary between individual D-SiNWs and air. The field distribution obtained by FDTD using effective permittivity tensor is shown in Figure 3.13 (b) and the result agrees well with that in Figure 3.13 (a). The beam is clearly shown to be bended negatively in the nanowire array and the agreement between Figs. 3.13 (a) and (b) confirms the applicability of the anisotropic effective medium approach. Note that thinner nanowires will be necessary for EMT to be applicable at shorter wavelengths. The reflection loss is relatively small due to the good impedance matching between air and D-SiNW arrays. This can be understood by the fact that ε'_x is close to 1 and $\varepsilon''_x \ll 1$ in the hyperbolic dispersion region as shown in Figure 3.11.

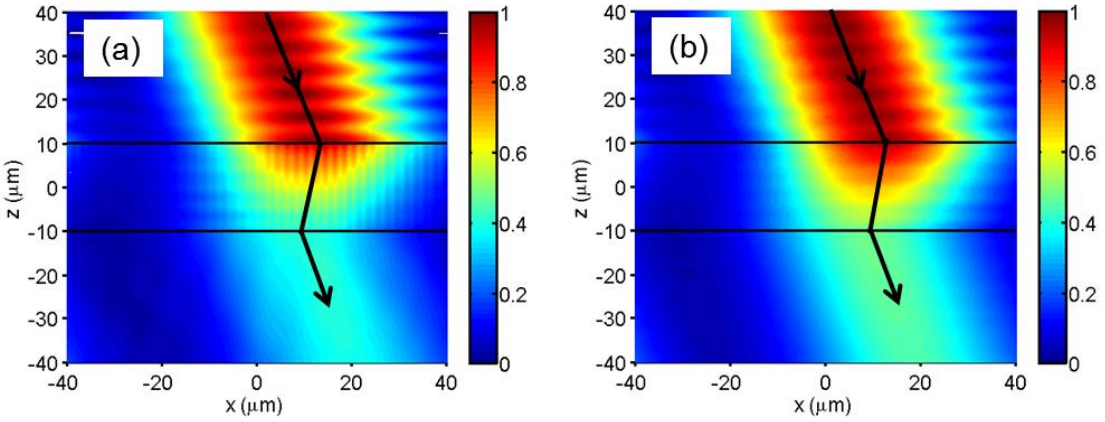

Figure 3.13 Dimensionless magnetic field amplitude |**H**| obtained by FDTD for a Gaussian beam at $\theta_0 = 20^o$ and λ = 10 μm: (a) with the actual nanowire structure for a = 2 μm; (b) with the effective permittivities.

The figure of merit (FOM) given in the following was introduced by Hoffman et al.[65] to describe the performance of a hyperbolic metamaterials in terms of light propagation

$$\mathrm{FOM} = \frac{\mathrm{Re}(k_z)}{\mathrm{Im}(k_z)} \tag{3.17}$$

A high FOM means that waves can propagate more freely with less loss inside the medium. This definition takes into account the dependence of loss on specific propagating direction. FOMs for different doping levels when θ_0 is at 20° and 60° are shown in Figure 3.14. Note that when $N = N_1$, negative refraction starts from $\lambda_T = 8.581$ μm as marked by the square symbols. With $N = N_1$, the FOM value at $\lambda = 10$ μm and $\theta_0 = 20°$ is 23.4, which is greater than those reported earlier [65, 163]. It can be seen that FOM increases monotonously with wavelength to more than 100 at $\lambda = 20$ μm. For hyperbolic materials made with nanowires, the Lorentz resonance is away from the wavelengths at which negative refraction occurs, implying that lower loss or less absorption can be achieved [162]. Note that the FOM values are much higher for N equal to N_2 than N_1. This is counterintuitive since the loss is much higher (i.e., ε_z'' is much greater) for $N = N_2$ than $N = N_1$. For $N = N_2$, the FOM at $\theta_0 = 20°$ and $\lambda = 10$ μm reaches 219, which is more than one order of magnitude greater than the previously reported values for multilayered hyperbolic metamaterials based on all semiconductors [65, 163]. The mechanism of loss-assisted FOM or transmission at oblique incidence is elucidated next.

From Figs. 3.11 (a) and (c), when $\lambda \geq \lambda_T$, ε_x'' could be one or even three orders of magnitude less than ε_x' especially for longer wavelengths. As a result, ε_x'' can be neglected and k_z can be simplified as

$$k_z \approx k_0\sqrt{\varepsilon_x'}\sqrt{1-\sin^2\theta_0/\varepsilon_z} = k_0\sqrt{\varepsilon_x'}\sqrt{1-\frac{\varepsilon_z'}{\varepsilon_z'^2+\varepsilon_z''^2}\sin^2\theta_0 + i\frac{\varepsilon_z''}{\varepsilon_z'^2+\varepsilon_z''^2}\sin^2\theta_0} \tag{3.18}$$

Figs. 3.11 (b) and (d) show that ε_z' is much smaller than $\varepsilon_z'^2+\varepsilon_z''^2$; thus, the second term inside the square root is much less than 1. Therefore,

$$k_z \approx k_0\sqrt{\varepsilon_x'}\sqrt{1+i\frac{\sin^2\theta_0}{\varepsilon_z''+\varepsilon_z'^2/\varepsilon_z''}} \tag{3.19}$$

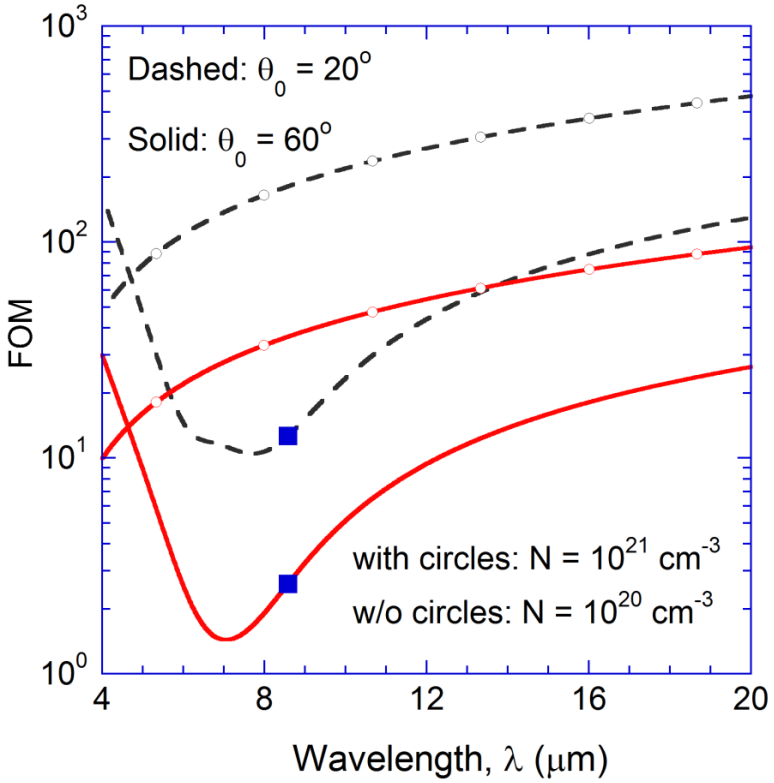

Figure 3.14 FOM as a function of wavelength at two incidence angles, θ_0 = 20° and 60°, for doping levels $N_1 = 10^{20}$ cm^{-3} and $N_2 = 10^{21}$ cm^{-3}. The squares denote the transition wavelength for N_1.

For $\lambda \geq \lambda_T$, $\frac{\sin^2\theta_0}{\varepsilon_z'' + \varepsilon_z'^2/\varepsilon_z''} << 1$ especially with high doping levels; therefore, the FOM can be approximated as follows when $\theta_0 \neq 0$

$$\text{FOM} \approx \frac{2\left(\varepsilon_z'' + \varepsilon_z'^2/\varepsilon_z''\right)}{\sin^2\theta_0} \tag{3.20}$$

It can be shown that for given θ_0 and ε_z', the FOM will increase with ε_z'' as long as $\varepsilon_z'' \geq |\varepsilon_z'|$, which is satisfied here. For $N = N_2$, $|\varepsilon_z'| << \varepsilon_z''$ and thus $\text{FOM} \approx 2\varepsilon_z''/\sin^2\theta_0$ at oblique incidence. In this case, the FOM will depend only on ε_z'' at a given θ_0. Since $\varepsilon_z'' = f\,\varepsilon_{\text{D-Si}}''$, higher doping concentrations, i.e., larger $\varepsilon_{\text{D-Si}}''$ and ε_z'', will lead to an enhanced FOM. It can be shown that Eq. (3.20) is a good approximation of the exact FOM. For example, compared with exact values of 23.3 and 219.1, the simplified formula predicts FOMs of 27.1 and 291.0 for doping levels N_1 and N_2, respectively, when λ = 10 μm and θ_0 = 20°. The agreement holds for other doping levels and incident angles as long as θ_0 is not too small. For near normal incidence, loss is dominated by ε_x'', i.e., ordinary waves. While Eq. (3.20) breaks down for very small θ_0, Eq. (3.17) is applicable to normal incidence, at which $\text{FOM} = n'/n''$ where n' and n'' are the real and imaginary parts of the ordinary refractive index, respectively.

While simple, Eq. (3.20) provides a physical insight into the loss-enhanced transmission and may be useful for estimation of FOM in practical design. This counter-intuitive loss-assisted FOM or transmission has been recently shown for ENZ metamaterials [167, 168]. Higher doping concentrations can increase both FOM and

transmission for sufficiently large θ_0. Moreover, with increasing doping level, θ_s will be significantly reduced and highly efficient collimators can be obtained. The doping concentration may be adjusted to achieve a desired FOM and θ_s in a suitable wavelength region to meet the requirements for specific applications.

3.4 Tunable Perfect Absorbers

A number of groups have demonstrated the use of metamaterials as coherent absorbers or emitters [169-174]. Nevertheless, different resonance peaks can interact with each other and thus reduce the absorption. Carbon nanotubes exhibit high absorptance over a broad range of wavelengths [52, 53, 175-178]. However, the absorption by carbon nanotubes tends to cover an overly broad spectral range that is not tunable. Therefore, realizing omnidirectional wavelength-selective absorbers with good tunability is still a challenge.

In this section, the radiative properties of D-SiNW arrays are theoretically investigated for wavelength selective, broadband ominidirectional absorbers (or emitters) operating near room temperature. Using silicon as the base material has many advantages due to its abundance, nontoxicity, and mature manufacturing and process technology. A number of techniques have been developed to fabricate SiNWs. Examples are the vapor-liquid-solid (VLS) process [179-182], physical and chemical vapor deposition [183, 184], electrodeposition [185], and the combination of patterning and catalytic etching [186-188], which allows wafer-scale fabrication of aligned SiNW arrays with defined shape, diameters, period, filling ratio, doping level and even growth direction. Since the doping concentration strongly affects the infrared absorption of bulk silicon and the effective

radiative properties of nanowire arrays depend strongly on the geometric properties and filling ratio, D-SiNW arrays may allow for flexible control of the infrared radiative properties. EMT is applied together with anisotropic thin-film optics to calculate the radiative properties. The FDTD method is also used to validate the EMT approach.

The basic structure of the D-SiNW array on a silicon film is shown in Figure 3.15. The top and bottom medium are air (medium 1 and 4). Here, H_2 and H_3 are the thickness of the nanowire array film and silicon film, respectively. When $H_3 = 0$, it becomes a free-standing D-SiNW array. This configuration can be viewed as if the nanowires are on a dielectric substrate with a refractive index close to 1. The diameter of the nanowires is *d*. It is assumed that the D-SiNWs form a periodic array with spacing of *a* in both the *x*- and *y*-directions. Thus the volume filling ratio can be calculated by $f = 0.25\pi d^2 / a^2$. A plane electromagnetic wave is incident from medium 1 at an incidence angle of θ_1, as illustrated in Figure 3.15. EMT treats medium 2 (D-SiNW array) as a homogeneous uniaxial medium whose optical axis is coincident with the *z*-axis.

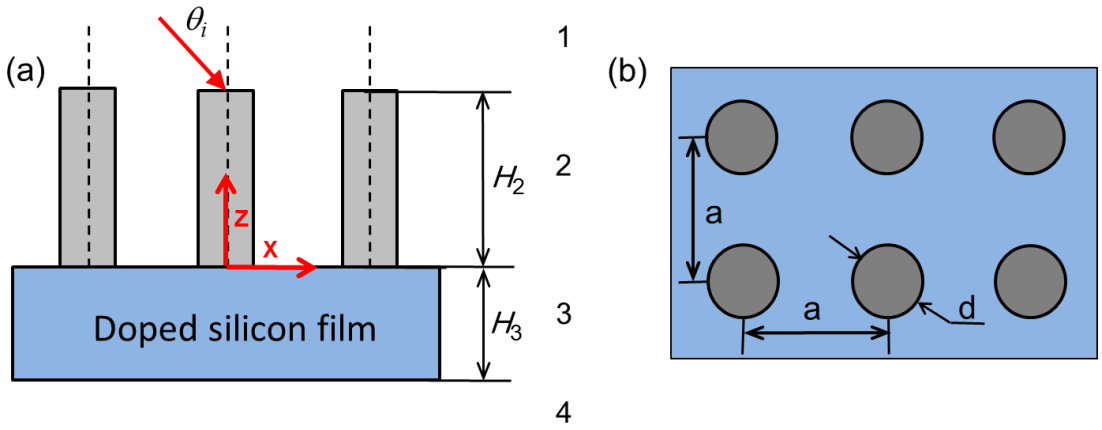

Figure 3.15 Schematic of a D-SiNWs array (medium 2) on a Si film (medium 3), where the top and bottom media (1 and 4) are assumed to be air: (a) cross-section view; (b) top view.

In order to verify the aforementioned theoretical model used to predict the absorptance of D-SiNWs, a comparison is made with the full-wave solution using a commercial FDTD package. In the FDTD simulation, it is assumed that a = 100 nm and d is determined from the filling ratio f used in the EMT calculation. Figure 3.16 compares the absorptance calculated from the EMT and anisotropic thin-film optics with that from FDTD for a free-standing D-SiNW array (i.e., $H_3 = 0$). The SiNW array has a height of H_2 = 100 μm and a doping concentration of $N = 10^{20}$ cm^{-3}. The comparison result is shown in Figure 3.16 (a) for the normal incidence when the SiNW array has volume filling ratios of 0.15 and 0.3. The FDTD simulation and the theoretical model agree with each other well, despite very small relative differences in the long wavelength region.

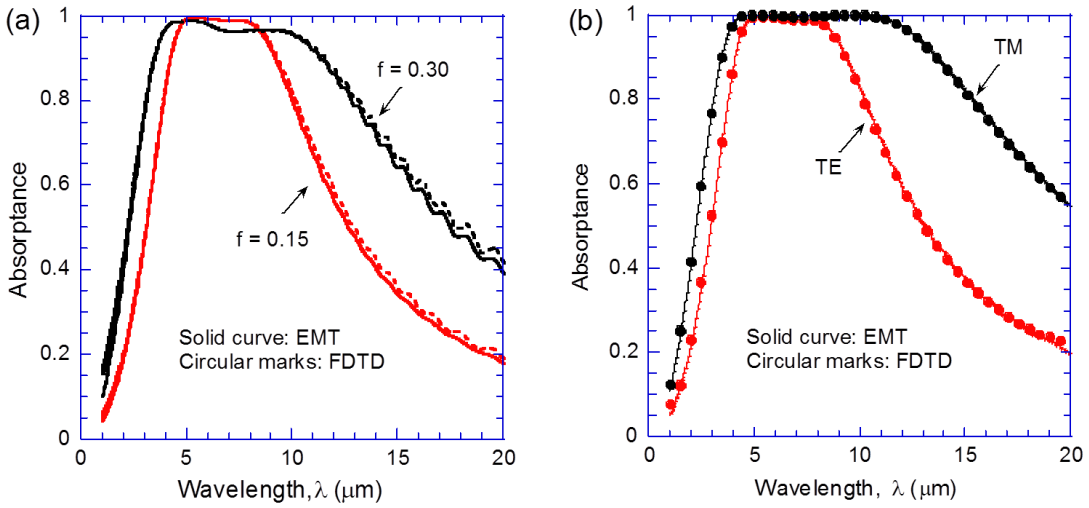

Figure 3.16 Comparison of the spectral absorptance of a free-standing D-SiNWs array, with H_2 = 100 μm and $N = 10^{20}$ cm^{-3}, predicted from the EMT and FDTD: (a) normal incidence for filling ratios f = 0.15 and 0.30; (b) incidence angle at 30 deg for both TE and TM waves with f = 0.15.

Both methods show that nearly perfect absorption with an absorptance exceeding

99% for f = 0.15 from 4.8 to 7.8 μm, which could hardly be obtained by exciting plasmonic resonances. If the nanowire length is changed to 50 μm, the agreement (not shown here) is also good. In order to further verify the anisotropic dielectric function model, Figure 3.16 (b) compares the absorptance at θ_1 = 30 deg for both polarizations with that obtained from FDTD. The agreement is also very good for θ_1 = 30 deg. While the agreement somewhat deteriorate at θ_1 = 80 deg (not shown), the results are still reasonable to confirm that the EMT model used here is reliable. Therefore, the anisotropic model with MG theory can accurately predict the radiative properties of D-SiNW arrays with small filling ratios in a wide angles of incidence in the wavelength region of interest ($\lambda >> d$). Because FDTD is computationally expensive and takes several orders of magnitude more time than EMT, in particular for calculating the absorptance at oblique angles, the EMT is employed in the following sections to calculate the optical radiative properties of D-SiNWs.

The effective refractive indices (n) and extinction coefficients (k) for both ordinary and extraordinary waves are plotted in Figure 3.17 for the D-SiNW array for f = 0.15 and $N = 10^{20}$ cm^{-3}. The calculated optical constants (n and k) for silicon with the same doping level are also shown for comparison. Note that n_E and k_E exhibit similar trends to those of doped silicon. The refractive index has a minimum and the extinction coefficient increases with wavelength. This is expected because the dielectric function for extraordinary waves can be obtained by diluting that of bulk doped silicon according to Eq. (4). On the other hand, the refractive index is around 1 and the extinction coefficient is generally much smaller for ordinary waves. However, there is a prominent peak in the extinction coefficient, which is responsible for the absorption peak in Figure 3.16.

Following Wang [57], the dielectric function for ordinary waves given in Eq. (3) can be rearranged into a Lorentz oscillator model using Eq. (10):

$$\varepsilon_O = \varepsilon_\infty + \frac{\omega_{p1}^2}{\omega_r^2 - \omega^2 - i\omega\gamma} \tag{3.21}$$

where

$$\varepsilon_\infty = \frac{\varepsilon_{bl} + 1 + f(\varepsilon_{bl} - 1)}{\varepsilon_{bl} + 1 - f(\varepsilon_{bl} - 1)} \tag{3.22a}$$

$$\omega_{p1}^2 = \frac{4f}{\left[\varepsilon_{bl} + 1 - f(\varepsilon_{bl} - 1)\right]^2}\omega_p^{\,2} \tag{3.22b}$$

and

$$\omega_r^2 = \frac{(1-f)}{\varepsilon_{bl} + 1 - f(\varepsilon_{bl} - 1)}\omega_p^2 \tag{3.22c}$$

In the above equations, ε_∞ can be treated as a high-frequency constant, ω_{p1} is the effective plasma frequency, and ω_r is the oscillator resonance frequency.

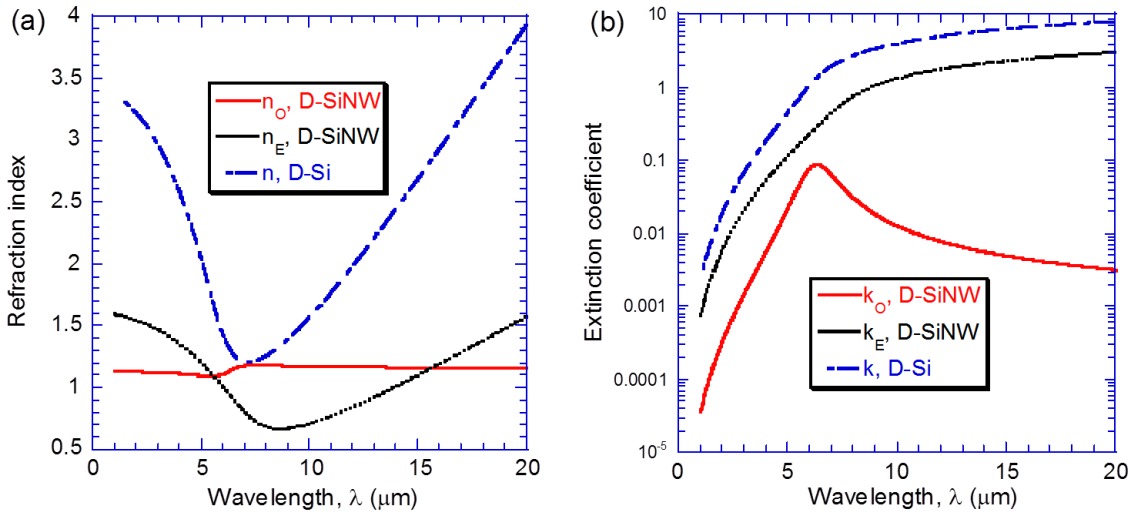

Figure 3.17 Optical constants of doped silicon and D-SiNWs for both ordinary and extraordinary wave with volume filling ratio as 0.15, doping level as 10^{20} cm^{-3}: (a) the refractive index; (b) the extinction coefficient.

The effect of volume filling ratio and doping concentration on the resonance frequency or wavelength can be assessed according to Eq. (3.22c), and the result is shown in Figure 3.18 for f = 0.15 and 0.3. The resonance wavelength decreases from about 20 μm with $N = 10^{19}$ cm^{-3} to 2 μm with $N = 10^{20}$ cm^{-21}. When the filling ratio increases, the resonance wavelength increases slightly. However, the filling ratio has strong effect on the plasma frequency which is related to the oscillation strength and allows the bandwidth to be modified to some extent. Therefore, the radiative properties of D-SiNWs may be tailored by varying the doping concentration or the filling ratio.

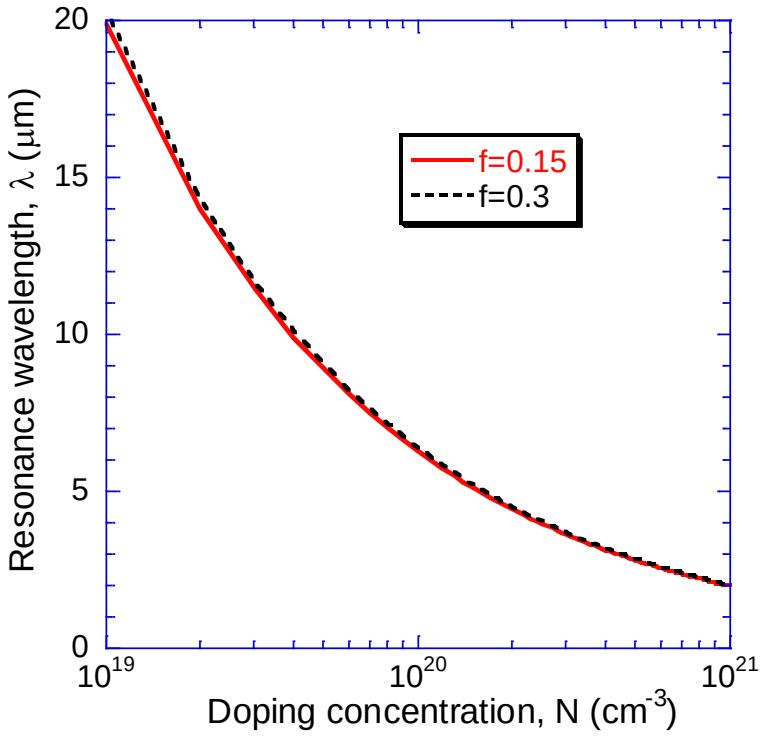

Figure 3.18 Dependence of the resonance wavelength on doping concentration for f = 0.15 and 0.30.

The absorptance of a free-standing D-SiNW array with H_2 = 100 μm and f = 0.15 is compared with that of a D-Si film of the same thickness as shown in Figure 3.19, with a doping concentration is 10^{20} cm^{-3}, at normal incidence. At such a high doping level, a

100-μm D-Si film is essentially opaque. Thus the absorptance of the D-Si film is the same as that of bulk D-Si, which is $1 - R$. The reflectance of Si has a dip between 5-6 μm close to the valley of the refractive index shown in Figure 3.17 (a), resulting in a peak in the absorptance spectrum. On the other hand, the reflectance of D-SiNWs is suppressed to be less than 2% (not shown) and subsequently, $A \approx 1 - T$. The near-zero reflectance can be explained by the index match between air and the D-SiNW array whose (ordinary) refraction index (n_O) is close to unity. In the short wavelength region (1 μm < λ < 4 μm), the absorptance of the D-SiNW array is smaller than that of D-Si due to the smaller k_O, i.e., the lack of absorption. There is a broadband near-unity absorptance region around the resonance wavelength, due to the reflection suppression and small penetration depth. At even longer wavelength, the absorptance of the D-SiNW drops again, which is consistent with the reduction of the extinction coefficient toward longer wavelengths as shown in Figure 3.17 (b).

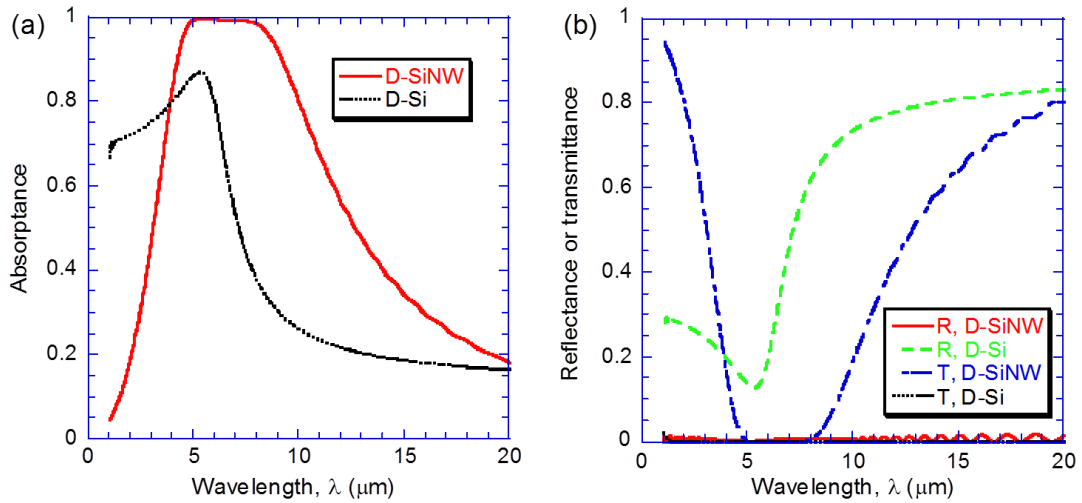

Figure 3.19 Absorptance at normal incidence for a free-standing D-SiNW array (f = 0.15) compared to a D-Si film with the same thickness (100 μm) and doping concentration of 10^{20} cm^{-3}.

In order to investigate the effects of incidence angle and polarization, the absorptance contours for TE and TM waves are plotted in Figure 3.20 (a) and (b), respectively. The absorptance is close to unity for both polarizations at wavelengths between 5 and 8 μm and is insensitive to the incidence angle, indicating that the SiNW array is a quasi-diffuse perfect absorber or emitter in this wavelength region. The absorption bandwidth is broader for TM waves than for TE waves at oblique angles. The high absorption for TM waves is because the extinction coefficient of a uniaxial medium is higher for extraordinary waves when the electric field is parallel to the wires or optical axis. The contour plot also shows some interference fringes for TE waves. These fringes are not seen in the absorption contour for TM waves since the waves cannot reach the other interface due to the high absorption in the D-SiNW array. The omnidirectional broadband absorbers with tunable operating wavelengths based on D-SiNWs may have important applications in energy harvesting devices, infrared filters, and radiation detectors.

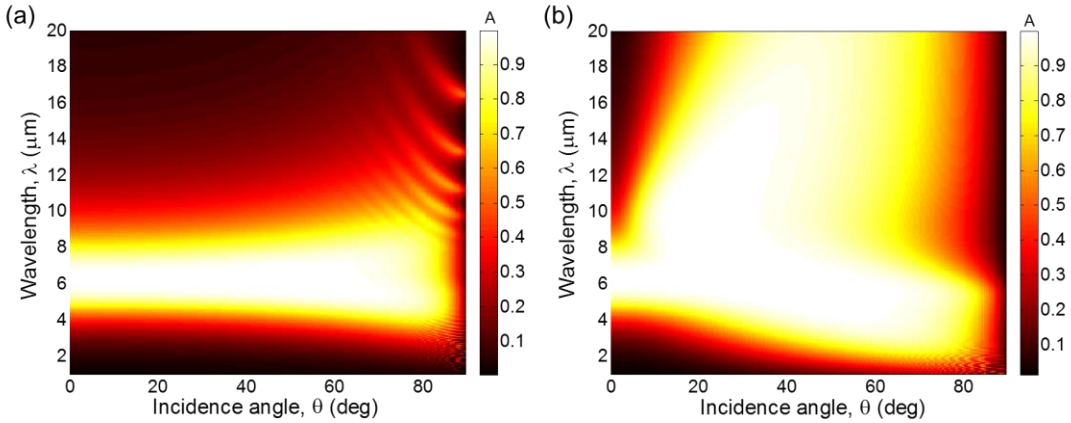

Figure 3.20 Contour plots of the absorptance as a function of wavelength and incidence angle for (a) TE waves; (b) TM waves.

From the comparison between D-SiNWs and D-Si, it is clear that large transmission for D-SiNWs and large reflection for D-Si are the main factors for preventing them being more absorbing. When D-SiNWs are deposited on a D-Si film, it can be expected that a larger absorption could be obtained by compensating the drawbacks with each other. This is demonstrated in Figure 3.21 (a) with both the EMT approach and FDTD simulation, using the following parameters, $f = 0.3$, $H_2 = H_3 = 100$ μm, and $N = 6\times10^{19}$ cm^{-3} for both D-SiNWs and D-Si. These two methods agree with each other well, except at the short wavelength cutoff, where interference effects are very strong. Interestingly, between 5 and 13 μm, EMT cannot predict the oscillations obtained from FDTD. This is due to the large absorption coefficients predicted by EMT, as shown in Figure 3(b), resulting in small penetration depths in the D-SiNW array and thus eliminating the interference effect. However, FDTD is a full wave solution that could account for wave diffraction. Beyond 13 μm, both methods are in excellent agreement. It can be seen that absorptance exceeding 0.9 can be achieved from 3 to 17 μm wavelength. The influence of D-Si substrate thickness is shown in Figure 3.21 (b). The absorptance improves significantly in the long wavelength region with a D-Si substrate of 10 μm thick. Further increase in the substrate thickness, i.e., increasing H_3 from 10 to 100 μm, only improves the absorptance in the short wavelength region. In the long wavelength region, the absorption is not enhanced when H_2 is varied from 10 to 100 μm. This is because the penetration depth of D-Si in the long wavelength region is very small due to the large extinction coefficient; therefore, larger substrate thickness does not change the absorptance.

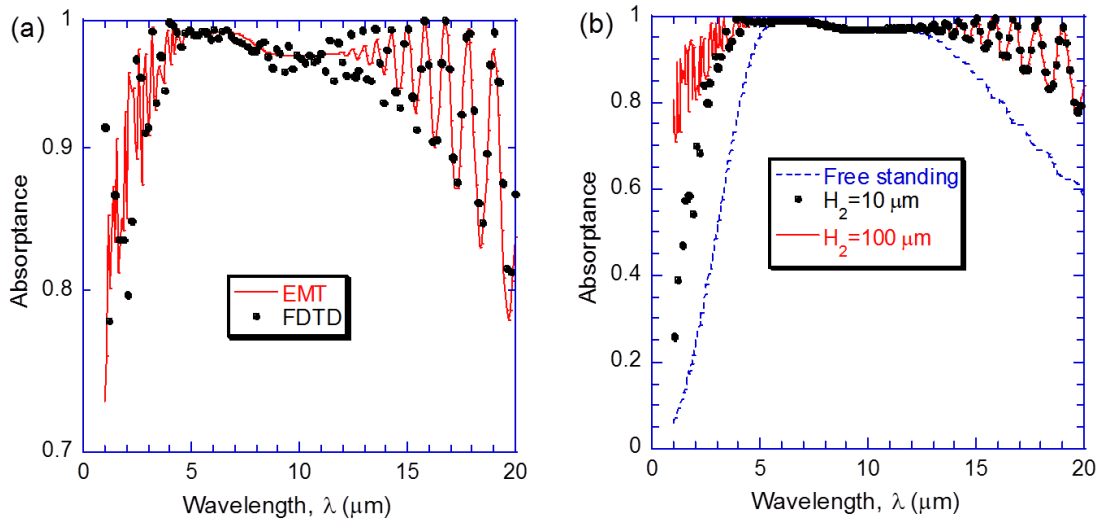

Figure 3.21 Spectral absorptance for D-SiNWs on D-Si substrate at normal incidence: (a) comparison of the EMT and FDTD results (note that the *y*-scale is from 0.7 to 1.0); (b) effect of substrate thickness.

Moreover, the broadband absorber based on D-SiNWs on a D-Si film is insensitive to both the incident angle and polarization status. In order to clearly show the influences of incident angle and polarizations, the directional distribution of absorptance for both TE and TM wave at three representative wavelengths: λ = 6, 10 and 16 μm is shown in Figure 3.22. The absorptance is close to unity for both TM and TE waves, though the interferences for TE waves are more obvious and TM waves have a little bit higher absorption. The high absorption does not begin to drop until 70 deg or so for both polarizations. Similar results can be obtained at other wavelengths in the considered spectral region and are not shown here. Note that the absorptance may be optimized by varying the thicknesses of D-SiNWs and D-Si substrate, the doping levels, and the volume filling ratio. The omnidirectional high absorptance from the D-SiNWs on a D-Si film structure could be realized in a broad spectral range and thus mimics the quasi-blackbody behavior, which may have applications for bolometers and spacer emitters.

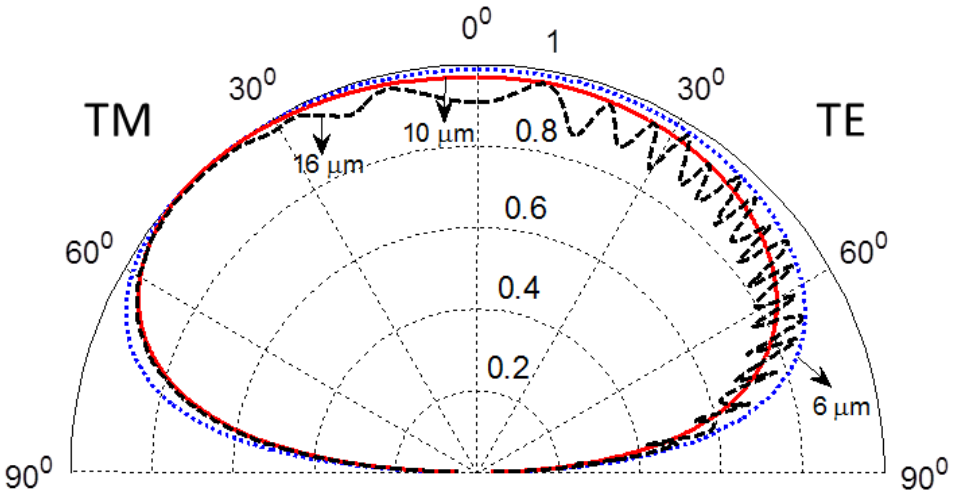

Figure 3.22 Angular dependence of the absorptance for both TE (right side) and TM (left side) waves at representative wavelengths. The blue dotted curve is for λ = 6 μm, red solid curve is for 10 μm, and black dashed curve is for 16 μm.

3.5 Summary

This chapter conducts a comprehensive investigation of the far-field radiative properties of metallic nanostructures. The major findings are summarized in the followings.

A design of broadband polarizers in the near infrared region is proposed with both good transmission and extremely high extinction ratio. The good performance holds until 60°. MPs are responsible for the high transmission and two simple LC models are developed to predict resonant transmission peaks quantitatively. The geometric parameters, such as grating thickness, spacer thickness, and period could be tuned for different applications. The design of high-performance polarizers, beamsplitters, filters, and transparent electrodes will be benefited.

Covering 1D and 2D Ag gratings with a single-layer graphene is found to counterintuitively increase the transmission several fold in certain wavelength region. Transmission preference can be obtained by exciting resonances which are not available in the long wavelength for simple 1D and 2D gratings. The enhancement is robust and alignment-free, and can be actively tuned by changing the chemical potential of graphene through electric gating. Coating graphene on both sides of the Ag grating provides another way to tune the resonance transmission. The anomalous blocking-assisted transmission is attributed to the excitation of MP, a localized resonance. A simple LC model is presented to quantitatively predict the wavelength of the transmittance peak for different geometric parameters and graphene chemical potentials. Replacing graphene by atomically thin metallic film will have similar effects though the fabrication is formidable. Covering graphene helps to enhance the transparency, improve the transmission coherence, and light confinement in nanoslits.

Metal-free all-angle negative refraction with low loss is theoretically demonstrated in the mid-infrared region using D-SiNW arrays. The performance is broadband and there is no upper limit for λ since the hyperbolic dispersion will hold as long as $\lambda > \lambda_T$. FDTD is used for the verification of negative refraction and effective anisotropic medium. The mechanism of loss-enhanced transmission is elucidated using an approximate expression of FOM. The proposed structure can achieve good tunability, by varying the doping concentration or volume filling ratio, to satisfy different specified needs. This helps to design low-loss flat lens for near-field thermal imaging and infrared collimators with large acceptance angles.

The spectral and directional radiative properties of D-SiNWs are investigated based on EMT of uniaxial medium and verified using the FDTD simulation. Omnidirectional wavelength-tunable wideband infrared absorbers have been theoretically predicted using D-SiNW arrays. Increasing the nanowire length will result in a broadening of the absorption plateau, while increasing the doping concentration can shift the plateau to short wavelengths. The composite of D-SiNWs and D-Si substrate acts as a quasi-blackbody, with an absorptance greater than 0.9 at wavelengths from 3 to 17 μm. Furthermore, the absorptance is insensitive to the incident angle and polarization status. These structures may be further optimized to enhance absorption considering different doping levels between the nanowire and substrate, as well as gradient doping levels along the nanowires. New routes are opened for achieving novel and highly efficient infrared absorbers and emitters for applications in thermal imaging, spectroscopic system, harvesting radiant energy, bolometers, and heat dissipaters in free space.

CHAPTER 4

NEAR-FIELD RADIATION OF METAMATERIALS BASED ON EMT AND ITS QUANTITATIVE VALIDITY CONDITION

In this chapter, EMT combined with FDT is used to calculate the near-field radiative heat flux between different metamaterials. In Sec. 4.1, four practically achievable nanostructures based on doped silicon are investigated for enhancement of near-field radiative heat transfer. Different mechanisms for the enhancements are identified. In Sec. 4.2, the near-field blackbody phenomena with perfect photon tunneling having near-unity probability across a broad frequency region and over a large k-space is theoretically demonstrated based on graphene-covered doped-silicon nanowires. Sec. 4.3, presents the quantitative condition of when EMT can be used, followed by a brief summary in Sec. 4.4.

4.1. Enhanced Thermal Radiation by Patterning Doped Silicon at the EMT limit

Near-field radiative heat transfer has attracted significant attention in recent years due to its wide potential applications in microscale thermophotovoltaic (TPV) cells [20, 189-194], thermal imaging [195, 196], non-contact thermal rectifiers [197-201], thermal modulators [202-204], and local thermal management [205, 206]. Planck's law of blackbody radiation breaks down when two objects at different temperatures are placed close enough, i.e., at a distance close to or smaller than the characteristic wavelength of thermal radiation. At nanometer distances, near-field radiative heat transfer could be

orders of magnitude greater than that between two blackbodies, especially when surface plasmon polaritons (SPPs) or surface phonon polaritons (SPhPs) are excited [3, 13].

Large heat transfer coefficients are desired for increased power throughput or heat dissipation in energy harvesting or cooling applications, respectively. However, the super-Planckian thermal radiation enabled by surface modes (either SPPs or SPhPs) is usually narrowband and has high-loss due to the inherent resonance effects, thus precluding more efficient heat transport. Reducing material loss (e.g., by reducing the electron scattering rate) could increase the cutoff wavevector and thus helps to improve near-field heat transfer [207, 208]. Another method to obtain higher radiative heat flux is to broaden the super-Planckian radiation band with the help of the resonance-free hyperbolic modes [66, 67, 209]. Hyperbolic dispersion or hyperbolic modes may exist in natural or artificial anisotropic materials in certainty frequency regions, where the electromagnetic waves with large transverse wavevector can propagate inside the hyperbolic metamaterials, unlike surface modes where the electromagnetic waves propagate only along the interface and decay into both media. Hyperbolic metamaterials, no matter whether they exist in nature (such as graphite) or are artificially synthesized, exhibit hyperbolic dispersion only in certain frequency ranges and are not ideally lossless [67, 69, 209, 210]. Therefore, achieving a great enhancement of near-field radiative thermal transport beyond bulks for more efficient thermal transport or heat dissipation is still a challenge.

Doped silicon (D-Si) has been shown to support surface modes in the infrared spectrum and can enhance near-field radiative transfer [211, 212] to similar magnitude as those for SiC and SiO_2 based on narrowband phonon modes. Furthermore, the doping

level can be varied to tune the far-field radiative properties [55] or near-field heat transfer [213]. Recent studies have shown that doped Si nanowires can enhance near-field radiation over bulk by several times [214]. Additionally, doped Si nanowires can exhibit hyperbolic modes and support negative refraction in a broad frequency range [54]. Different techniques have been successfully demonstrated to create controlled silicon nanostructures. It is envisioned that D-Si nanostructures may allow near-field radiative heat transfer to be significantly enhanced by enabling hyperbolic modes or by reducing loss for surface modes.

Four practically achievable nanostructures based on D-Si are considered here as shown in Figure 4.1, namely, nanowires, nanoholes, multilayers, and 1D gratings. Fluctuation-dissipation theorem is used to calculate the near-field and far-field radiative transfer, assuming that the nanostructures can be treated as an effective homogeneous medium with anisotropy.

Note that the minimum f for aligned D-SiNHs is $(1 - \pi/4)$, and the maximum f for aligned D-SiNWs is $\pi/4$, due to the geometrical limitations of the circular holes and wires, assuming the 2D lattice to be square. The dielectric function of Ge is largely independent of wavelength in the infrared region, and can be approximated as a constant with $\varepsilon_{\mathrm{Ge}} = 16$. EMT is used to obtain the anisotropic dielectric function and is combined with fluctuational electrodynamics to calculate the near-field radiative heat transfer coefficient. The aforementioned nanostructures are treated as homogenous uniaxial materials; this assumption is valid when the gap distance is much greater than the period of nanostructures. In the present study, the period of nanostructures is assumed to be sufficiently small, so that EMT can be applied to both the far and near fields.

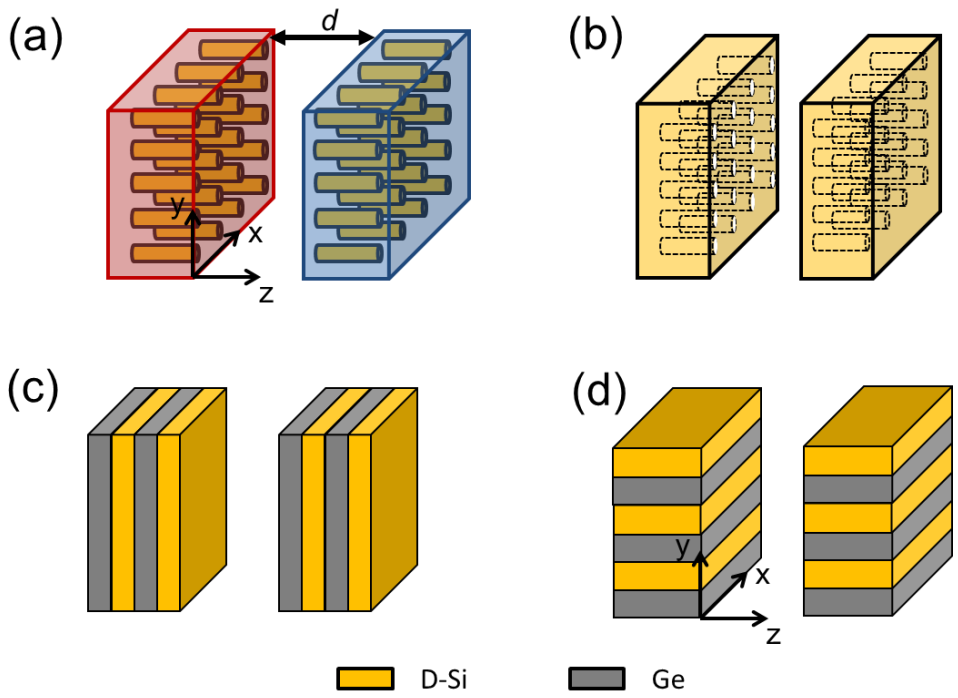

Figure 4.1 Schematics of two semi-infinite nanostructured metamaterials separated by a vacuum gap at a distance *d*: (a) D-SiNWs; (b) D-SiNHs; (c) multilayers composed of D-Si and Ge, which is modeled as a dielectric; (d) 1D gratings composed of D-Si and Ge.

The heat transfer coefficient at temperature T between two anisotropic planar media separated by a vacuum gap d can be calculated from Biehs et al. [38]

$$h = \frac{1}{8\pi^3}\int_0^\infty g(\omega,T)d\omega\int_0^{2\pi}\int_0^\infty \xi(\omega,\beta,\phi)\beta d\beta d\phi \tag{4.1}$$

$$g(\omega,T) = \frac{\partial}{\partial T}\left(\frac{\hbar\omega}{e^{\hbar\omega/k_B T}-1}\right) = \frac{(\hbar\omega)^2 e^{\hbar\omega/k_B T}}{k_B T^2\left(e^{\hbar\omega/k_B T}-1\right)^2} \tag{4.2}$$

For an anisotropic medium, cross-polarization can exist and, in general, $r_{sp}\neq 0$ and $r_{ps}\neq 0$. For aligned nanowires, nanoholes, and multilayer structures, the optical axis is in the z direction; subsequently, $r_{sp}=r_{ps}=0$. Thus, the transmission factor ξ is

independent of the azimuthal angle and can be written as $\xi(\omega,\beta,\phi)=\xi_{\mathrm{s}}(\omega,\beta)+\xi_{\mathrm{p}}(\omega,\beta)$, where [24, 44]

$$\xi_j(\omega,\beta)=\begin{cases}\left(1-\left|r_j\right|^2\right)^2\Big/\left|1-r_j^2e^{2ik_{z0}d}\right|^2, & \beta<k_0\\ 4\left[\mathrm{Im}(r_j)\right]^2e^{-2|k_{z0}|d}\Big/\left|1-r_j^2e^{2ik_{z0}d}\right|^2, & \beta>k_0\end{cases} \tag{4.3}$$

Here, *j* is for s or p polarization, and Im denotes the imaginary part. It should be noted that for a single polarization, the transmission factor is from 0 to 1. For s-polarized waves, the refraction in the uniaxial material is the same as in an isotropic medium with ordinary properties, since the electric field is perpendicular to the optical axis (*z* direction). Therefore, the s-polarization Fresnel coefficient r_{s} becomes

$$r_{\mathrm{s}}=\frac{k_{z0}-\sqrt{k_0^2\varepsilon_{\mathrm{O}}-\beta^2}}{k_{z0}+\sqrt{k_0^2\varepsilon_{\mathrm{O}}-\beta^2}} \tag{4.4}$$

For p polarization, the Fresnel coefficient r_{p} can be expressed as follows for uniaxial medium whose optical axis is parallel to the *z* axis

$$r_{\mathrm{p}}=\frac{\varepsilon_{\mathrm{O}}k_{z0}-\sqrt{k_0^2\varepsilon_{\mathrm{O}}-\beta^2\,\varepsilon_{\mathrm{O}}/\varepsilon_{\mathrm{E}}}}{\varepsilon_{\mathrm{O}}k_{z0}+\sqrt{k_0^2\varepsilon_{\mathrm{O}}-\beta^2\,\varepsilon_{\mathrm{O}}/\varepsilon_{\mathrm{E}}}} \tag{4.5}$$

For gratings, cross-polarization must be considered and the transmission factor can be determined based on the matrix formulation [215]. Considering the azimuthal angle ϕ, the angle between plane of incidence and the *x*-*z* plane as defined in Figure 4.1 (d), the Fresnel reflection coefficients can be explicitly expressed as follows [216]

$$r_{\mathrm{ss}}=\frac{n_{z\mathrm{O}}(n_z-n_{z\mathrm{O}})(\varepsilon_{\mathrm{O}}n_zn_{z\mathrm{E}}+n_{z\mathrm{O}}^2)\sin^2\phi+\varepsilon_{\mathrm{O}}(n_z-n_{z\mathrm{E}})(\varepsilon_{\mathrm{O}}n_z+n_{z\mathrm{O}})\cos^2\phi}{n_{z\mathrm{O}}(n_z+n_{z\mathrm{O}})(\varepsilon_{\mathrm{O}}n_zn_{z\mathrm{E}}+n_{z\mathrm{O}}^2)\sin^2\phi+\varepsilon_{\mathrm{O}}(n_z+n_{z\mathrm{E}})(\varepsilon_{\mathrm{O}}n_z+n_{z\mathrm{O}})\cos^2\phi} \tag{4.6}$$

$$r_{pp} = \frac{n_{zO}(n_z + n_{zO})(\varepsilon_O n_z n_{zE} - n_{zO}^2)\sin^2\phi + \varepsilon_O(n_z + n_{zE})(\varepsilon_O n_z - n_{zO})\cos^2\phi}{n_{zO}(n_z + n_{zO})(\varepsilon_O n_z n_{zE} + n_{zO}^2)\sin^2\phi + \varepsilon_O(n_z + n_{zE})(\varepsilon_O n_z + n_{zO})\cos^2\phi} \quad (4.7)$$

$$r_{sp} = -r_{ps} = \frac{2\varepsilon_O n_{zO} n_z (n_{zO} - n_{zE})\sin\phi\cos\phi}{n_{zO}(n_z + n_{zO})(\varepsilon_O n_z n_{zE} + n_{zO}^2)\sin^2\phi + \varepsilon_O(n_z + n_{zE})(\varepsilon_O n_z + n_{zO})\cos^2\phi} \quad (4.8)$$

where $n_{zE} = \sqrt{\varepsilon_E - (\beta/k_0)^2\left[\cos^2\phi + (\varepsilon_E/\varepsilon_O)\sin^2\phi\right]}$, $n_{zO} = \sqrt{\varepsilon_O - (\beta/k_0)^2}$, and $n_z = \sqrt{1-(\beta/k_0)^2}$. The expressions given above agree with the formulation given in Rosa et al. [215], except with a sign difference in the cross-polarization terms r_{sp} and r_{ps} due to the different definition of the rotation (azimuthal) angle. The plane of incidence is perpendicular to optical axis when $\phi = 0°$ and $180°$, and parallel to optical axis at $\phi = 90°$ and $270°$. It should be noted that integration over azimuthal angles is necessary since Fresnel's coefficients depend on ϕ, unlike in multilayer and other configurations. When the gratings are aligned as shown in Figure 4.1 (d), the relationship of azimuthal angles for the two gratings is $\phi_2 = -\phi_1$. If there is a relative rotation angle Δ between the two gratings, then $\phi_2 = -\phi_1 + \Delta$. If the two gratings are identical and aligned, $\mathbf{R}_1$ and $\mathbf{R}_2$ are transpose of each other, since $r_{ss}(-\phi) = r_{ss}(\phi)$, $r_{pp}(-\phi) = r_{pp}(\phi)$, $r_{sp}(-\phi) = -r_{sp}(\phi) = r_{ps}(\phi)$, and $r_{ps}(-\phi) = -r_{ps}(\phi) = r_{sp}(\phi)$. The results have been verified by comparison with Biehs et al. [202].

All the calculations are for room temperature with T = 300 K. Only n-type D-Si is considered in this work, while similar results can be obtained for p-type D-Si, though not shown in this work. In most of the calculations, the doping concentration is set to N = 10^{20} cm^{-3}, which will be the default value unless otherwise specified. The radiative heat

transfer coefficient versus the filling ratio of D-Si for the four nanostructures at a distance d = 10 nm is shown in Figure 4.2. The radiative heat transfer coefficient is normalized to that of bulk D-Si in order to show the enhancement or reduction of heat transfer by the nanostructures. Note that the heat transfer coefficient for bulk D-Si at this distance with the same doping level is 5022 W/m^2-K, which is 820 times the value between two blackbodies (i.e., $4\sigma T^3$ where σ is the Stefan-Boltzmann constant). The enhancement of heavily doped Si is due to surface waves [211-213]. Figure 4.2 suggests that D-SiNWs with f = 0.05 can achieve an enhancement factor of 12.5 over bulk D-Si. With the nanowires, the predicted heat transfer coefficient exceeds 60000 W/m^2-K at d = 10 nm, making D-SiNWs very attractive for applications ranging from high-efficiency near-field radiative cooling to local heating. The enhancement over bulk by nanoholes increases with decreasing f and reaches the maximum of 11.3 times when $f = 1 - \pi/4$. For 1D gratings, the calculation is based on $\Delta = 0°$ unless otherwise specified since the alignment case yields the maximum heat transfer. For 1D gratings, there is a slight enhancement when $f > 0.2$ and the maximum enhancement is around f = 0.4 with a ratio h / h_{bulk} = 1.19. However, the near-field radiative transfer coefficient between two multilayers is always smaller than that of the bulk and increases monotonously with f. Therefore, multilayer structures are not as effective in terms of enhancing near-field radiative transfer at ambient temperature at deep submicron gap distances. Similar trends can be obtained for d = 100 nm with reduced heat flux, although the results are not shown here.

In order to see whether the performance achieved with these nanostructures will still hold at different gap distances, relative heat transfer coefficient is plotted in Figure

4.3 (a). The filling ratios for nanowires and 1D gratings are taken as the optimized value at d = 10 nm, i.e., f = 0.05 and 0.4, respectively. For clearer comparison between multilayers and 1D gratings, the filling ratio is also chosen as 0.4 for multilayers. The filling ratio of nanoholes is taken as 0.3 based on practical consideration to stay away from the physical limitation. It is interesting to note that in the far field, multilayers give slightly higher heat transfer coefficient than nanoholes or 1D gratings. Among all the structures, D-SiNWs result in the largest heat transfer coefficient at any gap distance.

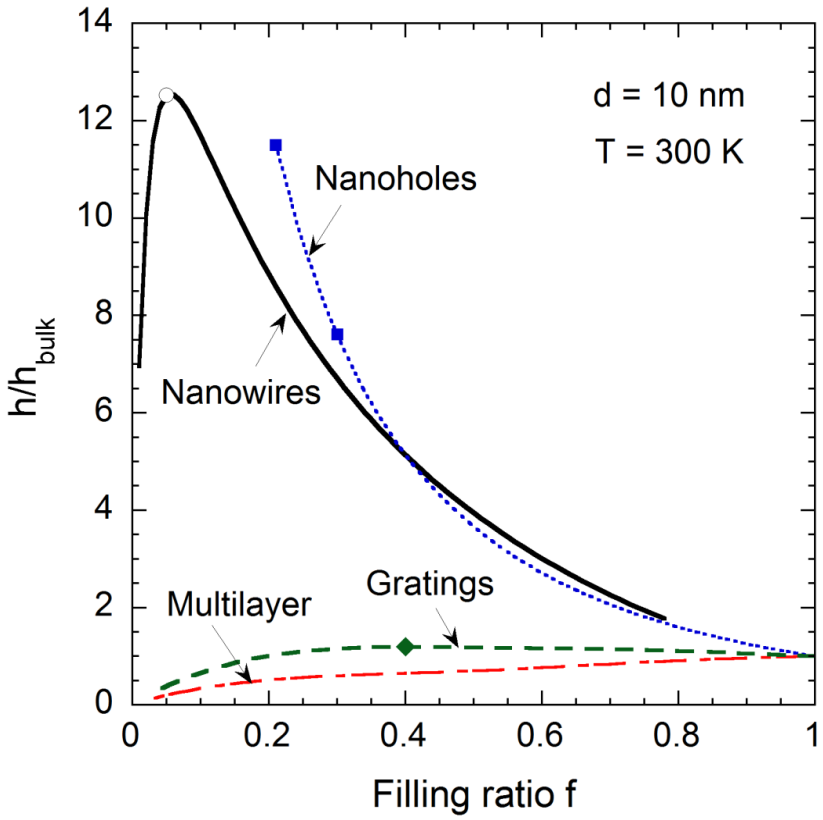

Figure 4.2 Ratio of the heat transfer coefficient of the nanostructures to bulk doped silicon and a gap distance of 10 nm.

The absolute heat transfer coefficients for all cases shown in Figure 4.3 (a) are plotted in Figure 4.3 (b), where the values for bulk D-Si and the far-field blackbody limit

are also shown. It can be seen that in the far field, the heat transfer coefficient between D-SiNWs is very close to that between blackbodies due to the good impedance matching and thus low reflectivity. D-SiNWs can yield a super-Planckian behavior when the gap distance is below 6 μm, while for D-Si the heat transfer coefficient exceeds the blackbody limit only when d < 0.8 μm. Therefore, nanowires can be used to extend the super-Planckian radiative transfer to micrometer gap distances and subsequently may benefit energy harvesting between micrometer gap distances. Meanwhile, nanoholes, multilayers, and gratings also extend near-field enhancement at greater gap distances though not as high in magnitude as nanowires. This could greatly relieve the fabrication barriers of near-field TPV cells.

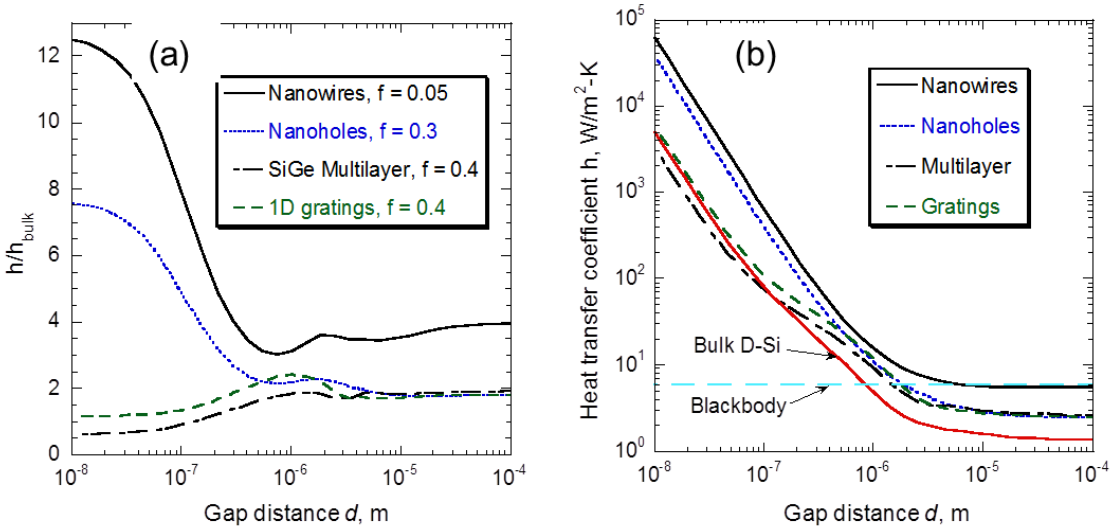

Figure 4.3 Heat transfer coefficients versus gap distance: (a) the ratio to bulk D-Si for each nanostructure with a selected filling ratio; (b) the absolute h values.

The mechanisms of near-field radiative heat transfer are elucidated to understand the performance of different nanostructures. Both nanowires and nanoholes could achieve an enhancement about one order of magnitude at tens of nanometer distances. The real

parts of the anisotropic dielectric functions of D-SiNWs with f = 0.05 and D-SiNHs with f = 0.3 are plotted in Figure 4.4. For D-SiNW, the real part of ε_x is almost a constant close to 1 and independent of wave frequency due to the small filling ratio. The imaginary part (not shown) of ε_x is generally much smaller than 1. Hence, for ordinary waves, the effective optical properties of the nanowire medium is essentially a dielectric. On the other hand, the effective dielectric function of the nanowires for extraordinary waves is described by the dilute Drude model and is therefore metallic. When $\varepsilon_x > 0$ and $\varepsilon_z < 0$, as shown in the shaded region of Figure 4.4 (a), the dispersion relation becomes hyperbolic with negative energy refraction (type I). For D-SiNHs, as shown in Figure 4.4 (b), both ε_x and ε_z are negative at the frequency region lower than 2.44×10^{14} rad/s. A narrow hyperbolic band, also type I, exists between 2.44×10^{14} rad/s and 2.74×10^{14} rad/s as shown in the shaded region in Figure 4.4 (b).

Figure 4.5 displays the contour plots of the transmission factors for p-polarization at d = 10 nm for both D-SiNWs and D-SiNHs corresponding to the dielectric functions shown in Figure 4.4. The contribution of s-polarization to near-field radiation is negligible. For D-SiNWs, as shown in Figure 4.5 (a), in the broad hyperbolic band below 1.72×10^{14} rad/s, as delineated by the arrows between the white line and the horizontal axis, both negative refraction and high-β propagating waves will be supported. As mentioned previously, the heat transfer coefficient between D-SiNWs at d = 10 nm reaches 12.5 times that between bulk D-Si. This is due to the broad hyperbolic band that allows photons to tunnel through the vacuum gap at very large β values and in a broad spectral region. In the case of hyperbolic modes, propagating waves exist in the

anisotropic medium; on the other hand, surface modes are manifested by evanescent waves in both media.

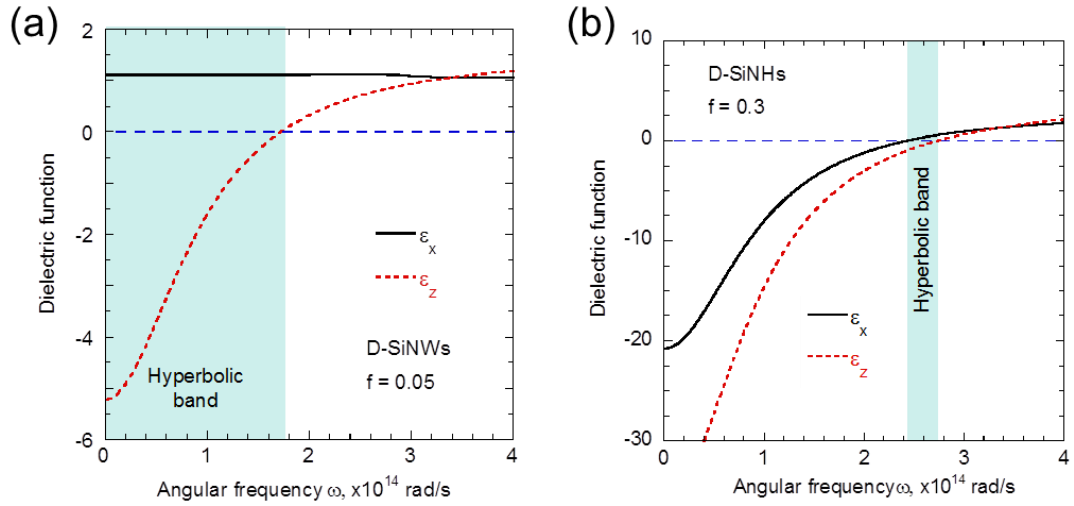

Figure 4.4 The effective dielectric functions (real part only) for (a) the D-SiNWs at f = 0.05 and (b) D-SiNHs with f = 0.3.

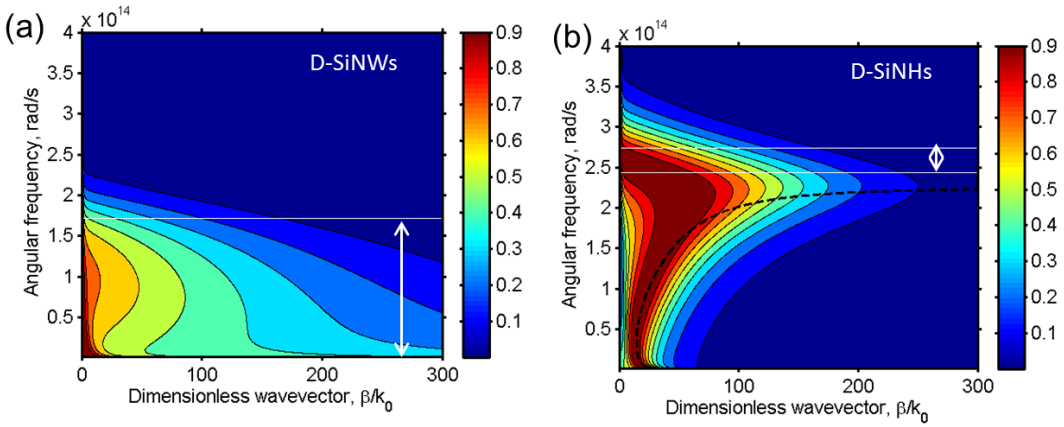

Figure 4.5 Contour plots of the energy transmission factor for p-polarization $\xi_p(\omega,\beta)$ of (a) D-SiNWs and (b) D-SiNHs for d = 10 nm.

As shown in Figure 4.4 (b), both ε_x and ε_z of D-SiNHs are negative at frequencies lower than 2.44×10^{14} rad/s. Therefore, coupled SPPs could be excited about the frequency corresponding to $\mathrm{Re}\left(\sqrt{\varepsilon_x\varepsilon_z}\right)=-1$, which is $\omega_m = 2.24\times10^{14}$ rad/s in this

case. The SPP dispersion relation for two metallic uniaxial media separated by a small gap exhibits a high-frequency branch ($\omega > \omega_m$) and a low-frequency branch ($\omega < \omega_m$). Both of the dispersion curves share the same asymptotic limit of $\omega = \omega_m$ at infinite wavevector (i.e., $\beta \to \infty$). For the low-frequency branch, surface charges are symmetric and the magnetic fields at the interface are in phase. The opposite is true for the high-frequency branch. The coupled-SPP dispersion can be obtained by zeroing the denominator of $\xi_p(\omega,\beta)$. For the symmetric modes or low-frequency branch, the dispersion relation can be expressed as follows [69, 214]

$$k_{z0} = \sqrt{\frac{k_0^2}{\varepsilon_x} - \frac{\beta^2}{\varepsilon_x \varepsilon_z}} \coth\left(\frac{ik_{z0}d}{2}\right) \tag{4.9}$$

The dispersion relation of the asymmetric modes is written by substitute "tanh" for the "coth" in Eq. (4.9). For real values of ω and β, solution of the SPP dispersion relation exists only when there is no loss. In the case with low loss, damping effect can be included, resulting in a peak broadening. When loss is very high, interpretation becomes difficult. It has been shown that near-field radiative heat transfer can still be enhanced about the surface plasmon frequency ω_m for both isotropic and anisotropic materials. This can also be seen in Figure 4.5 (b) where the cutoff wavevector is large near ω_m. Note that the cutoff wavevector is defined as the maximum β value beyond which the contribution to near-field heat transfer can be essentially neglected (or is a small percentage of the integral over β). By finding the minimum in the denominator of $\xi_p(\omega,\beta)$, the symmetric coupled-SPP dispersion is obtained and plotted in Figure 4.5 (b) as the black dashed curve, which agrees with the contour of transmission factor

reasonably well. The asymmetric branch is expected to lie between ω_m and the hyperbolic region if there were no loss. However, when loss is considered, there exist no minimum in the denominator of $\xi_p(\omega,\beta)$ in this region for real values of ω and β. The enhancement in $\xi_p(\omega,\beta)$ in this region mostly comes from the large numerator of $\xi_p(\omega,\beta)$. It seems that only the symmetric modes are excited in the considered case. For this reason, the asymmetric dispersion is not shown in Figure 4.5 (b). The contribution of the symmetric modes ($\omega < \omega_m$) to the heat transfer coefficient is 71.5%. The contribution from frequencies ranging from 2.24×10^{14} to 2.44×10^{14} rad/s is 14.2%. Whether the excitation is classified as SPPs or not, evanescent waves and phonon tunneling still exist in this frequency region [217]. Note that hyperbolic modes (2.44×10^{14} rad/s < ω < 2.74×10^{14} rad/s) contribute 10.8% to the heat transfer coefficient. Therefore, coupled SPPs or surface modes are largely responsible for the near-field heat transfer enhancement in D-SiNHs. While coupled-SPP modes can also exist between D-Si, due to the high loss in the bulk material, high $\xi_p(\omega,\beta)$ occurs at relatively small β values. The cutoff wavevector increases with reducing material loss [207, 208]. At the resonance frequency (2.88×10^{14} rad/s), the imaginary part of the dielectric function of D-Si is nearly twice of $\mathrm{Im}\left(\sqrt{\varepsilon_O\varepsilon_E}\right)$ at 2.24×10^{14} rad/s. Therefore, the number of contributing modes of low-loss D-SiNHs is much greater than that of D-Si, resulting in a much greater enhancement of near-field thermal radiation.

The effective dielectric functions of D-Si/Ge multilayers with f = 0.4 are shown in Figure 4.6 (a) (only the real part). When $\varepsilon_x < 0$ and $\varepsilon_z > 0$, the dispersion becomes hyperbolic (type II), as shown in Figure 4.6 (a) in the shaded area at frequencies below

1.55×10^{14} rad/s. The p-polarization transmission factor $\xi_p(\omega,\beta)$ is shown in Figure 4.6 (b) and the contribution from s-polarization to heat transfer is negligibly small at nanometer distances. In the multilayer configuration, type II hyperbolic materials do not yield negative refraction. Another uniqueness of type II hyperbolic modes is that $\xi_p(\omega,\beta)$ becomes non-trivial only when β is greater than the critical wavevector $k_{cr}=k_0\sqrt{\varepsilon_E}$ [218]. When $\beta > k_{cr}$, propagating hyperbolic modes will be supported with a high transmission factor in a broadband region independent of type I or type II. Therefore, the spectral heat flux can be enhanced over bulks in a broad band due to the high transmission factor for large β in either type of hyperbolic mode. Nevertheless, due to losses, the transmission factor decreases much faster for multilayer structure than for nanowires or nanoholes at large β values. Furthermore, in the high frequency region outside the hyperbolic band, especially near the surface resonance frequency of D-Si (2.90×10^{14} rad/s), the spectral flux between multilayered structures is much less than that between bulks. The overall effect is that the enhancement of heat transfer in the low-frequency region cannot compensate for the reduction in the high-frequency region, resulting in a net reduction of radiative heat transfer coefficient over bulk D-Si. The ratio h/h_{bulk} is 0.65 for multilayers with f = 0.4. Nevertheless, with increasing gap distance, the heat transfer coefficient for bulk D-Si decreases faster than that for multilayers as shown in Figure 4.3. For multilayers with f = 0.4, $h > h_{bulk}$ when d exceeds 120 nm and $h \approx 2h_{bulk}$ in the far field.

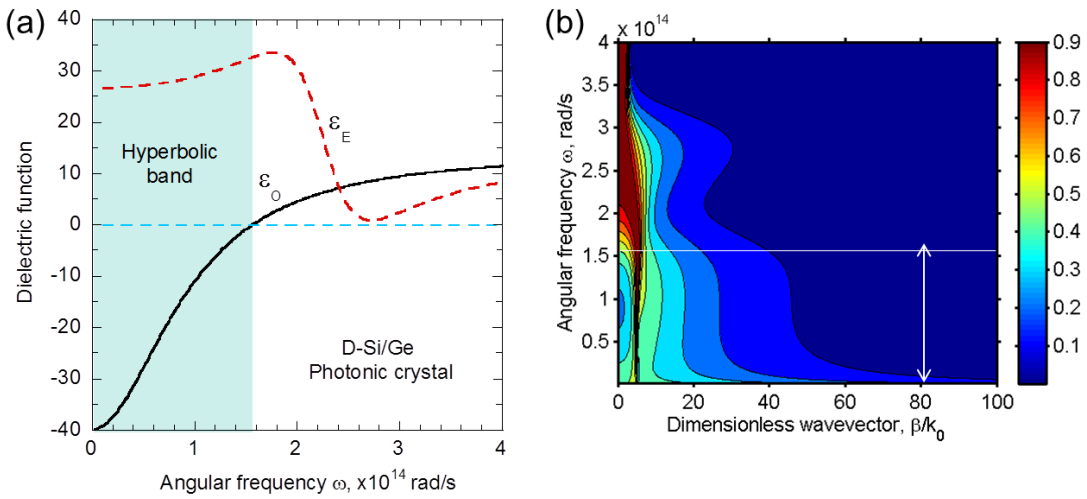

Figure 4.6 (a) Effective dielectric function of D-Si/Ge multilayers with f = 0.4; (b) contour plots of the p-polarization transmission factor at d = 10 nm.

The heat transfer mechanisms between gratings are more complicated. For nonmagnetic materials, s-polarized waves generally cannot excite surface modes except for the case with negative-permeability metamaterials [75]. However, for 1D gratings when the azimuthal angle is nonzero, s-polarized incident waves can also excite SPPs since there will be a magnetic field along the grooves and a wavevector component perpendicular to the grooves [219]. When the gratings are homogenized as an anisotropic medium, the nanoscale radiative transfer is governed by the transmission factor and more specifically by Fresnel's reflection coefficients when $\beta >> k_0$. A close examination of Eq. (4.8) suggests that the cross-polarization terms are negligibly small when $\beta >> k_0$. Therefore, polarization coupling will contribute little to the radiative heat transfer in the deep submicron region. Furthermore, regardless of the azimuthal angle, Im(r_{ss}) quickly approaches zero as β / k_0 increases. Hence, the contribution of s-polarization to nanoscale radiation is also negligible. Figure 4.7 shows the contours of the p-polarization transmission factor for f = 0.4 and d = 10 nm integrated over the azimuthal angle for

aligned and cross gratings, respectively. The shapes for Δ = 0° and 90° are similar with slightly larger transmission factors and cutoff wavevectors for the aligned case. Note that the ordinary and extraordinary dielectric functions are the same as shown in Figure 4.6 (a) for multilayers, except that for gratings $\varepsilon_z = \varepsilon_O$ and ε_x and ε_y depends on the rotation angle. Compared with Figure 4.6 (b), gratings can increase the transmission factor toward large β values over multilayers, especially near the frequency of 1.5 × 10^{14} rad/s. The reason is due to the large Im(r_{pp}) and subsequently larger transmission coefficients (ξ_p) for gratings. Therefore, the near-field radiative transfer of gratings is more than those of bulk D-Si and multilayers.

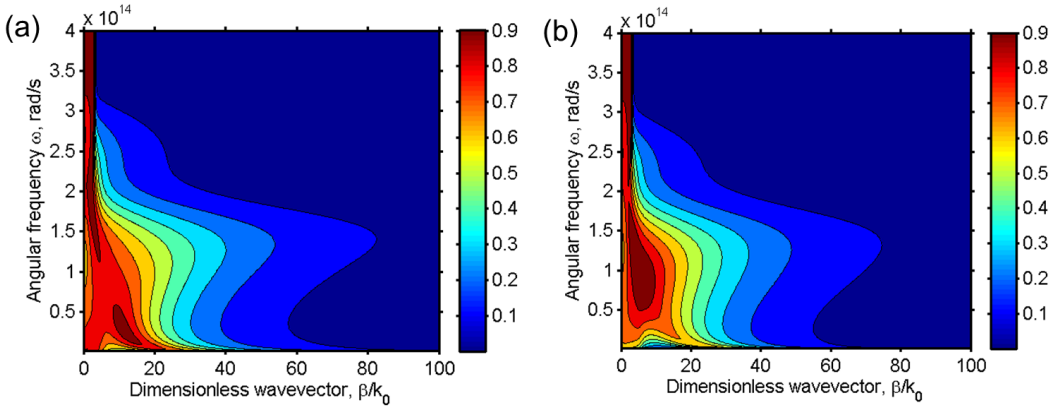

Figure 4.7 Contours of the transmission factor for p-polarization integrated over the azimuthal angle with d = 10 nm between aligned 1D gratings: (a) parallel aligned gratings with a relative rotation angle $\Delta = 0°$; (b) perpendicularly aligned gratings with $\Delta = 90°$.

The relative heat transfer coefficient as a function of relative rotation angle of the gratings is shown in Figure 4.8 for d = 10 nm and f = 0.4. It can be seen that h monotonically decreases as Δ is increased from 0° to 90° due to symmetry breaking. It has been proposed that 1D gratings may potentially be used as non-contact thermal modulators. Note that the maximum modification with D-Si/Ge multilayer is about 10%,

much lower than those with Au and SiC [202]; this is presumably due to the large scattering rate in D-Si.

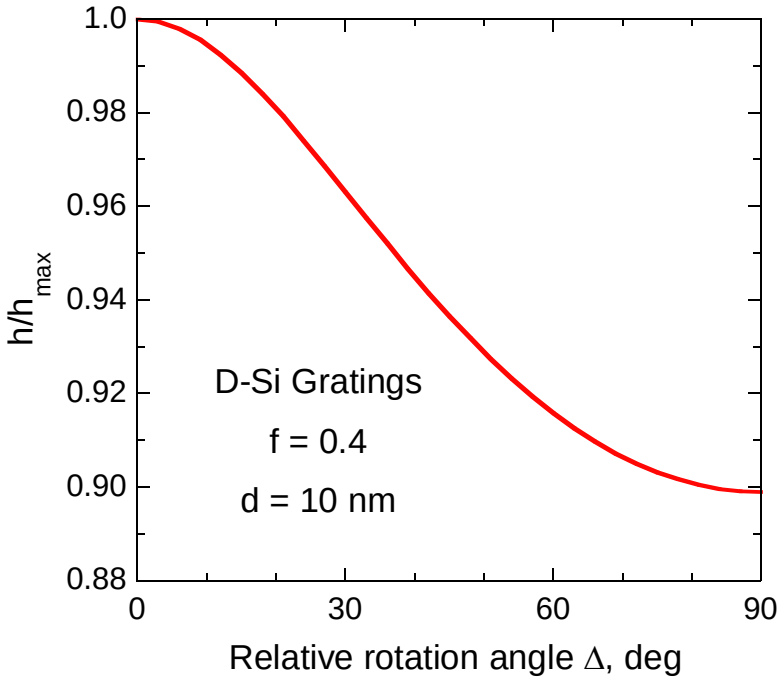

Figure 4.8 The near-field heat transfer coefficient for d = 10 nm as a function of the relative rotation angle of the gratings when f = 0.4.

4.2 Perfect Photon Tunneling by Hybridization of Hyperbolic Modes with Graphene Plasmons

Radiative heat transfer between macroscopic bodies in the far field will achieve the maximum value if every photon emitted by one substance with any direction can be totally absorbed by the other body, indicating that the photon transmission probability is unity. These two substances are called blackbodies, and the radiative heat transfer between them is governed by the well-known Stefan-Boltzmann law, an upper limit for propagating modes [3]. Capturing incident photons with near-unity efficiency is also a

desire in the near field due to the wide potential applications of near-field thermal radiation in local thermal management, thermal imaging [195, 220], contactless thermal modulators [197, 221], and thermophotovoltaic (TPV) cells [190, 194].

Tunneling of evanescent modes enables the radiative heat flux to be several orders of magnitude higher than that between far-field blackbodies, especially when surface modes are excited [3, 18, 222, 223]. Due to its unique characteristics, graphene can support surface plasmons with low loss and excellent tunability ranging from near-infrared to terahertz frequencies [224]. Graphene has been reported to tailor the near-field heat transfer [225-228], and improving the efficiency of TPV cells [194, 229]. However, the near-unity photon tunneling probability occurs only in narrow wavevector or *k*-space range, where coupled SPPs are excited. Hyperbolic materials, featuring unbounded density of states, have been shown to enhance the photon tunneling probability [66-69, 230]. However, since hyperbolic modes are resonance free, the tunneling probability unavoidably decays with increasing *k*. By combining graphene plasmons and hyperbolic modes, this work demonstrates photon tunneling with near-unity probability across a broad frequency range and large *k*-space.

The geometric arrangement of near-field thermal radiation between graphene-covered D-SiNW arrays is illustrated in Figure 4.9. Coating graphene on the top of silicon nanowires is a mature technology [231]. The optical conductivity of graphene $\sigma(\omega)$ can be found in Refs. [127, 194]. For convenience, the relaxation time is fixed to be $\tau = 10^{-13}$ s considering electron-phonon and electron-defects scattering [232], while μ is adjusted to maximize the performance.

The calculated heat transfer coefficient h between graphene-coved D-SiNWs with d = 200 nm, f = 0.02, and μ = 0.3 eV is 614.7 W/m^2-K, which is 4.5 times as large as that for D-SiNWs. In order to unveil the underlying mechanism for this enhancement, the photon tunneling probability for p-polarization is plotted in Figure 4.10 for D-SiNWs, suspended graphene, and graphene covered nanowires for p-polarization evanescent modes. Note that the contributions to near-field radiative transfer from both the propagating and s-polarized evanescent waves are negligible compared to that of p-polarization evanescent waves capable of supporting hyperbolic or surface modes. As shown in Figure 4.10 (a) by the color contour, the photon tunneling probability is much higher in the hyperbolic band than that in the non-hyperbolic region at frequencies exceeding 1.02×10^{14} rad/s. Due to the broadband hyperbolic modes, h for D-SiNWs achieves 135.3 W/m^2-K, which is 21 times greater than the blackbody limit of $4\sigma_{SB}T^3$ where σ_{SB} is the Stefan-Boltzmann constant. Nevertheless, $\xi_p(\omega,\beta)$ inevitably decreases with increasing β due to the exponential decay factor of $e^{-2|k_{z0}|d}$ in the numerator since no resonance is excited.

Figure 4.10 (b) gives ξ_p for suspended graphene sheets without substrates using μ = 0.3 eV. There exist two distinct bands with large tunneling probability. These two bands, splitting at low β values and merging together at a large β, are associated with the coupled SPPs caused by the graphene. The dispersion relation can be obtained by zeroing the denominator of ξ_p and is given as [233]

$$1+\frac{\sigma k_{z0}}{\omega\varepsilon_0}=\coth\left(\frac{ik_{z0}d}{2}\right),\ \text{symmetric branch} \tag{4.10}$$

$$1+\frac{\sigma k_{z0}}{\omega\varepsilon_0}=\tanh\left(\frac{ik_{z0}d}{2}\right),\ \text{antisymmetric branch} \tag{4.11}$$

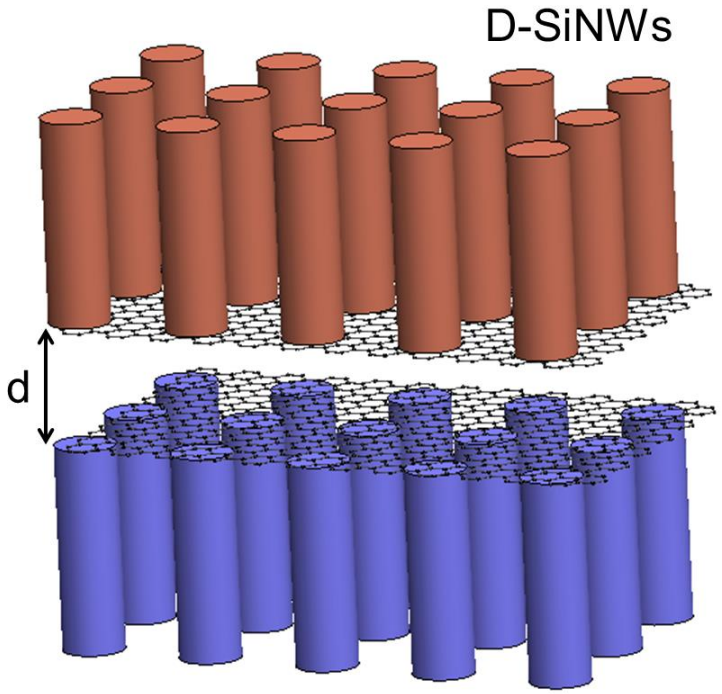

Figure 4.9 Schematic of near-field radiative heat transfer between graphene-covered semi-infinite doped silicon nanowires separated by a vacuum gap of distance *d*.

The low-frequency symmetric branch and the high-frequency antisymmetric branch are shown as the white lines in Figure 4.10 (b) and match well with the peaks in ξ_p. Instead of decaying exponentially with β, the tunneling probability is almost unity when either Eq. (4.10) or Eq. (4.11) is satisfied. The diminishing denominator can compensate the decay factor $e^{-2|k_{z0}|d}$ in the numerator, enabling a large tunneling probability at large β values. The coupled SPPs have a dominant contribution to the near-field radiative heat transfer. As a result, the calculated heat transfer coefficient for two free-standing graphene sheets at d = 200 nm is as high as 453.7 W/m^2-K, even larger than

that for D-SiNWs. However, the near-unity tunneling probability occurs in narrow β bands only.

When graphene covers the D-SiNWs for both the emitter and receiver, as shown in Figure 4.10 (c), ξ_p is very high across a broad frequency range up to 1.5×10^{14} rad/s and a large k-space up to $20k_0$. All the photons emitted in this regime will be absorbed, which is the blackbody behavior in the near field. As a result, the heat transfer coefficient of this hybrid structure could achieve 614.7 W/m^2-K, much larger than that for plain D-SiNWs or suspended graphene sheets alone.

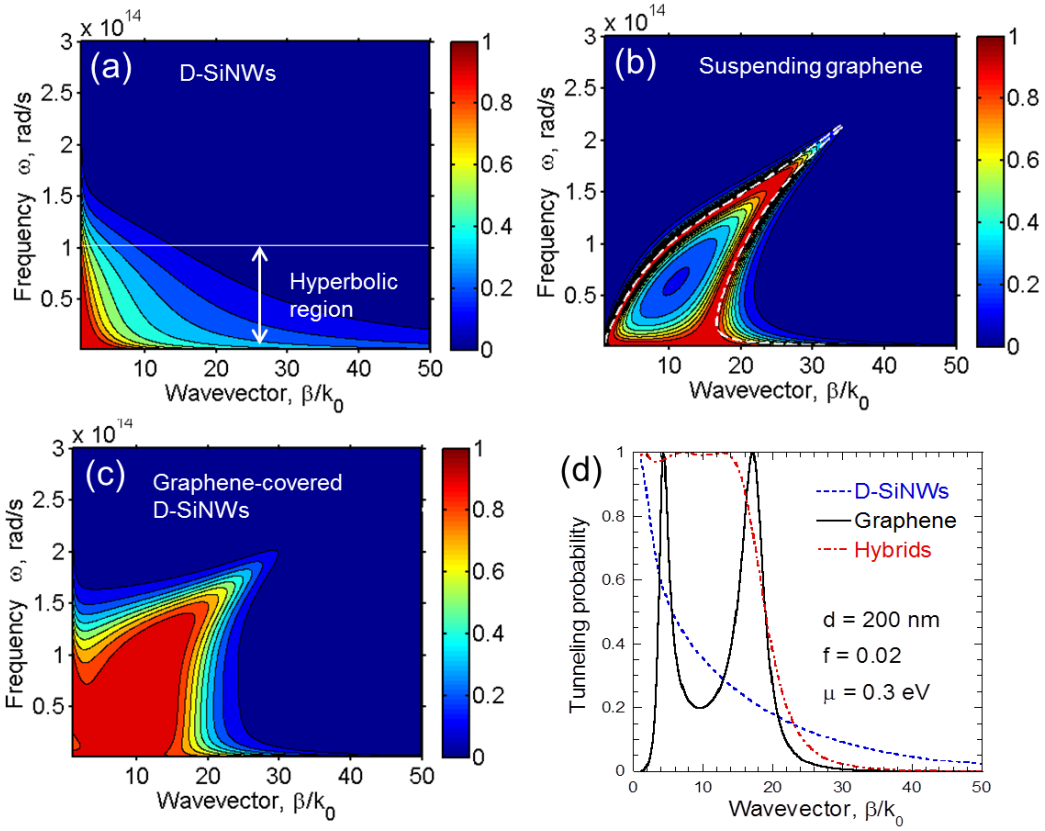

Figure 4.10 Photon tunneling probability for p-polarization at d = 200 nm (a) Two D-SiNWs with f = 0.02 without graphene. (b) Suspended graphene with a chemical potential of 0.3 eV. (c) Graphene-covered D-SiNWs. (d) Photon tunneling probability at ω = 5×10^{13} rad/s.

The variation of ξ_p with β can be more clearly seen by comparing the three configurations at $\omega = 5\times10^{13}$ rad/s, which lies in the hyperbolic region, as illustrated in Figure 4.10 (d). The tunneling probability of the resonance-free hyperbolic D-SiNWs decays quickly with increasing β; while that for the suspended graphene sheets has two resonance-like near-unity peaks. Interestingly, ξ_p for graphene-covered D-SiNWs can exceed 0.95 up to $\beta = 15k_0$. However, with further increasing β, the tunneling probability for graphene-covered D-SiNWs decreases rapidly and becomes lower than that between D-SiNWs for $\beta > 20k_0$. When $\beta \gg c_0\varepsilon_0k_0/|\sigma|$, $r_p = 1$ with a zero imaginary part. Subsequently, the photon tunneling probability becomes zero. Therefore, adding graphene suppresses phonon tunneling for very large β values, as can be seen from Figure 4.10 (d). Nevertheless, the contribution by the perfect photon tunneling region dominates the near-field radiative transfer, resulting in a net enhancement.

Note that the graphene coverage does not always improve heat transfer [226]. For very small μ, coupling between graphene plasmons and hyperbolic modes becomes so weak that the improvement diminishes. Since σ generally increases with μ, more modes are adversely affected if μ is too high, leading to a deterioration of heat transfer performance. For a given filling ratio and specified gap distance, there exists an optimal chemical potential that allows near-perfect photon tunneling to be achieved in a broad frequency and wavevector ranges. The filling ratio can have a significant influence on the near-field radiative transfer as demonstrated previously without graphene coverage. For very small f, the nanowire density is so dilute that the heat flux between graphene-covered nanowires approaches to that for suspended graphene. Too high a filling ratio

makes both ε_O and ε_E negative such that no hyperbolic modes and hybridized perfect tunneling can occur. In the present study, f is chosen to be 0.02, which allows great enhancement of near-field radiation over a large distance range.

Figure 4.11 (a) plots the heat transfer coefficient of D-SiNWs and graphene-covered nanowires at the optimal chemical potential given in Figure 4.11 (b), considering only p-polarized evanescent modes. The minimum d used here is 100 nm to ensure EMT is valid given that practical nanowire diameter cannot be infinitesimal. By optimizing the chemical potential, the inclusion of graphene can improve the near-field heat transfer between D-SiNWs. Heat transfer coefficient for graphene-covered D-SiNWs lies between that for D-SiNWs and the theoretical limit of hyperbolic materials given by [66]

$$h_{\text{limit}} = \frac{k_B^2 T \ln(2)}{12\hbar d^2} \tag{4.12}$$

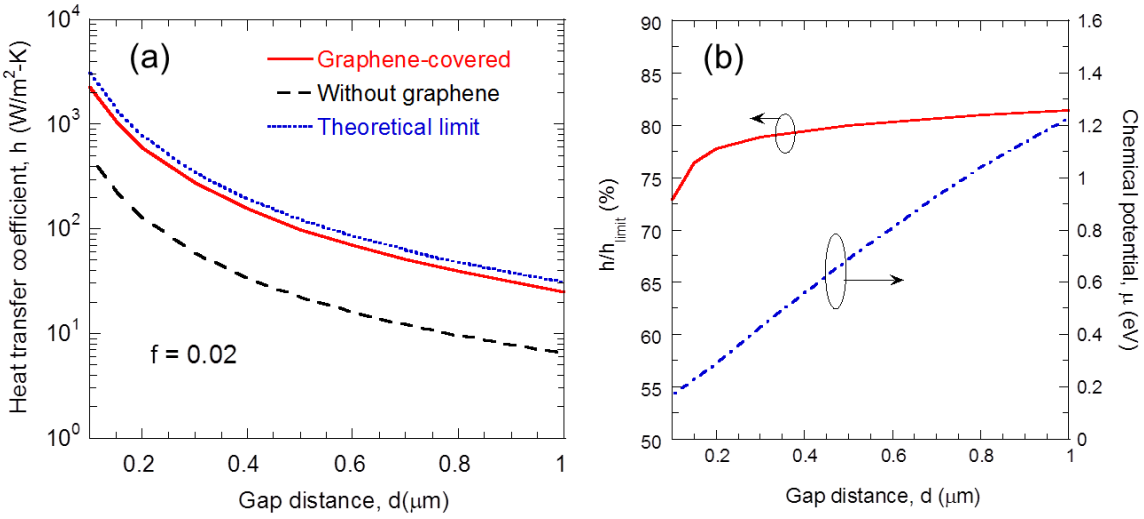

Figure 4.11 (a) Heat transfer coefficient vs. gap distance for D-SiNWs, graphene-covered D-SiNWs with optimal chemical potential, and the theoretical limit for hyperbolic metamaterials; (b) Enhancement of the heat transfer coefficient.

The ratio of heat transfer coefficient for graphene-covered D-SiNWs to the near-

field limit is plotted in Figure 4.11 (b). With increasing gap distance, the heat transfer coefficient gets closer to the near-field limit. Note that Eq. (4.12) is a theoretical limit only for hyperbolic materials rather than a physical upper limit for all materials. From Figure 4.11 (b), the optimal chemical potential increases monotonically with d from 100 nm to 1 μm. With decreasing gap distances, the number of contributing modes increases towards high β region in the k-space. In order to postpone the suppression region to larger β, the conductivity of graphene needs to be reduced according to the zero photon tunneling condition. This explains why the chemical potential should decrease with gap spacing.

4.3 Quantitative Validity Condition of EMT for Metallodielectric Metamaterials

Homogenization based on EMT has been widely used in combination with fluctuational electrodynamics to predict the near-field heat flux for designing the aforementioned thermal management devices due to its simplicity and low computational demand [66, 67, 69, 202, 203, 208, 234-236]. The characteristic thermal wavelength governed by Wien's law is indeed much greater than the structure unit cells. However, in the near field, large wavevector modes featured with small effective wavelength are not negligible, since these modes could effectively tunnel through the vacuum gap and may even become the dominant contribution to the heat flux. Hence, the applicability of EMT needs to be carefully examined in the near-field regime. Orlov et al. [237] noticed a strong nonlocal response when SPPs are exited at the interface between metal and dielectrics. Liu and Shen [230] showed that EMT will overestimate near-field radiative heat flux between a SiC film and metal nanowire arrays at small gap distances using the

Wiener Chaos expansion method. Tschikin et al. [210] pointed out that EMT may fail to predict the radiative transfer at small spacing when surface phonon polaritons (SPhP) exist between the layers on both sides of the vacuum gap. In general, for the EMT to be valid, the gap distance should be much greater than the period of the unit cell [208]. Nevertheless, quantitative criteria describing when EMT can be applied in predicting near-field heat transfer are desirable in order to choose the most effective methods for use in design calculations.

The objective of this section is to investigate the application condition of EMT in predicting near-field radiative heat transfer between multilayered metamaterials as shown in Figure 4.12. In addition to considering different filling ratios and gap distances, different configurations for the two layers adjacent to vacuum are considered, namely, metal-metal (MM), metal-dielectric (MD), and dielectric-dielectric (DD). The fluctuational electrodynamics is used to calculate near-field radiative transfer between planar structures. The approximate results based on homogenized effective media are compared with the exact calculations employing the transfer matrix formulation for multilayered structures.

For f = 0.5 and 0.8, the dielectric function components as a function of the angular frequency ω are plotted in Figure 4.13, where type I ($\varepsilon_x' > 0,\ \varepsilon_z' < 0$) and type II ($\varepsilon_x' < 0,\ \varepsilon_z' > 0$) hyperbolic regions are identified [234]. It is noted that when f = 0.8, in the region between type I and II bands, both ε_x' and ε_z' are negative as shown in Figure 4.13 (b). Therefore, coupled SPPs may be supported and the surface resonance frequency corresponds to $\mathrm{Re}\left(\sqrt{\varepsilon_x \varepsilon_z}\right) = -1$.

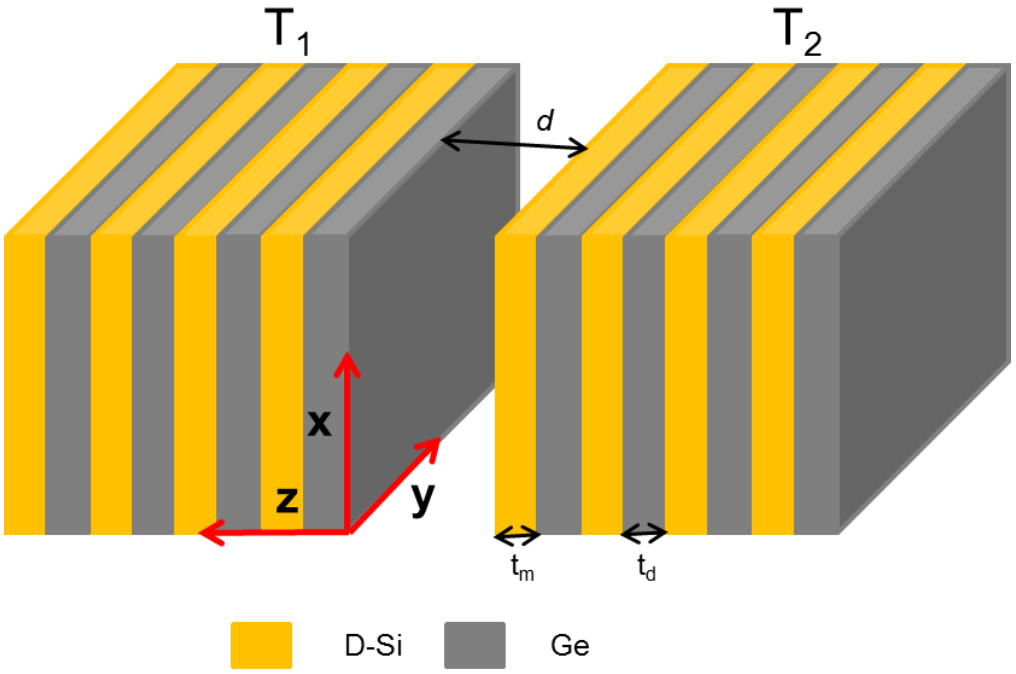

Figure 4.12 Illustration of radiative heat transfer between two multilayered metamaterials.

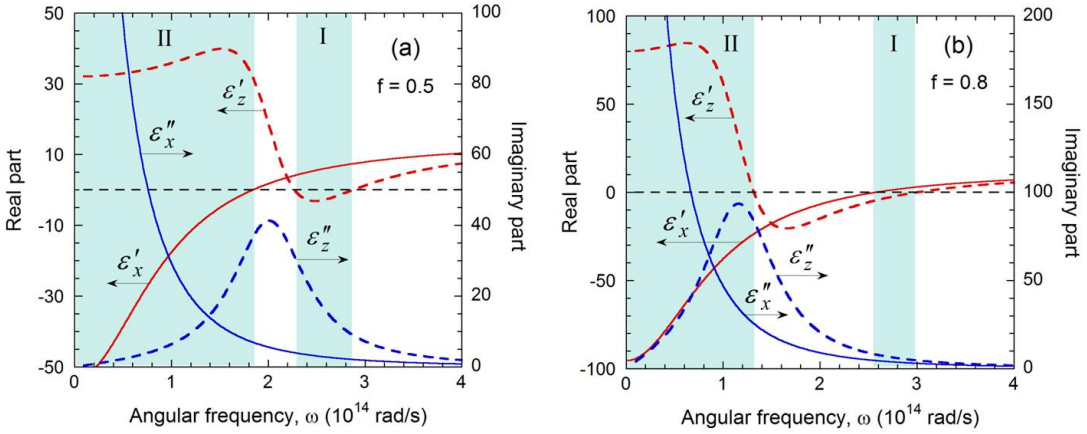

Figure 4.13 Effective dielectric function components for (a) f = 0.5 and (b) f = 0.8. Shaded regions denote hyperbolic dispersion (type I or type II).

Figure 4.14 plots the near-field radiative heat transfer versus the gap distance for three configurations (MM, DM, and DD) and the homogenized effective medium

described by EMT, for both s- and p-polarizations with f = 0.5 and 0.8, respectively. In the present study, the unit cell period P is set to be 100 nm, and the number of periods of both the emitter and the receiver is 40, which is sufficient for each structure to be approximate as semi-infinite. This is due to the small penetration depth in the near-field, and more details can be found from Ref. [238]. The temperatures T_1 and T_2 are taken as 300 K and 0 K, respectively. Since the characteristic wavelength for thermal radiation (on the order to 10 μm) is much greater than the period, it is expected that heat flux calculated from the exact method for different configurations and that predicted by EMT should agree when $d \gg P$. This is exactly what is observed from Figure 4.14. for both polarizations and different filling ratios when d approaches 10P or 1000 nm, although reasonable agreement can be seen as early as d = 100-300 nm. When d is comparable with or smaller than P, however, the heat fluxes deviate significantly for different configurations especially for p-polarization. Interestingly, EMT could still predict the amount of heat flux for a certain configuration and polarization status, even at nanometer gap distances.

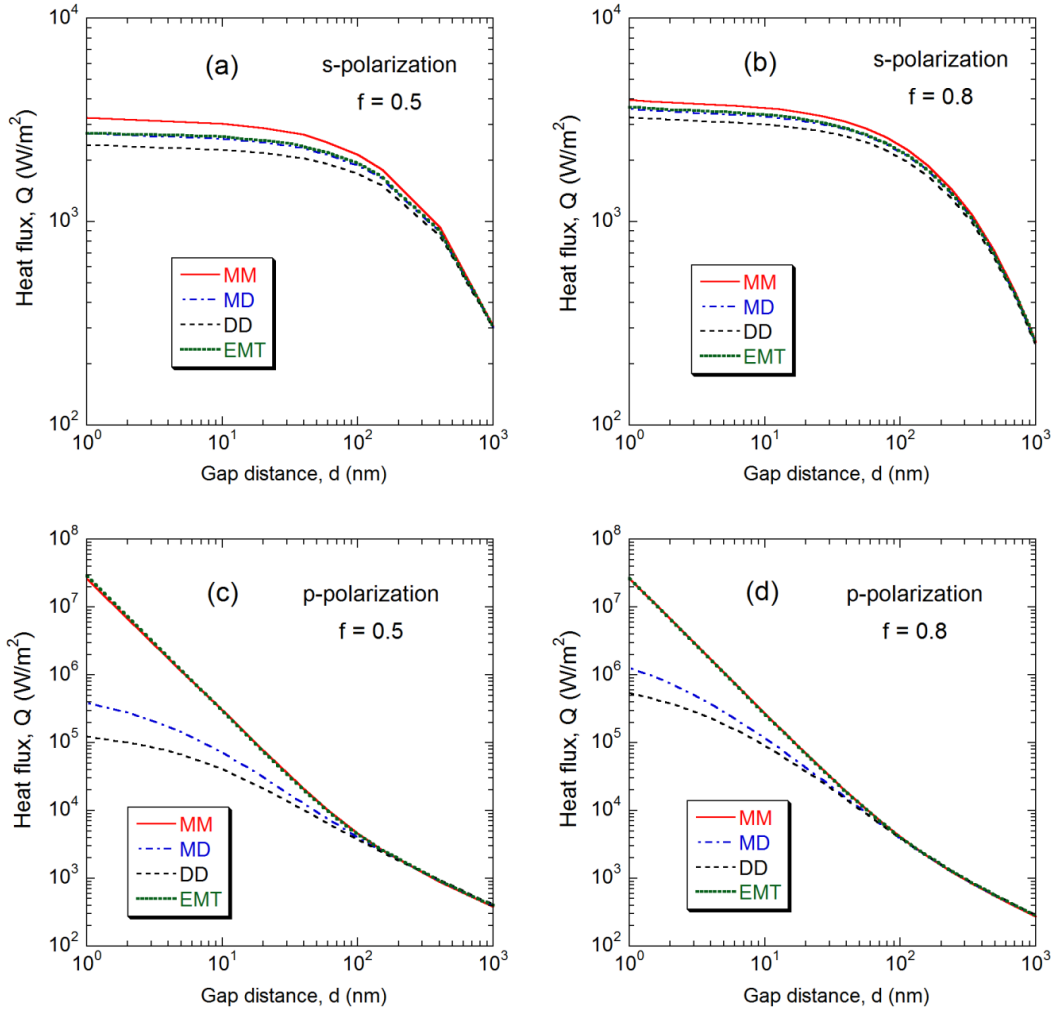

Figure 4.14 Total near-field radiative heat flux for different configurations as a function of gap distance: (a) s-polarization, f = 0.5; (b) s-polarization, f = 0.8; (c) p-polarization, f = 0.5; (d) p-polarization, f = 0.8.

When d is smaller than P, the s-polarization heat flux for MD and DD configurations starts to deviate from the EMT predictions, as shown in Figure 4.14 (a) and 4.14 (b). However, the heat flux for MD configuration agrees well (within 2.4%) with the EMT prediction for any gap distances. In general, the deviation of heat flux between different configurations and EMT prediction is relatively small for s-polarization (< 20% for f = 0.5 and < 11% for f = 0.8). This could be explained by the fact that no surface modes or hyperbolic modes are supported for s-polarized waves, so that only low-

β modes with large effective wavelength contribute to the flux. Hence, the deviation from the exact multilayer calculation and EMT is insignificant even at nanoscale distances. Furthermore, the effective permittivity for s-polarized waves (ordinary) is a weighted average of D-Si and Ge. As a result, compared to MM and DD, the MD configuration is physically more similar to the homogenized effective structure. This might be the reason why the heat flux for MD configuration agrees very well with that predicted by EMT. As shown in Figure 4.15 (a), good agreement between MD and EMT exists across the whole frequency region. While Figure 4.15 (a) is for a specific set of d and f, the spectral behaviors are similar for other distances and filling ratio for s-polarization. It should be noted that, at small gap distances, the heat flux by s-polarized waves saturates and reaches nearly a constant. The contribution to the overall heat flux by s-polarized waves becomes significantly smaller than that by the p-polarized waves, which can support surface and hyperbolic modes.

As shown in Figs. 4.14 (c) and 4.14 (d), the p-polarization heat flux deviates most significantly among the three configurations toward nanometer distances, as expected. What is surprising is that the heat flux predicted by EMT agrees well with that of MM configuration even at a nanometer gap distance. This is actually a coincidence. As revealed by Figure 4.15 (b) for d = 10 nm and f = 0.5, EMT over and under predicts the spectral flux of MM at lower and higher frequencies, respectively. However, the total heat flux is almost the same between these two cases. Such coincidence does not exist when D-Si is replaced by SiC due to the fact that SPhPs in SiC and hyperbolic modes with SiC/Ge multilayers are narrowband. It can be seen from Figure 4.15 (b) that the heat flux predicted by EMT is always higher than those for MD and DD. With increasing gap

distances, the deviation of spectral heat flux among different configurations reduces. This can be seen from Figure 5, which shows the spectral heat flux for p-polarization at d = 100, 200, and 300 nm. In general, as the gap distance increases, the agreement between EMT and the exact calculation for all three cases becomes better. The question is how large the gap distance needs to be to make the spectral heat flux for different configurations converge within, for example, 10%.

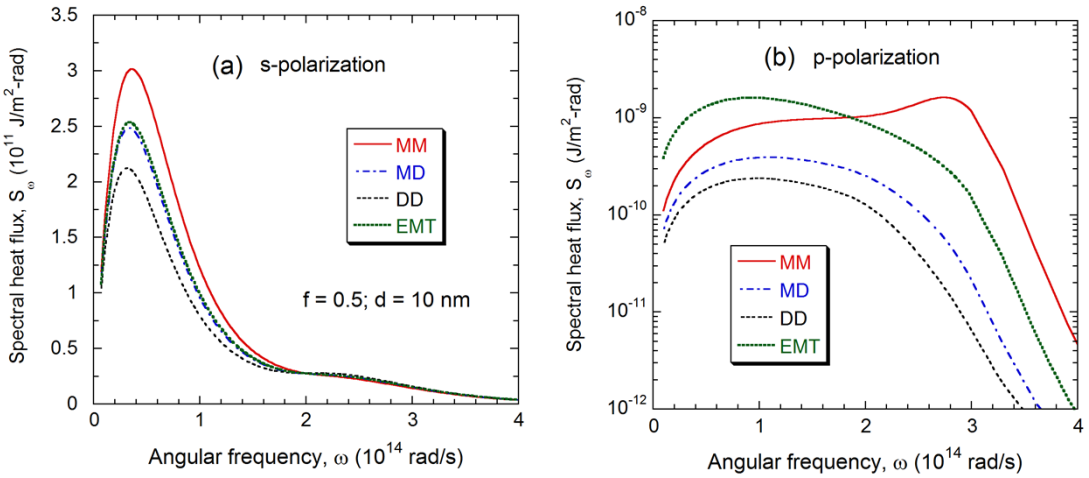

Figure 4.15 Spectral near-field radiative heat flux for different configurations at gap distance d = 10 nm for f = 0.5: (a) s-polarization; (b) p-polarization.

To elucidate the underlying mechanism for the agreement or disagreement of the heat fluxes for p-polarization, contour plots are generated in Figure 4.16 for different cases, to show the dependence of transmission coefficient ξ_p on the lateral wavevector β and angular frequency ω for f = 0.5 and d = 10 nm. As shown in Figure 4.16 (a) for EMT, large β modes with high transmission coefficients are supported in both the type I and type II hyperbolic regions. Unlike the type I hyperbolic band, modes with $\beta < \beta_{cr}$ for type II band are evanescent with near zero transmission coefficients and thus contribute

little to the heat flux [69]. Similar shapes appear for MM, MD, and DD configurations since, for small β values with large effective wavelength, EMT is valid and the transmission coefficient is almost the same independent of configurations. For large β values, EMT breaks down and the transmission coefficient depends heavily on specific configurations, as shown by Figure 4.16 (b), Figure 4.16 (c) and Figure 4.16 (d) for MM, MD, and DD configurations, respectively. The heat flux for MM configuration is the largest due to strong coupling of SPP with the surface resonance frequency around 3.0×10^{14} rad/s. DD configuration has the lowest heat flux since the distance between metallic D-Si layers of the emitter and receiver increases to $P + d$ and thus the coupling of SPP becomes weak. As d becomes sufficiently large, coupled SPPs become weak and the transmission coefficients become independent of the configuration. The requirement that the differences between various configurations become negligible will be discussed next, focusing on p-polarization only.

According to the Bloch theorem, the Bloch wavevector k_b for a one-dimensional photonic crystal is governed by [218]

$$\begin{aligned}\cos(k_b P) = &\cos\left(\gamma_m t_m\right)\cos\left(\gamma_d t_d\right) \\ &-\frac{1}{2}\left(\frac{\varepsilon_m\gamma_d}{\varepsilon_d\gamma_m}+\frac{\varepsilon_d\gamma_m}{\varepsilon_m\gamma_d}\right)\sin\left(\gamma_m t_m\right)\sin\left(\gamma_d t_d\right)\end{aligned} \tag{4.13}$$

where $\gamma_m = \sqrt{k_0^2\varepsilon_m - \beta^2}$ and $\gamma_d = \sqrt{k_0^2\varepsilon_d - \beta^2}$ are the z-component wavevectors for D-Si and Ge, respectively. It can be shown [218] that under the approximations, $\cos(k_b P) \approx 1 - k_b^2 P^2/2$, $\sin(\gamma_m t_m) \approx \gamma_m t_m$, and $\sin(\gamma_d t_d) \approx \gamma_d t_d$, Eq. (4.13) reduces to

$$\frac{\beta^2}{\varepsilon_z} + \frac{k_b^2}{\varepsilon_x} = k_0^2 \tag{4.14}$$

which is the dispersion relation for a uniaxial medium with a *z*-component wavevector, $k_z = k_b$. The general requirement for these approximations to be valid is that the *z*-component wavevectors ($k_z, \gamma_m,$ and γ_d) be much smaller than P^{-1}. For small β values, the *z*-component of the wavevector is on the same order of the magnitude as the wavevector. Therefore, the criterion for Eq. (4.14) to be valid is $\lambda >> P$. This explains why the agreement in different configurations is good in Figure 6 for small β values. In the far field, propagating waves exist in vacuum so that $\beta / k_0 \leq 1$, local EMT is usually a good approximation without considering spatial effect.

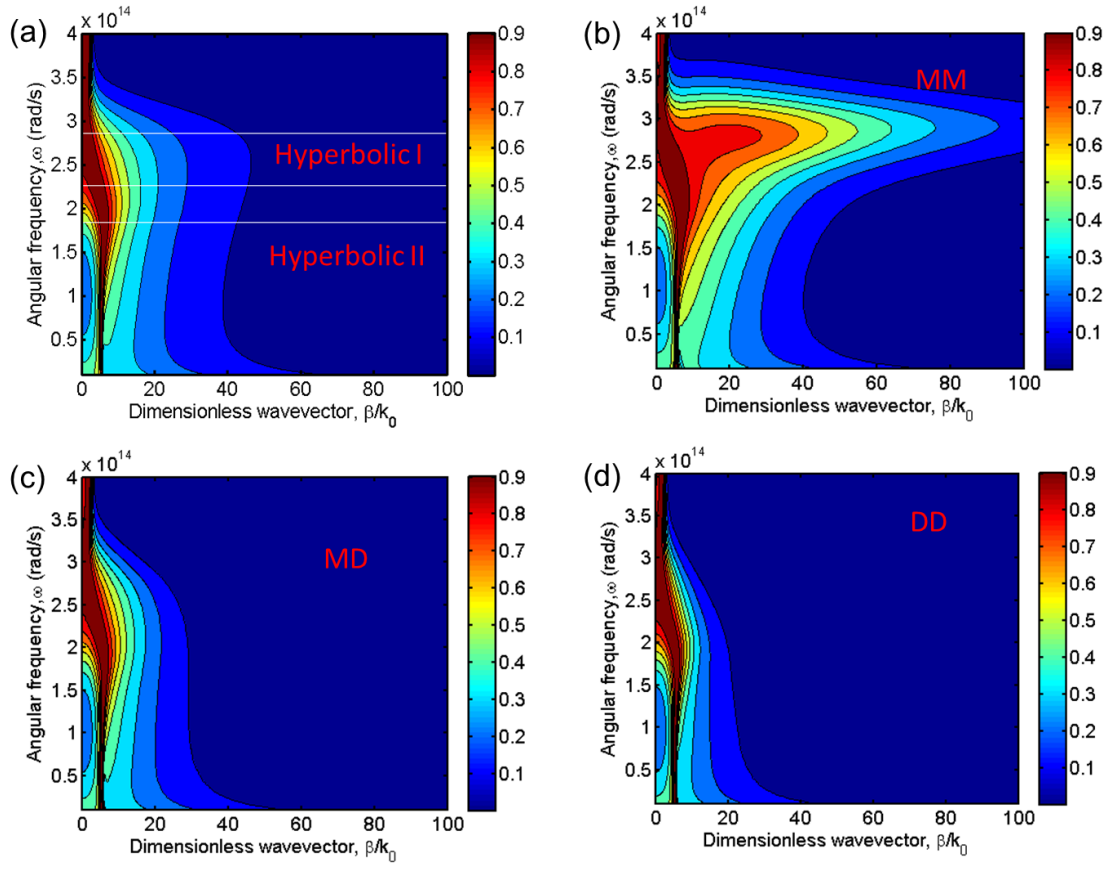

Figure 4.16 Transmission coefficient contours $\xi_p(\omega, \beta)$ for (a) effective medium, different hyperbolic region are delineated; (b) MM; (c) MD; (d) DD.

It is noted that when $x = 1.05$, the deviation between $1 - x^2/2$ and cos(x) is 10%. When $x = 0.75$, the deviation between x and sin(x) is 10%. After further numerical calculations and verifications considering complex variables, it is shown that the following criteria allow Eq. (4.14) to approximate Eq. (4.13) fairly accurately within about 10%:

$$|k_z| P \le 1.05,\ |\gamma_m| P \le 0.75,\ \text{and}\ |\gamma_d| P \le 0.75 \tag{4.15}$$

For large β values (as usually is the case in the near field), $|k_z|$ as well as γ_m and γ_d in Eq. (4.15) are proportional to β [239]. Thus, additional criteria in terms of β are needed to evaluate when EMT is a good approximation.

It is well known that SPP/SPhP-based surface modes can have a dominant contribution to the heat flux due to the high density of states [240-242]. The number of contribution modes achieves the maximum value when $\varepsilon' = \mathrm{Re}(\varepsilon) = -1$ at the singularity of SPP dispersion relation $\beta = k_0\sqrt{\varepsilon/(\varepsilon+1)}$ for two semi-infinite media consisting vacuum and an isotropic medium [207, 243]. For $\beta >> k_0$, $r_p = (\varepsilon-1)/(\varepsilon+1) = 1 + 2i/\varepsilon''$ when $\varepsilon = -1 + i\varepsilon''$. Thus, the transmission coefficient can be simplified as

$$\xi_p(\omega,\beta) = \frac{16}{2(4-\varepsilon''^2) + \varepsilon''^2\left[e^{2\beta d} + (1+4/\varepsilon''^2)^2 e^{-2\beta d}\right]} \tag{4.16}$$

The cutoff wavevector β_{cut} may be assessed from the following condition with 90% of the integral, i.e., a 10% relative error:

$$\frac{\int_0^{\beta_{cut}} \beta\xi_p(\omega,\beta)\,d\beta}{\int_0^{\infty} \beta\xi_p(\omega,\beta)\,d\beta} = 90\% \tag{4.17}$$

The result gives $\beta_{cut} d$ as a function of ε'', as shown in Figure 4.17 for ε'' from 0.01 to 100. The values of ε'' at the surface resonance frequency ω_{SP} for different real materials commonly used in thermal radiation lies in the range from 0.01 to 100. However, the relationship between β_{cut} and ε'' is neither intuitive nor convenient. The least-squares method is used to obtain a simple equation by fitting the numerical results given as

$$\beta_{cut} = \frac{2.55}{\varepsilon''^{0.21} d} \tag{4.18}$$

As shown in Figure 4.17, the agreement between Eq. (4.18) and the exact calculations is very good. Hence, Eq. (4.18) provides an easy way to evaluate β_{cut} and is applicable to most materials supporting surface modes. Because β_{cut} is the largest at the surface resonance frequency, in general, $\beta \in [0, \beta_{cut}]$ will contribute to more than 90% to the spectral heat flux.

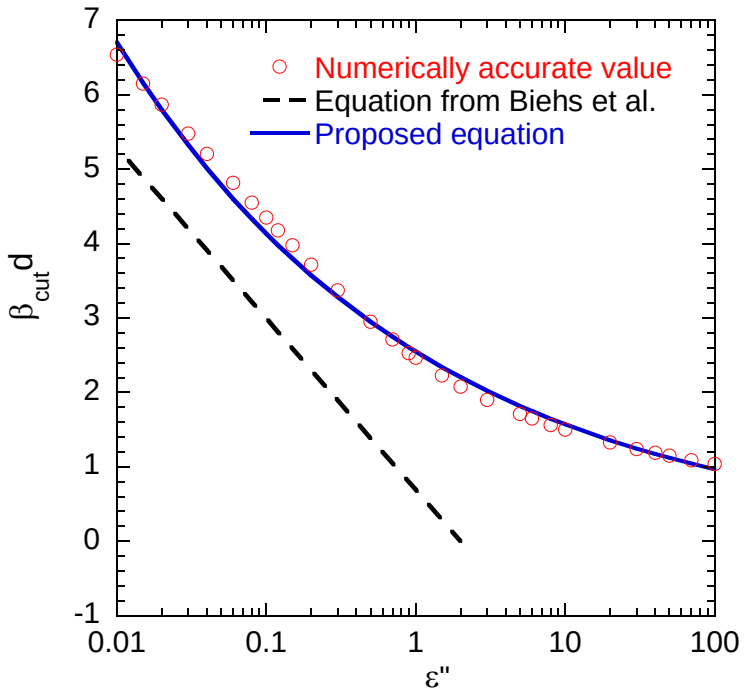

Figure 4.17 Loss-dependent cut-off wavevector at the surface resonance frequency.

For near-field radiative transfer between two uniaxial anisotropic materials, surface resonance is excited when $\mathrm{Re}\left(\sqrt{\varepsilon_x \varepsilon_z}\right) = -1$ with both ε_x' and ε_z' being negative [66]. The corresponding frequency is the surface resonance frequency ω_{SP} for uniaxial materials. Then, the cutoff wavevector at surface resonance becomes

$$\beta_{cut} = \frac{2.55}{\varepsilon_u''^{0.21} d} \tag{4.19}$$

where $\varepsilon_u'' = \mathrm{Im}\left(\sqrt{\varepsilon_x \varepsilon_z}\right)$ is evaluated at ω_{SP}. For small values of ε'', an approximation of β_{cut} was given by Biehs et al. [15] as $(1/d)\ln\left(2/\varepsilon''\right)$ based on the peak of the transmission coefficient where $\left(r_p'^2 + r_p''^2\right) e^{-2\beta d} = 1$ [14]. Here, r_p' and r_p'' are the real and imaginary parts, respectively, of the Fresnel reflection coefficient for p-polarization. However, the integrand to calculate the radiative heat flux is $\beta\xi(\omega,\beta)$ rather than $\xi(\omega,\beta)$ due to axial symmetry. When β is very small, $\beta\xi(\omega,\beta)$ could still be neglected even though $\xi(\omega,\beta)$ achieves the maximum value of unity. Similarly, at large β, $\beta\xi(\omega,\beta)$ is non-negligible even if $\xi(\omega,\beta)$ is far less than 1. Nevertheless, $\beta_{cut} \approx (1/d)\ln\left(2/\varepsilon''\right)$ is still reasonable for very small ε'' (with an offset) but will fail when ε'' is comparable to or greater than 2. With increasing loss, the cutoff wavevector decreases so that the contribution of surface modes will deteriorate. In other words, reducing the material's optical loss helps enhance radiative heat flux.

Attention is now paid to β_{cut} for hyperbolic modes. At large β, the transmission coefficient for hyperbolic metamaterials is given as

$$\xi_p(\omega,\beta)=\frac{4r_p''^2}{e^{2\beta d}+\left(r_p'^2+r_p''^2\right)e^{-2\beta d}-2\left(r_p'^2-r_p''^2\right)} \tag{4.20}$$

Compared with surface modes, the uniqueness of hyperbolic modes lies in the propagating nature of electromagnetic waves for large wavevectors due to the hyperbolic dispersion relation. Hence, the hyperbolic modes are essentially special frustrated total internal reflection modes [66]. For sufficiently large β, $\xi_p(\omega,\beta)\approx 4r_p''^2e^{-2\beta d}$. Then, the cutoff wavevector for hyperbolic mode can be assessed by letting

$$\frac{\int_0^{\beta_{cut}}\beta e^{-2\beta d}d\beta}{\int_0^{\infty}\beta e^{-2\beta d}d\beta}=1-e^{-2\beta_{cut}d}\left(1+2\beta_{cut}d\right)=90\% \tag{4.21}$$

From Eq. (4.21), one obtains

$$\beta_{cut}=\frac{1.94}{d} \tag{4.22}$$

Equation (4.22) is similar to the cutoff wavevector obtained for spontaneous emission enhancement of hyperbolic metamaterials in the literature [218] and is about three times that obtained by [66] based on the peak of energy transmission coefficient. It can be seen from Eq. (4.22) that β_{cut} for hyperbolic modes is independent of frequency and loss, although $\xi_p(\omega,\beta)$ is sensitive to frequency. Hence, the number of contributing modes is sensitive to frequencies in the hyperbolic region. This is completely different from the case of surface modes for which the number of modes decreases rapidly as the frequency is away from ω_{SP}. This is one of the reasons why the radiative heat flux based on surface modes tends to be narrowband or even monochromatic, while that based on hyperbolic modes could have a broadband super-Planckian behavior in the whole hyperbolic region.

If the Bloch dispersion relation could be effectively described by EMT up to the cutoff wavevector, then EMT should be valid in calculating the near-field radiative heat flux. For generalized SPP modes, $\gamma_m = \gamma_d = i\beta$ and $k_z = i\beta\sqrt{\varepsilon_x/\varepsilon_z}$ when $\beta \gg k_0$, $\varepsilon_x' < 0$, and $\varepsilon_z' < 0$. Combining these quantities with Eq. (4.19) and Eq. (4.15) gives the validity condition of EMT for calculating near-field radiative heat flux at SPP resonances as follows:

$$d / P \geq \max\left\{2.43\left|\sqrt{\varepsilon_x/\varepsilon_z}\right|\varepsilon_u''^{-0.21},\ 3.40\varepsilon_u''^{-0.21}\right\} \tag{4.23}$$

As an example, consider f = 0.8, a surface mode occurs at $\omega_{SP} = 2.58\times10^{14}$ rad/s with ε_u'' equal to 6.24. The maximum value of $\left|\sqrt{\varepsilon_x/\varepsilon_z}\right|$ is 0.71 in the region where coupled SPPs are supported. As a result, Eq. (4.23) becomes $d/P \geq 2.31$. In this case, the spectral heat fluxes (in pW/m^2 per rad/s) for different configurations are: S_{EMT} is 5.17, S_{MM} = 4.93, S_{MD} = 5.08, and S_{DD} = 5.29 at ω_{SP}. The maximum relative error of EMT in predicting the heat flux is 4.7%. Since the cut-off wavevector usually achieves the maximum value at the surface resonance frequency, Eq. (4.23) should be safe to use for other spectral regions as well. For example, when d = 231 nm, the total heat flux Q_{EMT} is 2771 W/m^2, Q_{MM} = 2800 W/m^2, Q_{MD} = 2741 W/m^2, and Q_{DD} = 2699 W/m^2. The maximum relative error of EMT is only 2.6%. Hence, in practice, if Eq. (4.23) is satisfied, using EMT to calculate heat flux will result in an error usually much less than 10%.

For hyperbolic modes, when $\beta >> k_0$ and $\varepsilon_x\varepsilon_z < 0$, $\gamma_m = \gamma_d = i\beta$ and $k_z = \beta\sqrt{-\varepsilon_x/\varepsilon_z}$. Hence, Eq. (4.15) can be rewritten as

$$\left|\sqrt{-\varepsilon_x/\varepsilon_z}\right|\beta P \leq 1.05 \text{ and } \beta P \leq 0.75 \tag{4.24}$$

Combining Eq. (4.15) and Eq. (4.22), one obtains

$$d / P \geq \max\left(1.85\left|\sqrt{-\varepsilon_x/\varepsilon_z}\right|,\ 2.59\right) \tag{4.25}$$

As long as Eq. (4.25) is satisfied, EMT should be reasonably accurate for calculating the near-field radiative heat flux in the hyperbolic region. For instance, the effective medium is hyperbolic at ω = 10^{14} rad/s with f = 0.5, and $\sqrt{-\varepsilon_x/\varepsilon_z} = 0.97$. Therefore, Eq. (4.25) requires $d \geq 2.59P$. For P = 100 nm, d = 259 nm, the spectral fluxes (in pW/m^2 per rad/s), S_{EMT} is 10.4, S_{MM} = 10.7, S_{MD} = 10.2, and S_{DD} = 9.92. The maximum relative error of EMT is only 1.9%. This justifies that Eq. (4.25) can guarantee that the EMT is reliable in predicting the near-field radiative heat transfer for hyperbolic modes. It should be noted that the above criteria hold for regions that do not support either the surface or hyperbolic mode since large β modes will have negligible contributions.

4.4 Summary

This chapter investigates the near-field radiation between nanostructures in the limit when the period is sufficiently small. The main contributions are summarized in the followings.

Different practically achievable nanostructures based on doped silicon are investigated for enhancement of near-field radiative heat transfer at ambient temperature. Three out of the four configurations (D-SiNWs, D-SiNHs, and D-Si gratings) can enhance radiative heat transfer over bulk D-Si from tens of nanometers to the far field. The fourth configuration, multilayers, can also give a radiative heat flux that is almost twice as large as that between bulks in the far field. It is predicted that D-SiNWs and D-

SiNHs can provide an enhancement over bulks by more than one order of magnitude in the deep submicron gap region, due to broadband hyperbolic modes and low-loss surface modes, respectively. These two configurations can be designed with optimal doping and geometrical criteria. The mechanism of near-field radiative transfer between gratings made of D-Si and Ge is also investigated. It is found that s-polarization and polarization coupling are negligible for near-field heat transfer analysis at deep submicron distances. Thus, the dominating mechanism for near-field radiation between gratings is the same as for other nonmagnetic materials; that is, the nontrivial transmission coefficients at large transverse wavevectors are enabled by p-polarized waves. The alignment between gratings has a relatively small effect on the near-field radiative transfer for D-Si/Ge gratings.

The near-field blackbody phenomena with perfect photon tunneling having near-unity probability across a broad frequency region and over a large *k*-space is theoretically demonstrated based on graphene-covered doped-silicon nanowires. As a result, the near-field radiative heat transfer coefficient achieves as high as 80% of a theoretical limit of hyperbolic materials. The underlying mechanism is due to hybridization of graphene plasmons and hyperbolic modes. So, a new way of achieving greatly enhanced photon tunneling is provided. This hybrid system will benefit the design of nanostructures in applications such as more efficient non-contact thermal management and microgap thermophotovoltaics.

The applicability of EMT to predict near-field radiative heat flux is evaluated by comparison with exact solutions for metal-dielectric multilayered metamaterials, where the layers adjacent to vacuum can be of different combinations. EMT is found to be able

to predict the s-polarized radiative heat flux for MD configuration at any gap distance, while some deviation exists for MM and DD configurations. For p-polarized waves, the cutoff wavevectors are quantitatively obtained for surface modes and hyperbolic modes in order for the EMT to be able to predict near-field radiative heat flux to within 10%. Combining the cutoff wavevectors with the criteria under which the Bloch dispersion can be approximated by the dispersion relation of a uniaxial anisotropic medium, a criterion is obtained for the ratio of d to P so that EMT can reliably predict the near-field radiative heat flux. The methodology may be extended to give the validity condition of EMT in predicting near-field thermal radiation for other types of metamaterials, such as nanowires and gratings.

CHAPTER 5

ENHANCED NEAR-FIELD RADIATION BY METAMATERIALS USING EXACT FORMULATIONS

Based on exact formulations, chapter 5 presents new routes to enhance the near-field radiative heat flux. Section 5.1 demonstrates that the heat flux between corrugated silica can be enhanced by more than one order of magnitude when covered with a graphene sheet on top of the grating on each side of the vacuum gap due to the hybridization of graphene plasmons with surface phonon modes. In Sec. 5,2, patterning thin films of moderate thicknesses into 1D and 2D metasurfaces is found to increase the heat flux for the first time. The underlying mechanism is due to the excitation of hyperbolic modes featured with high LDOS in a broad frequency and k-space regime. Section 5.3 presents a giant enhancement of near-field radiative heat flux over more than one order of magnitude by patterning graphene sheets into ribbon arrays to support hyperbolic graphene plasmons. In Sec. 5.4, the electroluminescent refrigeration rate is found to be enhanced by more than two orders of magnitude by pushing the hot object into the diode's close proximity. The underlying mechanism is attributed to the photon tunneling of evanescent waves. Section 5.5 briefly summarizes the main contributions of this chapter.

5.1. Graphene-Assisted Near-Field Radiation between Polar Grating

Silica is one of the best well known thermal emitters due to its two narrow band thermally excited surface phonon polariton (SPhP) modes. Unfortunately, corrugated

silica can hardly have a better performance than bulk silica since the radiative transfer is local due to the short lateral propagation length of SPhPs [83]. In this section we show that covering a single layer graphene can relieve this problem due to the low loss and long propagation length of graphene plasmons.

The schematic of thermal radiation between considered graphene-covered gratings separated by a vacuum gap of d is depicted in Figure 5.1. The temperatures of the emitter and receiver are set around room temperature with T_1 = 310 K and T_2 = 290 K, respectively. The dielectric function of fused silica (SiO_2) is obtained from Ref. [110].

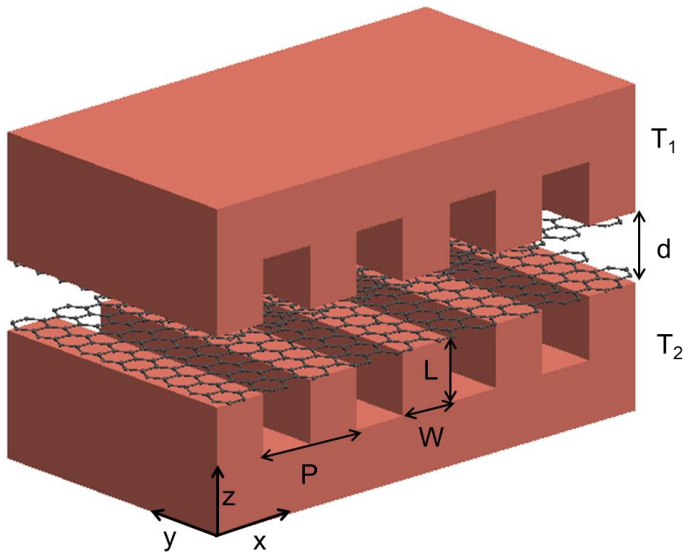

Figure 5.1 Schematics of radiative heat transfer between graphene-covered silica gratings separated by a vacuum gap of d. P is period, W is grating width, L is corrugation depth, and T_1 = 310 K, T_2 = 290 K.

The radiative heat flux between graphene-covered grating and bulk silica ($f = W/P = 1$) at gap distance of 100 nm is shown in Figure 5.2 (a) as a function of μ. The maximum heat flux for graphene-covered bulk silica is 22.7 kW/m^2 around μ = 0.28 eV, which is nearly four times as large as that between bulk silica, shown as the horizontal

dashed line. Further increasing or reducing μ will deteriorate the performance or even make graphene-covered silica inferior to bulk silica in terms of near-field heat flux. Nevertheless, for different gap distances, the chemical potential can in general be optimized to improve the heat transfer performance of bulk silica. Even greater heat flux is obtained for graphene-covered grating using f = 0.4, P = 500 nm, and L = 500 nm with a peak at about μ = 0.2 eV.

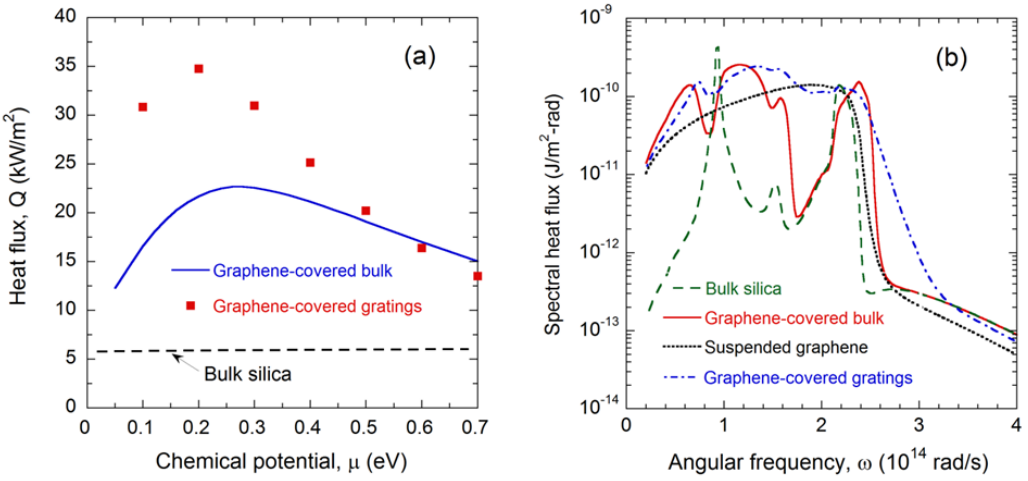

Figure 5.2 (a) Radiative heat flux between graphene-covered bulk silica as a function of chemical potential at d = 100 nm; (b) Spectral heat flux for four configurations.

The spectral heat fluxes for bulk silica, suspended graphene sheets, graphene-covered bulks, and graphene-coated gratings are plotted in Figure 5.2 (b) at d = 100 nm for comparison. The chemical potential of graphene is chosen as 0.3 eV, and grating parameters remain the same as for Figure 5.2 (a). The spectral heat flux between bulk silica is featured with two narrow peaks while suspended graphene has a broadband behavior. The heat flux between graphene-coated silica is feature with three wide bands, allowing the total flux to reach 22.6 kW/m^2, which is much greater than the value of 5.84

kW/m^2 between bulk silica. It should be noted that the heat flux between plain silica gratings is generally lower than that between bulk silica with a total heat flux of 2.74 KW/m^2. Hence, the spectral heat flux between silica gratings is not shown in Figure 5.2 (b). When the silica grating is covered by a graphene sheet on both side of the emitter and receiver, the total heat flux is enhanced by more than one order of magnitude to 31.0 KW/m^2. This is about 37% greater than that for graphene-covered bulk silica. As shown by Figure 5.2 (b), the largest difference of graphene-covered grating from graphene-covered bulk lies in the region between 1.6×10^{14} and 2.1×10^{14} rad/s where graphene plasmons are seriously suppressed by bulk silica (as to be discussed later). However, for graphene-covered gratings, the suppression is relieved. This is not surprising since geometrically 60% percent of graphene is not in contact with silica and thus the deterioration of graphene plasmons caused by silica in the above-mentioned frequency region will be lessened.

The underlying mechanism for the great enhancement enabled by graphene-covered bulk silica is explored next considering the interplay between graphene plasmons and silica phonon modes. For sub-micron gap distance, contributions of both propagating modes and the s-polarization evanescent modes become negligible compared with p-polarization evanescent waves capable of supporting surface modes. The p-polarized energy transmission coefficient $\xi_p(\omega,\beta)$ for evanescent modes is given as [3, 244]

$$\xi_p(\omega,\beta)=4\left[\mathrm{Im}(r_p)\right]^2 e^{-2|k_{z0}|d}\Big/\left|1-r_p^2e^{2ik_{z0}d}\right|^2,\quad \beta>k_0 \tag{5.1}$$

where the Fresnel coefficient r_p for graphene-covered isotropic substrates is given in Refs. [194, 226] and k_{z0} is the *z*-component of the wavevector. The contour plots for the

p-polarization energy transmission coefficient $\xi_p(\omega,\beta)$ are shown in Figure 5.3 (a), (b), and (c) for bulk silica, suspended graphene, and graphene-covered silica, respectively. As shown in Figure 5.3 (a), two narrow band SPhP modes dominantly contribute to the radiative heat flux of bulk silica, as has been well understood [3, 240]. The energy transmission coefficient for suspended graphene sheets is featured with two branches as shown in Figure 5.3 (b) due to coupling of SPPs. The dispersion relation of the coupling SPPs can be obtained by zeroing $1-r_p^2 e^{2ik_{z0}d}$ and the details have been discussed in Ref. [233]. The low-frequency symmetric and the high-frequency antisymmetric branches are shown as white lines, which cross over broad bands and tend to merge together at large β. These two branches of coupling surface modes match well with the peaks of energy transmission coefficient contour in Figure 5.3 (b). It is clear that the broadband graphene plasmons and narrow band phonon resonance modes contribute predominantly to the heat transfer performance for graphene and silica, respectively.

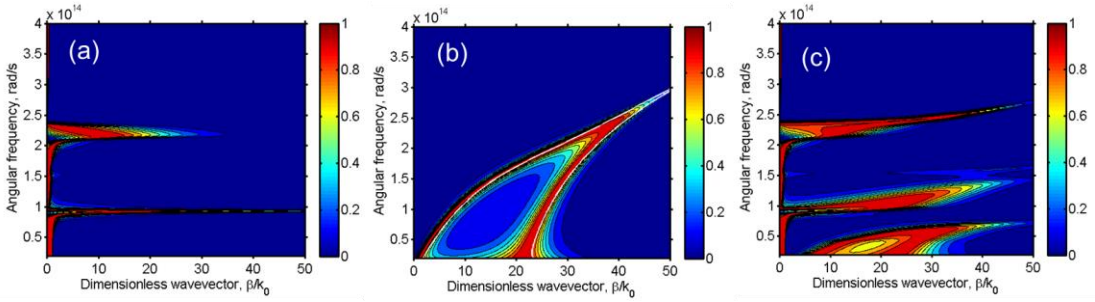

Figure 5.3 (a) Energy transmission coefficient contour of p-polarization at d = 100 nm for bulk silica; (b) Suspended graphene; (c) Graphene-covered silica.

When graphene is coated on silica, as shown in Figure 5.3 (c), the interplay between graphene plasmons and silica phonon resonance modes leads to three wide bands featured with high energy transmission coefficient. The lower frequency band up

to 7×10^{13} rad/s is mainly due to graphene plasmons. Silica is a dielectric with very small loss in this region, thus supports a much lower spectral heat flux than graphene. Nevertheless, the presence of the silica dielectric improves photon tunneling over suspended graphene as shown in Figure 5.2 (b). Near the first surface resonance frequency of silica at 9.3×10^{13} rad/s, the spectral heat flux is notably deteriorated compared with that for bulk silica. This is presumably because the resonant photon tunneling for silica is truncated by the presence of graphene at very large β modes. Due to the modification of the Fresnel coefficient by graphene, r_p becomes close to one with diminishing imaginary part at extremely large β, leading to zero energy transmission coefficient. Nevertheless, the presence of graphene results in a broader middle band from 1.0×10^{14} to 1.6×10^{14} rad/s, where silica behaves as a dielectric and the presence of graphene greatly improves the energy transmission coefficient. On the other hand, Figure 5.3 (c) shows that the graphene plasmon modes are entirely suppressed in the region from 1.6×10^{14} to 2.1×10^{14} rad/s, leading to the abrupt drop of spectral heat flux in this region as shown in Figure 5.2 (b). The third band in Figure 5.3 (c) ranges from 2.1×10^{14} to 2.5×10^{14} rad/s and is similar to phonon resonance band of silica. The presence of graphene plasmon enhances photon tunneling at frequencies close to but away from the phonon resonance of silica with the price of suppressing the phonon resonance mode at very large β. The overall improvement outweighs the deterioration as can be seen from Figure 5.2 (b) for this band. Comparing Figs. 5.2 (a) with 5.2 (c), it can be seen that the two narrow SPhP bands in silica turns out to be three wide hybridized bands with graphene, leading to nearly fourfold increase of radiative heat flux.

As discussed previously, graphene-covered grating can further enhance near-field

radiative heat transfer. However, its energy coefficient is not plotted in Figure 5.3 for direct comparison since it would require a 3D contour plot depending on both k_x and k_y, and besides, the modes are folded in the first Brillouin zone. Nevertheless, it can quantitatively understood that the significant enhancement is largely in the frequency region between 1.6×10^{14} and 2.1×10^{14} rad/s. When some part of the graphene is not in direct contact with silica, the suppression of graphene plasmon is diminished.

The radiative heat flux between gratings and micro-objects can be predicted by geometry-based Derjaguin's proximity approximation (PA) [83]. For 1D gratings, the PA can be written as

$$Q_{PA} = fQ_r + (1-f)Q_g \tag{5.2}$$

where Q_r and Q_g represent the plane-plane heat flux for the ridge and groove region, respectively. Figure 5.4 gives the heat flux for plain and graphene-covered silica gratings as a function of the volume filling ratio of silica, using both the exact calculation and PA. The gap distance and chemical potential remain at 100 nm and 0.3 eV, respectively. Both the period and the corrugation depth are chosen as 500 nm. From Figure 5.4, the heat flux of plain silica grating almost linearly increases with *f*, and the agreement between PA and exact method is very good. Therefore, the radiative heat transport or photon tunneling between plain silica gratings tends to be a local phenomenon due to the short lateral propagating length of surface phonon modes [83]. A disadvantage of local heat transfer is that gratings can hardly perform better than the counterpart bulks. Nevertheless, depositing a graphene sheet on top of the grating will make the heat transfer much more efficient and nonlocal. As shown in Figure 5.4, the heat flux for graphene-covered corrugated silica is much greater than that without graphene. Besides, the heat flux does

not increase linearly with f according to PA, which significantly underestimates the heat flux for filling ratio less than 1. The nonlocal behavior could be because graphene plasmons have low loss and thus have lateral propagation length close to or longer than the period.

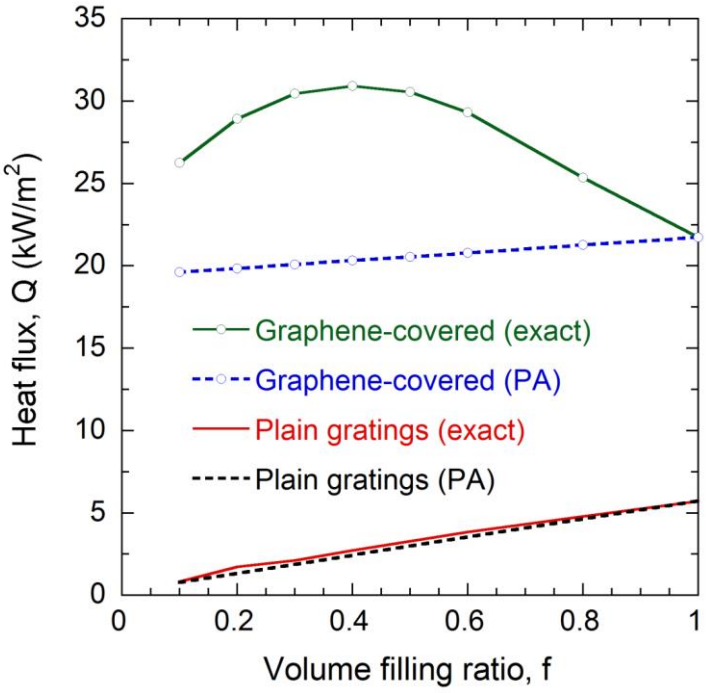

Figure 5.4 Near-field heat flux for plain and graphene-covered silica gratings at different filling ratios when d = 100 nm, P = 500 nm, L = 500 nm, f = 0.4.

Besides enhancing radiative heat transfer and breaking PA, it is worth noting that the presence of graphene helps relieve the performance sensitivity of silica gratings to the lateral shift between emitters and receivers, leading to robust thermal management devices. Misalignment will harm near-field heat transfer due to symmetry breaking and thus bad coupling of surface modes. The maximum misalignment or the minimum heat flux occurs when the emitter and receiver are laterally displaced by a half period. For example, at f = 0.2 the heat flux for a half period displacement is 728 W/m^2, which is

only 42% of that for the aligned case. When graphene is covered, this ratio increases to 84%. Similar results are obtained for f = 0.4, for which the ratio of heat flux for maximum misaligned gratings to that for aligned gratings increases from 59% to 77% with the presence of graphene.

5.2 Near-Field Thermal Radiation between Metasurfaces

Metasurfaces, planar metamaterials with subwavelength thicknesses, have been extensively investigated for far-field manipulation of light propagation, polarization states, and absorption in an unprecedented way,[245-249] and have some peculiar advantages over conventional metamaterials, such as less volumetric propagation loss, relative easy fabrication, and compatible integration with other nanodevices. However, their near-field radiative properties have not been investigated. Several groups have calculated near-field radiative heat transfer between structured materials, but rarely considered thin metamaterials. For instance, Guérout et al. theoretically demonstrated enhanced radiative heat transfer of gold nanostructures over bulk gold [82]. Liu et al. proposed to increase near-field radiative heat flux between polar gratings by covering graphene [84]. Chalabi et al. examined the effects of different shapes and the spatially resolved near-field radiative heat flux [250, 251]. An open question is whether the radiative heat flux of thin films can be further increased by pattering them into metasurfaces.

The schematics of near-field thermal radiation for considered 1D and 2D periodic metasurfaces are shown in Figs. 5.5 (a) and (b), respectively. The temperatures of the top and bottom metasurfaces, which have identical geometry and are separated by a vacuum gap of d, are T_1 = 310 K and T_2 = 290 K, respectively. The period, width, and thickness

of the patterned metasurfaces are denoted by *P*, *W*, and *h*. The unit cell of 2D metasurface contains a square nanopillar, while that of 1D metasurface contains a beam extending to the infinity in the *y* direction, i.e., 1D gratings.

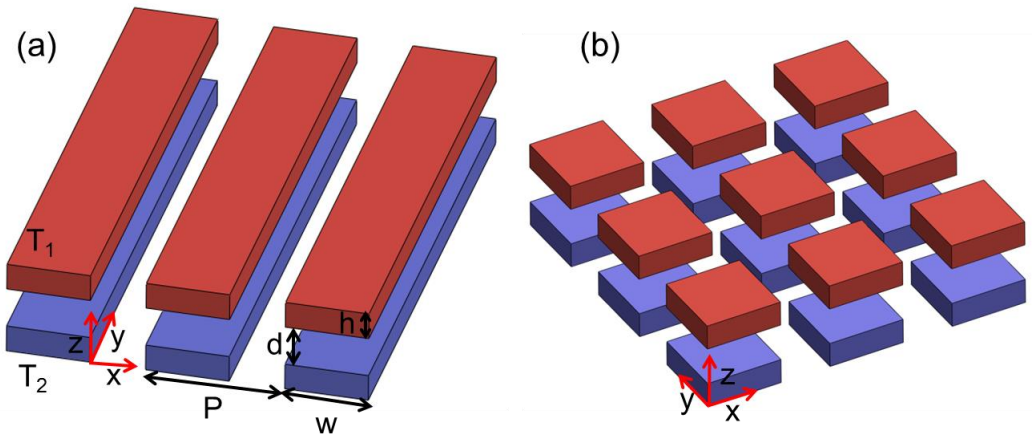

Figure 5.5 Schematic of near-field radiation between (a) 1D and (b) 2D metasurfaces.

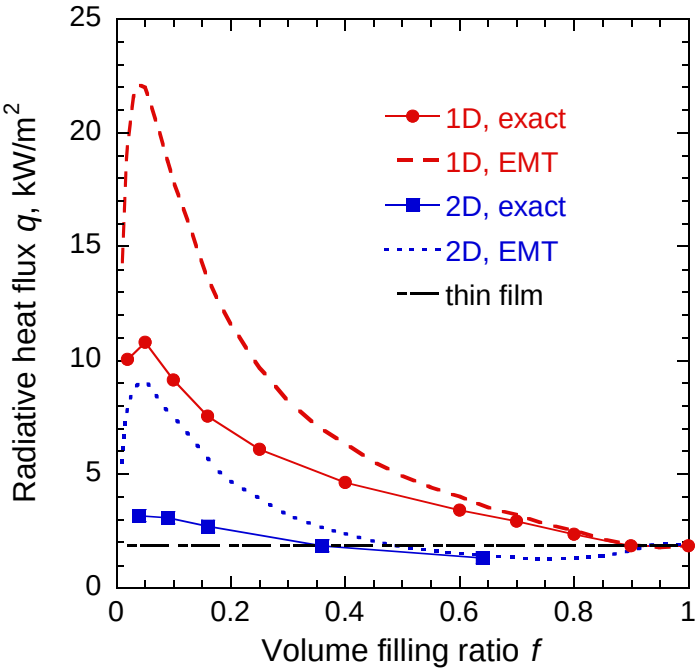

Figure 5.6 Radiative heat flux as a function of the volume filling ratio at P = 100 nm, d = 100 nm, and h = 400 nm.

Figure 5.6 gives the radiative heat flux for both configurations with varying volume filling ratios. The volume filling ratio f is defined as W/P and W^2/P^2 for 1D and 2D metasurfaces, respectively. The geometric parameters are taken as P = 100 nm, d = 100 nm, and h = 400 nm. These values are used as default in this work unless otherwise specified. The radiative heat flux between thin films (f = 1) of the same thickness (h = 400 nm) is denoted by the dash-dotted line and is 1860 W/m^2. This value exceeds that between bulk doped silicon of 1629 W/m^2 and is more than 15 times that between blackbodies. The underlying mechanism for the enhancement can be attributed to the coupling of SPPs inside the thin film, as discussed in Ref. [252] although different materials were used. Patterning the film into 1D metasurface can enhance thermal radiation for all practical volume filling ratios. Interestingly, while the 2D metasurface yields a radiative heat flux higher than that of thin films at moderate filling ratios, it does not support a heat flux as high as that of the 1D metasurface. Beyond f = 0.36, 2D patterning will deteriorate the radiative transfer as shown in Figure 5.6. The EMT approximation, which is valid only when P is sufficiently small, overpredicts the heat flux for both 1D and 2D configurations. The disagreement between the exact method and EMT is expected to be diminished when reducing the period, as was demonstrated for multilayered metamaterials [253]. The optimal heat flux supported by 1D and 2D metasurfaces reaches 10.79 kW/m^2 and 3.17 kW/m^2, respectively. Reducing P is expected to further increase the radiative flux. As indicated by the dashed and dotted curves predicted by EMT, the maximum possible heat flux of 1D and 2D configurations is 22.11 kW/m^2 and 9.16 kW/m^2, respectively. These values are about twelve and five

times as large as that between two films with the same thickness. Therefore, patterned thin metamaterials may increase the heat flux over the counterpart thin films and bulks.

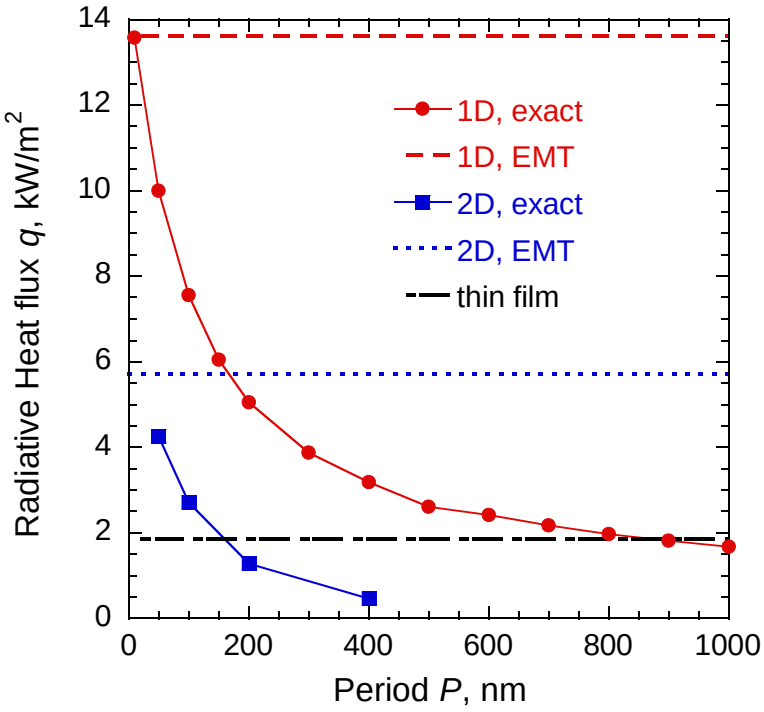

Figure 5.7 Effects of period on the radiative transfer of metasurfaces for $f = 0.16$.

The effects of period are shown in Figure 5.7 for $f = 0.16$ with other geometric parameters remaining the same. With decreasing period, the radiative heat flux for both configurations based on exact methods approaches the values predicted by corresponding EMT as expected. As an example, the heat flux of 2D metasurface at $P = 50$ nm is 4.26 kW/m^2, which is 25% less than that predicted by EMT. This discrepancy further decreases at small P. At $P = 10$ nm, the heat flux for 1D metasurface is 13.6 kW/m^2, which is essentially the same as that from EMT. With increasing P, the heat flux decreases and will eventually approach to the limit governed by the proximity approximation based on pair-wise addition, i.e., the heat flux of thin films multiplied by a

factor of *f*. Metasurfaces support a higher radiative heat flux than thin films unless the period exceeds 900 nm and 150 nm for 1D and 2D configurations, respectively. Understanding the underlying mechanism of the enhancement enabled by metasurfaces and the reason why 1D metasurface has a higher radiative heat flux than the 2D counterpart is necessary before turning this technique into practical applications.

The highest radiative heat flux for metasurfaces occurs when *P* becomes arbitrarily small when the periodic patterned structures can be homogenized as a thin layer of anisotropic effective medium characterized by EMT. The effective medium corresponding to both 1D and 2D metasurfaces is uniaxial with one distinction that the optical axis of homogenized 1D effective medium lies horizontally (the *y* direction) while that for 2D effective medium lies vertically (the *z* direction). The effective dielectric functions for ordinary ε_O and extraordinary ε_E can be calculated using expressions given in Refs. [253]. Then, the dielectric tensor of 1D and 2D effective medium is diag($\varepsilon_E, \varepsilon_O, \varepsilon_O$) and diag($\varepsilon_O, \varepsilon_O, \varepsilon_E$), respectively. The calculated values for the real parts of ε_O and ε_E as functions of the angular frequency are plotted in Figure 5.8 (a) for f = 0.16 and at a temperature of 300 K. It is assumed that the slight perturbation of temperature for the two metamaterials does not affect their dielectric functions. At frequencies below 2.46×10^{14} rad/s, the dielectric functions of orthogonal directions have opposite signs, implying that a hyperbolic dispersion is supported [68]. Therefore, both 1D and 2D metasurfaces are hyperbolic metamaterials (HMM) with a thickness of *h*. For *p*-polarized electromagnetic waves with high-*k*, evanescent waves in conventional elliptic materials become propagating. The evanescent waves in the vacuum are coupled with the propagating high-*k* modes inside the HMM, leading to broadband high local density of

states (LDOS) [61]. This is the basic mechanism for the efficient radiative transfer supported by 1D and 2D metasurfaces.

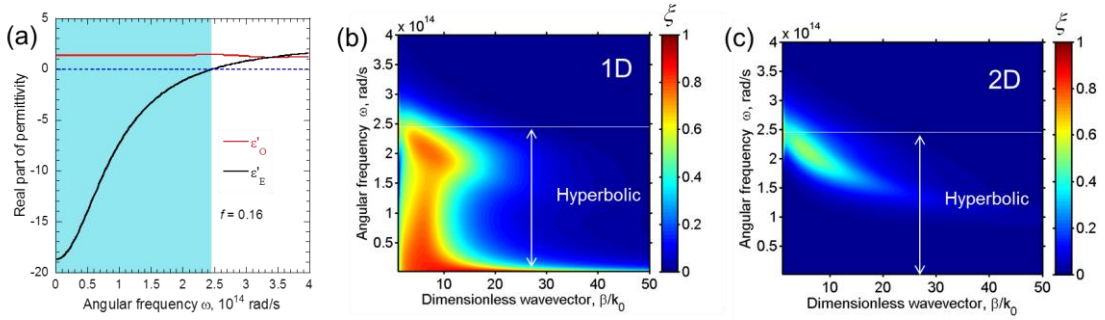

Figure 5.8 (a) Real part of the effective dielectric function for orthogonal directions for f = 0.16, the shaded region supports hyperbolic dispersion; (b) Photon tunneling probability at d = 100 nm when the period approaches to zero for 1D thin HMM; (c) 2D thin HMM.

To further confirm this scenario, the photon tunneling probability (defined in the section of METHODS) for homogenized effective medium of 1D and 2D metasurfaces is shown in Figs. 5.8 (b) and 5.8 (c), respectively. Only *p*-polarization is considered since waves of *s*-polarization support neither surface nor hyperbolic modes and thus have negligible contributions for mesoscopic gap distances. As seen from Figure 4b, large photon tunneling probabilities are supported mainly in the hyperbolic region, which has a major contribution to the radiative heat flux between 1D metasurfaces. Similar phenomenon can be found for 2D metasurfaces as shown in Figure 5.8 (c), but the photon tunneling probability at low frequencies is quite small. This is why 1D metasurface gives rise to a higher heat flux than the 2D counterparts as observed in Figs. 2 and 3. At higher frequencies, the imaginary part of $k_{z2D} = \sqrt{k_0^2 \varepsilon_O - \beta^2 \varepsilon_O / \varepsilon_E}$ becomes large due to the increase of k_0 and decrease of ε_E, then the field will decay so rapidly that

$\exp\left(2ik_{z2D}h\right)\to 0$. As a result, thin 2D HMM behaves as bulks as long as *h* is not too small.

On the contrary, the photon tunneling probability of 1D thin HMM remains high at low frequencies as shown in Figure 4b. The longitudinal wavevector inside 1D HMM is given as [55]

$$k_{z1D}=\sqrt{\varepsilon_O k_0^2-\beta^2\left[\cos^2\left(\varphi\right)+\frac{\varepsilon_O}{\varepsilon_E}\sin^2\left(\varphi\right)\right]} \tag{5.3}$$

where φ is the angle between the optical axis and the normal of plane of incidence, and should be integrated from 0 to $\pi/2$ to calculate the radiative heat flux [68]. For low frequencies and high-*k* modes, k_{z1D} becomes $i\beta$ for $\varphi=0$ and $\beta\sqrt{\varepsilon_O}/\sqrt{-\varepsilon_E}$ (the same as k_{z2D}) for $\varphi=\pi/2$. When $\varphi=\pi/2$, k_{z1D} is purely real if losses are not considered, and only purely hyperbolic modes, featured with slow decay, are present. When $\varphi=0$, k_{z1D} is purely imaginary and thus electromagnetic waves are not propagating but evanescent in 1D HMM, and pure surface modes featured with fast decay are excited due to the negative sign of ε_E. The above two scenarios can be confirmed from the surface resonance dispersion at the interface of vacuum and the effective anisotropic 1D grating, obtained from pole of the reflection coefficient as

$$\begin{aligned}&k_{zE}(k_{z0}+k_{zE})(\varepsilon_E k_{z0}k_{z1D}+k_{zE}^2)\sin^2\left(\varphi\right)\\&+\varepsilon_E k_0^2(k_{z0}+k_{z1D})(\varepsilon_E k_{z0}+k_{zE})\cos^2\left(\varphi\right)=0\end{aligned} \tag{5.4}$$

where $k_{zE}=\sqrt{\varepsilon_E k_0^2-\beta^2}$, $k_{z0}=\sqrt{k_0^2-\beta^2}$. It can be found that at $\varphi=\pi/2$, Eq. (5.4) cannot be satisfied, demonstrating the lack of surface modes. For $\varphi=0$, Eq. (5.4) becomes $k_{z0}+k_{zE}/\varepsilon_E=0$, which is exactly the same with the dispersion of surface

modes at the interface of the vacuum and a homogeneous metallic media characterized by ε_E, and the resonance frequency lies at $\varepsilon'_E = -1$. When φ lies between the two extremes, both hyperbolic and surface modes are supported in 1D HMM. In general, for any moderate value of φ, the imaginary part of k_{z1D} is larger than that of k_{z2D} due to the small magnitude of $\varepsilon_E^{-1/2}$, resulting in a more rapid decay. Therefore, the penetration depth for 1D thin HMM will be smaller, and a relative insensitivity of the heat flux of 1D thin HMM to the film thickness compared with 2D thin HMM is expected.

The thickness effects are shown in Figure 5.9 for different configurations. The radiative heat flux of 2D thin HMM increases monotonically with the thickness no matter when *P* is equal to 100 nm (exact Green's function method) or approaches zero (EMT limit). As discussed in Figure 5.8 (c), the low radiative flux of 2D thin HMM at small thicknesses is attributed to the poor photon tunneling at low frequencies. Thin films, on the other hand, tend to have an opposite rend. With decreasing thickness, the radiative heat flux for thin films monotonically increases due to the strengthened coupling of SPPs until the thickness is about 3 nm. For such small thicknesses, patterning thin films into 2D HMM will not lead to any increase but instead will reduce the heat flux by orders of magnitude compared even with the radiative heat flux of the films multiplied by *f*, the proximity approximation limit. As confirmed by both exact scattering theory and EMT, the radiative heat flux of 1D thin HMM has a weak dependence on the thickness due to the small penetration depth. It has a peak at *h* = 50 nm, which can be attributed to the coupling of surface modes, like thin films. The peak is small since only a part of the modes belongs to SPPs.

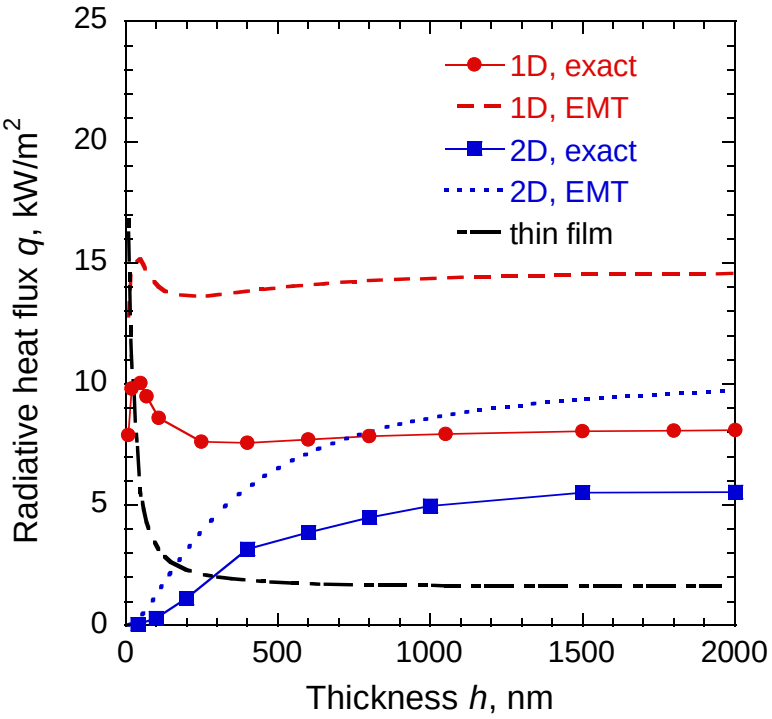

Figure 5.9 Near-field radiative heat flux as a function of the thickness for different configurations at d = 100 nm.

Optimal 1D and 2D HMMs with small periods provide higher radiative heat flux than thin films when h exceeds 15 nm and 170 nm, respectively, as indicated by the EMT curves. However, for smaller thicknesses, the radiative heat flux of thin films is the highest. The maximum q at d = 100 nm supported by thin films and 1D HMM is 24.4 kW/m^2 (h = 3 nm) and 24.0 kW/m^2 (f = 0.04, semi-infinite), respectively. Indeed, the photon tunneling probability approaches to the theoretical limit of unity when coupled SPPs are excited though ranging over a narrow k-space band [68]. One the other hand, the coupling of high-k waves with the hyperbolic modes is weak although in a broad k-space range. The photon tunneling probability will inevitably exponentially decay with tangential wavevectors since no resonances are excited to offset this decaying trend [131, 254]. Nevertheless, this balance is reversed for larger gap spacing. For example, at d =

1000 nm, the maximum q supported by thin films with varying thicknesses is 266 W/m^2 while that for 1D HMM and 2D HMM is 380 W/m^2 and 352 W/m^2, respectively.

5.3 Giant Enhancement of Nanoscale Thermal Radiation Based on Hyperbolic Graphene Plasmons

Despite that SPPs and hyperbolic material dispersions can lead to a high near-field radiative heat flux, both mechanisms have some limitations impeding a further increase of the heat flux. In Sec. 4.2, the hybridization of graphene plasmons and hyperbolic dispersion of doped silicon nanowires is proposed to overcome shortcomings of both modes. In this section, a totally different way is presented. The near-field radiative heat flux between graphene sheets is found to be further increased by more than one order of magnitude by patterning them into graphene ribbons. The mechanism is attributed to hyperbolic graphene plasmons that can boost the DOS in a board band to enhance the near-field energy transfer.

The near-field radiative transfer between two aligned graphene ribbon arrays separated by a vacuum gap of d is schematically shown in Figure 5.10 (a). The ribbon arrays are periodic in the x direction with a period P and width W, and extend to infinity in the y direction. One of the ribbon arrays is identified as the emitter that is at a relatively higher temperature and the other as the receiver. In the present study, the temperatures of the emitter and receiver are set around room temperature with T_1 = 310 K and T_2 = 290 K, respectively.

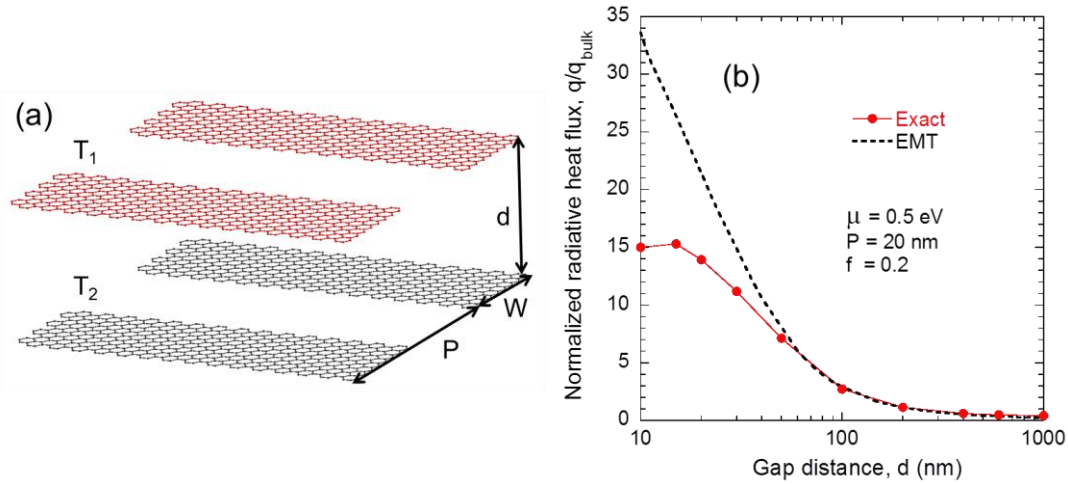

Figure 5.10 (a) Schematic of near-field radiative heat transfer between periodic graphene ribbon arrays. (b) Ratio of the near-field radiative heat flux between graphene ribbons (q) to that for graphene sheets (q_{sh}).

When the gap distance is much greater than the period of the graphene ribbons, to a certain extent, the calculation can be simplified based on the effective medium theory (EMT) [253]. Then, the graphene ribbon array can be homogenized into an anisotropic surface or 2D material, and its effective optical conductivity becomes a diagonal (2×2) tensor, diag(σ_x, σ_y), due to the different optical responses corresponding to the direction of the electric field. Based on the field average, σ_x and σ_y can be expressed as [255]

$$\sigma_x = \frac{\sigma\sigma_C}{f\sigma_C + (1-f)\sigma} \tag{5.5}$$

and

$$\sigma_y = f\sigma \tag{5.6}$$

where f is the filling ratio defined as W/P, and

$$\sigma_C = \frac{-i\omega\varepsilon_0 P}{\pi \ln\{\csc[0.5\pi(1-f)]\}} \tag{5.7}$$

is a static approximation considering the coupling of evanescent waves between adjacent unit cells. The calculation of near-field radiative heat flux between such anisotropic surfaces can be found in Refs. [68, 202].

The normalized near-field radiative heat flux between graphene ribbon arrays to that for graphene sheets is given in Figure 5.10 (b) for different gap distances at P = 20 nm, f = 0.2. Clearly, according to the exact formulations, the ratio of the heat flux with graphene ribbons to that with graphene sheets can reach 15.3 at d = 15 nm and is still more than 3 folds when d increases to 100 nm. Take d = 50 nm as an example, the near-field radiative heat flux between graphene sheets is already as high as 14.4 kW/m^2, about 120 times larger than the blackbody limit, due to the excitations of graphene plasmons along the graphene sheet. After pattering graphene into ribbons, the radiative heat flux further increases to be 122.8 kW/m^2, more than 1000 times higher than that for blackbodies. This giant enhancement may offer possible benefits to energy harvesting of thermal radiation by increased heating rate capability, potential thermal management enhancements, and augmented noncontact temperature measurement. When the gap distance is several times greater than the period, EMT predicts the real heat flux well, as has been quantitatively shown in Ref. [253]. Nevertheless, the enhancement induced by surface patterning becomes trivial and even adverse for large gap distances (the reason will be discussed later).

To explore the physical mechanism of the giant enhancement, consider the dispersion of SPPs at the interface between vacuum and the effective graphene ribbon arrays. Following the work of Patel and Grbic [256], the dispersion relation can be obtained from the pole of the reflection coefficient, and is given as

$$2\sigma_x\eta_0(k_x^2-k_0^2)+2\sigma_y\eta_0(k_y^2-k_0^2)+(\sigma_x\sigma_y\eta_0^2+4)k_0\sqrt{k_0^2-k_x^2-k_y^2}=0 \quad (5.8)$$

where η_0 is impedance of the vacuum. For graphene sheet, $\sigma_x = \sigma_y = \sigma$, Eq. (5.8) recovers to the familiar dispersion of graphene, given as [126]

$$\sqrt{k_0^2-\beta^2}=2k_0/\sigma\eta_0 \quad (5.9)$$

where $\beta=\sqrt{k_x^2+k_y^2}$ is the magnitude of the transverse wavevector. For a certain k_0 (or frequency ω), the allowed values of k_x and k_y define the DOS, which is limited to the circle with a radius as $\beta=2k_0/\sigma\eta_0$. At moderate *f*, $\sigma_x\sigma_y\eta_0^2$ is three orders of magnitude smaller than unity and thus can be neglected. When Im(σ_x) and Im(σ_y) have different signs, Eq. (5.8) becomes a hyperbolic equation without limitation on the allowed values of k_x and k_y, suggesting that the allowed DOS becomes infinite. Therefore, it is expected that the radiative heat flux will further increase when the graphene plasmons dispersion becomes hyperbolic. Note that the resonance-based hyperbolic surface modes obtained here are in stark difference from the hyperbolic modes supported by metamaterials like metallic nanowires [257], for which the denominator of the reflection coefficient is nonzero so that no resonances are excited.

The anisotropic optical conductivities for orthogonal directions are plotted in Figure 5.11 (a). Im(σ_y) remains positive in the whole frequency regime of interest, where the dominant contribution to the optical response of doped graphene comes from the scattering of free electrons. In the *x* direction, free electrons are confined in the ribbon, and Im(σ_x) is positive only for high frequencies and turns to be negative when the frequency is reduced to below the transition point of about 1.5×10^{14} rad/s. Figure 5.11 (b)

shows the spectral radiative heat flux for different configurations at d = 50 nm. Simple EMT can approximately predict the radiative heat flux across the whole frequency regime. It can be seen that it is the regime supporting hyperbolic graphene plasmons that a large enhancement of the radiative heat flux over graphene sheets exists. This low frequency regime up to the transition point contributes to more than 80% of the whole heat flux, confirming the vital role played by hyperbolic surface modes.

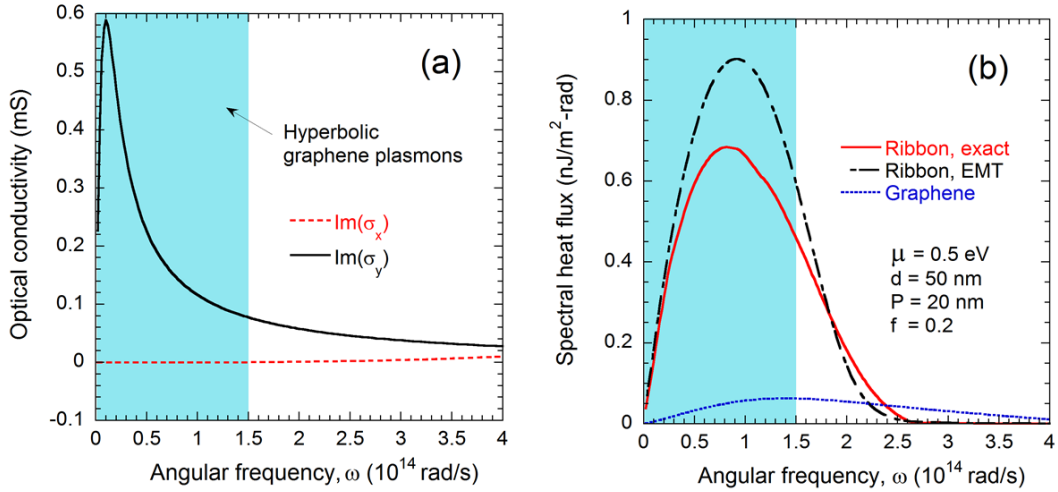

Figure 5.11 (a) Effective optical conductivity of graphene ribbons for different directions. Here, the unit of the surface conductivity is millisiemens. (b) Spectral radiative heat flux for different configurations.

To further confirm the above analysis, contours of the energy transmission coefficient at 5×10^{13} rad/s for graphene sheets and graphene ribbon arrays are plotted in Figs. 5.12 (a) and 5.12 (b), respectively. As shown in Figure 5.12 (a), large energy transmission coefficient exists only around two bright annuluses. The isofrequency curve of SPPs at the vacuum-graphene interface given by Eq. (5.9) is denoted as the white dashed circle with a radius of $\beta/k_0 = 4.6$. When two graphene sheets are in close

vicinity, this circle splits into two branches due to the coupling effects. The dispersion relations of the coupled graphene plasmons are given as [131]

$$1+\frac{\sigma k_{z0}}{\omega\varepsilon_0}=\coth\left(\frac{ik_{z0}d}{2}\right),\ \text{outer circle, symmetric branch} \tag{5.10}$$

$$1+\frac{\sigma k_{z0}}{\omega\varepsilon_0}=\tanh\left(\frac{ik_{z0}d}{2}\right),\ \text{inner circle, antisymmetric branch} \tag{5.11}$$

According to equations (5.10) and (5.11), the radius of the split two circles at the specified frequency becomes β/k_0 = 24.7 and 2.5, respectively. They are in good agreement with the two bright rings in Figure 5.12 (a).

As shown in Figure 5.12 (b), the regime featured with energy transmission coefficients for graphene ribbon arrays is no longer circles but hyperbolic lines. For high-*k* waves with $k_x >> k_0$ and $k_y >> k_0$, the dispersion relation of effective graphene ribbon arrays presented in Eq. (5.8) can be approximated by its asymptote, given as [255]

$$k_y=\pm k_x\sqrt{\frac{-\sigma_x}{\sigma_y}}\pm k_0\sqrt{1-\frac{4}{\sigma_y^2\eta_0^2}} \tag{5.12}$$

Equation (5.12) is represented by the white dashed curve on Figure 5.12 (b) at $\omega = 5\times10^{13}$ rad/s. It can be seen that they qualitatively agrees with the contour plot, confirming the transition from circular to hyperbolic relationship by pattering graphene into ribbons. Note that mode couplings lead to two split branches in the energy transmission coefficient contour in each quadrant as can be seen from Figure 3b. Since the hyperbolic curve is open, ideally, there is no limit on the DOS. Practically, the hyperbolic relationship will not hold when β goes to infinity [253]. Nevertheless, Figure 5.12 (b) clearly shows that hyperbolic graphene plasmons can couple with extremely high-*k*

waves with β/k_0 exceeding 300. On the other hand, the maximum β value for near-field coupling with graphene sheets is only about 30. That is why graphene ribbon arrays support a much higher near-field radiative heat flux than counterpart graphene sheets. In terms of near-field enhancement, there is a drawback of hyperbolic graphene plasmons, that is, the coupling with low-*k* waves is rather weak. As shown in Figure 5.12 (b), the energy transmission coefficient is low when β is smaller than $k_0\sqrt{1-4/(\sigma_y\eta_0)^2}$, the intercept of Eq. (5.12) with the coordinate axis. When the gap distance increases, the value of cutoff β decreases, and low-*k* waves will play a more important role in radiative transfer [253]. Therefore, pattering graphene will actually reduce the heat flux at large gap distances, as already shown in Figure 5.10 (b).

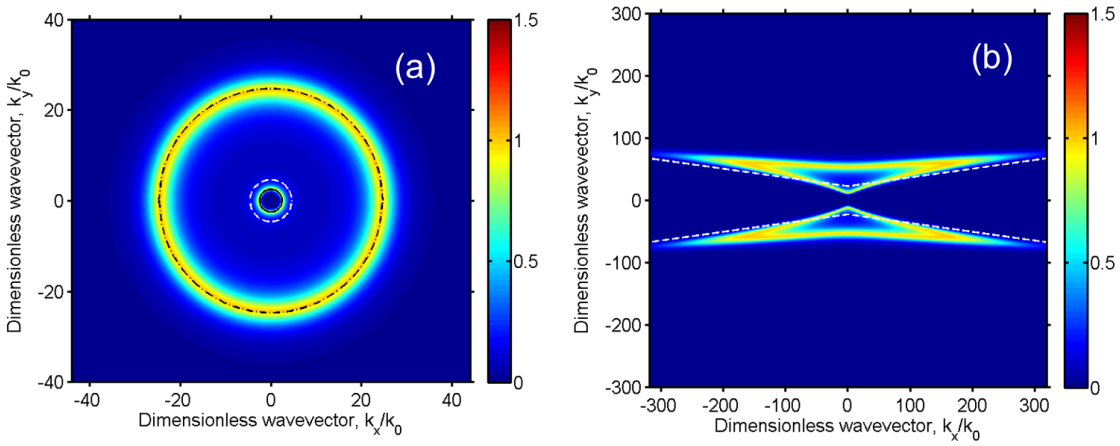

Figure 5.12 Energy transmission coefficient contours at $\omega = 5\times10^{13}$ rad/s for (a) graphene sheets and (b) graphene ribbon arrays.

One may further question whether the giant enhancement holds for different filling ratios and periods. As can be seen from Figure 5.13 (a), the enhancement holds for almost all practical filling ratios. Certainly, when *f* is infinitely small, the radiative heat

flux will diminish, and when f approaches unity, the radiative heat flux between ribbon arrays recovers to that for graphene sheets. Therefore, an optimal f featured with the maximum radiative heat flux is expected to exist. The optimal f is around 0.04 and 0.20 when d is equal to 20 nm and 50 nm, respectively. The sign of Im(σ_y) remains positive and does not change with f since Im(σ_y) is linearly proportional to Im(σ). σ_C is much smaller than σ, so that different values of $f/(1-f)$ at moderate f hardly change the sign of Im(σ_y). Therefore, hyperbolic graphene plasmons and large enhancement of the radiative heat flux will be supported for a broad range of f. Greater enhancement occurs at d = 20 nm than at 50 nm. The underlying reason is attributed to the weak coupling of hyperbolic SPPs with low-k waves, as previously discussed. As shown in Figure 5.13 (b), the maximum q/q_{sh} is 8.5 as denoted by the black square. This occurs when P approaches zero, which is the limit when EMT becomes accurate. With increasing period, the enhancement over graphene sheets deteriorates. This is because when the period becomes comparable to or larger than the gap spacing, EMT fails and the hyperbolic dispersion of graphene ribbon plasmons does not support a large heat flux. When the period is sufficiently large, the radiative heat flux between graphene ribbon arrays is expected to be the value obtained by multiplying the filling ratio with that for graphene sheets. Generally speaking, the period should be smaller than the gap distance in order to achieve significant heat flux enhancement.

In practical applications, the ribbon arrays will be deposited on certain substrates. If the substrate is a dielectric material with close to unity dielectric function, like porous polymers, the excitation of hyperbolic graphene plasmons and all the results presented will not be affected. However, if the substrate supports SPPs or SPhPs (i.e., surface

phonon polaritons), like polar SiC and SiO_2, the hybridization of the hyperbolic graphene plasmons with surface plasmon or phonon modes may be expected [84]. The substrate effect as well as for two graphene ribbon arrays that are not aligned may be further investigated. Note that the local dielectric function of graphene is assumed to be applicable to graphene ribbons. Quantum size effects and edge shapes may affect the optical response of graphene ribbons. Nevertheless, according to first principle calculations [258], if the ribbon width is larger than several nanometers, the local dielectric function still holds. As can be seen from Figure 5.13, large enhancements can be achieved for ribbon width ranging from several nanometers to a few hundred of nanometers.

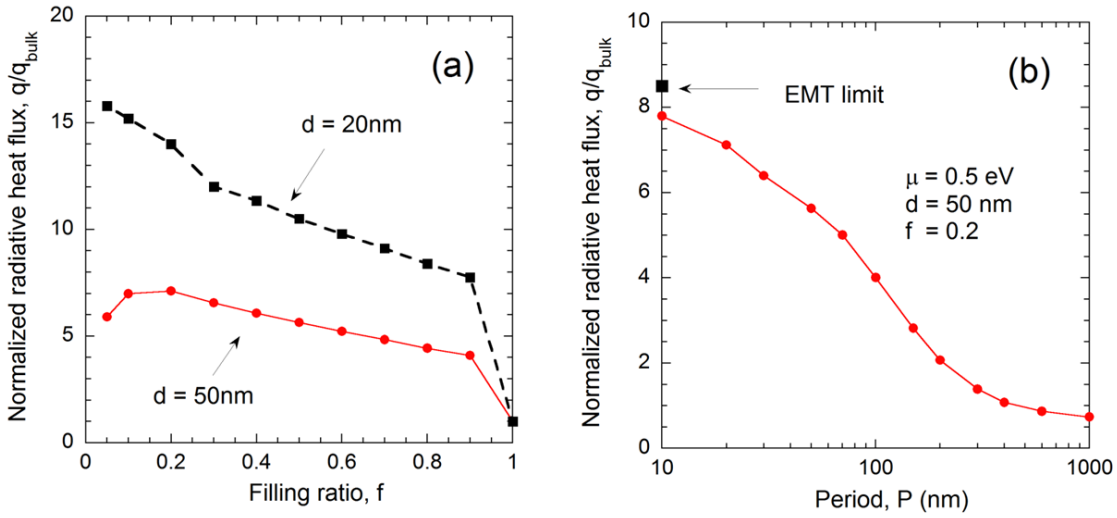

Figure 5.13 The radiative heat flux ratio for different values of (a) filling ratio *f* and (b) period *P*, while other parameters are fixed. The square mark in (b) is calculated from EMT.

5.4 Enhanced Electroluminescent Refrigeration Enabled by Near-Field Photon Tunneling

When applying a forward bias to a *p*-*n* diode, electrons and holes will be driven into the junction area with at least some of them recombining radiatively. If the energy carried by these output photons is higher than the input electric power, a cooling process called electroluminescence refrigeration occurs through pumping heat from the lattice [259, 260]. This solid-state refrigeration technique has several unique advantages over conventional thermoelectric refrigerators, such as higher efficiencies even close to the Carnot limit, easier integration with other optoelectronic devices, and broader operation temperature. A recent direct experimental observation of the refrigeration effect, although with a small refrigeration rate, retriggered people's interest [261]. In the past several decades, there have been some models proposed to simulate and predict the potential of biased semiconductors in refrigeration [262-269]. Berdahal [263] discussed the refrigeration effect from a biased junction to an external object of different temperatures considering only radiative recombination and assuming the extraction efficiency to be unit. Later, several groups studied the cooling effect induced by biasing semiconductor junctions considering various nonradiative recombination [262, 264-269]. Oksanen and Tulkki [270] investigated the refrigeration power density between two diodes under thermally non-equilibrium. However, most previous works only consider propagating waves. This is appropriate only when the biased junction and the ambient are far enough, for which the extra energy transfer channel via evanescent waves is lost. Besides, few of them consider the contributions of low-frequency phonon modes or intraband transitions,

which inexorably always lead to a flux flowing from the hot side to the cold side and thus offset the refrigeration effect.

As has been discussed before, recent experimental and theoretical work have demonstrated that when the gap distance between two objects of different temperatures is smaller than the characteristic wavelength, the radiative energy exchange rate can be orders of magnitude larger than the blackbody limit due to the photon tunneling of evanescent waves [3, 12, 13, 79, 88, 196, 222, 271-278]. Similarly, when the biased low-temperature junction is in a close proximity with a substrate of ambient temperature, evanescent waves may tunnel through and play an important role in mediating both the efficiency and refrigerate rate of the biased junction [279]. Chen et al. [279] investigated the heat transfer from a forward-biased junction to a higher temperature object considering contributions of evanescent waves and phonon modes, and found that refrigeration effects against a temperature difference of 10 K exist only when the gap separation ranges from tens to hundreds of nanometers, but did not consider the Planck radiation of regimes outside the active layer. Here, based on a more practical design and delicate choices of materials, the refrigeration rate is improved by more than one order of magnitude and predicted to exist from near- to far-field for certain range of temperature differences.

The considered configuration is schematically shown in Figure 5.14. The bottom object (emitter) is a standard GaSb *p-i-n* junction sandwiched by a top Ag strip and bottom Ag substrate acting as the anode and cathode, respectively. The top object (receiver) is a Ge film with a thickness of h_{Ge} on the Ag substrate. Unless specified, the thickness of p-typed doped GaSb h_p = 0.1 μm, n-type doped GaSb h_n = 0.1 μm, intrinsic

GaSb h_i = 1 μm, and h_{Ge} = 500 μm. The bottom and top objects separated by a gap distance of *d* hold a low temperature of T_1 and high temperature T_2 = 300 K, respectively.

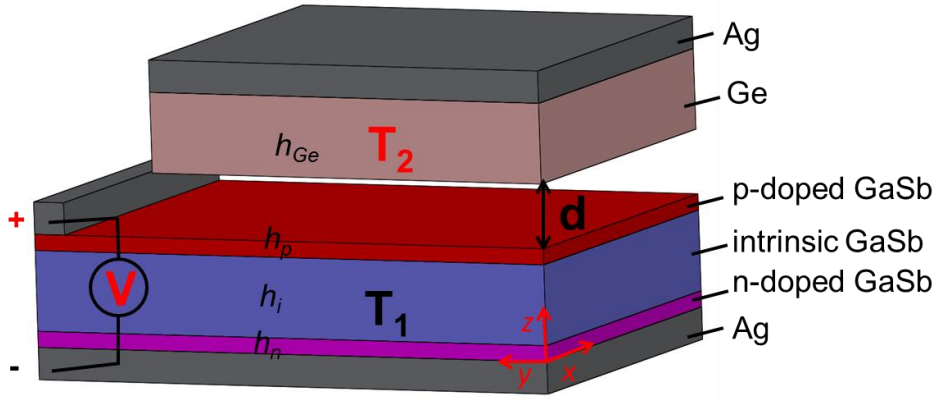

Figure 5.14 Schematic of a forward-biased *p-i-n* GaSb diode separated with a Ag substrate with Ge deposited on top with a gap distance of *d*.

The optical constants of Ge is tabulated in Ref. [110]. The dielectric function of Ag is obtained using a simple Drude model: $\varepsilon_{Ag} = 1 - \omega_p^2 / (\omega^2 + i\gamma\omega)$ with a scattering rate $\gamma = 2.73\times10^{13}$ rad/s and plasma frequency $\omega_p = 1.37\times10^{16}$ rad/s [3]. The dielectric function of GaSb for ultraviolet and visible wavelengths is from Ref. [110]. For near-infrared regime, the optical constants are obtained from Ferrini et al. [280]. The refractive index and extinction coefficient for mid-infrared regime come from Ref. [110] and Ref. [281], respectively. For long wavelengths beyond 30 μm, a Lorentz model is used to predict the dielectric function $\varepsilon = \varepsilon_\infty(\omega^2 - \omega_L^2 + j\gamma\omega)/(\omega^2 - \omega_T^2 + j\gamma\omega)$ [282], where ε_∞ = 14.63, γ =3.35×10^{11} rad/s, ω_T = 0.0286 eV, and ω_L = 0.0298 eV. For p- and n-doped GaSb, an extra Drude term $-\dfrac{15.1\omega_p^2}{\omega^2 + j\gamma_D\omega}$ is added to consider the contributions from free

electrons induced by doping, where the plasma frequency ω_p and scattering rate γ_D, corresponding to a Zn-doped p-type GaSb at the doping level of 1.3×10^{17} cm^{-3}, are 138 cm^{-1} and 114 cm^{-1}, respectively [283]. n-type GaSb may have different values of plasma frequency and scattering rate since the effective mass of holes and electrons may be different or the two doping levels are different. However, in order to make later analyses easier, we assume the n-type and p-type GaSb have the same dielectric function.

When externally applying a voltage through the electrodes on the emitter, let's assume the voltage *V* only appears across the active intrinsic GaSb layer. Inside the active regime, photons above the bandgap achieve equilibrium with the biased conduction and valence band through radiative generation and recombination. As a result, the photons emitted have a nonzero chemical potential of *qE*, where *q* is the elementary charge [284]. Photons outside the active regime or below the energy bandgap neither interact with the biased electron-hole system nor have enough energy to excite the interband transitions. Therefore, they are in equilibrium with the lattice instead, leading to a conventional Planck distribution with a vanishing chemical potential. Subsequently, the mean energy of Planck's oscillator depends on the position and frequency and can be given as

$$\Theta\left(\omega,z,T,E\right)=\begin{cases}\dfrac{\hbar\omega}{e^{(\hbar\omega-qV)/k_BT}-1}, \omega>\omega_g \text{ and } h_n<z<h_n+h_i \\ \dfrac{\hbar\omega}{e^{(\hbar\omega-qV)/k_BT}-1}, \text{otherwise}\end{cases} \tag{5.13}$$

where the angular frequency ω_g = 1.103×10^{15} rad/s corresponds to the bandgap energy of GaSb which is 0.726 eV.

Since there is a nonuniform distribution of the chemical potential of photons due to the nonequilibrium set by the applied voltage, Kirchhoff's law cannot be directly

applied to characterize the far-field radiative properties of a biased junction, nor is the scattering theory directly applicable to the near-field radiative properties. Here the dyadic Green function method combined with the fluctuation-dissipation theory is used to calculate the radiative heat transfer considering radiation with zero and nonzero chemical potentials. Random currents caused by thermal motion of the charge carriers are attributed to the emitted electromagnetic waves. The correlation of these random currents is given by the fluctuation-dissipation theory as [12, 285]

$$\left\langle J_i(\mathbf{r},\omega) J_k^*(\mathbf{r}',\omega') \right\rangle = \frac{4\omega\varepsilon_0 \Theta(\omega, z, T, E)\varepsilon_{ik}''(\mathbf{r},\omega)}{\pi} \delta(\mathbf{r}-\mathbf{r}')\delta(\omega-\omega') \tag{5.14}$$

where subscripts *i* or *k* refer to the vector component, ε_0 is the vacuum permittivity, ε_{ik}'' is the imaginary part of the dielectric tensor component, and $\delta(\mathbf{r}-\mathbf{r}')$ or $\delta(\omega-\omega')$ is the Dirac delta function indicating spatial or temporal incoherence, respectively. For isotropic media, $\varepsilon_{ik}'' = \varepsilon''\delta_{ik}$ where ε'' is the imaginary part of the dielectric function and δ_{ik} is the Kronecker delta [3, 12]. Note that Eq. (5.14) is applicable to consider both low and frequency photons inside and outside the active regime, provided $\Theta(\omega, z, T, E)$ is modified accordingly.

The electric field and magnetic field at any position *r* are related to the source current at *r′* by the corresponding electric and magnetic dyadic Green's function $\bar{\bar{G}}^E(r, r', \omega)$ and $\bar{\bar{G}}^H(r, r', \omega)$ [3]

$$\begin{aligned} \mathbf{E}(r,\omega) &= i\omega\mu_0 \int_{V'} \bar{\bar{G}}^E(r, r', \omega)\cdot\mathbf{J}(r',\omega)dr' \\ \mathbf{H}(r,\omega) &= \int_{V'} \bar{\bar{G}}^H(r, r', \omega)\cdot\mathbf{J}(r',\omega)dr' \end{aligned} \tag{5.15}$$

The radiative heat flux from the biased emitter to the receiver $Q_{1\to 2}$ can be obtained as

$$
\begin{aligned}
Q_{1\to 2} &= \int_0^\infty \frac{1}{2}\left\langle \mathrm{Re}[\mathbf{E}(\mathbf{r},\omega)\times\mathbf{H}^*(\mathbf{r},\omega)]\right\rangle d\omega \\
&= \frac{2k_0^2}{\pi}\int_0^\infty \Theta(\omega,z,T_1,E) \\
&\times \int_{-\infty}^{h_n+h_i+h_p} \mathrm{Re}\left[j\sum_{i=x,y,z} \varepsilon_{ii}''(\omega,z)(G_{xi}^E G_{yi}^{H*} - G_{yi}^E G_{xi}^{H*})\right] dz d\omega
\end{aligned}
\tag{5.16}
$$

The radiative energy flux from the receiver to the emitter $Q_{2\to 1}$ can be obtained similarly, and the net energy exchange flux is $Q_{12} = Q_{1\to 2} - Q_{2\to 1}$. $\bar{\bar{G}}^E(r,r',\omega)$ and $\bar{\bar{G}}^H(r,r',\omega)$ for this multilayer setup are obtained analytically by transfer matrix method [190, 286, 287].

Besides the energy exchange to the receiver, there is an extra electric power input to the emitter, which can be expressed as VJ_t. Assuming there is no current leakage caused by recombinations outside the active layer, $J_t = J_r + J_{nr}$, where J_r and J_{nr} consider the contributions from radiative and nonradiative recombination, respectively. Employing the reciprocity principle of Green's function, J_r can be simply expressed as

$$
\begin{aligned}
J_r &= \frac{2k_0^2 q}{\pi}\int_{\omega_g}^\infty \left[\frac{1}{e^{(\hbar\omega - qE)/k_B T_1} - 1} - \frac{1}{e^{\hbar\omega/k_B T_2} - 1}\right] \\
&\times \int_{h_n}^{h_n+h_i} \mathrm{Re}\left[j\sum_{i=x,y,z} \varepsilon_{ii}''(\omega,z)(G_{xi}^E G_{yi}^{H*} - G_{yi}^E G_{xi}^{H*})\right] dz d\omega
\end{aligned}
\tag{5.17}
$$

Assuming GaSb has a high quality and only Auger effect contributes to the nonradiative recombination. Therefore, J_{nr} can be expressed as

$$
J_{nr} = qh_i(C_n n + C_p p)(np - n_i^2) \tag{5.18}
$$

The Auger coefficient $C_0 = C_n n + C_p p$ is taken as 5×10^{-30} $cm^6 s^{-1}$ and the intrinsic carrier density $n_i = 1.5\times10^{12}$ cm^{-3} [288]. Then the net power output from the emitter is

$$Q_{\text{net}} = Q_{12} - EJ_{\text{t}} \tag{5.19}$$

The refraction index and extinction coefficient of intrinsic and doped GaSb as well as Ge are shown in Figure 5.15. It can be seen that the Drude term modifies the optical response of GaSb only for low frequency regime below 3×10^{14} rad/s, as expected. Below ω_{g}, the net spectral energy exchange between the emitter and receiver is negative since $T_1 < T_2$, and thus the conventional Planck's oscillator $\Theta(\omega, z, T_1, E)$ is smaller than $\Theta(\omega, z, T_2, E)$. However for high frequencies above the bandgap energy, the heat can flow in an opposite direction from the cold emitter to the hot receiver when $\Theta(\omega, z, T_1, E)$ is larger than $\Theta(\omega, z, T_2, E)$, i.e., $E > \frac{\hbar\omega}{q}(1-\frac{T_1}{T_2})$. Figure 5.16 (a) shows the net power output from the emitter Q_{net} as a function of the applied voltage E for d = 10 μm and T_1 = 290 K, which lies in the far-field and further increasing d will hardly affect Q_{net} as will be shown later. As expected, in order to get refrigeration effects (positive Q_{net}), the applied E should be large enough so that the positive spectral energy exchange above the bandgap can at least compete with the low frequency negative values. If E is very large but still far below the lasing threshold $\hbar\omega_g/q$, it can be found that EJ_{t} scales with $Ee^{3qE/2k_BT_1}$ while Q_{net} scales with e^{qE/k_BT_1}, leading to a negative Q_{net} at a large E, as can be seen from Figure 3a. The maximum far-field refrigeration rate against a temperature difference of 10 K is 7.86 W/m^2 occurring at E = 0.50 V.

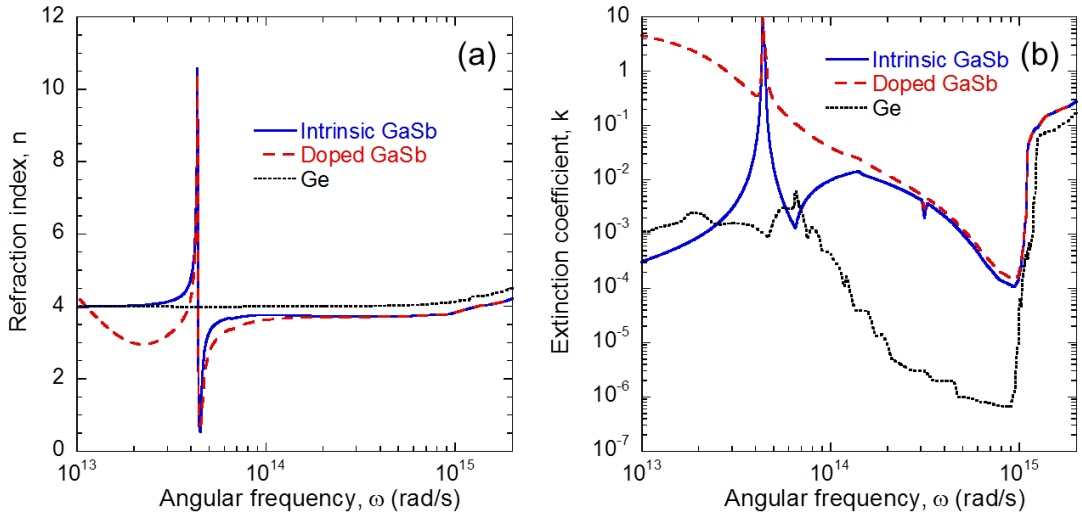

Figure 5.15 Optical response of intrinsic GaSb, doped GaSb, and Ge. (a) Refraction index. (b) Extinction coefficient.

Pushing the two objects into the close proximity with d = 100 nm, as shown in Figure 5.16 (b), Q_{net} versus E has a similar trend but the maximum refrigeration rate is enhanced by more than two orders of magnitude to 1548 W/m^2. This is because for large gap separations, only propagating waves contribute to the energy exchange and refrigeration effect while for small d, evanescent waves start to tunnel through and play a dominant role especially for nanometer gap distance. Similar photon tunneling effects have been demonstrated to lead to highly efficient nanoscale thermal radiation beyond Planck's law [66-68, 95, 131, 235]. Compared with the previous work by Chen et al. [279], the maximum refrigeration rate is improved by more than one order of magnitude and the refrigeration effect against a temperature difference of 10 K is extended to the far-field. The main mechanism for this improvement lies in the good match of optical response of GaSb and Ge above the bandgap while a mismatch of phonon or plasmon modes below the bandgap, as can be clearly seen from Figure 5.15 (b).

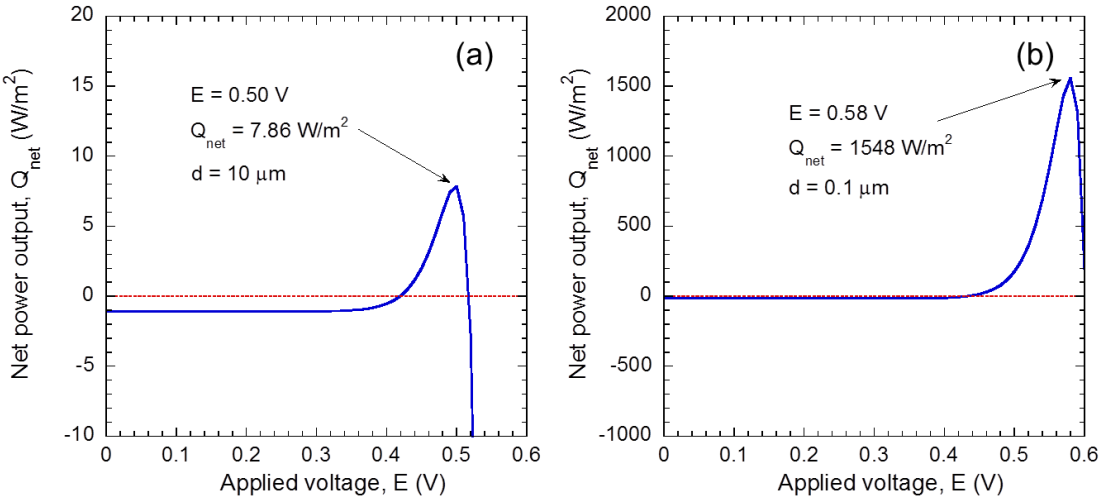

Figure 5.16 The net power output from the biased diode as a function of applied voltage for (a) d = 10 μm and (b) d = 0.1 μm.

Figure 5.17 (a) gives the maximum refrigeration rate as a function of the gap distance, obtained by optimizing the applied voltage E for each d. The maximum refrigeration rate stays positive for all the gap distances, demonstrating the refrigeration capability of the proposed design ranging from near-field to far-field. When d is larger than 5 μm, Q_{net} approaches a constant and will be independent of the gap distance. This regime is called far-field since both interference and photon tunneling effects are negligible. With decreasing d, a wavy feature shows up due to the interference effects, which appear when d is in the same magnitude of the interested wavelength (1.7 μm corresponding to the bandgap). Further decreasing d, a dip occurs at 0.7 μm. In order to explore the underying mechanism, Figure 5.17 (b) presents the spectral radiative energy exchange between the emitter and the receiver at E = 0.5 V for different gap distances. Compared with d = 10 μm, it can be found that the spectral energy exchange at d = 0.7 μm for high frequencies above the bandgap stays almost the same but is enhanced greatly for low frequencies. It is not surprising since the gap distance of 0.7 μm although much

smaller than the wavelength (around 10 μm) where phonon or plasmon modes play a dominant role is still comparable to the bandgap wavelength, meaning that 0.7 μm lies in the near-field regime for phonon or plasmon modes but still in the far-field regime to some extent for high frequencies. As a result, the negative energy exchange below the bandgap is enhanced while the positive one above the bandgap does not change much, leading to the shrinking refrigeration rate. Reducing *d* down to 0.1 μm, the negative low frequency energy exchange is further enhanced but the positive high frequency energy exchange is improved more prominently, leading to the increased refrigeration rate, as shown in Figure 5.17 (a).

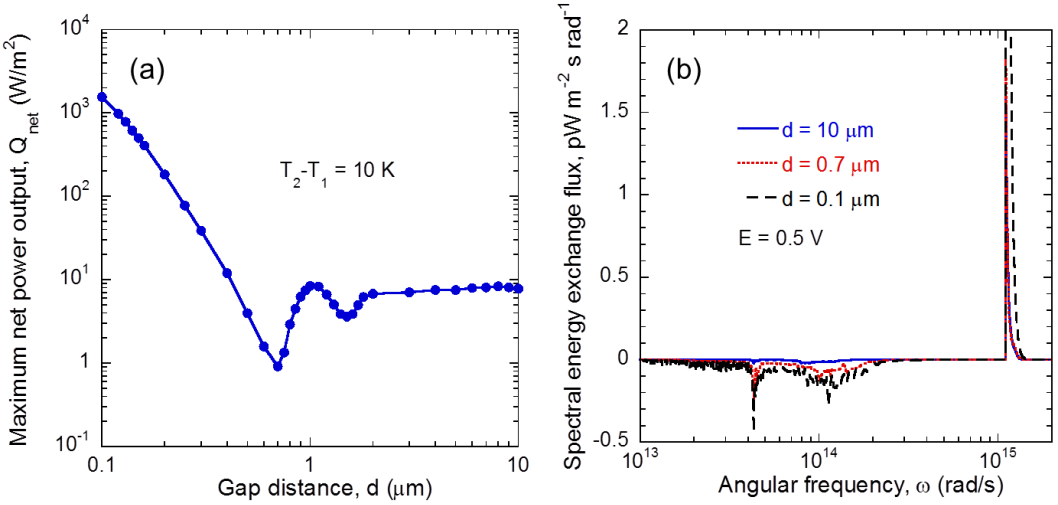

Figure 5.17 (a) The maximum net power output from the biased diode versus the gap distance. (b) The spectral radiative energy exchange between the diode and the top Ge-Ag object at different gap distances with E = 0.5 V.

The previous analysis is only for the temperature difference of 10 K, so, one may wonder what the maximum achievable temperature difference can be achieved through this electroluminescence refrigeration technique (assuming T_2 is a constant of 300 K). The maximum net power output from the emitter versus the temperature difference at d =

10 μm and 0.1 μm is given in Figure 5.18 (a) and 5.18 (b), respectively. With increasing temperature difference or the decrease of T_1, the difference between $1/(e^{(\hbar\omega - qE)/k_B T_1} - 1)$ and $1/(e^{\hbar\omega/k_B T_2} - 1)$ at a certain E shrinks so that the positive energy exchange at high frequencies decreases while the negative energy exchange at low frequencies is enhanced, leading to low refrigeration rate. When the net energy exchange is not large enough to compensate the input electric power, the net power output becomes negative and there will be no refrigeration but heating. The maximum temperature difference occurs when the net power output is zero. For d = 10 μm, the maximum temperature difference is 16.6 K, beyond which the heat starts to flow in rather than being extracted out. Pushing the emitter and receiver into the near-field with a gap distance of 100 nm, the maximum temperature difference achievable is increased to be 25.2 K. The much higher refrigeration rate at 0.1 μm means that the positive high frequency energy exchange flux is much larger than its negative counterpart. Therefore, there is no wondering why the maximum temperature difference rises so that the negative energy exchange can be enhanced greatly enough to compete with the high positive flux. It is also worth to note that for a temperature difference different from 10 K, the refrigeration effect may not show up for all gap distances. For example, for T_1 = 280 K, the net refrigeration rate is negative in the far-field, and becomes positive only when the gap distance is smaller than 0.176 μm. So, near-field radiation can also make the otherwise heating effect into refrigeration.

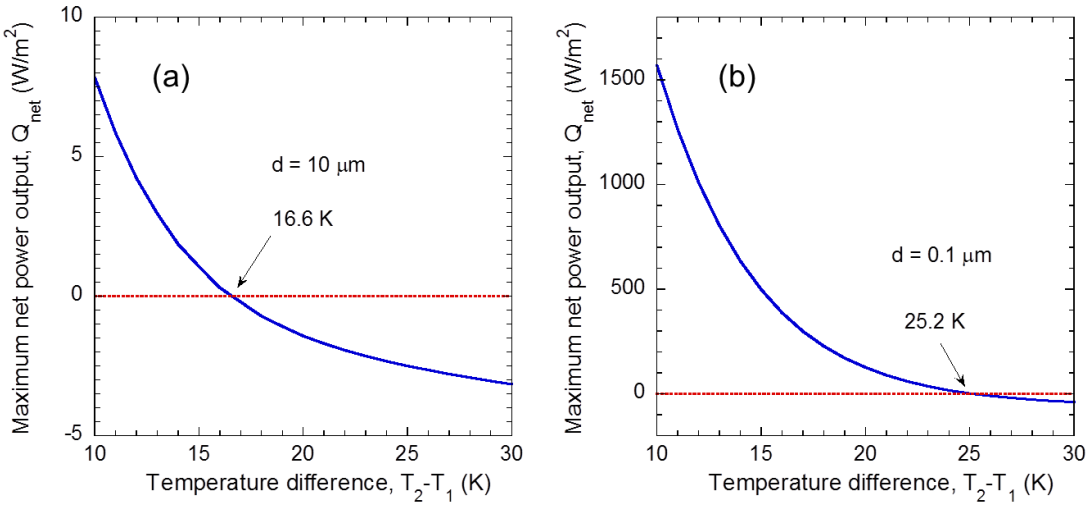

Figure 5.18 The maximum net power output from the biased diode as a function of the temperature difference for (a) d = 10 μm and (b) d = 0.1 μm.

5.5 Summary

This chapter studies the near-field thermal radiation between various nanostructures based on exact approaches. The major finds are summarized in the followings.

The exact calculation of the near-field radiative heat transfer between graphene-covered silica gratings demonstrates that the heat flux between corrugated silica can be enhanced by more than one order of magnitude when covered with a graphene sheet on top of the grating on each side of the vacuum gap. It is found that depositing graphene makes the local radiative heat transport between silica gratings nonlocal, and the performance sensitivity to lateral shift can also be greatly relieved. Similar observations can be expected for other polar materials supporting narrow band SPhP, such as SiC and MgO. The proposed design can be used to achieve highly efficient heat dissipation, increase the power output of thermophotovoltaic cells, and improve the contrast of non-contact thermal modulation.

The near-field radiative heat transfer of 1D and 2D metasurfaces is investigated based on the exact methods and EMT approximation. The photon tunneling probability between thin films is high only when resonances are excited over narrow *k*-space regime. Patterning thin films of moderate thicknesses into 1D and 2D metasurfaces can increase the heat flux. The underlying mechanism is due to the excitation of hyperbolic modes featured with high LDOS in a broad frequency and *k*-space regime. The radiative heat flux for thin 2D HMM increases monotonically with the thickness while the heat flux for thin 1D HMM is not as sensitive to the thickness and is higher than that of 2D HMM due to the relatively rapid decay of high-*k* modes supported by surface waves.

A giant enhancement of near-field radiative heat flux over more than one order of magnitude is predicted at nanoscale distances based on exact formulations by patterning graphene sheets into ribbon arrays. The underlying mechanism is that the originally closed circular isofrequency dispersion of graphene plasmons is opened to be hyperbolic, leading to broadband singularities of DOS. The hyperbolic graphene plasmons can couple strongly with extremely high-*k* modes but weakly with low-*k* waves, enabling very efficient radiative energy transport mainly at small gap distances. The fundamental understanding of near-field thermal radiation between graphene ribbon arrays is deepened, and a new route for further enhancing the radiative heat flux is presented.

The electroluminescent refrigeration of a proposed practical design is investigated by employing the fluctuation-dissipation theory and the dyadic Green's function method. Pushing the cold forward biased diode and a hot object into the near-field regime with a gap distance of 100 nm, the refrigeration power rate is enhanced by more than two orders of magnitude. The operation range of the temperature difference is also broadened from

16.6 K to 25.2 K. Moreover, the unachievable refrigeration effect in the far-field may be possible by reducing the gap distance down to the near-field.

CHAPTER 6

MANIPULATION OF CASIMIR FORCE BY METAMATERIALS

In previous two chapters, we tried to enhance the near-field thermal radiation by metamaterials for application in energy harvesting and thermal management. The Casimir interaction, arising from momentum exchange between fluctuating electromagnetic waves, always accompanies near-field heat transfer [22, 23, 93]. Subsequently, in practical applications of microelectromechanical systems (MEMS) and nanoelectromechanical systems (NMES) for thermal management, the Casimir stiction between working parts has to be considered even in the vacuum. Indeed, the Casimir force can be as large as 130 kPa at a gap spacing of 10 nm, and thus could cause a failure of mesoscopic systems and devices [8]. Section 6.1 demonstrates enhanced near-field energy transport and suppressed momentum exchange simultaneously. In Sec. 6.2, a design of achieving tunable levitation based on repulsive Casimir force is proposed, followed by a brief summary in Sec. 6.3.

6.1. Enhanced Near-Field Thermal Radiation and Reduced Casimir Stiction Between Doped-Si Gratings

A high near-field radiative heat flux is usually desired due to wide applications in energy harvesting and thermal management. However, the momentum exchange (small Casimir stiction) is often preferred in the practical applications of MEMS devices. So, the question is: can we realize them simultaneously although they seem to be controversy? The schematic of considered nanostructure is shown in Figure 6.1, where P is the period, W is the grating

width, and H is the grating thickness. Note that δ is the lateral displacement between the two gratings with identical geometry. In all the calculations, temperatures of the emitter and receiver are set to T_1 = 310 K and T_2 = 290 K, respectively. The following geometric parameters are chosen as the default values unless otherwise specified: P = 200 nm, d = 400 nm, f = 0.2, H = 1 μm, and δ = 0 (aligned case).

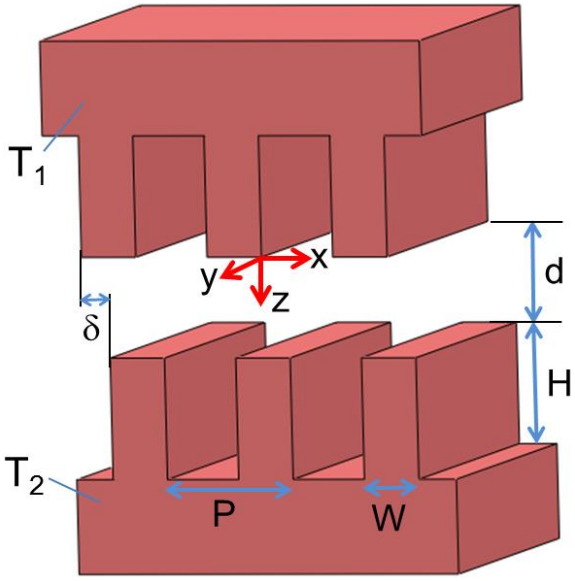

Figure 6.1 Schematic of near-field energy transfer and momentum exchange between two one-dimensional doped-silicon gratings with a lateral displacement of δ.

The radiative heat flux between two gratings as a function of the filling ratio is plotted in Figure 6.2 (a), while other geometric parameters are set as the default values. When f = 1, both results reduce to the case for two planar substrates (bulk doped silicon) for which the near-field heat flux is 294 W/m^2. The radiative heat flux predicted by PA decreases linearly as f is reduced, which is in opposite to the trend calculated by the scattering theory (exact). When f = 0.05, the heat flux achieves a maximum value of 1154

W/m^2, which is 20.7 times as large as what is predicted by PA, breaking down the assumption of localized radiative transport. Further decreasing f will result in a reduction of the heat flux. Of course, $f = 0$ implies the situation between two planar media with a gap distance $d + 2H$ and both the exact solution and PA method give the same result. However, even though the filling ratio is as small as 0.01, the heat flux is enhanced to over 1000 W/m^2 as predicted by the scattering theory. The radiative heat transfer for doped-silicon gratings is very efficient with higher heat flux at any practical filling ratio than that for bulk doped silicon. This is in contrast to aligned gratings made of polar materials, such as silica, which have been demonstrated to support localized heat transport due to the short lateral propagation length of surface phonon modes [83]. For this reason, PA works well for aligned silica gratings and, as such, silica nanostructures can barely outperform bulk materials in terms of near-field radiative heat transfer [83, 84]. For doped-silicon gratings, reducing the filling ratio can result in an enhancement of more than two orders of magnitude over that predicted by the geometry-based PA.

As shown in Figure 6.2 (b), the near-field heat flux increases with the grating depth according to the exact solution, while PA predicts an opposite trend. When H is close to zero, the calculated radiative heat flux based on the exact solution recovers the value of 294 W/m^2, *i.e.*, between two planar substrates. The heat flux between gratings increases slowly and tends to saturate when the grating thickness exceeds 10 μm, suggesting that the radiation penetration depth of the grating film is on the order of several micrometers. When H is further increased, the substrates beyond the grating region contribute little to near-field radiative transfer.

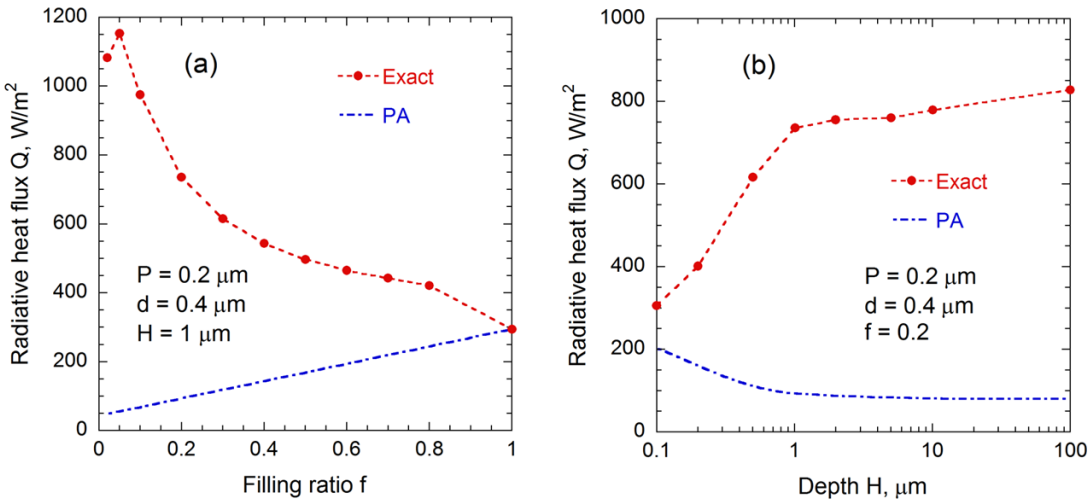

Figure 6.2 Radiative heat flux as a function of (a) filling ratio $f = W / P$ and (b) grating height *H*, calculated from both the scattering theory (indicated as exact) and the PA method for aligned gratings.

The near-field radiative heat flux between gratings based on the scattering theory is compared with the predictions from EMT and PA as shown in Figure 6.3. In order to identify the region where doped-silicon gratings perform better than bulk counterparts, the radiative heat flux for bulk doped silicon is also shown in Figure 6.3. The effect of period on the calculated heat flux is shown in Figure 6. 3 (a), in which *d*, *f*, and *H* are kept at the default values of 400 nm, 0.2, 1 μm, respectively. The predicted heat fluxes by EMT and PA are independent of the period for aligned identical gratings and thus are flat lines. Interestingly, as the period decreases, the heat flux predicted by the scattering theory (exact) approaches and finally coincides with that by EMT. For example, when *P* = 20 nm the heat flux from the exact solution is 941.54 W/m^2, which is essentially the same as the EMT prediction of 941.58 W/m^2. With decreasing period and the width of the gratings, it becomes difficult for waves to sense the small features and, therefore, homogenizing the grating as an effective medium becomes more reasonable. Similar observations were shown for metallodielectric metamaterials in Ref. [253], where

quantitative criteria for the validity of EMT in predicting radiative heat transfer between multilayers are given.

On the other hand, if the period becomes large enough, the radiative heat transfer is expected to achieve the value predicted by PA due to the negligible interactions between different unit cells nearby. At P = 20 μm, the heat flux of 96.0 W/m^2 as predicted by the scattering theory is only slightly higher than the PA limit of 93.3 W/m^2. The exact solutions lie between the upper asymptotic line governed by the EMT limit and the lower asymptotic line governed by the PA limit. Corrugating bulk doped silicon helps to enhance the radiative heat flux for small periods, where the many-body interactions between neighboring unit cells become nontrivial.

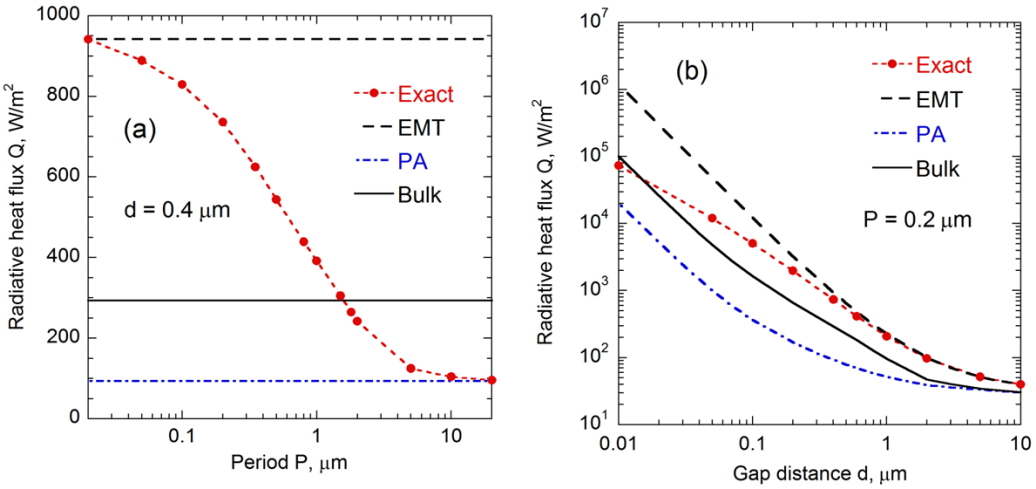

Figure 6.3 Comparison of heat flux calculated from the scattering theory with EMT, PA limit, and bulks. (a) Effects of period for d = 0.4 μm; (b) Effects of gap distance at P = 0.2 μm.

The near-field radiative heat flux for gap distance varying from 10 nm to 10 μm is shown in Figure 6.3 (b) when other geometric parameters are fixed at the default values. The agreement between the scattering theory and EMT is excellent when d > 0.6 μm. The

reason is that the number of contributing modes decreases with increasing gap spacing [207, 253]. Then, at large *d*, the major contribution comes from low-*k* modes with longer effective wavelengths. EMT is valid when the effective wavelength is greater than the period. However, when the gap spacing exceeds 10 μm, beyond the characteristic wavelength of thermal radiation, photon tunneling effects become weak and the radiative heat flux will converge to the far-field values when the energy transfer is dominated by propagating modes and independent of the gap spacing anymore.

With decreasing *d*, the exact solution deviates from the EMT result but approaches the PA prediction. Hence, the near-field radiative heat transfer tends to be localized at small gap spacing since the field will be highly confined due to the dominant contribution of high-*k* modes. Figure 3b also demonstrates that for the chosen values of *f*, *H*, and *P*, doped-silicon gratings outperform the bulk counterparts in terms of the heat transfer enhancement for $d > 15$ nm. Another interesting phenomenon is that the near-field heat flux of doped-silicon grating exhibits a power law close to d^{-1} for sub-micron gap spacing rather than the well-known d^{-2} (obtained by assuming *p*-polarized waves have dominant contributions [289]) as is the case for both bulk and homogenized media supporting surface resonances.

The underlying mechanism for the efficient radiative heat transfer is further explored by considering the spectral distribution, effective dielectric functions, and contour plot of the energy transmission coefficient. Using the default values, the exact solution gives a heat flux of 736 W/m^2, which is about eight times as high as the PA limit and 78% of the EMT limit. The heat flux spectra predicted by the three methods are plotted in Figure 6. 4 (a). It can be seen that the spectral heat flux predicted by the

scattering theory is much higher than that by PA from 3×10^{13} rad/s to 3×10^{14} rad/s. The surface resonance mode of doped Si lies at 2.88×10^{14} rad/s [68], where there is a small rise in the PA prediction. However, this feature does not show up according to the exact solution and EMT, both of which give very similar trend in the spectral heat flux. The reason is further explored by considering the dielectric functions predicted by EMT.

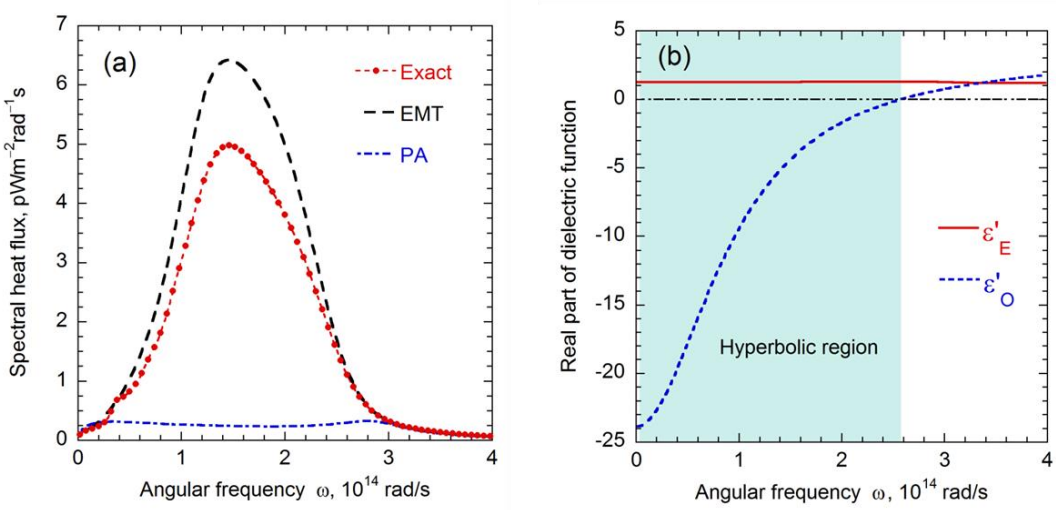

Figure 6.4 (a) Spectral radiative heat flux predicted by the scattering theory, EMT, and PA with the default parameters; (b) Effective dielectric functions for orthogonal directions for doped silicon gratings with $f = 0.2$.

The real parts of the dielectric function in orthogonal directions, ε'_O and ε'_E, are shown in Figure 6.4 (b). When ε'_O and ε'_E have different signs, the dispersion becomes hyperbolic with unbounded density of states [61, 67]. As a result, high-*k* modes become propagating in the homogenized grating region. The local density of states (LDOS) becomes high, leading to broadband efficient photon tunneling [66]. The hyperbolic band ranges from very low frequencies to 2.58×10^{14} rad/s as denoted by the shaded region in Figure 6.4 (b).

The energy transmission coefficient contour for $k_y = 0$ and $0 \le k_x \le \pi / P$ based on the scattering theory and EMT is given in Figure 6.5 (a) and Figure 6.5 (b), respectively. Because the cutoff wave vector for hyperbolic modes, defined as 1.94/*d* [253], is less than 2π/*P*, only modes in the first Brillouin zone have nontrivial contributions to the radiative heat flux and the folding of other diffraction orders has negligible contributions. For EMT, the calculation is set to $\phi = 0°$ and $0 \le \beta \le \pi / P$, in which case the cross-polarization terms become zero. The energy transmission coefficient considers both *s* and *p* polarizations and hence the upper limit is two instead of one [68]. The agreement of the energy transmission coefficient predicted by both the scattering theory with the EMT is quite good. For *s*-polarized waves at frequencies below 2.58×10^{14} rad/s where $\varepsilon'_{\mathrm{O}} < 0$, the gratings behave like a metal and give a very small ξ. At high frequencies, the energy transmission coefficient for *s*-polarized waves is large for propagating waves since $\varepsilon'_{\mathrm{O}}$ is greater than zero and $\varepsilon''_{\mathrm{O}}$ is small. However, photon tunneling for *s*-polarized waves contributes little to near-field radiation because of the negligibly small energy transmission coefficient (or tunneling probability). Attention is now paid to *p*-polarized waves as discussed next.

When $k_y = 0$, the reflection coefficient at the interface between vacuum and homogenized gratings for *p*-polarized waves is given as [68, 216]

$$r_{\mathrm{pp}} = \frac{\sqrt{k_0^2 - k_x^2}\sqrt{k_0^2\varepsilon_{\mathrm{E}} - k_x^2\varepsilon_{\mathrm{E}}/\varepsilon_{\mathrm{O}}} - \left(k_0^2 - k_x^2/\varepsilon_{\mathrm{O}}\right)}{\sqrt{k_0^2 - k_x^2}\sqrt{k_0^2\varepsilon_{\mathrm{E}} - k_x^2\varepsilon_{\mathrm{E}}/\varepsilon_{\mathrm{O}}} + \left(k_0^2 - k_x^2/\varepsilon_{\mathrm{O}}\right)} \tag{6.1}$$

Only r_{pp} is considered since neither *s*-polarized waves nor polarization coupling effects are important for high-*k* evanescent waves [68]. Considering $\varepsilon''_{\mathrm{E}}$ (the imaginary part) is

close to zero though not shown here, ε_E can be replaced by its real part ε'_E and Eq. (6.1) can be recast as follows:

$$r_{pp} = \frac{\sqrt{\varepsilon'_E}\sqrt{k_0^2 - k_x^2} - \sqrt{k_0^2 - k_x^2/\varepsilon_O}}{\sqrt{\varepsilon'_E}\sqrt{k_0^2 - k_x^2} + \sqrt{k_0^2 - k_x^2/\varepsilon_O}} \tag{6.2}$$

Note that for evanescent waves the imaginary part of r_{pp} must not be zero in order for the ξ to become nontrivial [68]. For the high-frequency region beyond the hyperbolic band, $\varepsilon'_O > 0$ and ε''_O is negligible, as a result, $\sqrt{k_0^2 - k_x^2/\varepsilon_O}$ becomes purely imaginary when k_x/k_0 is greater than $\sqrt{\varepsilon'_O}$, which is about 1 as shown in Figure 4b. The result is a very low tunneling probability at high frequencies. For propagating waves at high frequencies, ξ can still be large for *p*-polarized waves due to the dielectric behavior for both ordinary and extraordinary waves. Even though the combination of *s*- and *p*-polarized waves gives large ξ values (1.0 to 1.8) in this region, the contribution from the high-frequency region to the total radiative heat flux is less than 10%.

In the hyperbolic region, $\varepsilon'_O < 0$ and ε''_O is large, so that $\sqrt{k_0^2 - k_x^2/\varepsilon_O}$ has a dominant real part at low frequencies, leading to nontrivial energy transmission coefficients of evanescent waves. Doped-silicon gratings exhibit the unique property of hyperbolic modes with large photon tunneling probability in a broad frequency band. This is the main reason for the enhancement of near-field radiation by gratings over bulk doped silicon. As shown in Figure 6.5, even in the hyperbolic region, ξ is very small for low-k_x modes. When the hyperbolic film representing the grating region is thin, smaller than the penetration depth of the slow-decaying low-k_x modes, the film becomes

transparent. Due to the metallic feature of the doped-silicon substrate, the resulting ξ is very small in the hyperbolic band for low k_x values. This has been confirmed by calculations with increasing *H*, which results in higher energy transmission coefficient for low-k_x modes (although not shown here).

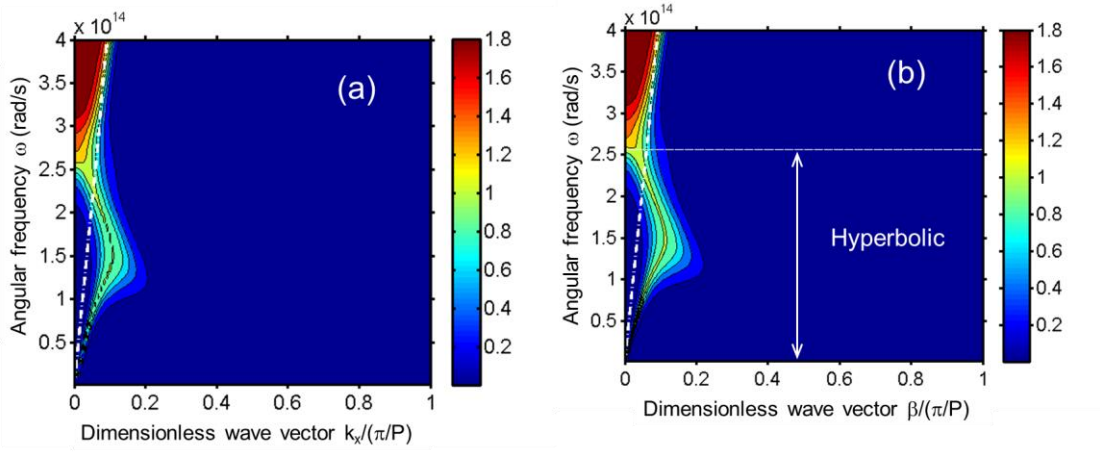

Figure 6.5 Contour plots of the energy transmission coefficient at $k_y = 0$ for the default parameters: (a) Exact solution based the scattering theory using RCWA; (b) EMT by setting $\phi = 0$.

It is worth noting that thin-film effects also play a role such that the doped-silicon substrates act together with the hyperbolic film to enhance near-field heat flux for high-k_x modes. The demonstrated hyperbolic nature may come from the coupling with short-range SPPs [290]. The slight difference between Figure 6.5 (a) and Figure 6.5 (b) is that the hyperbolic band featured with a large energy transmission coefficient is slightly broader for an effective medium described by EMT, suggesting that the hyperbolic dispersion at large wave vectors fails to hold for actual doped-silicon grating. This explains why EMT tends to predict a higher radiative heat flux than the exact solution. Similar phenomena have been noticed in multilayered metamaterials [61, 210, 253].

Overall, it can be clearly seen that the photon tunneling is effective in the hyperbolic region with a large number of k_x modes except those very close to the light line. That is the reason why doped-silicon gratings support a much higher heat flux than bulk materials. Furthermore, since high k_x modes become propagating in the gratings and the propagation length can exceed one period, near-field radiative transport with doped-silicon gratings tends to be delocalized; this explains why PA fails as the period becomes sufficiently small.

The formula for predicting the Casimir stiction between doped Si grating based on the scattering theory has been given in Sec. 2.4. The dielectric function of doped silicon at the imaginary frequency $\zeta = i\omega$ is given as [291]

$$\varepsilon(\zeta) = 1.035 + \frac{10.835\omega_0^2}{\omega^2 + \omega_0^2} + \frac{\omega_p^2}{\omega(\omega + \gamma)} \tag{6.3}$$

Note that the first two terms on the right side of Eq. (6.3) are the high-frequency dielectric response of silicon and are independent of the doping level. Here, ω_0 = 6.6×10^{15} rad/s is a fitted resonance frequency used to describe the interband transition for intrinsic silicon [291]. The last term of Eq. (6.3) represents the intraband contribution, where the values of ω_p and γ are given in Section II for a doping concentration of 10^{20} cm^{-3}. Note that the high-frequency dielectric response of silicon can be treated as a constant in the calculation of radiative heat transfer, since the contribution from frequencies higher than 4.0×10^{14} rad/s is negligible. However, for the Casimir interaction, these high-frequency modes are significant and even dominant for gap distances below hundreds of nanometers. The Casimir force of doped-silicon gratings F_g normalized by that of bulk doped silicon F_b is plotted in Figure 6.6 for varying submicron gap distances

with two periods P = 0.2 μm and 1.0 μm with f = 0.2 and H = 1 μm. The dashed lines with marks represent the results from the scattering theory using RCWA. As shown as the dash-dotted line, the PA prediction is independent of the period and gap distance. Since Casimir force is a strong function of the distance between two parallel planar surfaces, the ratio F_g / F_b in the PA limit approaches to the filling ratio of 0.2 for aligned gratings. In contrast to near-field energy transfer, the Casimir force is always reduced by surface corrugation as predicted by both the scattering theory and the PA method. Similar results were demonstrated for intrinsic silicon and metal gratings [28, 29, 31, 32]. Nevertheless, the PA method may under- or over-predict the Casimir force as compared with the exact method. It is interesting to note, according to the exact solution, the Casimir force of doped-silicon gratings is reduced to below the PA limit at gap distances below several hundred nanometers, which fall in the desired separation range for near-field energy harvesting and thermal management due to the prominently high radiative heat flux. The reason for the reduction of Casimir force below the PA limit may be attributed to the strong interactions of the fields between the ridges and those inside the grooves. Virtual photons confined between the ridges of the emitter and the receiver tend to leak when being close to the edges. The Casimir force predicted by the scattering theory for P = 1 μm tends to be closer to the PA limit than for P = 0.2 μm. This is expected since both the edge effects and interactions between neighboring unit cells will become weak for increasing grating period. Therefore, besides improving the near-field radiative heat flux, patterning doped-silicon surfaces helps to relieve the Casimir stiction.

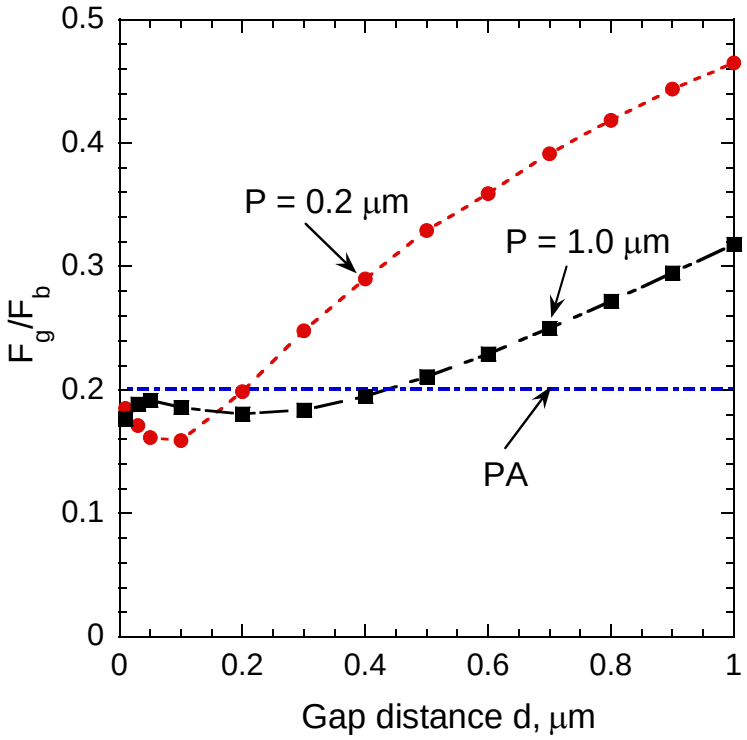

Figure 6.6 Casimir force between aligned doped-silicon gratings normalized to that for bulk counterparts as a function of the gap distances.

The heat flux and Casimir force generally decrease when some lateral displacement δ is introduced between the top and bottom gratings since mode coupling is deteriorated due to symmetry breaking. Such an effect has been considered for potential devices such as thermal modulators [83]. Before possible applications of doped-silicon gratings in modulating the heat flux and attraction force, it is necessary to study the effects of lateral displacement. To simplify the analysis, the relative lateral displacement δ/P is chosen to be 0.5, i.e., the maximum misalignment, so that the heat flux and Casimir attraction force should be the smallest. The ratio of the radiative heat flux and Casimir force between the misaligned case and the aligned case, $Q_{\delta=0.5P}/Q_{\delta=0}$ and $F_{\delta=0.5P}/F_{\delta=0}$, are shown in Figure 7a and 7b, respectively, for varying grating period. When the period is small, below 200 nm, both the radiative heat flux and Casimir

force remain the same despite of the misalignment. This is not surprising since when the period is shorter than the wavelength of the dominating modes, gratings behave as a homogeneous film according to the EMT. Even when d = 0.5 μm, the heat flux and Casimir force for misaligned case are still very close to that for the aligned case. Therefore, when the period is small, the heat flux and Casimir force for the doped-silicon gratings are insensitive to the displacement. As the period increases, there exists a strong dependence of both the radiative energy transfer and momentum transfer on the lateral displacement. As expected, if P exceeds 10 μm, both of the ratios approach those as governed by the PA limit. The PA limit of $Q_{\delta=0.5P}/Q_{\delta=0}$ is 56% as seen from Figure 6.7 (a), while that of $F_{\delta=0.5P}/F_{\delta=0}$ is only 2% as seen from Figure 6.7 (b). This is because the Casimir interaction is more sensitive to the gap spacing (d^{-4}) compared with the near-field radiative heat flux (d^{-2}).

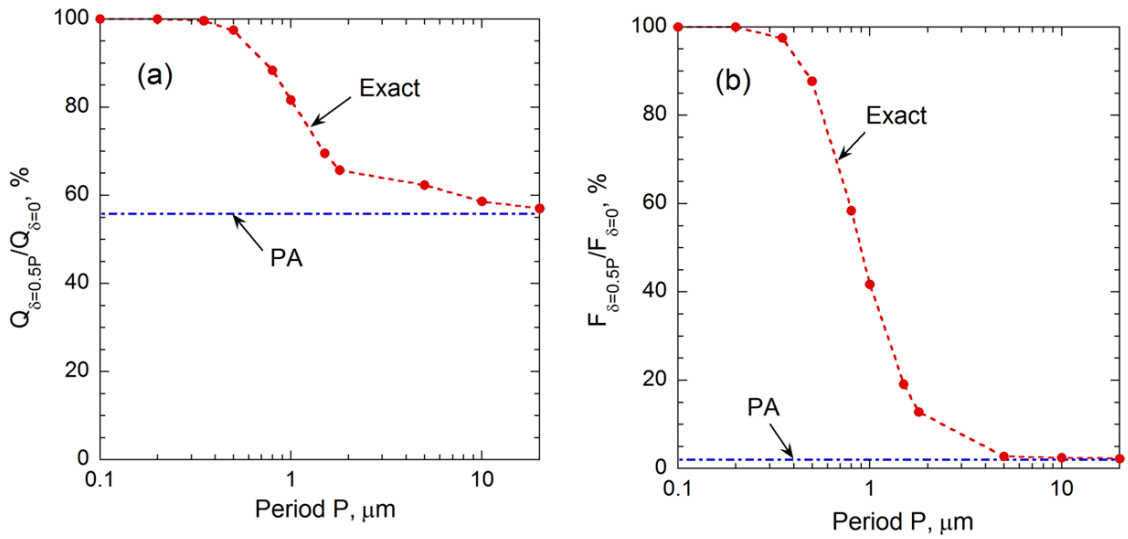

Figure 6.7 Ratio of (a) the radiative heat flux or (b) Casimir force for the misaligned grating when δ/P = 0.5 to that corresponding to the aligned gratings as a function of the period.

6.2 Tunable Stable Levitation Based on Repulsive Casimir Interactions

The desire of overcoming the Casimir stiction of MEMS devices has been one of the major driving forces for realizing repulsive force. Magnetic materials were introduced to achieve the Casimir repulsion through the vacuum gap [292, 293]. However, both these cases are based on nonphysical assumptions since infinite permeability is used by Boyer [292] and the independence of frequency for both permittivity and permeability is employed by Kenneth et al. [293]. Indeed, materials supporting non-unity permeability in the optical region which usually has the dominant contribution to the Casimir force do not exist in nature. This is because the interaction of materials with the magnetic field of electromagnetic waves is weak especially for short wavelengths due to the small value of the Sommerfeld fine-structure constant. Fortunately, artificial metamaterials with subwavelength unit cells such as split-ring resonators have been both theoretically and experimentally demonstrated to support strong magnetic responses. Based on EMT, both metamaterials supporting effective magnetic resonances and chiral materials with strong anisotropy have been claimed to induce repulsive Casimir force [294-299]. Nevertheless, the validity of EMT at small gap spacing is questionable [253], and exact calculations have recently proved effects of chirality to be small [300]. Therefore, achieving repulsive force in vacuum is still very challenging, although it has been demonstrated for ferromagnetic dielectrics [301] or in some situations out of thermal equilibrium [302]. Besides, very recent theories have ascertained that achieving stable levitation in vacuum to be impossible since Casimir free energy in vacuum for nonmagnetic materials has no minima [303-305].

Replacing the vacuum with an intervening fluid helps realize repulsion force, and stable levitation has been demonstrated based on dissimilar bulk substrates, changing the density of charge carriers by laser pulses, and more recently thin-film coatings [306-313]. However, the stable levitation is not actively tunable. The present study theoretically demonstrates stable suspension supporting on-site tunability by using one-dimensional (1D) gratings as shown in Figure 6.8.

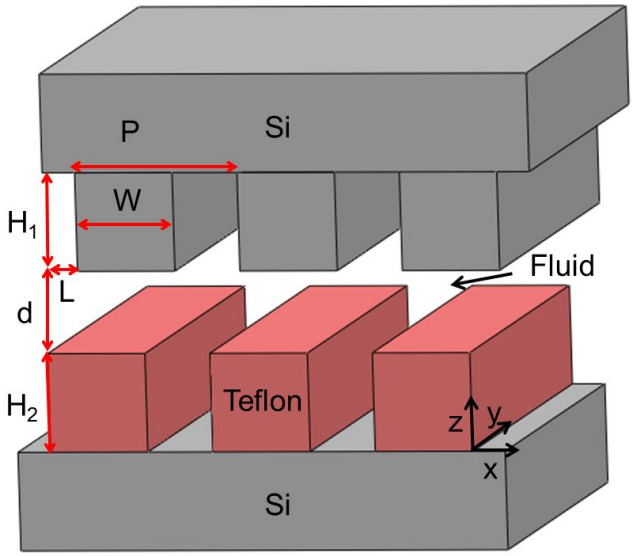

Figure 6.8 Schematic of Casimir interaction between one-dimensional gratings of dissimilar materials with a separation gap distance of d immersed in fluid bromobenzene.

To achieve repulsive Casimir force or even stable levitation, let us consider the simplest configuration, i.e., two different substrates separated by a thin layer of fluid. Making the Casimir force repulsive is very challenging if the fluid is vacuum, however, it will be a different story for a fluid whose (relative) permittivity (or dielectric function) is ε_f . The repulsive Casimir force is readily achievable without exciting magnetic resonances as long as Dzyaloshinskii's condition: $\varepsilon_1(i\omega) < \varepsilon_f(i\omega) < \varepsilon_2(i\omega)$ is satisfied

in a suitable frequency range. Here, ε_1 and ε_2 are the dielectric functions for the two nonmagnetic plates at the imaginary frequency [92]. Munday et al. [312] experimentally demonstrated repulsive Casimir force between gold and silica separated by bromobenzene whose permittivity lies between those of the two substrates for a broad frequency range, and their results agree with the general Lifshitz's formula for a wide range of gap distances [91]. When the fluid thickness is only a few nanometers where the retardation effects considering finite speed of light can be neglected, repulsive forces featured with negative Hamaker constant have also been experimentally demonstrated [314, 315]. Repulsive forces can lead to ultralow friction and good surface wetting [314, 316]. Some potential applications can be realized if the Casimir force can change sign with the distance. One such example is stable quantum levitation [306, 307, 317], which can be used to design frictionless gears and develop passive-suspension techniques [24].

The requirement of stable levitation is that the Casimir interaction should be repulsive for small gap spacings and turns into an attractive force when the two objects move away from each other to a certain extent. If the Casimir interaction exhibits an opposite behavior, the state is dynamically instable though the magnitude of the force becomes zero at that transition position. To achieve stable separation between two bulk isotropic substrates, the following guide inequalities should be satisfied [317]

$$\begin{aligned} &\varepsilon_1 < \varepsilon_f < \varepsilon_2 \quad \text{at low frequencies} \\ &\varepsilon_f < \min\left(\varepsilon_1, \varepsilon_2\right) \text{ or } \varepsilon_f > \max\left(\varepsilon_1, \varepsilon_2\right) \text{ at high frequencies} \end{aligned} \tag{6.4}$$

It is not difficult to understand the above criteria since the low and high frequencies play a major role in determining the Casimir force for large and small gap distances, respectively. However, these criteria are only approximate and should be

treated as guideline only [317]. Even if both inequalities in Eq. (6.4) are satisfied, it is not guaranteed that there will definitely be a stable position, since the contribution of different frequencies may vary largely. Therefore, realizing stable levitation based on proper choices of dielectric functions of the fluid and two bulk substrates is challenging though feasible for only a few delicately designed cases [317].

The three materials satisfying Eq. (6.4) selected in this work are a Si substrate, a bromobenzene fluid, and a Teflon substrate. The dielectric function of intrinsic Si is described by a Sellmeier model as [291]

$$\varepsilon_{\mathrm{Si}}\left(i\omega\right)=\varepsilon_{\infty}+\frac{\left(\varepsilon_{0}-\varepsilon_{\infty}\right)\omega_{0}^{2}}{\omega^{2}+\omega_{0}^{2}} \tag{6.5}$$

where the cutoff frequency ω_0 is equal to 6.6×10^{15} rad/s, ε_∞ and ε_0 are 11.87 and 1.035, respectively. For bromobenzene, a two-oscillator model is employed [312, 318]

$$\varepsilon_{f}\left(i\omega\right)=1+\frac{C_{\mathrm{IR}}\omega_{\mathrm{IR}}^{2}}{\omega^{2}+\omega_{\mathrm{IR}}^{2}}+\frac{C_{\mathrm{UV}}\omega_{\mathrm{UV}}^{2}}{\omega^{2}+\omega_{\mathrm{UV}}^{2}} \tag{6.6}$$

$\omega_{\mathrm{IR}} = 5.47\times10^{14}$ rad/s and $\omega_{\mathrm{UV}} = 1.286\times10^{16}$ rad/s are the characteristic absorption frequencies in the infrared and ultraviolet range, respectively, $C_{\mathrm{IR}} = 2.967$ and $C_{\mathrm{UV}} = 1.335$ are the corresponding absorption strengths. For Teflon, multiple oscillator models are used, the corresponding parameters obtained by combining Kramers-Kronig analysis and measured dielectric constants are given in a recent paper by van Zwol and Palasantzas [319]. The permittivities of these three materials at imaginary frequencies are shown in Figure 6.9. It can be clearly seen that the permittivity of bromobenzene lies between that of Si and Teflon until the crossing frequency at 1.612×10^{16} rad/s. Although

Eq. (6.4) is satisfied, as will be shown later, the Casimir force stays repulsive for all gap distances and stable levitation is not feasible with semi-infinite substrates.

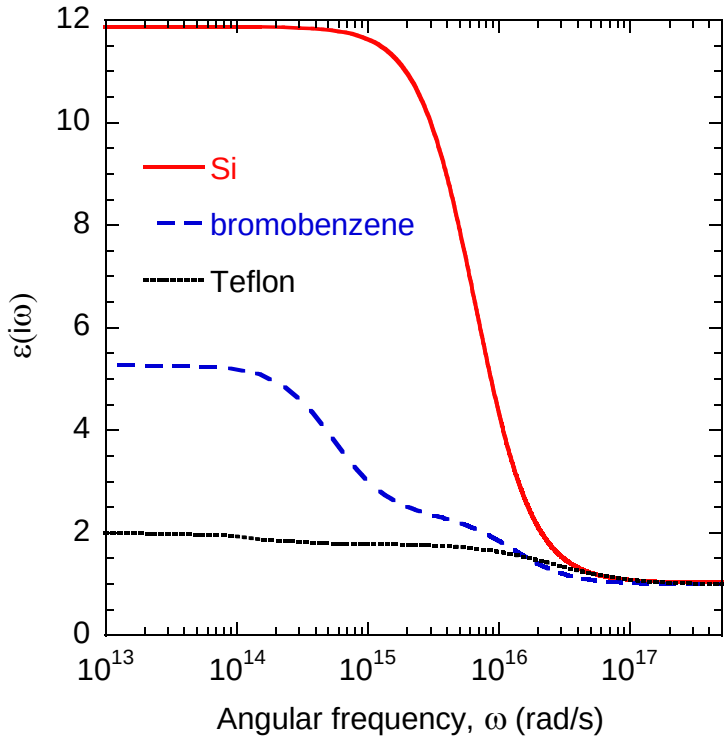

Figure 6.9 Relative permittivity of Si, bromobenzene, and Teflon at imaginary frequencies.

Using multilayer structures such as a thin film coated on a substrate may facilitate stable levitation [307]. Here, the configuration of fluid bromobenzene sandwiched between intrinsic Si and a thin film of Teflon coated on Si substrate is considered, as shown in Figure 6.10 (a). The Casimir force per unit area normalized to that between perfect conductors F_c for the considered planar configuration is shown in Figure 6.10 (b) for different thicknesses of Teflon. When the Teflon film thickness is zero, it recovers to the Si-bromobenzene-Si configuration. As expected, the Casimir force for this symmetric configuration as shown by the solid line is always attractive (positive sign) since r_1 is

equal to r_2 for both polarizations. On the other hand, as shown by the dotted line, Casimir repulsion at all gap distances is supported for Si-bromobenzene-Teflon where Teflon film thickness is infinitely large, although it is noted that Eq. (6.4) is satisfied with the transition frequency as 1.612×10^{16} rad/s, below and beyond which the spectral force becomes repulsive and attractive, respectively. The reason is because contributions from higher frequencies are relatively small compared with those from frequencies below the transition. Indeed, the permittivities of these three materials are very close and approach to unity at high frequencies as can be seen from Figure 6.9. As a result, the field confinement in the gap becomes weak, leading to small Casimir interactions. When the Teflon film thickness is finite, say 50 nm, the Casimir force lies between the above two limiting cases of pure attraction and pure repulsion, as illustrated by the dashed line. Stable position with diminishing force occurs at 195.2 nm as denoted by the solid circle, and the sign becomes positive and negative by further increasing and decreasing the gap spacing, respectively. Figure 6.10 (b) shows that the Casimir force considering thin film Teflon of 50 nm approaches the force for bulk Teflon (repulsion) and bulk Si (attraction) at small and large gap distances, respectively. Given this situation, there should be a middle point at which the transition occurs. In order to elucidate this phenomenon, it is necessary to take a look at the reflection coefficient for the thin Teflon coating on bulk Si, which is given as [3]

$$r_2^{\mathrm{s,p}} = \frac{r_{\mathrm{Br\text{-}Te}}^{\mathrm{s,p}} + r_{\mathrm{Te\text{-}Si}}^{\mathrm{s,p}} e^{-2k_{z,\mathrm{Te}}H_2}}{1 + r_{\mathrm{Br\text{-}Te}}^{\mathrm{s,p}} r_{\mathrm{Te\text{-}Si}}^{\mathrm{s,p}} e^{-2k_{z,\mathrm{Te}}H_2}} \tag{6.7}$$

where $k_{z,\mathrm{Te}} = \sqrt{\varepsilon_{\mathrm{Te}}\,\omega_n^2/c^2 + \beta^2}$ is the z-direction wavevector in Teflon, $r_{\mathrm{Br\text{-}Te}}$ and $r_{\mathrm{Te\text{-}Si}}$ are the Fresnel reflection coefficients are the interface of bromobenzene-Teflon and

Teflon-Si, respectively. At high frequencies, $k_{z,\mathrm{Te}}$ becomes so large that $e^{-2k_{z,\mathrm{Te}}H_2}$ will approach zero, then $r_2 \approx r_{\mathrm{Br\text{-}Te}}$. This means that the underlying Si substrate will not affect the reflection coefficient, and the thin Teflon film can be treated as bulk although its thickness is finite with the value of H_2. That explains the overlap of the Casimir force considering Teflon of 50 nm and that for bulk Teflon at gap distances smaller than 20 nm, as can be clearly seen from Figure 6.10 (b). At low frequencies, relatively small $k_{z,\mathrm{Te}}$ multiplies with nanometer scale H_2 will make $e^{-2k_{z,\mathrm{Te}}H_2}$ close to one. After some math work, it can be found that $r_2 \approx r_{\mathrm{Br\text{-}Si}}$, meaning that the existence of thin Teflon film will not lead to a large modification of the Casimir force between bulk Si substrates at large gap distances, where the Casimir force is dominated by low frequencies. Therefore, thin film coatings can help achieve stable levitation.

The stable separation distance can be adjusted by changing the thickness of Teflon film as shown in Figure 6.10 (c). The stable position decreases with reducing Teflon thickness, and the separation is 6.3 nm when H_2 is 5 nm. When Teflon thickness becomes larger, the deviation of the corresponding Casimir force from that of bulk Teflon will be postponed to larger gap distances. On the other hand, the gap spacing needed to make the substrate effects large enough to achieve attraction should increase. This is why the stable levitation position increases monotonically with the thickness of Teflon. Nevertheless, the adjustment of stable separation is based on changing Teflon film thickness and cannot be made on-site or dynamically to meet different requirements of various applications. The above limitation can be overcome by the proposed design shown in Figure 6.8 and the details are given in the next section.

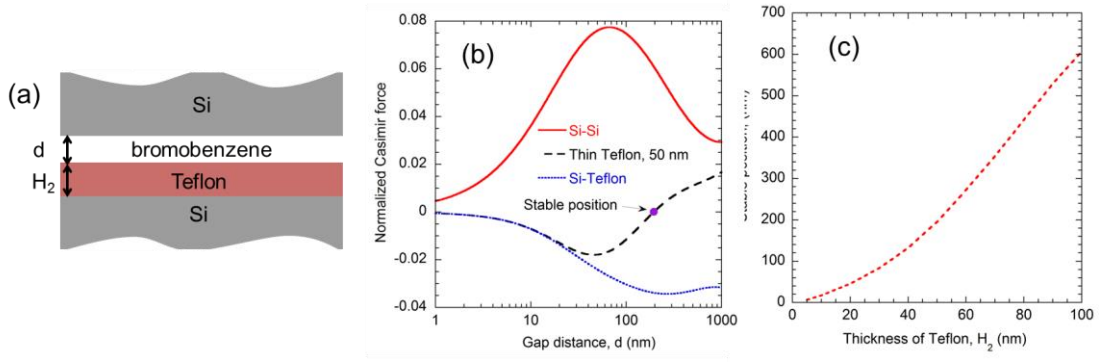

Figure 6.10 (a) The configuration of Casimir interaction between bulk Si and thin film Teflon deposited on Si substrate. (b) Normalized Casimir force as a function of the gap spacing for different bottom configurations: bulk Si, thin Teflon of 50 nm on Si, and bulk Teflon. (c) The variation of stable levitation position versus the thickness of Teflon film.

The Casimir force between Si grating and Teflon grating as a function of the fluid gap distance is given in Figure 6.11. Here, P = 1000 nm, W = 500 nm, L = 0 nm, and H_2 = 50 nm are set as default unless otherwise specified. The agreement between the exact method represented by marks and proximity force approximation (PFA) denoted by the dash or dotted line is good for different values of H_1. Stable separation occurs at 125.6 nm and 115.7 nm for H_1 equal to 50 nm and 30 nm, respectively. These values agree with 136.6 nm and 122.9 nm obtained from PFA to some extent. For small gap distances, the Casimir force at two different values of H_1 coincides, as is confirmed from both the exact method and PFA. It is expected since the contribution to the force from the ridges (Si and Teflon) becomes more dominant over that from the grooves (Si and Si) with decreasing d. This is essentially due to the power law dependence of Casimir force on the gap spacing. Though variations of H_1 do not affect the Casimir interaction for small d, an apparent difference occurs for relatively large d. Decreasing H_1 will increase the attractive force between the grooves, while the repulsive force between the ridges remains the same. In order to balance the increased attractive force, the gap spacing has

to be reduced to produce enough repulsion from the ridges. As a result, the stable levitation position shifts from 125.6 nm to 115.7 nm when decreasing H_1 from 50 nm to 30 nm. The equilibrium position can also be modified by changing H_2 and W.

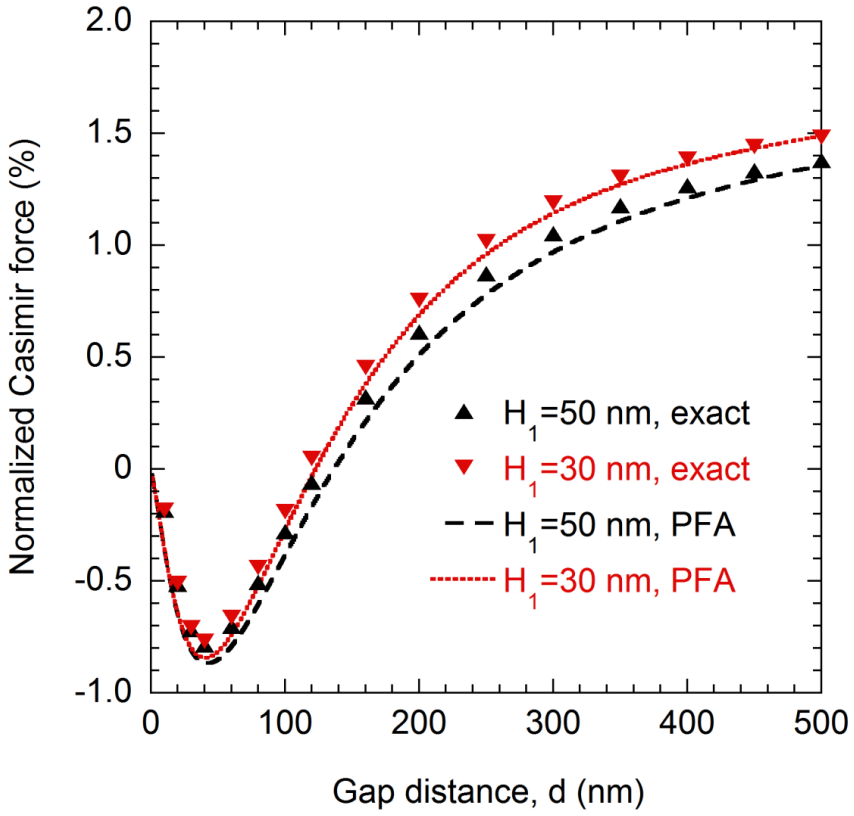

Figure 6.11 Normalized Casimir force between grating structures varying with gap distances based on both exact method (marks) and PFA (lines).

As shown in Figure 6.12 (a), the stable levitation position at W = 500 nm, H_1 = 30 nm, and H_2 = 50 nm, decreases with the lateral displacement between the top and bottom gratings. In the present study, lateral Casimir force is not considered although it exists for misaligned cases except when the lateral shift is half of the period due to symmetry. It is assumed that the lateral shift is controlled externally. The curve is symmetric with respect to $L = 0.5P$; as such the other half period for L = 500 nm to 1000 nm is not drawn. With

increasing the lateral displacement, the dominant repulsion force from the ridges of the two gratings will decrease since the facing area becomes smaller while the dominant attraction force from the ridge of the top grating to the groove of the bottom grating increases. Subsequently, the separation distance for stable levitation will decrease. The agreement between the exact method and PFA is excellent except for the two extreme cases of L = 0 nm and L = 500 nm. PFA overestimates and underestimates the equilibrium position when L is close to 0 nm and 500 nm, respectively. The reason lies that PFA does not consider the edge effects. For example, when L = 0 nm, according to PFA, the equilibrium is settled when the repulsion force between the ridges and the attraction force between the grooves are equal. However, the field confinement between the ridges cannot be as perfect as that between bulks, so that the real repulsion will be smaller than the PFA value due to the leakage. This explains why the exact values of Casimir force are all above the PFA curves in Figure 6.11. Then, there is no wondering that the PFA predicts a larger stable separation for aligned gratings. For the purely misaligned case of L = 500 nm, balance of the repulsion from the groove of the top grating and the ridge of the bottom grating with the attraction from the corresponding remaining parts leads to the equilibrium position. However, the repulsion between the ridges, which is nontrivial especially for small gap distances, is not considered by PFA. As a result, the exact values of Casimir force will lie below the PFA predictions although the results are not shown here. This explains why the stable separation predicted by PFA, 15.4 nm, is smaller than the exact value of 35.7 nm at L = 500 nm. Nevertheless, the overall accuracy of PFA is still good except close to the two extremes. If the period is

large enough, the edge effects are expected to diminish, and the accuracy of PFA will further improve.

It is clearly shown that by laterally moving the bottom grating relative to the top one, the stable levitation position can be tuned on-site. It is noted that both the magnitude of the vertical displacement and its shape can be adjusted to meet different demands by changing the ridge width W. The equilibrium position varying with the lateral displacement for W = 300 nm is given in Figure 6.12 (b). The stable separation first decreases with L, as expected, and reaches a constant for L larger than 300 nm. This provides rich vertical motions, which might be useful for different applications. The maximum vertical displacement induced when L changes from 0 to 300 nm is 73.1 nm, which is slightly smaller than 79.9 nm in Figure 5a. The stable position in Figure 6.12 (b) for W = 300 nm is lower than that in Figure 5a for any value of the later shift. It is expected since the reducing W will decrease the repulsion between the ridges but enlarge the attraction between the grooves. Besides the conventional applications for stable levitation, the proposed design can be used as for position control. It can also work as mechanical transducers by converting lateral displacement into motion in the vertical direction. Instead of relying on classical mechanics or electromagnetism, this envisioned device is based on quantum electrodynamics, and no contact is required so that the friction is expected to be ultralow. The ratio of maximum vertical displacement to the lateral shift is inversely proportional to the period, thus can be tuned to meet different needs. Besides, the device size can be scalable from macroscale down to microscale. Another advantage of the proposed configuration is that the alignment of the two gratings can be self-acquired to some extent. If a certain misalignment is introduced, the Casimir

force will be repulsive and attractive for regimes with smaller and larger gap separations, respectively. As a result, the gap distance between the two gratings would tend to approach the same value across the whole sample.

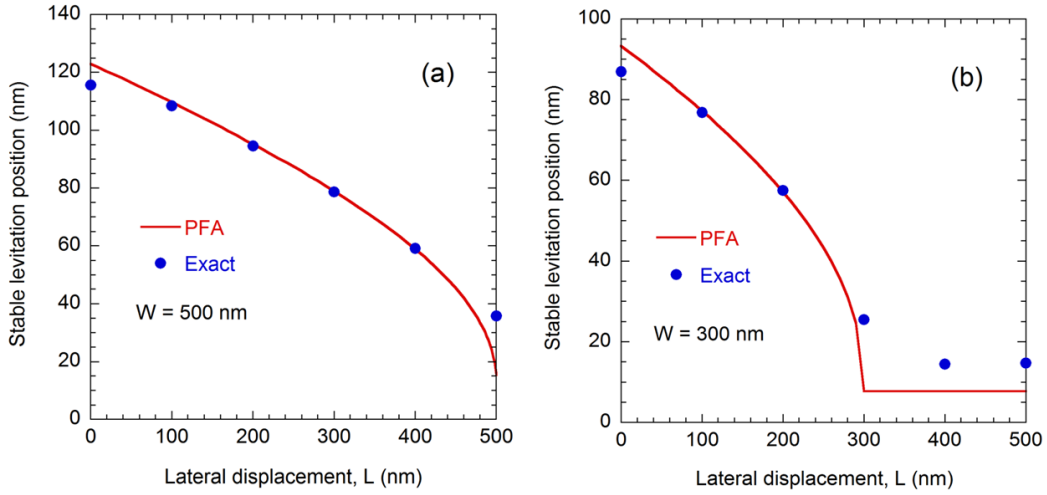

Figure 6.12 Stable levitation position tuned by the lateral displacement for different grating widths. (a) W = 500 nm; (b) W = 300 nm.

In practice, the effects of temperature and gravity on the stable position should also be considered. The effect of thermal fluctuations may be nontrivial for bulk materials when the gap spacing is on the order of $\hbar c/k_B T$, which is 7.6 μm at T = 300 K [91]. Around room temperature, modifications of the Casimir force due to temperature changes are typically negligible [320]. However, Guérout et al. [47] found that the grating structure could augment the thermal contribution to the Casimir interactions. Therefore, it is necessary to check the sensitivity of proposed device to temperature changes. The liquid phase of fluid bromobenzene holds when the temperature is between 242.3 K and 429 K at atmospheric pressure. Since the stable separation distance is around 100 nm, the Casimir force is calculated for aligned gratings with default geometric parameters at d =

100 nm for T = 250 K and 420 K. The relative difference is only three percent, demonstrating that the temperature has a negligible effect on the Casimir force. The stable position for L = 0 nm changes slightly from 115.66 nm to 115.57 nm when the temperature increases from 250 K to 420 K. It should be noted that according to the PFA, the stable position is changed from 122.97 nm to 122.55 nm, which qualitatively agree with the exact calculations. Therefore, it is safe to assert that the stable levitation of proposed nanostructures is robust to temperature variations.

The gravitational force generally needs to be considered for application with the proposed configuration shown in Figure 6.8, although when the z axis horizontal, gravity will not have an effect to the preceding results. In order to consider the gravitational effect, it is assumed that the top grating is beneath a thin Si film with a thickness H_{Si} of 5 μm. The medium above the Si film is vacuum. Taking the gravitational acceleration rate g = 9.8 m/s^2, the density of Si ρ_{Si} = 2329 kg/m^3, and the density of BB ρ_{BB} = 1492 kg/m^3, the force per unit area exerted on the top grating due to gravity is $F_g = \rho_{\mathrm{Si}} g H_{\mathrm{Si}} + \rho_{\mathrm{Si}} g H_1 f - \rho_{\mathrm{BB}} g H_1 f$. The last term considers the buoyancy of the grooves immersed in the fluid. For default geometry parameters, i.e., P = 1000 nm, W = 500 nm, H_1 = 30 nm, and H_2 = 50 nm, F_{g} is equal to 0.11424 Pa. So, the Casimir force between the two nanostructures should be repulsive and the magnitude should be equal to F_{g} for stable levitation in the presence of gravity. As can be seen from Figure 6.11, the Casimir force is always repulsive when the gap distance is smaller than the original stable levitation separation. Therefore, the stable levitation considering the gravity still exists but will shift to a smaller gap separation for the balance of gravitational force and the repulsive Casimir force is balanced.

Figure 6.13 is given to illustrate the gravity effect on the variation of the stable levitation position of the top grating with the thin Si substrate. Clearly, the stable separation distance is always smaller than the case without gravity for different values of lateral shifts as expected. Another prominent feature of Figure 6 is that the difference of the stable levitation separation with or without gravity becomes smaller as the lateral shift increases. Note that the stable levitation gap distance is smaller at a larger lateral shift. Because the Casimir force is very sensitive to the gap distance when it is small, even a tiny further decrease of the gap distance will lead to a repulsive Casimir force comparable to the gravitational force. As shown in Figure 6.13, for L equal to 500 nm, there is only a small decrease in the stable levitation separation.

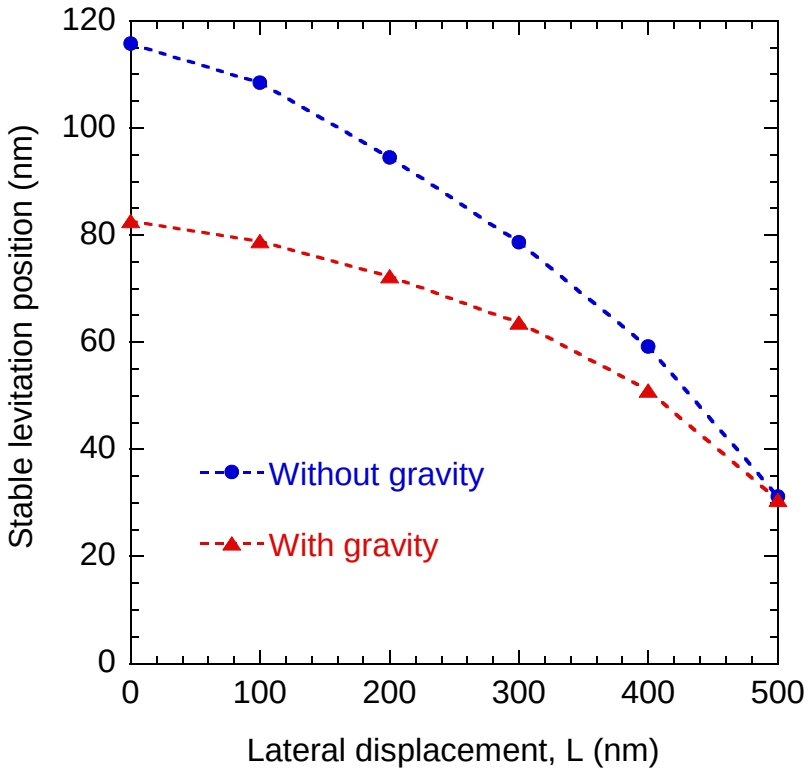

Figure 6.13 Effect of the gravity on the tunable levitation when the top grating is attached to a thin Si substrate, H_{Si} = 5 μm, and the other geometry parameters are default.

6.3 Summary

This chapter investigates the momentum exchange or Casimir interaction between metamaterials. The major contributions are presented in the followings.

Highly efficient radiative heat flux between doped-silicon gratings is demonstrated and the amount can be as high as three times that between planar substrates. Furthermore, the exact solution based on the scattering theory predicts the heat flux to be 1-2 orders of magnitude higher than that given by the geometry-based approximation. The excitation of hyperbolic modes, which support broadband and large energy transmission coefficient for high-k modes, is attributed to be the main reason of the enhanced near-field energy transport. Meanwhile, the issue of Casimir stiction is demonstrated to be greatly relieved with gratings as compared to the bulk counterparts. New possibilities of enhancing radiative energy transfer while simultaneously suppressing momentum exchange by patterning doped-silicon surfaces are opened. The findings hold promise for applications in contactless thermal management, near-field energy harvesting, and relieving adhesion problems of MEMS and MEMS devices.

The Casimir interaction between two nanostructures separated by an intervening fluid is investigated. While stable levitation is achievable when one substrate and a thin film coated on another substrate are separated by a non-vacuum fluid, the levitation position depending on the film thickness is fixed rather than actively tunable. This limitation can be overcome by using dissimilar gratings, whereby the stable separation position changes when the two gratings move relative to each other laterally. Besides, how the levitation position changes with the lateral shift depends on the grating width. Thus, the grating width can be adjusted to meet different applications. In addition, the

position of stable levitation is insensitive to temperature variations. The proposed design may turn quantum Casimir force into real applications in macroscopic devices, such as microposition control and mechanical transduction.

CHAPTER 7

CONCLUSIONS AND RECOMMENDATIONS

This dissertation investigates the unusual far-field and near-field radiative properties of metamaterials for potential applications in energy harvesting, thermal management, and light manipulation. The uniqueness and major contributions are divided into the following four parts.

Firstly, the extraordinary transmission, refraction, and absorption of infrared light are theoretically demonstrated based on proper designs of metamaterials. Based on the extraordinary transmission of metallic nanoslits, an efficient polarizer working in the near-infrared regime with wide acceptance angle and extremely high extinction coefficient is proposed. Later, based on the excitation of magnetic polaritons, the counterintuitive blocking-assisted transmission is presented. Besides metals, doped semiconductors also possess metallic responses in the infrared regime. Negative refraction and tunable perfect absorption of the middle infrared light are theoretically predicted based on free-standing and substrate-backed doped silicon nanowires, respectively.

Secondly, the potential of metamaterials on enhancing the near-field thermal radiation is investigated based on the effective medium theory combined with fluctuation electrodynamics. Excitation of broadband hyperbolic modes and reducing the loss of surface modes are proposed as two important methods of enhancing near-field thermal radiation. The effects of polarization coupling is found to be trivial for nanoscale thermal radiation. Perfect photon tunneling across broad frequency regimes and wavevector space is theoretically presented for the first time based on the hybridization of hyperbolic modes and graphene plasmons. Then, the quantitative application criteria of the effective medium theory is given for the first time.

Thirdly, based on exact approaches including the semi-analytical RCWA and numerical FDTD, new routes and mechanism for enhancing the near-field thermal radiation are presented. Due to the hybridization of graphene plasmons with surface phonon modes, covering a thin layer of graphene sheet is found to improve the radiative heat flux between silica gratings by more than one order of magnitude and alleviate the performance sensitivity to lateral shifts. Near-field thermal radiation between metasurfaces is investigated for the first time, and 1D metasurface is found to be surprisingly outperform 2D metasurface due to the excitations of both surface modes and hyperbolic modes. Pattering a graphene sheet into graphene ribbon arrays is demonstrated to further improve the near-field radiative heat flux by about one order of magnitude, and the physical mechanism is attributed to the excitation of hyperbolic graphene plasmons. New applications of near-field radiation, like enhancing the refrigeration rate and broadening the operation temperature range of electroluminescent refrigeration technique are also presented.

Finally, the near-field momentum exchange or Casimir interaction is tailored for different applications based on metamaterials. Enhanced near-field thermal radiation and suppressed Casimir force are presented simultaneously. Based on repulsive Casimir force, a design for realizing tunable stable levitation is proposed for applications in propulsion and nanoscale position control.

The future work will go to the radiative entropy analysis of metamaterials. Although metamaterials have been proposed to harvest energy based on TPV devices, the maximum thermodynamic efficiency is still not clear. The investigation of radiative entropy transfer is still in its infancy, and there are some other unresolved problems, some examples are listed. How to consider light interference effects on the entropy transfer? How to calculate the entropy transfer between two objects separated by a

nanoscale vacuum gap? Where does the entropy generation come from, at the material interface or inside the vacuum or the hot body? Can the Boltzmann's definition of entropy $k_B \ln \Omega$ be applied to calculate entropy transfer considering real surfaces and near-field radiation? If it works, how to define the microstates Ω? Will the emitted entropy flux be dependent on the distance from the hot body? Therefore, a deep understanding of the entropy transfer and generation considering non-ideal surfaces and near-field radiation is still needed.

Moreover, the experimental demonstration of the enhanced near-field thermal radiation between large area metamaterials will be performed in the future. In the last past decade, there have been some experimental efforts on measuring the near-field thermal radiation between planar substrates or between a sphere and a planar substrate. However, the near-field thermal radiation between metamaterials, such as silica grating, metasurfaces, and graphene ribbons, has not been experimentally reported. Experiments on this field will not only help to further understand nanoscale radiative heat transport but also pave the way for turning near-field thermal radiation into real-world applications and commercializing the relevant devices.

REFERENCES

[1] Howell, J. R., Siegel, R., and Mengüç, M. P., 2010, Thermal Radiation Heat Transfer, 5 ed. Boca Raton: CRC Press Taylor & Francis.

[2] Modest, M. F., 2013, Radiative Heat Transfer, 3 ed.: Academic Press.

[3] Zhang, Z. M., 2007, Nano/Microscale Heat Transfer. New York: McGraw-Hill.

[4] Cai, W. and Shalaev, V. M., 2010, Optical Metamaterials 10: Springer.

[5] Cahill, D. G., Braun, P. V., Chen, G., Clarke, D. R., Fan, S., Goodson, K. E., Keblinski, P., King, W. P., Mahan, G. D., Majumdar, A., Maris, H. J., Phillpot, S. R., Pop, E., and Shi, L., 2014, "Nanoscale Thermal Transport. Ii. 2003–2012," Appl. Phys. Rev., **1**, p. 011305.

[6] Maldovan, M., 2013, "Sound and Heat Revolutions in Phononics," Nature, **503**, pp. 209-217.

[7] Cola, B., Daiguji, H., Dames, C., Fang, N., Fushinobu, K., Inoue, S., Kikugawa, G., Kohno, M., Kumar, S., and Li, D., 2013, "Report on the Seventh Us–Japan Joint Seminar on Nanoscale Transport Phenomena—Science and Engineering," Nanoscale and Microscale Thermophysical Engineering, **17**, pp. 25-49.

[8] Casimir, H. B. G., 1948, Proc. K. Ned. Akad. Wet. , **51**, p. 793.

[9] Ebbesen, T. W., Lezec, H. J., Ghaemi, H. F., Thio, T., and Wolff, P. A., 1998, "Extraordinary Optical Transmission through Sub-Wavelength Hole Arrays," Nature, **391**, pp. 667-669.

[10] Smith, D. R., Padilla, W. J., Vier, D. C., Nemat-Nasser, S. C., and Schultz, S., 2000, "Composite Medium with Simultaneously Negative Permeability and Permittivity," Phys. Rev. Lett., **84**, pp. 4184-4187.

[11] Veselago, V. G., 1968, Sov. Phys. USPEKHI, p. 509.

[12] Rytov, S. M., Kravtsov, Y. A., and Tatarskii, V. I., 1989, Principles of Statistical Radiophysics. New York: Springer.

[13] Joulain, K., Mulet, J. P., Marquier, F., Carminati, R., and Greffet, J. J., 2005, "Surface Electromagnetic Waves Thermally Excited: Radiative Heat Transfer, Coherence Properties and Casimir Forces Revisited in the near Field," Surface Science Reports, **57**, pp. 59-112.

[14] Pendry, J. B., 1999, "Radiative Exchange of Heat between Nanostructures," J. Phys.: Condens. Matter, **11**, pp. 6621-6633.

[15] Biehs, S. A., Rousseau, E., and Greffet, J. J., 2010, "Mesoscopic Description of Radiative Heat Transfer at the Nanoscale," Phys. Rev. Lett., **105**, p. 234301.

[16] Zhang, Z. M. and Mengüç, M. P., 2007, "Special Issue on Nano/Microscale Radiative Transfer," Journal of Heat Transfer, **129**, pp. 1-2.

[17] Zhang, Z., Norris, P., and Peterson, G. P. B., 2013, "Foreword to Special Issue on Micro/Nanoscale Heat and Mass Transfer," Journal of Heat Transfer, **135**, p. 090501.

[18] Park, K. and Zhang, Z., 2013, "Fundamentals and Applications of near-Field Radiative Energy Transfer," Frontiers in Heat and Mass Transfer, **4**, p. 013001.

[19] Basu, S., Chen, Y. B., and Zhang, Z. M., 2007, "Microscale Radiation in Thermophotovoltaic Devices—a Review," Int. J. Energy Res., **31**, pp. 689-716.

[20] Basu, S., Zhang, Z. M., and Fu, C. J., 2009, "Review of near-Field Thermal Radiation and Its Application to Energy Conversion," International Journal of Energy Research, **33**, pp. 1203-1232.

[21] Jones, A. C., O'callahan, B. T., Yang, H. U., and Raschke, M. B., 2013, "The Thermal near-Field: Coherence, Spectroscopy, Heat Transfer, and Optical Forces," Prog. Surf. Sci., **88**, pp. 349-392.

[22] Klimchitskaya, G. L., Mohideen, U., and Mostepanenko, V. M., 2009, "The Casimir Force between Real Materials: Experiment and Theory," Rev. Mod. Phys., **81**, p. 1827.

[23] Rodriguez, A. W., Capasso, F., and Johnson, S. G., 2011, "The Casimir Effect in Microstructured Geometries," Nat. Photon., **5**, pp. 211-221.

[24] Capasso, F., Munday, J. N., Iannuzzi, D., and Chan, H. B., 2007, "Casimir Forces and Quantum Electrodynamical Torques: Physics and Nanomechanics," IEEE J. Sel. Top. Quantum Electron., **13**, pp. 400-414.

[25] Genet, C., Lambrecht, A., and Reynaud, S., 2008, "The Casimir Effect in the Nanoworld," Eur. Phys. J. Spec. Top., **160**, pp. 183-193.

[26] Dalvit, D., Milonni, P., Roberts, D., and Da Rosa, F., 2011, Casimir Physics 834. Berlin: Springer.

[27] Bordag, M., Klimchitskaya, G. L., Mohideen, U., and Mostepanenko, V. M., 2009, Advances in the Casimir Effect. Oxford: Oxford University Press.

[28] Chan, H. B., Bao, Y., Zou, J., Cirelli, R. A., Klemens, F., Mansfield, W. M., and Pai, C. S., 2008, "Measurement of the Casimir Force between a Gold Sphere and a Silicon Surface with Nanoscale Trench Arrays," Phys. Rev. Lett., **101**, p. 030401.

[29] Bao, Y., Guérout, R., Lussange, J., Lambrecht, A., Cirelli, R. A., Klemens, F., Mansfield, W. M., Pai, C., and Chan, H. B., 2010, "Casimir Force on a Surface with Shallow Nanoscale Corrugations: Geometry and Finite Conductivity Effects," Phys. Rev. Lett., **105**, p. 250402.

[30] Zou, J., Marcet, Z., Rodriguez, A. W., Reid, M. T. H., Mccauley, A. P., Kravchenko, I. I., Lu, T., Bao, Y., Johnson, S. G., and Chan, H. B., 2013, "Casimir Forces on a Silicon Micromechanical Chip," Nat Commun., **4**, p. 1845.

[31] Intravaia, F., Koev, S., Jung, I. W., Talin, A. A., Davids, P. S., Decca, R. S., Aksyuk, V. A., Dalvit, D. a. R., and López, D., 2013, "Strong Casimir Force Reduction through Metallic Surface Nanostructuring," Nat. Commun., **4**,

[32] Lambrecht, A. and Marachevsky, V. N., 2008, "Casimir Interaction of Dielectric Gratings," Phys. Rev. Lett., **101**, p. 160403.

[33] Bimonte, G., Emig, T., and Kardar, M., 2014, "Casimir-Polder Interaction for Gently Curved Surfaces," Phys. Rev. D, **90**, p. 081702.

[34] Rodriguez, A., Mccauley, A., Joannopoulos, J., and Johnson, S., 2009, "Casimir Forces in the Time Domain: Theory," Phys. Rev. A, **80**, p. 012115.

[35] Liu, X. L., Zhao, B., and Zhang, Z. M., 2015, "Enhanced near-Field Thermal Radiation and Reduced Casimir Stiction between Doped-Si Gratings," Phys. Rev. A, **91**, p. 062510.

[36] Chiu, H.-C., Klimchitskaya, G. L., Marachevsky, V. N., Mostepanenko, V. M., and Mohideen, U., 2009, "Demonstration of the Asymmetric Lateral Casimir Force between Corrugated Surfaces in the Nonadditive Regime," Phys. Rev. B, **80**, p. 121402.

[37] Chiu, H.-C., Klimchitskaya, G. L., Marachevsky, V. N., Mostepanenko, V. M., and Mohideen, U., 2010, "Lateral Casimir Force between Sinusoidally Corrugated Surfaces: Asymmetric Profiles, Deviations from the Proximity Force Approximation, and Comparison with Exact Theory," Phys. Rev. B, **81**, p. 115417.

[38] Banishev, A., Wagner, J., Emig, T., Zandi, R., and Mohideen, U., 2013, "Demonstration of Angle-Dependent Casimir Force between Corrugations," Phys. Rev. Lett., **110**, p. 250403.

[39] Banishev, A. A., Wagner, J., Emig, T., Zandi, R., and Mohideen, U., 2014, "Experimental and Theoretical Investigation of the Angular Dependence of the Casimir Force between Sinusoidally Corrugated Surfaces," Phys. Rev. B, **89**, p. 235436.

[40] Drosdoff, D. and Woods, L. M., 2014, "Quantum and Thermal Dispersion Forces: Application to Graphene Nanoribbons," Phys. Rev. Lett., **112**, p. 025501.

[41] Bordag, M., Klimchitskaya, G. L., and Mostepanenko, V. M., 2012, "Thermal Casimir Effect in the Interaction of Graphene with Dielectrics and Metals," Phys. Rev. B, **86**, p. 165429.

[42] Biehs, S. A. and Agarwal, G. S., 2014, "Anisotropy Enhancement of the Casimir-Polder Force between a Nanoparticle and Graphene," Phys. Rev. A, **90**, p. 042510.

[43] Volokitin, A. I. and Persson, B. N. J., 2013, "Influence of Electric Current on the Casimir Forces between Graphene Sheets," Europhys. Lett., **103**, p. 24002.

[44] Klimchitskaya, G. L., Mostepanenko, V. M., and Sernelius, B. E., 2014, "Two Approaches for Describing the Casimir Interaction in Graphene: Density-Density Correlation Function Versus Polarization Tensor," Phys. Rev. B, **89**, p. 125407.

[45] Sernelius, B. E., 2015, "Casimir Effects in Systems Containing 2d Layers Such as Graphene and 2d Electron Gases," J. Phys.: Condens. Matter, **27**, p. 214017.

[46] Sushkov, A. O., Kim, W. J., Dalvit, D. a. R., and Lamoreaux, S. K., 2011, "Observation of the Thermal Casimir Force," Nature Phys., **7**, p. 230.

[47] Guérout, R., Lussange, J., Chan, H. B., Lambrecht, A., and Reynaud, S., 2013, "Thermal Casimir Force between Nanostructured Surfaces," Phys. Rev. A, **87**, p. 052514.

[48] Brevik, I. and Høye, J. S., 2014, "Temperature Dependence of the Casimir Force," Eur. J. Phys., **35**, p. 015012.

[49] Decca, R. S., López, D., Fischbach, E., Klimchitskaya, G. L., Krause, D. E., and Mostepanenko, V. M., 2007, "Novel Constraints on Light Elementary Particles and Extra-Dimensional Physics from the Casimir Effect," Eur. Phys. J. C, **51**, p. 963.

[50] Chang, C.-C., Banishev, A. A., Castillo-Garza, R., Klimchitskaya, G. L., Mostepanenko, V. M., and Mohideen, U., 2012, "Gradient of the Casimir Force between Au Surfaces of a Sphere and a Plate Measured Using an Atomic Force Microscope in a Frequency-Shift Technique," Phys. Rev. B, **85**, p. 165443.

[51] Banishev, A. A., Klimchitskaya, G. L., Mostepanenko, V. M., and Mohideen, U., 2013, "Demonstration of the Casimir Force between Ferromagnetic Surfaces of a Ni-Coated Sphere and a Ni-Coated Plate," Phys. Rev. Lett., **110**, p. 137401.

[52] Wang, X. J., Wang, L. P., Adewuyi, O. S., Cola, B. A., and Zhang, Z. M., 2010, "Highly Specular Carbon Nanotube Absorbers," Appl. Phys. Lett., **97**, p. 163116.

[53] Ye, H., Wang, X. J., Lin, W., Wong, C. P., and Zhang, Z. M., 2012, "Infrared Absorption Coefficients of Vertically Aligned Carbon Nanotube Films," Appl. Phys. Lett, **101**, p. 141909.

[54] Liu, X. L. and Zhang, Z. M., 2013, "Metal-Free Low-Loss Negative Refraction in the Mid-Infrared Region," Appl. Phys. Lett., **103**, p. 103101.

[55] Liu, X. L., Wang, L. P., and Zhang, Z. M., 2013, "Wideband Tunable Omnidirectional Infrared Absorbers Based on Doped-Silicon Nanowire Arrays," J. Heat Transfer, **135**, p. 061602.

[56] Wang, X. J., Abell, J. L., Zhao, Y. P., and Zhang, Z. M., 2012, "Angle-Resolved Reflectance of Obliquely Aligned Silver Nanorods," Appl. Optics, **51**, pp. 1521-1531.

[57] Wang, X., 2012, "Study of the Radiative Properties of Aligned Carbon Nanotubes and Silver Nanorods," PhD thesis, Georgia Institute of Technology (Atlanta, Georgia, 2011).

[58] Basu, S., Lee, B. J., and Zhang, Z. M., 2010, "Infrared Radiative Properties of Heavily Doped Silicon at Room Temperature," J. Heat Transfer, **132**, p. 023301.

[59] Carr, G., Perkowitz, S., and Tanner, D., 1985, "Far-Infrared Properties of Inhomogeneous Materials," Infrared and millimeter waves., **13**, pp. 171-263.

[60] Bohren, C. F. and Huffman, D. R., 2008, Absorption and Scattering of Light by Small Particles: John Wiley & Sons.

[61] Cortes, C. L., Newman, W., Molesky, S., and Jacob, Z., 2012, "Quantum Nanophotonics Using Hyperbolic Metamaterials," J. Opt., **14**, p. 063001.

[62] Drachev, V. P., Podolskiy, V. A., and Kildishev, A. V., 2013, "Hyperbolic Metamaterials: New Physics Behind a Classical Problem," Opt. Express, **21**, pp. 15048-15064.

[63] Yao, J., Liu, Z. W., Liu, Y. M., Wang, Y., Sun, C., Bartal, G., Stacy, A. M., and Zhang, X., 2008, "Optical Negative Refraction in Bulk Metamaterials of Nanowires," Science, **321**, pp. 930-930.

[64] Liu, X. and Zhang, Z. M., 2013, "Metal-Free Low-Loss Negative Refraction," Appl. Phys. Lett.,

[65] Hoffman, A. J., Alekseyev, L., Howard, S. S., Franz, K. J., Wasserman, D., Podolskiy, V. A., Narimanov, E. E., Sivco, D. L., and Gmachl, C., 2007, "Negative Refraction in Semiconductor Metamaterials," Nat. Mater., **6**, pp. 946-950.

[66] Biehs, S. A., Tschikin, M., and Ben-Abdallah, P., 2012, "Hyperbolic Metamaterials as an Analog of a Blackbody in the near Field," Phys. Rev. Lett., **109**, p. 104301.

[67] Guo, Y., Cortes, C. L., Molesky, S., and Jacob, Z., 2012, "Broadband Super-Planckian Thermal Emission from Hyperbolic Metamaterials," Appl. Phys. Lett., **101**, p. 131106.

[68] Liu, X. L., Zhang, R. Z., and Zhang, Z. M., 2014, "Near-Field Radiative Heat Transfer with Doped-Silicon Nanostructured Metamaterials," International Journal of Heat and Mass Transfer, **73**, pp. 389-398.

[69] Liu, X. L., Zhang, R. Z., and Zhang, Z. M., 2013, "Near-Field Thermal Radiation between Hyperbolic Metamaterials: Graphite and Carbon Nanotubes," Appl. Phys. Lett., **103**, p. 213102.

[70] Philipp, H. R., 1977, "Infrared Optical Properties of Graphite," Phys. Rev. B, **16**, pp. 2896-2900.

[71] Draine, B. T. and Lee, H. M., 1984, "Optical-Properties of Interstellar Graphite and Silicate Grains," Astrophysical Journal, **285**, pp. 89-108.

[72] Callen, H. B. and Welton, T. A., 1951, "Irreversibility and Generalized Noise," Physical Review, **83**, p. 34.

[73] Lifshitz, E. and Pitaevskii, L.,1980, "Statistical Physics Part 2: Landau and Lifshitz Course of Theoretical Physics," ed: Pergamon Press, Oxford.

[74] Eroglu, A., 2010, Wave Propagation and Radiation in Gyrotropic and Anisotropic Media: Springer, New York.

[75] Zheng, Z. and Xuan, Y., 2011, "Theory of near-Field Radiative Heat Transfer for Stratified Magnetic Media," International Journal of Heat and Mass Transfer, **54**, pp. 1101-1110.

[76] Joulain, K., Drevillon, J., and Ben-Abdallah, P., 2010, "Noncontact Heat Transfer between Two Metamaterials," Physical Review B, **81**, p. 165119.

[77] Basu, S. and Francoeur, M., 2014, "Near-Field Radiative Heat Transfer between Metamaterial Thin Films," Optics Letters, **39**, pp. 1266-1269.

[78] Bai, Y., Jiang, Y., and Liu, L., 2014, "Role of Surface Plasmon Polaritons on the Enhancement of the near-Field Thermal Radiation from Fishnet Metamaterial," J. Phys. D: Appl. Phys. , **47**, p. 445304.

[79] Biehs, S.-A., Ben-Abdallah, P., and Rosa, F. S., edited by V. Morozhenko (InTech, Rijeka, Croatia, 2012), Chap. 1., "Nanoscale Radiative Heat Transfer and Its Applications," Infrared Radiation,

[80] Bimonte, G. and Santamato, E., 2007, "General Theory of Electromagnetic Fluctuations near a Homogeneous Surface in Terms of Its Reflection Amplitudes," Phys. Rev. A, **76**, p. 013810.

[81] Messina, R. and Antezza, M., 2011, "Casimir-Lifshitz Force out of Thermal Equilibrium and Heat Transfer between Arbitrary Bodies," Europhysics Letters, **95**, p. 61002.

[82] Guérout, R., Lussange, J., Rosa, F. S. S., Hugonin, J. P., Dalvit, D. a. R., Greffet, J. J., Lambrecht, A., and Reynaud, S., 2012, "Enhanced Radiative Heat Transfer between Nanostructured Gold Plates," Phys. Rev. B, **85**, p. 180301.

[83] Lussange, J., Guérout, R., Rosa, F. S. S., Greffet, J. J., Lambrecht, A., and Reynaud, S., 2012, "Radiative Heat Transfer between Two Dielectric Nanogratings in the Scattering Approach," Phys. Rev. B, **86**, p. 085432.

[84] Liu, X. L. and Zhang, Z. M., 2014, "Graphene-Assisted near-Field Radiative Heat Transfer between Corrugated Polar Materials," Appl. Phys. Lett., **104**, p. 251911.

[85] Didari, A. and Mengüç, M. P., 2014, "Analysis of near-Field Radiation Transfer within Nano-Gaps Using Fdtd Method," J. Quant. Spectrosc. Radiat. Transf., **146**, pp. 214-226.

[86] Datas, A., Hirashima, D., and Hanamura, K., 2013, "Fdtd Simulation of near-Field Radiative Heat Transfer between Thin Films Supporting Surface Phonon Polaritons: Lessons Learned," J. Therm. Sci. Technol., **8**, pp. 91-105.

[87] Rodriguez, A. W., Ilic, O., Bermel, P., Celanovic, I., Joannopoulos, J. D., Soljačić, M., and Johnson, S. G., 2011, "Frequency-Selective near-Field Radiative Heat Transfer between Photonic Crystal Slabs: A Computational Approach for Arbitrary Geometries and Materials," Phys. Rev. Lett., **107**, p. 114302.

[88] Otey, C. R., Zhu, L., Sandhu, S., and Fan, S., 2014, "Fluctuational Electrodynamics Calculations of near-Field Heat Transfer in Non-Planar Geometries: A Brief Overview," Journal of Quantitative Spectroscopy and Radiative Transfer, **132**, pp. 3-11.

[89] Luo, C., Narayanaswamy, A., Chen, G., and Joannopoulos, J. D., 2004, "Thermal Radiation from Photonic Crystals: A Direct Calculation," Phys. Rev. Lett., **93**, p. 213905.

[90] Chan, D. L. C., Soljačić, M., and Joannopoulos, J. D., 2006, "Thermal Emission and Design in One-Dimensional Periodic Metallic Photonic Crystal Slabs," Physical Review E, **74**, p. 016609.

[91] Lifshitz, E. M., 1956, "The Theory of Molecular Attractive Forces between Solids," Sov. Phys. JETP, **2**, p. 73.

[92] Dzyaloshinskii, I. E., Lifshitz, E. M., and Pitaevskii, L. P., 1961, "The General Theory of Van Der Waals Forces," Adv. Phys., **10**, p. 165.

[93] Zheng, Y. and Narayanaswamy, A., 2011, "Lifshitz Theory of Van Der Waals Pressure in Dissipative Media," Phys. Rev. A, **83**, p. 042504.

[94] Liu, X. L. and Zhang, Z. M., 2015, "Giant Enhancement of Nanoscale Thermal Radiation Based on Hyperbolic Graphene Plasmons," Appl. Phys. Lett., **107**, p. 143114.

[95] Liu, X. L. and Zhang, Z. M., 2015, "Near-Field Thermal Radiation between Metasurfaces," ACS Photonics, **2**, p. 1320.

[96] Pang, Y. T., Meng, G. W., Fang, Q., and Zhang, L. D., 2003, "Silver Nanowire Array Infrared Polarizers," Nanotechnol., **14**, pp. 20-24.

[97] Zhou, L. B. and Liu, W., 2005, "Broadband Polarizing Beam Splitter with an Embedded Metal-Wire Nanograting," Opt. Lett., **30**, pp. 1434-1436.

[98] Chen, Y. B., Lee, B. J., and Zhang, Z. M., 2008, "Infrared Radiative Properties of Submicron Metallic Slit Arrays," J. Heat Transf.-Trans. ASME, **130**, p. 082404.

[99] Ekinci, Y., Solak, H. H., David, C., and Sigg, H., 2006, "Bilayer Al Wire-Grids as Broadband and High-Performance Polarizers," Opt. Express, **14**, pp. 2323-2334.

[100] Ahn, S. W., Lee, K. D., Kim, J. S., Kim, S. H., Park, J. D., Lee, S. H., and Yoon, P. W., 2005, "Fabrication of a 50 Nm Half-Pitch Wire Grid Polarizer Using Nanoimprint Lithography," Nanotechnol., **16**, pp. 1874-1877.

[101] Chen, L., Wang, J. J., Walters, F., Deng, X. G., Buonanno, M., Tai, S., and Liu, X. M., 2007, "Large Flexible Nanowire Grid Visible Polarizer Made by Nanoimprint Lithography," Appl. Phys. Lett., **90**, p. 063111.

[102] Miyamaru, F. and Hangyo, M., 2005, "Anomalous Terahertz Transmission through Double-Layer Metal Hole Arrays by Coupling of Surface Plasmon Polaritons," Phys. Rev. B, **71**, p. 165408.

[103] Cheng, C., Chen, J., Shi, D. J., Wu, Q. Y., Ren, F. F., Xu, J., Fan, Y. X., Ding, J. P., and Wang, H. T., 2008, "Physical Mechanism of Extraordinary Electromagnetic Transmission in Dual-Metallic Grating Structures," Phys. Rev. B, **78**, p. 075406.

[104] Wang, L. P. and Zhang, Z. M., 2010, "Effect of Magnetic Polaritons on the Radiative Properties of Double-Layer Nanoslit Arrays," J. Opt. Soc. Am. B, **27**, pp. 2595-2604.

[105] Chan, H. B., Marcet, Z., Woo, K., Tanner, D. B., Carr, D. W., Bower, J. E., Cirelli, R. A., Ferry, E., Klemens, F., Miner, J., Pai, C. S., and Taylor, J. A., 2006, "Optical Transmission through Double-Layer Metallic Subwavelength Slit Arrays," Opt. Lett., **31**, pp. 516-518.

[106] Yang, Z. Y. and Lu, Y. F., 2007, "Broadband Nanowire-Grid Polarizers in Ultraviolet-Visible-near-Infrared Regions," Opt. Express, **15**, pp. 9510-9519.

[107] Peltzer, J. J., Flammer, P. D., Furtak, T. E., Collins, R. T., and Hollingsworth, R. E., 2011, "Ultra-High Extinction Ratio Micropolarizers Using Plasmonic Lenses," Opt. Express, **19**, pp. 18072-18079.

[108] Lee, B. J., Chen, Y. B., and Zhang, Z. M., 2008, "Transmission Enhancement through Nanoscale Metallic Slit Arrays from the Visible to Mid-Infrared," J. Comput. Theor. Nanosci., **5**, pp. 201-213.

[109] Modest, M. F., 2003, Radiative Heat Transfer, 2nd ed. San Diego: Academic Press.

[110] Palik, E. D., 1998, Handbook of Optical Constants of Solids 1. New York: Academic Press.

[111] Zhang, Z. M., Gentile, T. R., Migdall, A. L., and Datla, R. U., 1997, "Transmittance Measurements for Filters of Optical Density between One and Ten," Appl. Opt., **36**, pp. 8889-8895.

[112] Kang, G., Fang, Y., Vartiainen, I., Tan, Q., and Wang, Y., 2012, "Achromatic Polarization Splitting Effect of Metallic Gratings with Sub-50 Nm Wide Slits," Appl. Phys. Lett., **101**, p. 211104.

[113] Li, W.-D., Hu, J., and Chou, S. Y., 2011, "Extraordinary Light Transmission through Opaque Thin Metal Film with Subwavelength Holes Blocked by Metal Disks," Opt. Express, **19**, pp. 21098-21108.

[114] Zhao, Y., Belkin, M. A., and Alù, A., 2012, "Twisted Optical Metamaterials for Planarized Ultrathin Broadband Circular Polarizers," Nat. Commun., **3**, p. 870.

[115] Xie, S., Li, H., Fu, S., Xu, H., Zhou, X., and Liu, Z., 2010, "The Extraordinary Optical Transmission through Double-Layer Gold Slit Arrays," Opt. Commun., **283**, pp. 4017-4024.

[116] Ye, Z., Peng, Y., Zhai, T., Zhou, Y., and Liu, D., 2011, "Surface Plasmon-Mediated Transmission in Double-Layer Metallic Grating Polarizers," J. Opt. Soc. Am. B, **28**, pp. 502-507.

[117] Deng, L. Y., Teng, J. H., Zhang, L., Wu, Q. Y., Liu, H., Zhang, X. H., and Chua, S. J., 2012, "Extremely High Extinction Ratio Terahertz Broadband Polarizer Using Bilayer Subwavelength Metal Wire-Grid Structure," Appl. Phys. Lett., **101**, pp. 011101-011104.

[118] Huang, X.-R. and Peng, R.-W., 2010, "General Mechanism Involved in Subwavelength Optics of Conducting Microstructures: Charge-Oscillation-Induced Light Emission and Interference," J. Opt. Soc. Am. A, **27**, pp. 718-729.

[119] Wang, L. P. and Zhang, Z. M., 2012, "Wavelength-Selective and Diffuse Emitter Enhanced by Magnetic Polaritons for Thermophotovoltaics," Appl. Phys. Lett., **100**, p. 063902.

[120] Zhao, B., Wang, L. P., Shuai, Y., and Zhang, Z. M., 2013, "Thermophotovoltaic Emitters Based on a Two-Dimensional Grating/Thin-Film Nanostructure," Int. J. Heat Mass Transfer,

[121] Cui, Y. and He, S., 2009, "Enhancing Extraordinary Transmission of Light through a Metallic Nanoslit with a Nanocavity Antenna," Opt. Lett., **34**, pp. 16-18.

[122] García De Abajo, F. J., 2014, "Graphene Plasmonics: Challenges and Opportunities," ACS Photonics, **1**, pp. 135-152.

[123] Jablan, M., Soljacic, M., and Buljan, H., 2013, "Plasmons in Graphene: Fundamental Properties and Potential Applications," Proc. IEEE, **101**, pp. 1689-1704.

[124] Hadiseh, N. and Mohammad Sadegh, A., 2014, "Magnetically Tunable Focusing in a Graded Index Planar Lens Based on Graphene," J. Opt., **16**, p. 105502.

[125] Low, T. and Avouris, P., 2014, "Graphene Plasmonics for Terahertz to Mid-Infrared Applications," ACS Nano, **8**, pp. 1086-1101.

[126] Ilic, O., Jablan, M., Joannopoulos, J. D., Celanovic, I., Buljan, H., and Soljačić, M., 2012, "Near-Field Thermal Radiation Transfer Controlled by Plasmons in Graphene," Phys. Rev. B, **85**, p. 155422.

[127] Falkovsky, L. A., 2008, "Optical Properties of Graphene," J. Phys. Conf. Ser., **129**, p. 012004.

[128] Zhao, B. and Zhang, Z. M., 2014, "Study of Magnetic Polaritons in Deep Gratings for Thermal Emission Control," J. Quant. Spectrosc. Radiat. Transf., **135**, pp. 81-89.

[129] Liu, X. L., Zhao, B., and Zhang, Z. M., 2013, "Wide-Angle near Infrared Polarizer with Extremely High Extinction Ratio," Opt. Express, **21**, pp. 10502-10510.

[130] Wang, L. P. and Zhang, Z. M., 2009, "Resonance Transmission or Absorption in Deep Gratings Explained by Magnetic Polaritons," Appl. Phys. Lett., **95**, p. 111904.

[131] Liu, X. L., Zhang, R. Z., and Zhang, Z. M., 2014, "Near-Perfect Photon Tunneling by Hybridizing Graphene Plasmons and Hyperbolic Modes," ACS Photonics, **1**, pp. 785-789.

[132] Zhao, B., Zhao, J. M., and Zhang, Z. M., 2014, "Enhancement of near-Infrared Absorption in Graphene with Metal Gratings," Appl. Phys. Lett., **105**, p. 031905.

[133] Piper, J. R. and Fan, S., 2014, "Total Absorption in a Graphene Monolayer in the Optical Regime by Critical Coupling with a Photonic Crystal Guided Resonance," ACS Photonics, **1**, pp. 347-353.

[134] Lee, B. J., Wang, L. P., and Zhang, Z. M., 2008, "Coherent Thermal Emission by Excitation of Magnetic Polaritons between Periodic Strips and a Metallic Film," Opt. Express, **16**, pp. 11328-11336.

[135] Zhao, B., Wang, L., Shuai, Y., and Zhang, Z. M., 2013, "Thermophotovoltaic Emitters Based on a Two-Dimensional Grating/Thin-Film Nanostructure," Int. J. Heat Mass Transf., **67**, pp. 637-645.

[136] Wang, H., O'dea, K., and Wang, L., 2014, "Selective Absorption of Visible Light in Film-Coupled Nanoparticles by Exciting Magnetic Resonance," Opt. Lett., **39**, pp. 1457-1460.

[137] Feng, R., Qiu, J., Cao, Y., Liu, L., Ding, W., and Chen, L., 2014, "Omnidirectional and Polarization Insensitive Nearly Perfect Absorber in One Dimensional Meta-Structure," Appl. Phys. Lett., **105**, pp. -.

[138] Huang, X.-R., Peng, R.-W., and Fan, R.-H., 2010, "Making Metals Transparent for White Light by Spoof Surface Plasmons," Phys. Rev. Lett., **105**, p. 243901.

[139] Alu, A., D'aguanno, G., Mattiucci, N., and Bloemer, M. J., 2011, "Plasmonic Brewster Angle: Broadband Extraordinary Transmission through Optical Gratings," Phys. Rev. Lett., **106**, p. 123902.

[140] Alonso-González, P., Nikitin, A. Y., Golmar, F., Centeno, A., Pesquera, A., Vélez, S., Chen, J., Navickaite, G., Koppens, F., Zurutuza, A., Casanova, F., Hueso, L. E., and Hillenbrand, R., 2014, "Controlling Graphene Plasmons with Resonant Metal Antennas and Spatial Conductivity Patterns," Science, **344**, pp. 1369-1373.

[141] Yao, Y., Kats, M. A., Genevet, P., Yu, N., Song, Y., Kong, J., and Capasso, F., 2013, "Broad Electrical Tuning of Graphene-Loaded Plasmonic Antennas," Nano Lett., **13**, pp. 1257-1264.

[142] Slipchenko, T. M., Nesterov, M. L., Martin-Moreno, L., and Nikitin, A. Y., 2013, "Analytical Solution for the Diffraction of an Electromagnetic Wave by a Graphene Grating," J. Opt., **15**, p. 114008.

[143] Ju, L., Geng, B., Horng, J., Girit, C., Martin, M., Hao, Z., Bechtel, H. A., Liang, X., Zettl, A., and Shen, Y. R., 2011, "Graphene Plasmonics for Tunable Terahertz Metamaterials," Nature Nanotechnol., **6**, pp. 630-634.

[144] Feng, R., Qiu, J., Liu, L., Ding, W., and Chen, L., 2014, "Parallel Lc Circuit Model for Multi-Band Absorption and Preliminary Design of Radiative Cooling," Opt. Express, **22**, pp. A1713-A1724.

[145] Chen, Y. B. and Zhang, Z. M., 2007, "Design of Tungsten Complex Gratings for Thermophotovoltaic Radiators," Opt. Commun., **269**, pp. 411-417.

[146] Wang, H. and Wang, L., 2013, "Perfect Selective Metamaterial Solar Absorbers," Opt. Express, **21**, pp. A1078-A1093.

[147] Lee, B. J., Chen, Y. B., and Zhang, Z. M., 2008, "Confinement of Infrared Radiation to Nanometer Scales through Metallic Slit Arrays," J. Quant. Spectrosc. Radiat. Transf., **109**, pp. 608-619.

[148] Shalaev, V. M., 2007, "Optical Negative-Index Metamaterials," Nat. Photonics, **1**, pp. 41-48.

[149] Cai, W. S. and Shalaev, V. M., 2009, Optical Metamaterials: Fundamentals and Applications. New York: Springer.

[150] Shelby, R. A., Smith, D. R., and Schultz, S., 2001, "Experimental Verification of a Negative Index of Refraction," Science, **292**, pp. 77-79.

[151] Chettiar, U. K., Kildishev, A. V., Klar, T. A., and Shalaev, V. M., 2006, "Negative Index Metamaterial Combining Magnetic Resonators with Metal Films," Opt. Express, **14**, pp. 7872-7877.

[152] Zhang, S., Fan, W. J., Panoiu, N. C., Malloy, K. J., Osgood, R. M., and Brueck, S. R. J., 2005, "Experimental Demonstration of near-Infrared Negative-Index Metamaterials," Phys. Rev. Lett., **95**, p. 137404.

[153] Dolling, G., Wegener, M., Soukoulis, C. M., and Linden, S., 2007, "Negative-Index Metamaterial at 780 Nm Wavelength," Opt. Lett., **32**, pp. 53-55.

[154] García-Meca, C., Hurtado, J., Martí, J., Martínez, A., Dickson, W., and Zayats, A. V., 2011, "Low-Loss Multilayered Metamaterial Exhibiting a Negative Index of Refraction at Visible Wavelengths," Phys. Rev. Lett., **106**, p. 067402.

[155] Smith, D. R., Pendry, J. B., and Wiltshire, M. C. K., 2004, "Metamaterials and Negative Refractive Index," Science, **305**, pp. 788-792.

[156] Soukoulis, C. M., Kafesaki, M., and Economou, E. N., 2006, "Negative-Index Materials: New Frontiers in Optics," Adv. Mater., **18**, pp. 1941-1952.

[157] Pendry, J. B., 2000, "Negative Refraction Makes a Perfect Lens," Phys. Rev. Lett., **85**, pp. 3966-3969.

[158] Zhang, Z. and Lee, B. J., 2006, "Lateral Shift in Photon Tunneling Studied by the Energy Streamline Method," Opt. Express, **14**, pp. 9963-9970.

[159] Fang, N., Lee, H., Sun, C., and Zhang, X., 2005, "Sub-Diffraction-Limited Optical Imaging with a Silver Superlens," Science, **308**, pp. 534-537.

[160] Smith, D. R., Kolinko, P., and Schurig, D., 2004, "Negative Refraction in Indefinite Media," J. Opt. Soc. Am. B, **21**, pp. 1032-1043.

[161] Shin, H. and Fan, S., 2006, "All-Angle Negative Refraction and Evanescent Wave Amplification Using One-Dimensional Metallodielectric Photonic Crystals," Appl. Phys. Lett., **89**, p. 151102.

[162] Liu, Y. M., Bartal, G., and Zhang, X., 2008, "All-Angle Negative Refraction and Imaging in a Bulk Medium Made of Metallic Nanowires in the Visible Region," Opt. Express, **16**, pp. 15439-15448.

[163] Naik, G. V., Liu, J., Kildishev, A. V., Shalaev, V. M., and Boltasseva, A., 2012, "Demonstration of Al:Zno as a Plasmonic Component for near-Infrared Metamaterials," Proc. Nat. Acad. Sci. , **109**, p. 8834.

[164] Taubner, T., Korobkin, D., Urzhumov, Y., Shvets, G., and Hillenbrand, R., 2006, "Near-Field Microscopy through a Sic Superlens," Science, **313**, pp. 1595-1595.

[165] Liu, X. L., Wang, L. P., and Zhang, Z. M., 2013, "Wideband Tunable Omnidirectional Absorbers Based on Doped Silicon Nanowires," J. Heat Transfer,

[166] Wang, H., Liu, X. L., Wang, L. P., and Zhang, Z. M., 2013, "Anisotropic Optical Properties of Silicon Nanowire Arrays Based on Effective Medium Calculation," Int. J. Thermal Sciences, **65**, p. 62.

[167] Feng, S., 2012, "Loss-Induced Omnidirectional Bending to the Normal in ϵ-near-Zero Metamaterials," Phys. Rev. Lett., **108**, p. 193904.

[168] Sun, L., Feng, S., and Yang, X., 2012, "Loss Enhanced Transmission and Collimation in Anisotropic Epsilon-near-Zero Metamaterials," Appl. Phys. Lett, **101**, p. 241101.

[169] Landy, N. I., Sajuyigbe, S., Mock, J. J., Smith, D. R., and Padilla, W. J., 2008, "Perfect Metamaterial Absorber," Phys. Rev. Lett., **100**, p. 207402.

[170] Liu, N., Mesch, M., Weiss, T., Hentschel, M., and Giessen, H., 2010, "Infrared Perfect Absorber and Its Application as Plasmonic Sensor," Nano Lett, **10**, pp. 2342-2348.

[171] Chen, S. Q., Cheng, H., Yang, H. F., Li, J. J., Duan, X. Y., Gu, C. Z., and Tian, J. G., 2011, "Polarization Insensitive and Omnidirectional Broadband near Perfect Planar Metamaterial Absorber in the near Infrared Regime," Appl. Phys. Lett., **99**, p. 253104.

[172] Cui, Y., Xu, J., Fung, K. H., Jin, Y., Kumar, A., He, S., and Fang, N. X., 2011, "A Thin Film Broadband Absorber Based on Multi-Sized Nanoantennas," Appl. Phys. Lett., **99**, p. 253101.

[173] Hendrickson, J., Guo, J., Zhang, B., Buchwald, W., and Soref, R., 2012, "Wideband Perfect Light Absorber at Midwave Infrared Using Multiplexed Metal Structures," Opt. Lett., **37**, pp. 371-373.

[174] Wang, L. and Zhang, Z., 2013, "Measurement of Coherent Thermal Emission Due to Magnetic Polaritons in Subwavelength Microstructures," Journal of Heat Transfer, **135**, p. 091505.

[175] Yang, Z.-P., Ci, L., Bur, J. A., Lin, S.-Y., and Ajayan, P. M., 2008, "Experimental Observation of an Extremely Dark Material Made by a Low-Density Nanotube Array," Nano Lett., **8**, pp. 446-451.

[176] Mizuno, K., Ishii, J., Kishida, H., Hayamizu, Y., Yasuda, S., Futaba, D. N., Yumura, M., and Hata, K., 2009, "A Black Body Absorber from Vertically Aligned Single-Walled Carbon Nanotubes," Proc. Natl. Acad. Sci. USA., **106**, pp. 6044-6047.

[177] Lehman, J., Sanders, A., Hanssen, L., Wilthan, B., Zeng, J. A., and Jensen, C., 2010, "Very Black Infrared Detector from Vertically Aligned Carbon Nanotubes and Electric-Field Poling of Lithium Tantalate," Nano Lett., **10**, pp. 3261-3266.

[178] Zhang, R. Z., Liu, X., and Zhang, Z. M., 2015, "Modeling the Optical and Radiative Properties of Vertically Aligned Carbon Nanotubes in the Infrared Region," Journal of Heat Transfer, **137**, p. 091009.

[179] Wu, Y., Cui, Y., Huynh, L., Barrelet, C. J., Bell, D. C., and Lieber, C. M., 2004, "Controlled Growth and Structures of Molecular-Scale Silicon Nanowires," Nano Letters, **4**, pp. 433-436.

[180] Ke, Y., Weng, X., Redwing, J. M., Eichfeld, C. M., Swisher, T. R., Mohney, S. E., and Habib, Y. M., 2009, "Fabrication and Electrical Properties of Si Nanowires Synthesized by Al Catalyzed Vapor−Liquid−Solid Growth," Nano Lett., **9**, pp. 4494-4499.

[181] Chou, L.-W., Shin, N., Sivaram, S. V., and Filler, M. A., 2012, "Tunable Mid-Infrared Localized Surface Plasmon Resonances in Silicon Nanowires," Journal of the American Chemical Society, **134**, pp. 16155-16158.

[182] Shin, N., Chi, M., Howe, J. Y., and Filler, M. A., 2013, "Rational Defect Introduction in Silicon Nanowires," Nano letters, **13**, pp. 1928-1933.

[183] Yu, D. P., Bai, Z. G., Ding, Y., Hang, Q. L., Zhang, H. Z., Wang, J. J., Zou, Y. H., Qian, W., Xiong, G. C., Zhou, H. T., and Feng, S. Q., 1998, "Nanoscale Silicon Wires Synthesized Using Simple Physical Evaporation," Appl. Phys. Lett., **72**, pp. 3458-3460.

[184] Colli, A., Fasoli, A., Beecher, P., Servati, P., Pisana, S., Fu, Y., Flewitt, A., Milne, W., Robertson, J., and Ducati, C., 2007, "Thermal and Chemical Vapor Deposition of Si Nanowires: Shape Control, Dispersion, and Electrical Properties," J. Appl. Phys., **102**, p. 034302.

[185] Mallet, J., Molinari, M., Martineau, F., Delavoie, F., Fricoteaux, P., and Troyon, M., 2008, "Growth of Silicon Nanowires of Controlled Diameters by Electrodeposition in Ionic Liquid at Room Temperature," Nano Lett., **8**, pp. 3468-3474.

[186] Huang, Z., Fang, H., and Zhu, J., 2007, "Fabrication of Silicon Nanowire Arrays with Controlled Diameter, Length, and Density," Advanced Materials, **19**, pp. 744-748.

[187] Choi, W. K., Liew, T. H., Dawood, M. K., Smith, H. I., Thompson, C. V., and Hong, M. H., 2008, "Synthesis of Silicon Nanowires and Nanofin Arrays Using Interference Lithography and Catalytic Etching," Nano Lett., **8**, pp. 3799-3802.

[188] Hsu, C. M., Connor, S. T., Tang, M. X., and Cui, Y., 2008, "Wafer-Scale Silicon Nanopillars and Nanocones by Langmuir-Blodgett Assembly and Etching," Appl. Phys. Lett., **93**,

[189] Laroche, M., Carminati, R., and Greffet, J. J., 2006, "Near-Field Thermophotovoltaic Energy Conversion," J. Appl. Phys., **100**, p. 063704.

[190] Park, K., Basu, S., King, W. P., and Zhang, Z. M., 2008, "Performance Analysis of near-Field Thermophotovoltaic Devices Considering Absorption Distribution," Journal of Quantitative Spectroscopy and Radiative Transfer, **109**, pp. 305-316.

[191] Narayanaswamy, A. and Chen, G., 2003, "Surface Modes for near Field Thermophotovoltaics," Appl. Phys. Lett., **82**, pp. 3544-3546.

[192] Francoeur, M., Vaillon, R., and Mengüç, M. P., 2011, "Thermal Impacts on the Performance of Nanoscale-Gap Thermophotovoltaic Power Generators," IEEE Trans. Energy Convers., **26**, pp. 686-698.

[193] Ilic, O., Jablan, M., Joannopoulos, J. D., Celanovic, I., and Soljačić, M., 2012, "Overcoming the Black Body Limit in Plasmonic and Graphene near-Field Thermophotovoltaic Systems," Optics Express, **20**, pp. A366-A384.

[194] Messina, R. and Ben-Abdallah, P., 2013, "Graphene-Based Photovoltaic Cells for near-Field Thermal Energy Conversion," Sci. Rep., **3**,

[195] De Wilde, Y., Formanek, F., Carminati, R., Gralak, B., Lemoine, P. A., Joulain, K., Mulet, J. P., Chen, Y., and Greffet, J. J., 2006, "Thermal Radiation Scanning Tunnelling Microscopy," Nature, **444**, pp. 740-743.

[196] Kittel, A., Muller-Hirsch, W., Parisi, J., Biehs, S. A., Reddig, D., and Holthaus, M., 2005, "Near-Field Heat Transfer in a Scanning Thermal Microscope," Phys. Rev. Lett., **95**, p. 224301.

[197] Otey, C. R., Lau, W. T., and Fan, S., 2010, "Thermal Rectification through Vacuum," Phys. Rev. Lett., **104**, p. 154301.

[198] Basu, S. and Francoeur, M., 2011, "Near-Field Radiative Transfer Based Thermal Rectification Using Doped Silicon," Appl. Phys. Lett., **98**, p. 113106.

[199] Iizuka, H. and Fan, S., 2012, "Rectification of Evanescent Heat Transfer between Dielectric-Coated and Uncoated Silicon Carbide Plates," J. Appl. Phys., **112**, p. 024304.

[200] Wang, L. P. and Zhang, Z. M., 2013, "Thermal Rectification Enabled by near-Field Radiative Heat Transfer between Intrinsic Silicon and Other Materials," Nanoscale and Microscale Thermophysical Engineering,

[201] Huang, J. G., Li, Q., Zheng, Z. H., and Xuan, Y. M., 2013, "Thermal Rectification Based on Thermochromic Materials," Int. J. Heat Mass Transf., **67**, pp. 575-580.

[202] Biehs, S.-A., Rosa, F. S. S., and Ben-Abdallah, P., 2011, "Modulation of near-Field Heat Transfer between Two Gratings," Appl. Phys. Lett., **98**, p. 243102.

[203] Cui, L., Huang, Y., Wang, J., and Zhu, K.-Y., 2013, "Ultrafast Modulation of near-Field Heat Transfer with Tunable Metamaterials," Appl. Phys. Lett., **102**, p. 053106.

[204] Van Zwol, P. J., Ranno, L., and Chevrier, J., 2012, "Tuning near Field Radiative Heat Flux through Surface Excitations with a Metal Insulator Transition," Phys. Rev. Lett., **108**, p. 234301.

[205] Guha, B., Otey, C., Poitras, C. B., Fan, S., and Lipson, M., 2012, "Near-Field Radiative Cooling of Nanostructures," Nano Lett., **12**, pp. 4546-4550.

[206] Tschikin, M., Biehs, S. A., Rosa, F. S. S., and Ben-Abdallah, P., 2012, "Radiative Cooling of Nanoparticles Close to a Surface," Eur. Phys. J. B, **85**, p. 233.

[207] Wang, X. J., Basu, S., and Zhang, Z. M., 2009, "Parametric Optimization of Dielectric Functions for Maximizing Nanoscale Radiative Transfer," J. Phys. D-Appl. Phys., **42**, p. 245403.

[208] Biehs, S. A., Ben-Abdallah, P., Rosa, F. S. S., Joulain, K., and Greffet, J. J., 2011, "Nanoscale Heat Flux between Nanoporous Materials," Opt. Express, **19**, pp. A1088-A1103.

[209] Biehs, S.-A., Tschikin, M., Messina, R., and Ben-Abdallah, P., 2013, "Super-Planckian near-Field Thermal Emission with Phonon-Polaritonic Hyperbolic Metamaterials," Appl. Phys. Lett., **102**, p. 131106.

[210] Tschikin, M., Biehs, S. A., Messina, R., and Ben-Abdallah, P., 2013, "On the Limits of the Effective Description of Hyperbolic Materials in the Presence of Surface Waves," J. Opt., **15**, p. 105101.

[211] Basu, S., Lee, B. J., and Zhang, Z. M., 2010, "Near-Field Radiation Calculated with an Improved Dielectric Function Model for Doped Silicon," J. Heat Transfer, **132**, p. 023302.

[212] Rousseau, E., Laroche, M., and Greffet, J.-J., 2010, "Radiative Heat Transfer at Nanoscale: Closed-Form Expression for Silicon at Different Doping Levels," J. Quant. Spectrosc. Radiat. Transf., **111**, pp. 1005-1014.

[213] Shi, J., Li, P., Liu, B., and Shen, S., 2013, "Tuning near Field Radiation by Doped Silicon," Appl. Phys. Lett., **102**, p. 183114.

[214] Basu, S. and Wang, L., 2013, "Near-Field Radiative Heat Transfer between Doped Silicon Nanowire Arrays," Appl. Phys. Lett., **102**, p. 053101.

[215] Rosa, F. S. S., Dalvit, D. a. R., and Milonni, P. W., 2008, "Casimir Interactions for Anisotropic Magnetodielectric Metamaterials," Phys. Rev. A, **78**, p. 032117.

[216] Malone, C. G., Choi, B. I., Flik, M. I., and Cravalho, E. G., 1993, "Spectral Emissivity of Optically Anisotropic Solid Media," J. Heat Transfer, **115**, pp. 1021-1028.

[217] Fu, C. and Zhang, Z., 2006, "Nanoscale Radiation Heat Transfer for Silicon at Different Doping Levels," International Journal of Heat and Mass Transfer, **49**, pp. 1703-1718.

[218] Kidwai, O., Zhukovsky, S. V., and Sipe, J. E., 2012, "Effective-Medium Approach to Planar Multilayer Hyperbolic Metamaterials: Strengths and Limitations," Phys. Rev. A, **85**, p. 053842.

[219] Marquier, F., Laroche, M., Carminati, R., and Greffet, J. J., 2007, "Anisotropic Polarized Emission of a Doped Silicon Lamellar Grating," J. Heat Transfer, **129**, p. 11.

[220] Jones, A. C. and Raschke, M. B., 2012, "Thermal Infrared near-Field Spectroscopy," Nano Lett., **12**, pp. 1475-1481.

[221] Ben-Abdallah, P. and Biehs, S.-A., 2014, "Near-Field Thermal Transistor," Phys. Rev. Lett., **112**, p. 044301.

[222] Shen, S., Narayanaswamy, A., and Chen, G., 2009, "Surface Phonon Polaritons Mediated Energy Transfer between Nanoscale Gaps," Nano Letters, **9**, pp. 2909-2913.

[223] Francoeur, M., Basu, S., and Petersen, S. J., 2011, "Electric and Magnetic Surface Polariton Mediated near-Field Radiative Heat Transfer between Metamaterials Made of Silicon Carbide Particles," Opt. Express, **19**, pp. 18774-18788.

[224] Grigorenko, A. N., Polini, M., and Novoselov, K. S., 2012, "Graphene Plasmonics," Nat. Photonics, **6**, pp. 749-758.

[225] Van Zwol, P. J., Thiele, S., Berger, C., De Heer, W. A., and Chevrier, J., 2012, "Nanoscale Radiative Heat Flow Due to Surface Plasmons in Graphene and Doped Silicon," Phys. Rev. Lett., **109**, p. 264301.

[226] Lim, M., Lee, S. S., and Lee, B. J., 2013, "Near-Field Thermal Radiation between Graphene-Covered Doped Silicon Plates," Optics Express, **21**, pp. 22173-22185.

[227] Volokitin, A. I. and Persson, B. N. J., 2011, "Near-Field Radiative Heat Transfer between Closely Spaced Graphene and Amorphous Sio(2)," Physical Review B, **83**, p. 241407(R).

[228] Svetovoy, V. B., Van Zwol, P. J., and Chevrier, J., 2012, "Plasmon Enhanced near-Field Radiative Heat Transfer for Graphene Covered Dielectrics," Physical Review B, **85**, p. 155418.

[229] Ilic, O., Jablan, M., Joannopoulos, J. D., Celanovic, I., and Soljačić, M., 2012, "Overcoming the Black Body Limit in Plasmonic and Graphene near-Field Thermophotovoltaic Systems," Opt. Express, **20**, pp. A366-A384.

[230] Liu, B. and Shen, S., 2013, "Broadband near-Field Radiative Thermal Emitter/Absorber Based on Hyperbolic Metamaterials: Direct Numerical Simulation by the Wiener Chaos Expansion Method," Phys. Rev. B, **87**, p. 115403.

[231] Fan, G., Zhu, H., Wang, K., Wei, J., Li, X., Shu, Q., Guo, N., and Wu, D., 2011, "Graphene/Silicon Nanowire Schottky Junction for Enhanced Light Harvesting," ACS Appl. Mater. Interfaces, **3**, pp. 721-725.

[232] Jablan, M., Buljan, H., and Soljačić, M., 2009, "Plasmonics in Graphene at Infrared Frequencies," Phys. Rev. B, **80**, p. 245435.

[233] Wang, B., Zhang, X., Yuan, X., and Teng, J., 2012, "Optical Coupling of Surface Plasmons between Graphene Sheets," Appl. Phys. Lett., **100**, p. 131111.

[234] Guo, Y. and Jacob, Z., 2013, "Thermal Hyperbolic Metamaterials," Optics Express, **21**, pp. 15014-15019.

[235] Liu, B., Shi, J., Liew, K., and Shen, S., 2014, "Near-Field Radiative Heat Transfer for Si Based Metamaterials," Opt. Commun., **314**, pp. 57-65.

[236] Zhang, R. Z., Liu, X., and Zhang, Z. M., 2015, "Near-Field Radiation between Graphene-Covered Carbon Nanotube Arrays," AIP Advances, **5**, p. 053501.

[237] Orlov, A. A., Voroshilov, P. M., Belov, P. A., and Kivshar, Y. S., 2011, "Engineered Optical Nonlocality in Nanostructured Metamaterials," Physical Review B, **84**, p. 045424.

[238] Bright, T. J., Liu, X. L., and Zhang, Z. M., 2014, "Energy Streamlines in near-Field Radiative Heat Transfer between Hyperbolic Metamaterials," Opt. Express,

[239] Basu, S. and Zhang, Z. M., 2009, "Ultrasmall Penetration Depth in Nanoscale Thermal Radiation," Appl. Phys. Lett., **95**, p. 133104.

[240] Mulet, J.-P., Joulain, K., Carminati, R., and Greffet, J.-J., 2002, "Enhanced Radiative Heat Transfer at Nanometric Distances," Microscale Thermophys. Eng., **6**, pp. 209-222.

[241] Francoeur, M., Mengüç, M. P., and Vaillon, R., 2011, "Coexistence of Multiple Regimes for near-Field Thermal Radiation between Two Layers Supporting Surface Phonon Polaritons in the Infrared," Phys. Rev. B, **84**, p. 075436.

[242] Shen, S., Mavrokefalos, A., Sambegoro, P., and Chen, G., 2012, "Nanoscale Thermal Radiation between Two Gold Surfaces," Appl. Phys. Lett., **100**, p. 233114.

[243] Basu, S. and Zhang, Z. M., 2009, "Maximum Energy Transfer in near-Field Thermal Radiation at Nanometer Distances," J. Appl. Phys., **105**, p. 093535.

[244] Francoeur, M. and Mengüç, M. P., 2008, "Role of Fluctuational Electrodynamics in near-Field Radiative Heat Transfer," J. Quant. Spectrosc. Radiat. Transf., **109**, pp. 280-293.

[245] Kildishev, A. V., Boltasseva, A., and Shalaev, V. M., 2013, "Planar Photonics with Metasurfaces," Science, **339**, p. 1232009.

[246] Dabidian, N., Kholmanov, I., Khanikaev, A. B., Tatar, K., Trendafilov, S., Mousavi, S. H., Magnuson, C., Ruoff, R. S., and Shvets, G., 2015, "Electrical Switching of Infrared Light Using Graphene Integration with Plasmonic Fano Resonant Metasurfaces," ACS Photon., **2**, pp. 216-227.

[247] Aydin, K., Ferry, V. E., Briggs, R. M., and Atwater, H. A., 2011, "Broadband Polarization-Independent Resonant Light Absorption Using Ultrathin Plasmonic Super Absorbers," Nat. Commun., **2**, p. 517.

[248] Alali, F., Kim, Y. H., Baev, A., and Furlani, E. P., 2014, "Plasmon-Enhanced Metasurfaces for Controlling Optical Polarization," ACS Photon., **1**, pp. 507-515.

[249] Campione, S., Guclu, C., Ragan, R., and Capolino, F., 2014, "Enhanced Magnetic and Electric Fields Via Fano Resonances in Metasurfaces of Circular Clusters of Plasmonic Nanoparticles," ACS Photon., **1**, pp. 254-260.

[250] Chalabi, H., Hasman, E., and Brongersma, M. L., 2015, "Effect of Shape in near-Field Thermal Transfer for Periodic Structures," Physical Review B, **91**, p. 174304.

[251] Chalabi, H., Hasman, E., and Brongersma, M. L., 2015, "Near-Field Radiative Thermal Transfer between a Nanostructured Periodic Material and a Planar Substrate," Phys. Rev. B, **91**, p. 014302.

[252] Francoeur, M., Mengüç, M. P., and Vaillon, R., 2008, "Near-Field Radiative Heat Transfer Enhancement Via Surface Phonon Polaritons Coupling in Thin Films," Appl. Phys. Lett., **93**, p. 043109.

[253] Liu, X. L., Bright, T. J., and Zhang, Z. M., 2014, "Application Conditions of Effective Medium Theory in near-Field Radiative Heat Transfer between Multilayered Metamaterials," J. Heat Transfer, **136**, p. 092703.

[254] Miller, O. D., Johnson, S. G., and Rodriguez, A. W., 2014, "Effectiveness of Thin Films in Lieu of Hyperbolic Metamaterials in the near Field," Phys. Rev. Lett., **112**, p. 157402.

[255] Gomez-Diaz, J. S., Tymchenko, M., and Alù, A., 2015, "Hyperbolic Plasmons and Topological Transitions over Uniaxial Metasurfaces," Phys. Rev. Lett., **114**, p. 233901.

[256] Patel, A. M. and Grbic, A., 2013, "Modeling and Analysis of Printed-Circuit Tensor Impedance Surfaces," IEEE Trans. Antennas Propag., **61**, pp. 211-220.

[257] Liu, Y. and Zhang, X., 2013, "Metasurfaces for Manipulating Surface Plasmons," Appl. Phys. Lett., **103**, p. 141101.

[258] Thongrattanasiri, S., Manjavacas, A., and García De Abajo, F. J., 2012, "Quantum Finite-Size Effects in Graphene Plasmons," ACS Nano, **6**, pp. 1766-1775.

[259] Weinstein, M., 1960, "Thermodynamic Limitation on the Conversion of Heat into Light," Journal of the Optical Society of America A, **50**, pp. 597-602.

[260] Dousmanis, G., Mueller, C., Nelson, H., and Petzinger, K., 1964, "Evidence of Refrigerating Action by Means of Photon Emission in Semiconductor Diodes," Physical Review, **133**, p. A316.

[261] Santhanam, P., Gray Jr, D. J., and Ram, R. J., 2012, "Thermoelectrically Pumped Light-Emitting Diodes Operating above Unity Efficiency," Phys. Rev. Lett., **108**, p. 097403.

[262] Yen, S.-T. and Lee, K.-C., 2010, "Analysis of Heterostructures for Electroluminescent Refrigeration and Light Emitting without Heat Generation," J. Appl. Phys., **107**, p. 054513.

[263] Berdahl, P., 1985, "Radiant Refrigeration by Semiconductor Diodes," J. Appl. Phys., **58**, pp. 1369-1374.

[264] Heikkilä, O., Oksanen, J., and Tulkki, J., 2010, "The Challenge of Unity Wall Plug Efficiency: The Effects of Internal Heating on the Efficiency of Light Emitting Diodes," J. Appl. Phys., **107**, p. 033105.

[265] Gray Jr, D. J., Santhanam, P., and Ram, R. J., 2013, "Design for Enhanced Thermo-Electric Pumping in Light Emitting Diodes," Appl. Phys. Lett., **103**, p. 123503.

[266] Lee, K.-C. and Yen, S.-T., 2012, "Photon Recycling Effect on Electroluminescent Refrigeration," J. Appl. Phys., **111**, p. 014511.

[267] Mal'shukov, A. and Chao, K., 2001, "Opto-Thermionic Refrigeration in Semiconductor Heterostructures," Phys. Rev. Lett., **86**, p. 5570.

[268] Han, P., Jin, K.-J., Zhou, Y., Wang, X., Ma, Z., Ren, S.-F., Mal'shukov, A., and Chao, K.-A., 2006, "Analysis of Optothermionic Refrigeration Based on Semiconductor Heterojunction," J. Appl. Phys., **99**, p. 074504.

[269] Yu, S.-Q., Wang, J.-B., Ding, D., Johnson, S., Vasileska, D., and Zhang, Y.-H., 2007, "Impact of Electronic Density of States on Electroluminescence Refrigeration," Solid-State Electronics, **51**, pp. 1387-1390.

[270] Oksanen, J. and Tulkki, J., 2010, "Thermophotonic Heat Pump—a Theoretical Model and Numerical Simulations," J. Appl. Phys., **107**, p. 093106.

[271] Xuan, Y. M., 2014, "An Overview of Micro/Nanoscaled Thermal Radiation and Its Applications," Photonics and Nanostructures - Fundamentals and Applications, **12**, pp. 93-113.

[272] Shen, S., 2013, "Experimental Studies of Radiative Heat Transfer between Bodies at Small Separations," Annual Review of Heat Transfer, **16**, pp. 327-343.

[273] Liu, X. L., Wang, L. P., and Zhang, Z. M., 2015, "Near-Field Thermal Radiation: Recent Progress and Outlook," Nanoscale and Microscale Thermophysical Engineering, **19**, pp. 98-126.

[274] Rousseau, E., Siria, A., Jourdan, G., Volz, S., Comin, F., Chevrier, J., and Greffet, J. J., 2009, "Radiative Heat Transfer at the Nanoscale," Nat. Photonics, **3**, pp. 514-517.

[275] St-Gelais, R., Guha, B., Zhu, L., Fan, S., and Lipson, M., 2014, "Demonstration of Strong near-Field Radiative Heat Transfer between Integrated Nanostructures," Nano Letters, **14**, pp. 6971-6975.

[276] Song, B., Ganjeh, Y., Sadat, S., Thompson, D., Fiorino, A., Fernández-Hurtado, V., Feist, J., Garcia-Vidal, F. J., Cuevas, J. C., Reddy, P., and Meyhofer, E., 2015, "Enhancement of near-Field Radiative Heat Transfer Using Polar Dielectric Thin Films," Nature Nanotechnology, **10**, pp. 253-258.

[277] Shi, J., Liu, B., Li, P., Ng, L. Y., and Shen, S., 2015, "Near-Field Energy Extraction with Hyperbolic Metamaterials," Nano letters, **15**, pp. 1217-1221.

[278] Kim, K., Song, B., Fernández-Hurtado, V., Lee, W., Jeong, W., Cui, L., Thompson, D., Feist, J., Reid, M. H., and García-Vidal, F. J., 2015, "Radiative Heat Transfer in the Extreme near Field," Nature, **528**, pp. 387-391.

[279] Chen, K., Santhanam, P., Sandhu, S., Zhu, L., and Fan, S., 2015, "Heat-Flux Control and Solid-State Cooling by Regulating Chemical Potential of Photons in near-Field Electromagnetic Heat Transfer," Physical Review B, **91**, p. 134301.

[280] Ferrini, R., Patrini, M., and Franchi, S., 1998, "Optical Functions from 0.02 to 6 Ev of Alxga1− Xsb/Gasb Epitaxial Layers," J. Appl. Phys., **84**, pp. 4517-4524.

[281] Wakaki, M., Shibuya, T., and Kudo, K., 2007, Physical Properties and Data of Optical Materials. Beijing: CRC Press.

[282] Chen, K., Santhanam, P., and Fan, S., 2015, "Suppressing Sub-Bandgap Phonon-Polariton Heat Transfer in near-Field Thermophotovoltaic Devices for Waste Heat Recovery," Appl. Phys. Lett., **107**, p. 091106.

[283] Hu, Z., Perera, A., Paltiel, Y., Raizman, A., and Sher, A., 2005, "Zn-Doped Gasb Epitaxial Film Absorption Coefficients at Terahertz Frequencies and Detector Applications," J. Appl. Phys., **98**, p. 023511.

[284] Wurfel, P., 1982, "The Chemical Potential of Radiation," Journal of Physics C: Solid State Physics, **15**, p. 3967.

[285] Henry, C. H. and Kazarinov, R. F., 1996, "Quantum Noise in Photonics," Reviews of Modern Physics, **68**, p. 801.

[286] Sipe, J. E., 1987, "New Green-Function Formalism for Surface Optics," J. Opt. Soc. Am. B-Opt. Phys., **4**, pp. 481-489.

[287] Francoeur, M., Mengüç, M. P., and Vaillon, R., 2009, "Solution of near-Field Thermal Radiation in One-Dimensional Layered Media Using Dyadic Green's Functions and the Scattering Matrix Method," Journal of Quantitative Spectroscopy and Radiative Transfer, **110**, pp. 2002-2018.

[288] Stollwerck, G., Sulima, O. V., and Bett, A. W., 2000, "Characterization and Simulation of Gasb Device-Related Properties," IEEE Transactions on Electron Devices, **47**, pp. 448-457.

[289] Loomis, J. J. and Maris, H. J., 1994, "Theory of Heat Transfer by Evanescent Electromagnetic Waves," Phys. Rev. B, **50**, pp. 18517-18524.

[290] Zhukovsky, S. V., Kidwai, O., and Sipe, J. E., 2013, "Physical Nature of Volume Plasmon Polaritons in Hyperbolic Metamaterials," Opt. Express, **21**, pp. 14982-14987.

[291] Pirozhenko, I. and Lambrecht, A., 2008, "Influence of Slab Thickness on the Casimir Force," Phys. Rev. A, **77**, p. 013811.

[292] Boyer, T., 1974, "Van Der Waals Forces and Zero-Point Energy for Dielectric and Permeable Materials," Phys. Rev. A, **9**, pp. 2078-2084.

[293] Kenneth, O., Klich, I., Mann, A., and Revzen, M., 2002, "Repulsive Casimir Forces," Phys. Rev. Lett., **89**, p. 033001.

[294] Rosa, F. S. S., Dalvit, D. a. R., and Milonni, P. W., 2008, "Casimir-Lifshitz Theory and Metamaterials," Phys. Rev. Lett., **100**, p. 183602.

[295] Zhao, R., Zhou, J., Koschny, T., Economou, E., and Soukoulis, C., 2009, "Repulsive Casimir Force in Chiral Metamaterials," Phys. Rev. Lett., **103**, p. 103602.

[296] Pappakrishnan, V. K., Mundru, P. C., and Genov, D. A., 2014, "Repulsive Casimir Force in Magnetodielectric Plate Configurations," Phys. Rev. B, **89**, p. 045430.

[297] Yang, Y., Zeng, R., Xu, J., and Liu, S., 2008, "Casimir Force between Left-Handed-Material Slabs," Phys. Rev. A, **77**, p. 015803.

[298] Ulf, L. and Thomas, G. P., 2007, "Quantum Levitation by Left-Handed Metamaterials," New J. Phys., **9**, p. 254.

[299] Rodriguez-Lopez, P. and Grushin, A. G., 2014, "Repulsive Casimir Effect with Chern Insulators," Phys. Rev. Lett., **112**, p. 056804.

[300] Mccauley, A., Zhao, R., Reid, M., Rodriguez, A., Zhou, J., Rosa, F., Joannopoulos, J., Dalvit, D., Soukoulis, C., and Johnson, S., 2010, "Microstructure Effects for Casimir Forces in Chiral Metamaterials," Phys. Rev. B, **82**, p. 165108.

[301] Geyer, B., Klimchitskaya, G. L., and Mostepanenko, V. M., 2010, "Thermal Casimir Interaction between Two Magnetodielectric Plates," Phys. Rev. B, **81**, p. 104101.

[302] Antezza, M., Pitaevskii, L. P., and Stringari, S., 2005, "New Asymptotic Behavior of the Surface-Atom Force out of Thermal Equilibrium," Phys. Rev. Lett., **95**, p. 113202.

[303] Rahi, S. J., Kardar, M., and Emig, T., 2010, "Constraints on Stable Equilibria with Fluctuation-Induced (Casimir) Forces," Phys. Rev. Lett., **105**, p. 070404.

[304] Levin, M., Mccauley, A. P., Rodriguez, A. W., Reid, M. H., and Johnson, S. G., 2010, "Casimir Repulsion between Metallic Objects in Vacuum," Phys. Rev. Lett., **105**, p. 090403.

[305] Krüger, M., Bimonte, G., Emig, T., and Kardar, M., 2012, "Trace Formulas for Nonequilibrium Casimir Interactions, Heat Radiation, and Heat Transfer for Arbitrary Objects," Phys. Rev. B, **86**, p. 115423.

[306] Rodriguez, A., Munday, J., Joannopoulos, J., Capasso, F., Dalvit, D., and Johnson, S., 2008, "Stable Suspension and Dispersion-Induced Transitions from Repulsive Casimir Forces between Fluid-Separated Eccentric Cylinders," Phys. Rev. Lett., **101**, p. 190404.

[307] Dou, M., Lou, F., Boström, M., Brevik, I., and Persson, C., 2014, "Casimir Quantum Levitation Tuned by Means of Material Properties and Geometries," Phys. Rev. B, **89**, p. 201407.

[308] Phan, A. D., Woods, L. M., Drosdoff, D., Bondarev, I., and Viet, N., 2012, "Temperature Dependent Graphene Suspension Due to Thermal Casimir Interaction," Appl. Phys. Lett., **101**, p. 113118.

[309] Inui, N., 2014, "Levitation of a Metallic Sphere near Gas-Liquid and Liquid-Liquid Interfaces by the Repulsive Casimir Force," Phys. Rev. A, **89**, p. 062506.

[310] Klimchitskaya, G. L., Mohideen, U., and Mostepanenko, V. M., 2007, "Pulsating Casimir Force," J. Phys. A: Math. Theor., **40**, p. F841.

[311] Ninham, B. and Parsegian, V., 1970, "Van Der Waals Interactions in Multilayer Systems," J. Chem. Phys., **53**, p. 3398.

[312] Munday, J. N., Capasso, F., and Parsegian, V. A., 2009, "Measured Long-Range Repulsive Casimir–Lifshitz Forces," Nature, **457**, p. 170.

[313] Parsegian, V. and Ninham, B., 1969, "Application of the Lifshitz Theory to the Calculation of Van Der Waals Forces across Thin Lipid Films," Nature, **224**, p. 1197.

[314] Feiler, A. A., Bergström, L., and Rutland, M. W., 2008, "Superlubricity Using Repulsive Van Der Waals Forces," Langmuir, **24**, p. 2274.

[315] Lee, S.-W. and Sigmund, W. M., 2002, "Afm Study of Repulsive Van Der Waals Forces between Teflon Af™ Thin Film and Silica or Alumina," Colloids Surf. A, **204**, p. 43.

[316] Elbaum, M. and Schick, M., 1991, "Application of the Theory of Dispersion Forces to the Surface Melting of Ice," Phys. Rev. Lett., **66**, p. 1713.

[317] Rodriguez, A., Mccauley, A., Woolf, D., Capasso, F., Joannopoulos, J., and Johnson, S., 2010, "Nontouching Nanoparticle Diclusters Bound by Repulsive and Attractive Casimir Forces," Phys. Rev. Lett., **104**, p. 160402.

[318] Milling, A., Mulvaney, P., and Larson, I., 1996, "Direct Measurement of Repulsive Van Der Waals Interactions Using an Atomic Force Microscope," J. Colloid Interface Sci., **180**, p. 460.

[319] Van Zwol, P. and Palasantzas, G., 2010, "Repulsive Casimir Forces between Solid Materials with High-Refractive-Index Intervening Liquids," Phys. Rev. A, **81**, p. 062502.

[320] Rodriguez, A., Woolf, D., Mccauley, A., Capasso, F., Joannopoulos, J., and Johnson, S., 2010, "Achieving a Strongly Temperature-Dependent Casimir Effect," Phys. Rev. Lett., **105**, p. 060401.

VITA

XIANGLEI LIU

Xianglei Liu was born in Shangqiu, Henan Province, China in 1989. He received bachelor's degree from the Xi'an Jiaotong University in 2011, and came to the School of Mechanical Engineering at Georgia Tech in Fall 2011 as a PhD student in Prof. Zhuomin Zhang's group. His research mainly focuses on near-field thermal radiation, Casimir interactions, solar energy harvesting, and metamaterials. He has authored and co-authored more than 20 journal publications in Applied Physics Letters, ACS Photonics, Physical Review A, International Journal of Heat and Mass Transfer, Optics Express, and other peer-reviewed journals. He has also co-authored over 15 conference presentations, including an invited talk in 6th International Conference on Metamaterials, Photonic Crystals and Plasmonics in New York. He got travel awards supported by the National Science Foundation to attend both 2012 and 2013 ASME International Mechanical Engineering Congress and Exposition. He is a member of ASME, APS, AIAA, and OSA. He serves as reviewers for Physical Review B, Optics Express, Journal of Quantitative Spectroscopy and Radiative Transfer, International Journal of Thermophysics and Heat Transfer, and so on. Besides the research experience, Xianglei Liu also worked as teaching assistant for the thermal-fluids labs of ME 4056 Mechanical Engineering System Laboratory for two semesters.